Coherence Characterization with a Superconducting Flux Qubit through NMR Approaches
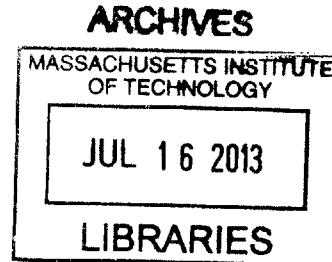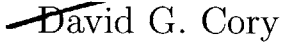
by

Fei Yan

Submitted to the Department of Nuclear Science and Engineering
in partial fulfillment of the requirements for the degree of

Doctor of Philosophy in Nuclear Science and Engineering

at the

MASSACHUSETTS INSTITUTE OF TECHNOLOGY

June 2013

Author ....
Department of Nuclear Science and Engineering
May 8, 2013

Certified by...................
David G. Cory
Professor of Chemistry, University of Waterloo
Thesis Supervisor

Certified by.............
Terry P. Orlando
Professor of Electrical Engineering and Computer Science
Thesis Reader

Certified by.....................
Paola Cappellaro
Assistant Professor of Nuclear Science and Engineering
Thesis Reader

Accepted by ....
Mujid S. Kazimi
TEPCO Professor of Nuclear Engineering
Chair, Department Committee on Graduate Students

Coherence Characterization with a Superconducting Flux Qubit through NMR Approaches

by

Fei Yan

Submitted to the Department of Nuclear Science and Engineering
on May 8, 2013, in partial fulfillment of the
requirements for the degree of
Doctor of Philosophy

Abstract

This thesis discusses a series of experimental studies that investigate the coherence properties of a superconducting persistent-current or flux qubit, a promising candidate for developing a scalable quantum processor. A collection of coherence-characterization experiments and techniques that originate from the field of nuclear magnetic resonance (NMR) are implemented. In particular, one type of dynamical-decoupling techniques that uses refocusing pulses to recover coherence is successfully realized for the first time. This technique is further utilized as a noise spectrum analyzer in the megahertz range, by which a $1/f$-type dependence is observed for the flux noise. Then, a novel method of performing low-frequency noise spectroscopy is developed and successfully implemented. New techniques used in the readout scheme and data processing result in an improved spectral range and signal visibility over conventional methods. The observed power law dependence below kilohertz agrees with separate measurements at higher frequencies. Also, the noise is found to be temperature independent. Finally, a robust noise spectroscopy method is presented, where the spin-locking technique is employed to extract noise information by measuring the driven-evolution longitudinal relaxation. This technique shows improved accuracy over other methods, due to its insensitivity to low-frequency noise. Spectral signatures of coherent fluctuators are resolved, and further confirmed in a time-domain spin-echo experiment.

Thesis Supervisor: David G. Cory
Title: Professor of Chemistry, University of Waterloo

Thesis Reader: Terry P. Orlando
Title: Professor of Electrical Engineering and Computer Science

Thesis Reader: Paola Cappellaro
Title: Assistant Professor of Nuclear Science and Engineering

感谢这一刻为我弹吉他的人

感谢吉他让我想起爱过的人

Acknowledgments

Now as I am writing this last part of my own thesis on my 27th birthday, many faces and things are brought to mind. This unique journey of pursuing a PhD is a mixture of various feelings, and I could not have made it through without the guidance and support from many people.

First, I want to thank my mother Rongxia and father Yong for their generous love and support throughout my life. Making them proud has been an important motivation behind everything I have accomplished in my life. Being their only child, I often feel guilty that I spent too less time with my family during these five years. To them is dedicated this thesis.

I left my hometown, Nanjing, and started my journey in Cambridge under the supervision of Prof. David Cory, to whom I am exceptionally grateful for bringing me to MIT, for introducing me to the fascinating quantum world, for offering me precious research opportunities, for guiding my academic life, for helping me explore my future. Since David moved to Waterloo in 2010, we have had much less overlap. However, it was in my senior years that I started to realize that many things he said about research in the very early days of my PhD life are true! To me, he seems to know everything but touches only a little bit, and lets myself explore. I would really die for understanding his provident ideas and visions. In many senses, he is a myth to me, which makes me respect him even more.

I would also like to thank all the Cory group members - past and present - with whom I have worked, in particular Clarice Aiello, Sarah Sheldon, Kevin Krsulich and Leslie Dewan for all the classes attended together; Troy Borneman, Jonathan Hodges and Kai Iamsumang, with whom I shared the office and had fruitful discussions; Paola Cappellaro for being my academic advisor and sharing ideas in research; and Chandrasekhar Ramanathan for teaching me quantum mechanics. Many thanks also to all the other group members: Mohamed Abutaleb, Cecilia Lopez, Dmitry Pushin, Jamie Yang, Rui Xian. I am also thankful to Jennifer Choy, a former group member, for a great time shared during a conference.

Since I entered MIT, I have also been closely associated with Prof. Terry Orlando's superconducting circuits and quantum computation group. In fact, due to the collaboration between Terry and David, I did most of my research in the Orlando lab. I really appreciate him for the great research opportunities and generous support throughout my PhD life. Terry is the kind of person who is likely to accept whatever the fate is and be happy about it. Although he intervenes with lab issues less often in these years, whenever you need help, he is always there and sets up everything in a nice manner.

Will Oliver is a senior research scientist in the Orlando group. He is effectively the manager of this lab, motivating and guiding everyone. To me, he is a real mentor, who teaches me a lot about the field of superconducting qubits, helps me explore my academic life, pushes me to challenge myself, influences me with his character. Will is truely a wise man. He is knowledgeable, but never brags about. He is confident, but never ignores anyone who needs his attention. He appreciates others' nice work, but never looks down on ourselves. He is ambitious, but always does things with patience. He is a thinker, but always communicates with everyone effectively. He is a busy scientist, but always gets his husband and father job done. All of these make me feel honored to be working with him.

Jonas Bylander and Simon Gustavsson, two Swedish postdocs in the Orlando group, are the guys I have the most overlap with during my PhD life. Jonas is the very first person who teaches me how to be an experimentalist. I learned a lot from him on how to run the dilution fridge, how to properly use electronics and how to present results. I am grateful for his trust on me to run my own experiments in the million-dollar lab. He is a kind and humorous person, who also helps me a lot in life issues. On the other hand, Simon contributes the most to my final PhD works. Since I started to do my own experiments in my third year, he has become the most helpful person in the lab. Whenever I encounter some problems that I cannot figure out, he is always willing to help me and teach me with patience. In addition, he is the most efficient guy I have ever seen, in terms of the speed of finishing work, in terms of the number of quality papers in a year and in terms of enjoying life on mountains every

Contents

List of Figures

16

17

List of Tables

Chapter 1

Introduction

1.1 Quantum Computer and Decoherence

In the past decade, the field of quantum information and quantum computation [1] has developed rapidly and become a hotspot of the physical science. Richard Feynman first suggested the possibly better efficiency in simulating a quantum system by a quantum computer, made of quantum bits (qubits), than the classical computer, made of classical bits [2]. Such quantum computer harnesses the power of quantum superpositions and entanglement to speed up computation. The concept did not draw much attention though until Peter Shor introduced his algorithm [3] and quantum error correction [4].

The power of this super fast computing comes from the natural parallelism created by quantum superposition. Unlike classical bits, whose instantaneous value must be either 0 or 1, a qubit can be the superposition of both eigenstates, $|0\rangle$ and $|1\rangle$. In quantum mechanics [5], the system's state is described by the wave function $|\Psi\rangle$. For N qubits, the wave function of the whole system is generally a linear combination of all the possible 2^N eigenstates,

$$|\Psi\rangle = c_1 |000\cdots000\rangle + c_2 |000\cdots001\rangle + \ldots + c_{2^N} |111\cdots111\rangle , \qquad (1.1)$$

where c_j $(j = 1, 2, \ldots, 2^N)$ is a complex number whose norm squared gives the proba-

bility of observing the qubit at the jth state in measurement. The magic of quantum mechanics is that a quantum transformation of this system, $|\Psi\rangle \rightarrow U |\Psi\rangle$, operates on all the 2^N states simultaneously. Unlike classical parallelism, where multiple circuits are built to execute a same operation (which would require $N \times 2^N$ identical bits), quantum parallelism only requires N qubits. However, measurement will cause the system to collapse to only one of the states with certain probability. To make the quantum parallelism useful, this requires the ability to extract information from the superposition state, and this is called a quantum algorithm. It has been shown that a quantum computer can be substantially more efficient than its classical counterpart for certain classes of problems. One famous example of a quantum algorithm is Shor's algorithm which finds the prime factors of an integer in polynomial time [3].

There are various candidates for the physical realization of a quantum processor. Some early examples include photons [6], atoms in cavity [7], nuclear spins [8], trapped ions [9]. These are traditional types of qubits, because they are mostly real atoms. They are smaller in size, and usually have decent lifetimes. The quantum properties are very well understood. However, in these natural systems, we have limited design flexibility, and it is extremely hard to integrate many qubits together. On the other hand, newer modalities such as semiconductor quantum dots [10] and superconducting Josephson-junction qubits [11, 12, 13], based on modern lithography which patterns solid-state structures on chip, are promising candidates for scalable quantum computing. In this thesis, one particular design of superconducting qubits, the persistent-current or flux qubit [14, 15], is explored. In general, superconducting qubits are superconducting loops interrupted by Josephson junctions [16] and other circuit elements. The nonlinearity introduced by Josephson junctions makes such circuits exhibit anharmonic energy structure and behave just like atoms. This is how the superconducting qubits get the name of artificial atoms.

Superconducting qubits exhibit several advantages over the other candidates. The first and the most important of which is its potential scalability. Because superconducting qubits are basically on-chip circuits, the modern integrated-circuit technology can be implemented straightforwardly. Also taking advantage of artificiality, it is flex-

ible to engineer the quantum properties of these systems. Moreover, since electrical or magnetic elements can be designed to be strongly coupled with each other, we have easy access to control and readout in these systems. These properties makes the superconducting qubits promising in satisfying DiVincenzo's five criteria for a scalable quantum computer [17].

However, an important challenge, related to one of the five criteria, remains for such solid-state quantum devices. That is decoherence, i.e., the systems loss of coherence due to coupling with its noisy environment. When we seek for better control and readout, we unavoidably enter the strong-coupling regime. It is usually accompanied by unwanted strong interactions between the qubit and other degrees of freedom, which leads to decoherence. The main task of the community is thus to fight decoherence.

Encouragingly, the community has made tremendous progress over the last decade or so. From 1999 when Nakamura et al. first showed coherent oscillations at a timescale of 1 nanosecond [18], coherence times has been extended by 10^5 times to $\sim 100\,\mu$s with the recent result from IBM [19]. The history of improvement exhibits a quantum version of Moores law [20]. Notably, the device that is experimentally studied in this thesis held the world record for almost two years [21]. Indeed, superconducting qubits are a leading quantum information processing (QIP) modality

On the other hand, direct manipulation of nuclear spins using radiofrequency electromagnetic pulses is a well-developed field known as nuclear magnetic resonances (NMR) [22, 23]. These techniques are used to measure properties of various types of chemicals, to determine the structure of molecules, and to perform magnetic resonance imaging (MRI). NMR has also been a candidate for realizing a quantum computer. Cory et al. proposed the scheme to use an ensemble of nuclei at room temperature for quantum computation [24].

Since late 1990s, NMR has provided a testbed for many quantum algorithms. For example, Grover's algorithm [25], quantum error correction [26], quantum simulation [27] and Shor's algorithm [28]. Also, many lessons are learned from NMR, for example, techniques of quantum control, coherence characterization, decoherence

mitigation and how to implement full quantum algorithms on entire systems. In this thesis, we demonstrate a series of experiments originating from the field of NMR on a superconducting qubit to explore their potential as basic coherence-characterization tools.

In addition, it is worth noting that the study of superconducting qubits boosts understanding of other physical fields such as macroscopic quantum phenomena, qubit-photon interaction and strongly coupled systems. The pursuit of coherence also facilitates progress in material science. The flux qubit, for example, was used to explore macroscopic superposition [29], quantum physics of artificial atoms [30], active cooling technique [31], a new type of spectroscopy [32] and adiabatic quantum computing [33].

1.2   Outline of this Thesis

This thesis presents coherence-characterization experiments borrowed from NMR and applied to a superconducting persistent-current (PC) qubit or flux qubit, with a focus on the analogy between free- and driven-evolution experiments and the methods to perform noise spectroscopy over a wide frequency range by combining the results.

Chapter 2 sets the theoretical background for most of the experiments explored in this thesis. We begin with a brief introduction of the Bloch representation for visualizing the quantum dynamics of quantum states. We then discuss decohering phenomena during both free and driven evolution, between which exists a well-rounded analogy. Several experiments that are closely related to the rest of the thesis will be introduced.

Chapter 3 introduces the reader to the superconducting flux qubit. We begin with a brief review of the quantum LC resonator, and how Josephson junction introduces anharmonicity into the circuit. We derive the Hamiltonian of the flux qubit, and show how the qubit states is measured by using a SQUID magnetometer. Description of the device in use and experimental setup are given.

Chapter 4 presents experimental details and results of several coherence charac-

terization methods. In the free-evolution category, the T_1 relaxation gives a way to extract high-frequency noise information; the free-induction decay is associated with the integrated inhomogeneity at low frequency; spin echo and more advanced dynamical-decoupling sequences can be used as a intermediate-frequency noise spectrum analyzer. In addition, we have also studied the temperature dependence of the noise. In the driven evolution category, Rabi and rotary echo can be considered as the analogue of free induction and spin echo, respectively, which are related to corresponding rotating-frame noise.

Chapter 5 introduces a novel method to perform low-frequency noise spectroscopy, based on a repeated fixed-time free-induction experiment. A brief overview of low-frequency noise spectroscopy is presented. We then give the detailed recipe of our method, featuring a specific readout scheme and accompanied data processing. The peculiarity of this technique allows us to measure noise spectra up to frequencies limited only by achievable repetition rates of the measurements. Temperature independencies are found in the device by measuring noise spectra at various temperatures up to $200\,\mathrm{mK}$.

Chapter 6 details the spin-locking or $T_{1\rho}$ experiment which is the driven-evolution analogue of the T_1 relaxation. The ability to lock the qubit state with the driving field leads to much less sensitivity to low-frequency noise, compared to Rabi. By measuring the rotating-frame longitudinal relaxation at tunable Rabi frequencies with robust pulse sequences, we obtain noise spectra with better accuracy. We resolve "bump"-like features in the improved spectrum, possibly due to a set of two-level systems, e.g., surface electron spins. We further demonstrate that the underlying noise mechanisms associated with these particular spectral features are also active during free evolution by observing their signature in a time-domain spin-echo experiment.

Chapter 7 concludes with a summary of the major results of the thesis, along with a summary of future work.

Chapter 2

System Dynamics with NMR-like Manipulation

2.1 Introduction

The quantum state of a two-level system (TLS) can be manipulated by techniques inspired from the field of NMR. These techniques are basic building blocks for quantum information science, and have proven useful tools for studying decohering phenomena of a quantum system.

This chapter sets the theoretical background for the entire thesis. We first briefly introduce the Bloch representation for visualizing the quantum state of a TLS, as well as the system dynamics during free and driven evolution. We then elaborate on decohering phenomena during both types of evolution, between which there exists an analogy. Several important coherence-characterization experiments that are closely related to the rest of the thesis will also be introduced.

2.2 Bloch Sphere Representation

We are able to conveniently visualize the dynamics of a quantum two-level system (qubit) in a 3D space by the Bloch sphere representation [34]. The tool facilitates understanding and utilizing quantum mechanics by making sense from classical physics.

Within the density matrix formalism, the (ensemble averaged) state of the qubit can be mapped onto a vector in the Bloch sphere (Fig. 2-1) in a certain reference frame $\{x, y, z\}$:

$$\hat{\rho} = \begin{pmatrix} \rho_{11} & \rho_{12} \\ \rho_{21} & \rho_{22} \end{pmatrix}$$
$$= \frac{1}{2} \left(\hat{\mathbb{1}} + \mathcal{R}_x \hat{\sigma}_x + \mathcal{R}_y \hat{\sigma}_y + \mathcal{R}_z \hat{\sigma}_z \right) = \frac{1}{2} \left(\hat{\mathbb{1}} + \vec{\mathcal{R}} \cdot \vec{\hat{\sigma}} \right) , \tag{2.1}$$

where $\hat{\rho}$ is the density matrix of the two-level system, which is a unity-traced and positive 2-by-2 matrix. $\vec{\mathcal{R}} = (\mathcal{R}_x, \mathcal{R}_y, \mathcal{R}_z)$ represents the 3D vector in Cartesian coordinates. In the operator terms (indicated by $\wedge$), $\hat{\mathbb{1}}$ is the identity matrix, and $\vec{\hat{\sigma}} = (\hat{\sigma}_x, \hat{\sigma}_y, \hat{\sigma}_z)$ are the Pauli matrices:

$$\hat{\mathbb{1}} = \begin{pmatrix} 1 & 0 \\ 0 & 1 \end{pmatrix} ; \ \hat{\sigma}_x = \begin{pmatrix} 0 & 1 \\ 1 & 0 \end{pmatrix} ; \ \hat{\sigma}_y = \begin{pmatrix} 0 & -i \\ i & 0 \end{pmatrix} ; \ \hat{\sigma}_z = \begin{pmatrix} 1 & 0 \\ 0 & -1 \end{pmatrix} . \tag{2.2}$$

The corresponding eigenstates and eigenvalues (E) for the Pauli operators are:

$$\hat{\sigma}_x : |+x\rangle = \frac{1}{\sqrt{2}} \begin{pmatrix} 1 \\ 1 \end{pmatrix} , E = 1 \text{ and}$$

$$|-x\rangle = \frac{1}{\sqrt{2}} \begin{pmatrix} 1 \\ -1 \end{pmatrix} , E = -1;$$

$$\hat{\sigma}_y : |+y\rangle = \frac{1}{\sqrt{2}} \begin{pmatrix} 1 \\ i \end{pmatrix} , E = 1 \text{ and}$$

$$|-y\rangle = \frac{1}{\sqrt{2}} \begin{pmatrix} 1 \\ -i \end{pmatrix} , E = -1;$$

$$\hat{\sigma}_z : |+z\rangle = \begin{pmatrix} 1 \\ 0 \end{pmatrix} , E = 1 \text{ and}$$

$$|-z\rangle = \begin{pmatrix} 0 \\ 1 \end{pmatrix} , E = -1; \tag{2.3}$$

The mapping is unique,

$$\mathcal{R}_x = \rho_{12} + \rho_{21} \, ,$$

$$\mathcal{R}_y = i(\rho_{12} - \rho_{21}) \, ,$$

$$\mathcal{R}_z = \rho_{11} - \rho_{22} \, . \tag{2.4}$$

The length of the Bloch vector $\vec{\mathcal{R}}$ must not exceed unity, i.e., $|\vec{\mathcal{R}}| \leq 1$. The equality holds if and only if the system is in a pure state.
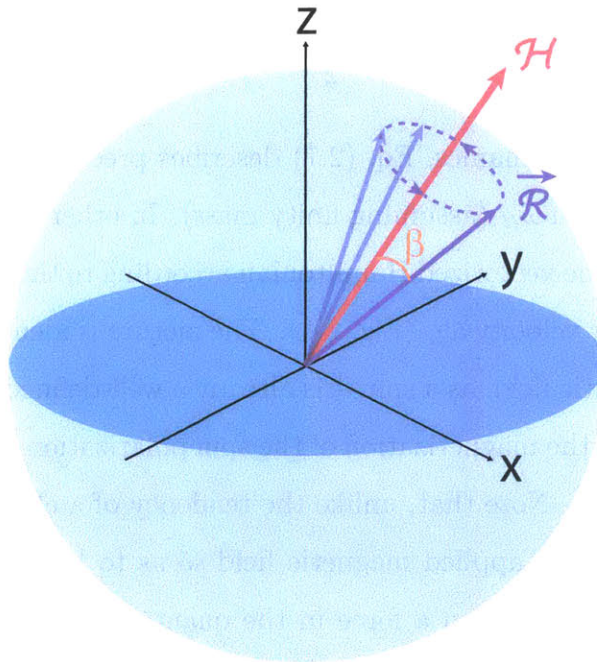
Figure 2-1: Bloch picture of the quantum Larmor precession of a qubit's state vector.

For an arbitrary system Hamiltonian $\hat{\mathcal{H}}$ ($\hat{\mathcal{H}}$ might or might not be static), the evolution of the qubit state is equivalent to a spin-$\frac{1}{2}$ in a magnetic field. In the case of a pure state, the motion is governed by the Schrödinger equation,

$$i\hbar \frac{d}{dt} \Psi = \hat{\mathcal{H}} \Psi \, , \tag{2.5}$$

where Ψ is the wave function. In the case of a general mixed state, it is governed by

the Liouville-von Neumann equation,

$$\frac{d\hat{\rho}}{dt} = \frac{-i}{\hbar}[\hat{\mathcal{H}}, \hat{\rho}] \,, \tag{2.6}$$

which can be rewritten in the Bloch representation as

$$\frac{d\vec{\mathcal{R}}}{dt} = \vec{\omega}_H \times \vec{\mathcal{R}} \,. \tag{2.7}$$

Here, the Hamiltonian is also vectorized in the same 3D space:

$$\hat{\mathcal{H}} = \frac{1}{2}\hbar\vec{\omega}_H \cdot \vec{\sigma} \,. \tag{2.8}$$

Compared to classical mechanics, Eq. (2.7) describes precession of a classical object with angular momentum $\vec{\omega}_H$ (assuming unity mass). In other words, the state vector would rotate around the vectorized Hamiltonian according to the right-hand rule at an instantaneous angular velocity ω_H (Fig. 2-1). The picture is identical to the dynamics of a spin-$\frac{1}{2}$ in a magnetic field, as a spin-$\frac{1}{2}$ is already a well-defined TLS [35]. The state vector is analogous to the magnetization of the spin polarization, and the Hamiltonian acts as a fictitious field. Note that, unlike the tendency of a classical compass needle to be in parallel with the applied magnetic field so as to lessen its energy, the field behaves as a torque rather than a force in the quantum world, driving the spins or qubits to rotate around it. The fixed point of the quantum case of dissipation is the classical result.

For a static Hamiltonian, the rotation persists at the same frequency. The state vector moves on a cone, keeping a constant angle β away from the field, and β depends exclusively on the initial state (Fig. 2-1). The static field is defined as the quantizing field whose orientation sets the quantization axis, because the energy eigenstates of the system are the parallel and anti-parallel vector state along this axis. The energy difference or splitting is $\Delta E = \hbar\omega_H$. The dynamics is exactly the quantum version of Larmor precession. It is also called free evolution or free precession, as the fixed Hamiltonian usually stands for the system's intrinsic or internal field. In

general situations, however, when the Hamiltonian becomes time-dependent, both the rotational axis and angular velocity may change over time.

We now extend our model by including into the Hamiltonian an additional fluctuating part, i.e., $\hat{\mathcal{H}} = \hat{\mathcal{H}}_{\text{static}} + \delta\hat{\mathcal{H}}$ and $\langle \delta\hat{\mathcal{H}} \rangle = 0$. While the static part keeps the precession going, the fluctuating part can cause decoherence in the system. Decoherence here is a more general concept, which includes both longitudinal relaxation and transverse dephasing (to be defined later). Phenomenologically, the decohering dynamics can be modeled by adding longitudinal and transverse decay terms to Eq. (2.7), all with respect to the quantization axis (the static field). Assume $\hat{\mathcal{H}}$ is collinear with the z-axis, i.e., $\hat{\mathcal{H}}_{\text{static}} = \frac{1}{2}\hbar\omega_H\hat{\sigma}_z$, the famous Bloch equations [36] then read

$$
\begin{aligned}
\frac{\mathrm{d}\mathcal{R}_x}{\mathrm{d}t} &= [\vec{\omega}_H \times \vec{\mathcal{R}}]_x - \frac{\mathcal{R}_x}{T_2} \, , \\
\frac{\mathrm{d}\mathcal{R}_y}{\mathrm{d}t} &= [\vec{\omega}_H \times \vec{\mathcal{R}}]_y - \frac{\mathcal{R}_y}{T_2} \, , \\
\frac{\mathrm{d}\mathcal{R}_z}{\mathrm{d}t} &= -\frac{\mathcal{R}_z - \overline{\mathcal{R}}_z}{T_1} \, ,
\end{aligned}
\tag{2.9}
$$

where T_1 and T_2 are the longitudinal and transverse relaxation times. Governed by Eq. (2.9), the state vector keeps rotating around z at a cycling rate of $\omega_H/2\pi$, while simultaneously relaxing to the steady state $\vec{\mathcal{R}} = (0, 0, \overline{\mathcal{R}}_z)$. The steady-state longitudinal polarization $\overline{\mathcal{R}}_z$ is determined by the energy splitting and temperature. Eq. (2.9) is identical to the version in the NMR theory, except that the state vector and the Hamiltonian are replaced by the magnetization and the magnetic field.

From the above discussions, it can be seen that the formalism applied to a general qubit shares many similarities with spin dynamics. This allows us to describe our system by referencing the well-established NMR theories. Moreover, we can manipulate the qubit by using techniques inspired from NMR. Many examples are demonstrated in the rest of this thesis. In fact, various NMR techniques are already extensively implemented in various qubit modalities, especially after the field of quantum computation and information started to flourish in the 1990s. Note that terminologies may

31

be used interchangeably in this thesis, e.g., "spin" for "qubit", "field" for "Hamiltonian", "polarization" for "population" or "probability".

2.3   Laboratory Frame and Quantization

Assume a fairly general model for a two-level system:

$$\hat{\mathcal{H}} = \frac{h}{2}\left[\Delta\hat{\sigma}_z + \varepsilon\hat{\sigma}_x\right], \qquad (2.10)$$

where Δ and ε are parameters closely related to physical quantities in the system. In this sense, the $\{x, y, z\}$-frame are named the physical frame or laboratory frame (Fig. 2-2), despite that the coordinates might not necessarily indicate the real 3D space. For the example of the superconducting flux qubit (to be introduced in detail in Chap. 3), Δ represents the tunnel-coupling strength between two circulating-current states and ε is a quantity linear with the magnetic flux threading a superconducting loop.

In the model, we usually have control over in at least one parameter. Without loss of generality, ε is supposed to be controlled with both DC and AC modulation. Such system represents a typical model for many qubit modalities, in particular, the superconducting qubits, and is completely consistent with the superconducting flux qubit focused in this thesis. The model described in Eq. (2.10), together with subsequent discussions in this chapter, is nevertheless applicable to many other controllable qubit modalities, or requires minor modifications.

The qubit dynamics driven by a static Hamiltonian is described in Sec. 2.2, so, given the Hamiltonian in Eq. (2.10), the qubit will execute Larmor precession around the vectorized Hamiltonian.

Decoherence during free precession is conveniently described in a rotated reference frame $\{x', y', z'\}$, in which the Hamiltonian is quantized or diagonalized along z'. For

Laboratory frame - Qubit frame
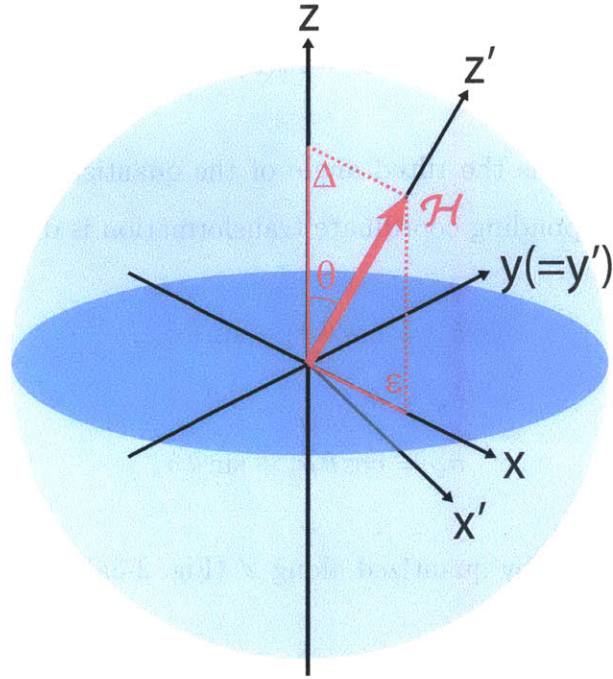
Figure 2-2: Bloch representation of a static Hamiltonian in the laboratory frame $\{x, y, z\}$ and its quantization, as transformed into the qubit frame $\{x', y', z'\}$.

a unitary transformation,

$$\Psi \to \Psi' = \hat{U}^\dagger \Psi \ \text{ or } \ \rho \to \rho' = \hat{U}^\dagger \rho \hat{U} \ , \tag{2.11}$$

where $\hat{U}$ is unitary and, for a TLS, can be represented by a rotational operator, $\hat{U} = \hat{\mathbb{R}}_n(\Theta) = e^{-i\Theta\sigma_n/2}$, where Θ is the rotated angle and n indicates the rotational axis. Substituting the reverse relations in Eq. (2.11) into Eq. (2.5) or Eq. (2.6), we obtain identical equations of motion in this new frame, but with a transformed Hamiltonian,

$$\hat{\mathcal{H}} \to \hat{\mathcal{H}}' = \hat{U}^\dagger \hat{\mathcal{H}} \hat{U} - i\hbar \hat{U}^\dagger \frac{\mathrm{d}\hat{U}}{\mathrm{d}t} \ . \tag{2.12}$$

33

To diagonalize Eq. (2.10), the unitary transformation is a y-rotation,

$$\hat{U} = \hat{\mathbb{R}}_y(\theta) \, , \tag{2.13}$$

where $\theta = \arctan(\varepsilon/\Delta)$ is the tilted angle of the quantization axis from the z-axis (Fig. 2-2). The corresponding coordinate transformation is described by

$$\hat{\sigma}_{x'} = \cos\theta \, \hat{\sigma}_x - \sin\theta \, \hat{\sigma}_z \, ,$$

$$\hat{\sigma}_{y'} = \hat{\sigma}_y \, ,$$

$$\hat{\sigma}_{z'} = \cos\theta \, \hat{\sigma}_z + \sin\theta \, \hat{\sigma}_x \, . \tag{2.14}$$

The Hamiltonian is thereby quantized along z' (Fig. 2-3a):

$$\hat{\mathcal{H}}' = \frac{h}{2}\nu_q\hat{\sigma}_{z'} \, , \tag{2.15}$$

where

$$\nu_q = \sqrt{\varepsilon^2 + \Delta^2} \tag{2.16}$$

is called the qubit frequency, since $h\nu_q$ gives the energy splitting between the two eigenstates, $|+z'\rangle$ and $|-z'\rangle$. The Hilbert space is spanned by these two energy eigenbases, so the new reference frame is named the qubit eigenbasis frame or simply the qubit frame.

The "south pole ↔ ground state" convention

According to Eq. (2.15), the ground (excited) state can be graphically represented by $|-z'\rangle$ ($|+z'\rangle$), or south (north) pole on a unit Bloch sphere (Fig. 2-3a). In many places in the literature, we frequently see the opposite convention, where the ground state is traditionally defined at the north pole (Fig. 2-3b). However, in terms of the Hamiltonian, it would be so if an additional minus sign is placed in Eq. (2.15). The convention historically derives from treating a spin of a negative gyromagnetic ratio, such as an electron spin, in the presence of a static magnetic field. Such system would
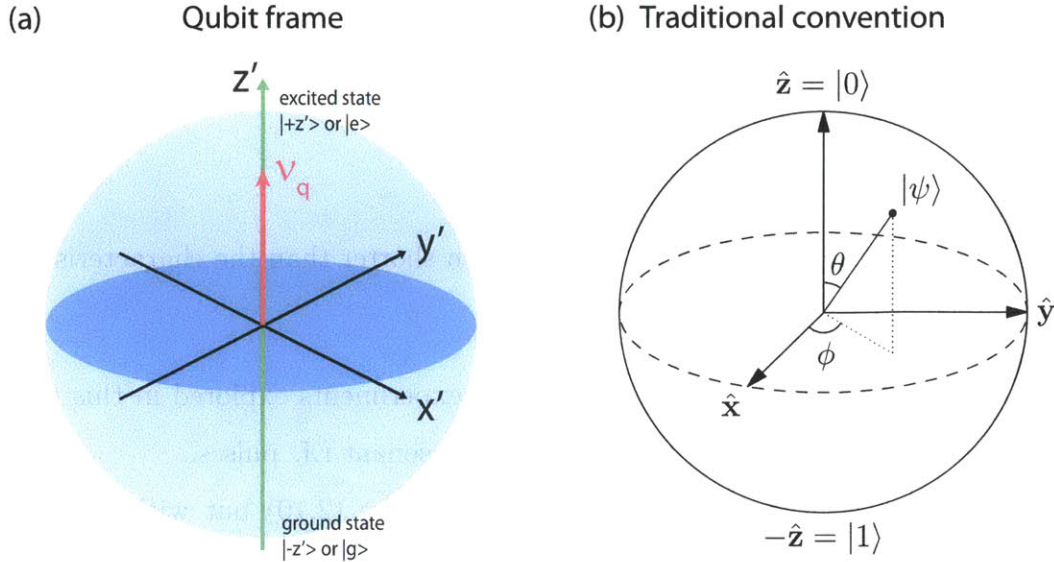
Figure 2-3: (a) Bloch representation of a static Hamiltonian quantized along z' in the qubit frame. The ground (excited) state corresponds to the south (north) pole of the Bloch sphere. (b) The traditional convention, in which $|0\rangle$ at the north pole is considered as the ground state.

have a lower energy when the spin is oriented in the same way as the field. Computer scientists are also used to this convention, since they focus more on the computational indication brought by $|0\rangle$'s and $|1\rangle$'s than on the physical meaning.

However, throughout this thesis, we will follow the "south pole $\leftrightarrow$ ground state" convention to circumvent the minus-sign confusion. A more natural reason for such choice is that it is more intuitive to visualize a system where the pointer of a least energized state is downwards oriented.

2.4 Radiofrequency Pulse

In this section, we will discuss how the qubit is affected by external (time-dependent) control.

A unitary gate operation is equivalent to a length-preserving (trace-preserving in terms of density matrix) rotation of the state vector. In order to implement a qubit operation, experimentally, at least one of the parameters in the Hamiltonian has to

be modulated in either of the following ways [37]:

- (near) resonant radiofrequency (r.f.) pulses,

- adiabatic pulses,

- non-adiabatic DC pulses (rise time much shorter than the characteristic evolution time).

Since only the first approach pertains to the experiments explored in this thesis, we will focus on the dynamics in the presence of resonant r.f. pulses.

Assume the same system Hamiltonian as in Eq. (2.10) but with an additional harmonic drive (Fig. 2-4):

$$\hat{\mathcal{H}} = \frac{h}{2}\left[\Delta\hat{\sigma}_z + \varepsilon\hat{\sigma}_x + A_{\rm rf}\cos(2\pi\nu_{\rm rf}t + \phi)\hat{\sigma}_x\right] . \qquad (2.17)$$

The static part of the Hamiltonian, $\hat{\mathcal{H}}_{\rm static} = \frac{h}{2}\left[\Delta\hat{\sigma}_z + \varepsilon\hat{\sigma}_x\right]$, represents the qubit's internal field, while the oscillating term, $\hat{\mathcal{H}}_{\rm rf} = \frac{h}{2}A_{\rm rf}\cos(2\pi\nu_{\rm rf}t + \phi)\hat{\sigma}_x$, represents the external harmonic drive with amplitude $A_{\rm rf}$, carrier frequency (or r.f. frequency) $\nu_{\rm rf}$ and phase ϕ. The AC control only modulates the tunable parameter, ε, so that the sinusoidal term oscillates along the x-axis.

The question is whether the AC part can produce a large effect on the qubit state, even if the oscillation is weak compared to the static field, i.e., $\nu_{\rm rf} \ll \nu_{\rm q}$, and how. First, we rewrite the Hamiltonian in Eq. (2.17) in the qubit frame (Fig. 2-4):

$$\hat{\mathcal{H}}' = \frac{h}{2}\left[\nu_{\rm q}\hat{\sigma}_{z'} + A_{\rm rf}\cos\theta\cos(2\pi\nu_{\rm rf}t + \phi)\hat{\sigma}_{x'} + A_{\rm rf}\sin\theta\cos(2\pi\nu_{\rm rf}t + \phi)\hat{\sigma}_{z'}\right] . \quad (2.18)$$

The second and third term on the r.h.s. represent the transverse and longitudinal perturbation to the qubit, respectively. From the perturbation theory, to effectively induce transition between the two eigenstates ($|+z'\rangle$ and $|-z'\rangle$) requires two conditions,

- **Transverse coupling:** the perturbation is transverse, i.e., the perturbating term couples the two states between which the transition is desired.

36
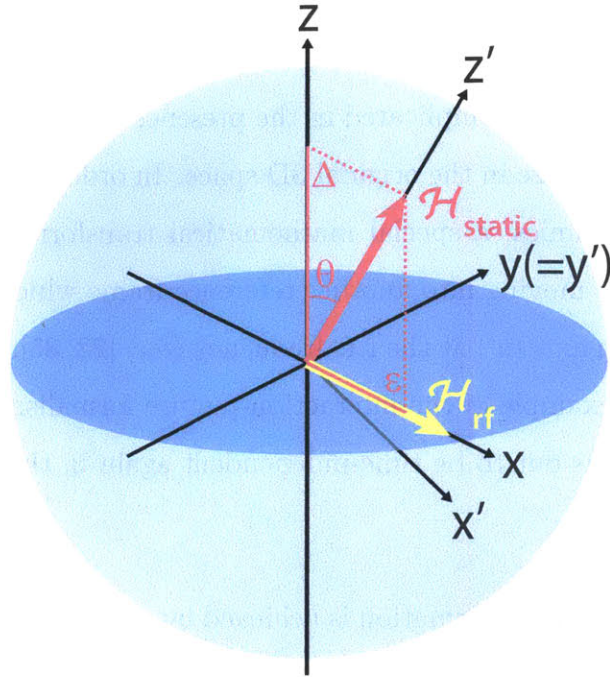
Figure 2-4: Bloch representation of a driven Hamiltonian in Eq. (2.17).

- **Frequency resonance:** the perturbation is near resonant, i.e., the frequency of the perturbation, up to a Planck constant, is equivalent or very close to the energy difference between the two states.

For a TLS with harmonic drive, the resonance condition is expressed by equating the oscillation frequency to the qubit frequency:

$$\nu_{\mathrm{rf}} = \nu_{\mathrm{q}} .$$ (2.19)

The effect is analogous to its classical counterpart, e.g., periodically driving a pendulum, where the swinging of the pendulum only gets significant when the frequency of the periodic driving force matches the natural (eigen-) frequency of the pendulum.

2.4.1 Rotating Frame

The motion becomes more complicated in the presence of an fast oscillating Hamiltonian, and hard to visualize in the original 3D space. In order to conveniently describe and analyze the dynamics, a special mathematical transformation is applied. The transform is done by moving into another reference frame which revolves around the original quantization axis (z') at the r.f. frequency (ν_{rf}) [22, 35]. In fact, the transformation is a special example of the interaction-picture formalism. We will show that, the Hamiltonian turns out to be time-independent again in this rotating frame with proper approximations.

The rotating-frame transformation is achieved by a time-dependent unitary transformation,

$$\hat{U} = \hat{\mathbb{R}}_{z'}(2\pi\nu_{\text{rf}}t) \,, \tag{2.20}$$

with corresponding coordinate transformation,

$$\hat{\sigma}_X = \cos(2\pi\nu_{\text{rf}}t)\hat{\sigma}_{x'} + \sin(2\pi\nu_{\text{rf}}t)\hat{\sigma}_{y'} \,,$$
$$\hat{\sigma}_Y = \cos(2\pi\nu_{\text{rf}}t)\hat{\sigma}_{y'} - \sin(2\pi\nu_{\text{rf}}t)\hat{\sigma}_{x'} \,,$$
$$\hat{\sigma}_Z = \hat{\sigma}_{z'} \,. \tag{2.21}$$

Following the same procedures prescribed in Eq. (2.11) and Eq. (2.12) or the interaction-picture formalism, we can derive, from the original Hamiltonian in Eq. (2.18), a rotating-frame Hamiltonian,

$$\tilde{\tilde{\mathcal{H}}} = \hat{U}^\dagger \hat{\mathcal{H}}'\hat{U} - h\nu_{\text{rf}}\hat{\sigma}_Z/2 \,. \tag{2.22}$$

The second term on the r.h.s. is the quantum analogue of the classical inertial field that arises from transforming to a non-inertial frame. For our example, Eq. (2.22)

38
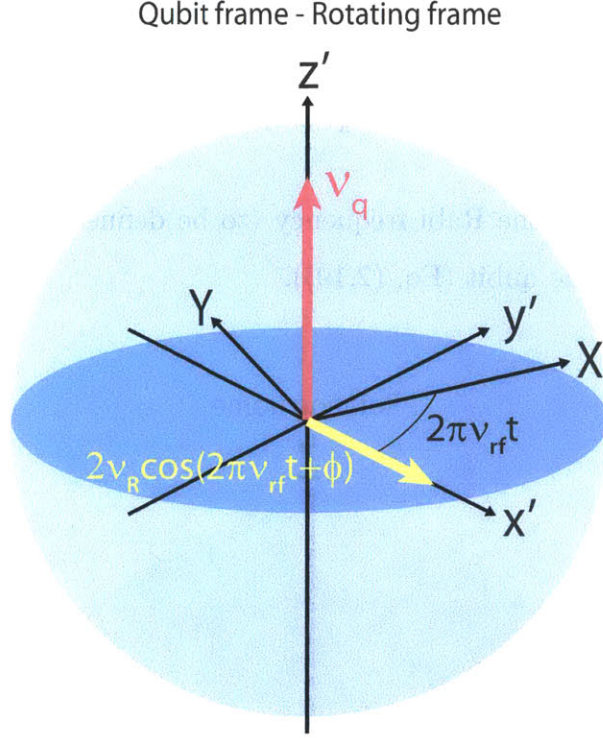
Figure 2-5: Geometric illustration of the transformation between the qubit frame $\{x', y', z'\}$ and the rotating frame $\{X, Y, Z\}$.

can be explicitly expressed by

$$
\begin{aligned}
\hat{\tilde{\mathcal{H}}} = \frac{h}{2} \Big[& \Delta\nu\hat{\sigma}_Z + \frac{1}{2}A_{\mathrm{rf}}\cos\theta\,(\cos\phi\,\hat{\sigma}_X + \sin\phi\,\hat{\sigma}_Y) \\
& + \frac{1}{2}A_{\mathrm{rf}}\cos\theta\,(\cos(-2\pi\cdot 2\nu_{\mathrm{rf}}t - \phi)\hat{\sigma}_X + \sin(-2\pi\cdot 2\nu_{\mathrm{rf}}t - \phi)\hat{\sigma}_Y) \\
& + A_{\mathrm{rf}}\sin\theta\cos(2\pi\nu_{\mathrm{rf}}t + \phi)\hat{\sigma}_Z \Big] \,,
\end{aligned}
\tag{2.23}
$$

where $\Delta\nu = \nu_{\mathrm{q}} - \nu_{\mathrm{rf}}$ is the frequency detuning between the qubit and the driving field.

In the weak driving limit $(A_{\mathrm{rf}} \ll \nu_{\mathrm{rf}})$, the last two lines in Eq. (2.23) can be omitted, since these rapid oscillations average to zero on any appreciable time scale of qubit dynamics in the rotating frame. It is known as the rotating-wave approximation (RWA) [38], which is generally satisfied in the experiments explored in this thesis.

39

The Hamiltonian after approximation is given by (Fig. 2-6)

$$\hat{\tilde{\mathcal{H}}} = \frac{h}{2} \left[\Delta\nu\hat{\sigma}_Z + \nu_{\mathrm{R}} (\cos\phi\,\hat{\sigma}_X + \sin\phi\,\hat{\sigma}_Y) \right], \qquad (2.24)$$

where $\nu_{\mathrm{R}} = \frac{1}{2} A_{\mathrm{rf}} \cos\theta$ is the Rabi frequency (to be defined later) when the driving field is resonant with the qubit (Eq. (2.19)).
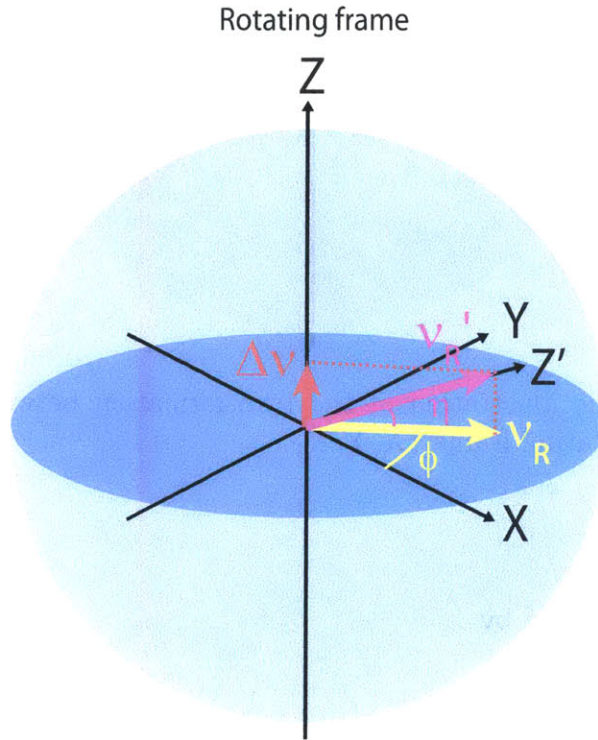
Figure 2-6: Bloch representation of the driven Hamiltonian in the rotating frame after rotating-wave approximation.

Eq. (2.24) describes a static field but in a new reference frame. According to the rules of state evolution (Sec. 2.2), the qubit will execute Larmor precession around the new static driving field (the Z'-axis in Fig. 2-6) in the rotating frame (choice of the reference frame does not affect dynamics as long as equations of motion are identical). Such rotating-frame precession is known as nutation in the NMR language.

The nutation is usually called Rabi precession, and the nutation frequency is named the Rabi frequency after I.I. Rabi who did the pioneering work on the effect of

a gyrating field in magnetic resonance [39]. The effective Rabi frequency in Eq. (2.24),

$$\nu'_{\rm R} = \nu_{\rm R} \sqrt{1 + (\Delta\nu/\nu_{\rm R})^2} \, , \tag{2.25}$$

equates to $\nu_{\rm R}$ when on-resonance. The axis of the vectorized field is tilted from the equatorial plane by an angle $\eta = \arctan(\Delta\nu/\nu_{\rm R})$. For a resonant pulse, the nutation axis lies in the $X{-}Y$ plane (Fig. 2-7). The pulse phase derives from the initial phase of the harmonic drive. Routinely, it is called an X-pulse if $\phi = 0$, or a Y-pulse if $\phi = \pi/2$.
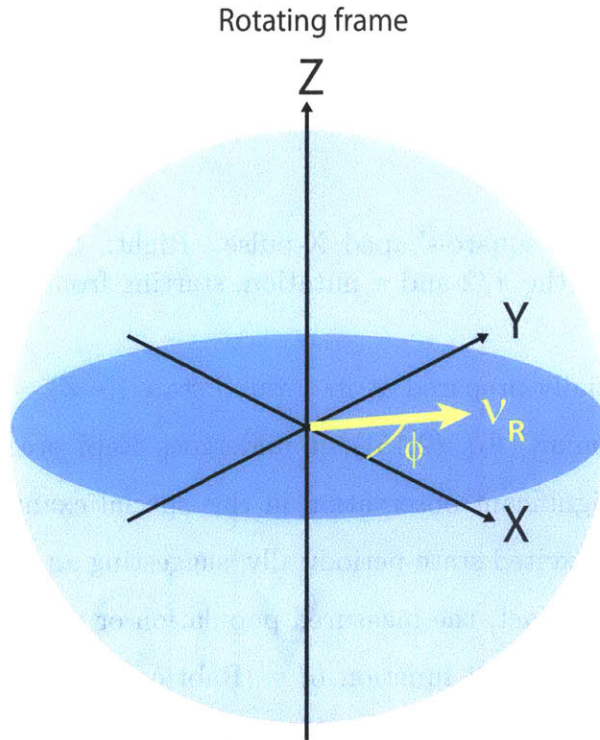
Figure 2-7: The resonantly driven Hamiltonian in the rotating frame.

In the absence of the r.f. pulse, the qubit precesses around the Z-axis at the detuning frequency $\Delta\nu$ in the rotating frame.

2.4.2 Single Pulse

Now, let's look at what a single r.f. pulse does to the qubit in terms of measurement. To begin with, assume the pulse is a resonant X-pulse ($\Delta\nu = 0$, $\phi = 0$) and has

41

a square-profiled envelope (constant amplitude over duration τ) (Fig. 2-8). Driven by the Hamiltonian in Eq. (2.24), the qubit rotates around the X-axis at a constant cycling rate of ν_R over the pulse duration.
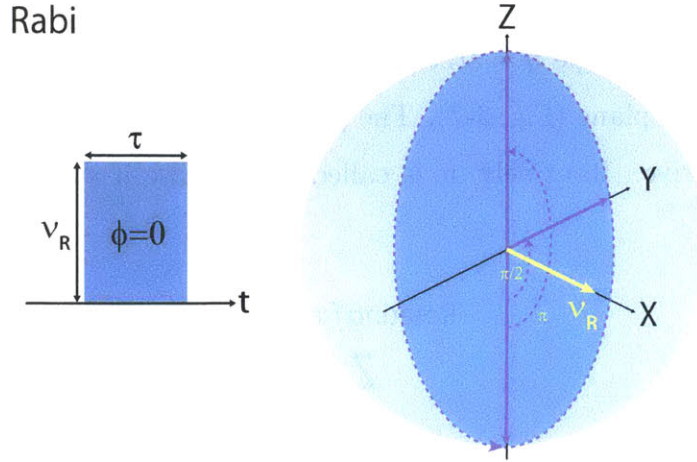
Figure 2-8: Left: single square-shaped X-pulse. Right: Rabi precession. Dashed arrows are examples of the $\pi/2$ and π nutation, starting from the ground state.

If the qubit is initially prepared at its ground state ($|-Z\rangle = |-z'\rangle$), with respect to the static Hamiltonian (Eq. (2.15)), it undergoes Rabi precession in the $Y - Z$ plane (Fig. 2-8). A significant observation in this special example is that the qubit will coincide with the excited state periodically, suggesting an efficient way to induce population inversion. In fact, the measured population or probability of either state after this pulse is a sinusoidal function of τ (Rabi oscillation), and the oscillating frequency is exactly ν_R. If the pulse is off-resonance, the nutation axis is tilted from the X-axis, along with tilt of the precession plane. Consequently, the population cycling becomes less complete, and the system cannot be fully excited.

For Y-pulse ($\phi = \pi/2$), the population-cycling phenomenon is identical to that of the X-pulse. Actually, the observed Rabi oscillation is the same for an arbitrary ϕ, since we only measure the z'-component. This suggests that, for single pulse, the drive phase does not matter to the dynamics. In fact, because we can always choose an arbitrary time-point as our starting time ($t = 0$), the initial phase can be defined at will.

42

Take a look at two important examples of single pulse. If the pulse is configured such that $2\pi\nu_R\tau = \pi$ (the total area integrated over the pulse envelope), we call it a π-pulse. A π-pulse executes exactly half a Rabi cycle, so it can fully excite the qubit from the ground state to the excited state. For an arbitrary initial state, it simply mirrors the state vector against the nutation axis. For example, $\pi)_x$-pulse (subscript indicates the pulse phase) can perform the translation: $|-Z\rangle \rightarrow |+Z\rangle$, $|+Y\rangle \rightarrow |-Y\rangle$, and $|+X\rangle \rightarrow |+X\rangle$. If the pulse is configured such that $2\pi\nu_R\tau = \pi/2$, we call it $\pi/2$-pulse. A $\pi/2$-pulse executes exactly a quarter Rabi cycle, so it is used to create a superposition state from the ground state. For example, $\pi/2)_x$-pulse can perform the translation: $|-Z\rangle \rightarrow |+Y\rangle = \frac{|+Z\rangle+i|-Z\rangle}{\sqrt{2}}$. These two types of pulses are frequently used in practical experiments, and are elementary building blocks of quantum gates.

The square profile of a pulse is only an ideal case. In practice, the actual pulse shape finally seen by the qubit hardly exhibits sudden rise or fall due to bandwidth limit of electronics ubiquitous at different steps (pulse generation, cable transmission, on-chip production). To make the transition smooth, a finite rise and fall time is necessary. Because the frequency response of a Gaussian pulse has a rather narrow bandwidth, the pulses used in our experiments generally have a Gaussian profile for short pulses like the π- and $\pi/2$-pulse, or Gaussian rise and fall (typically $5 \sim 10\,\text{ns}$ rise/fall time) for long pulses. The nutation angle by these shaped pulses is simply the total area integrated over the pulse envelope. In practice, the parameters for the π- or $\pi/2$-pulse configuration are calibrated from Rabi oscillations. That is, measure the qubit after a single pulse with either the pulse amplitude or width updated. The pulse parameters for a desired nutation angle can thus be determined from measured Rabi oscillations.

2.4.3 Multiple Pulses

What if there are multiple pulses? In Sec. 2.4.2, we already saw that a single pulse can be treated as a Rabi field which is turned on for a certain duration in the rotating frame. The combined effect from multiple pulses (same frequency) can be considered as a series of individual fields in the order of their positions over the timeline. However,

a little more attention should be paid to the complication brought by the pulse phase. Because we can only choose one frame as the reference frame, the phases of different pulses should always be referenced to a same starting time, no matter when the pulses are turned on or off. This is equivalent to saying that, if the first pulse is defined as an X-pulse (we can always do this whatever value ϕ_1 is, since we can choose any t as the starting time), the pulse phase in the rotating frame of the k-th pulse is then $\phi_k - \phi_1$. This suggests that the only important quantity is the relative phase with respect to the first pulse. For example, if $\phi_2 - \phi_1 = \pi/2$, the second pulse is effectively a Y-pulse after the first X-pulse. Also, due to the ϕ_1-invariance, the X-Y phase order in the two-pulse example is equivalent to $\overline{Y}$-X or $\overline{X}$-$\overline{Y}$ (bar indicates a 180-degrees phase-shift or negative orientation).

2.5   Free Evolution and Related Experiments

Here, free-evolution related experiments does not mean that the qubit undergoes free precession without any external control throughout the experiment. Rather, it indicates that we will only focus on decohering phenomena associated with the free-evolution or pulse-free periods within the measurement protocol. To put in another way, the desired noise information is encoded during the free-evolution periods. In fact, properly designed pulse sequences are required to manipulate the qubit so that the concerned noise processes manifest themselves in the observations.

These experiments typically consist of multiple short pulses like $\pi/2$- and π-pulses, with a particular pulse-spacing setting, so that noise information is encoded in a desired way.

2.5.1   Free Evolution and Its Decoherence

Here, we discuss the qubit's decohering dynamics during free evolution. As shown in Sec. 2.3, under the internal Hamiltonian (Eq. (2.15)), the qubit undergoes free precession at the qubit frequency (ν_q) around the quantization axis (z') in the qubit frame. The azimuthal angle of the qubit's Bloch vector β depends on the initial

state. For example, if the qubit starts from the ground ($|-z'\rangle$) or excited state ($|+z'\rangle$), $\beta = 180°$ or $0°$. In either case, the qubit state remains unchanged during free precession. If the qubit is initially prepared at an equal-superposition state, e.g., $|\pm x'\rangle$ or $|\pm y'\rangle$, $\beta = 90°$ and the qubit will precess around the equatorial plane. In general, for an arbitrary value of β, the qubit leaves a cone-like trace symmetric about z' (Fig. 2-1).

Now we include decoherence into the system by introducing an additional perturbative Hamiltonian,

$$\hat{\mathcal{H}}_{\mathrm{I}} = \frac{h}{2} \big[\hat{Q}_\Delta \, \hat{\sigma}_z + \hat{Q}_\varepsilon \, \hat{\sigma}_x \big] \ . \tag{2.26}$$

The Hamiltonian describes the system's coupling to a noisy environment. $\hat{Q}_\Delta(t)$ ($\hat{Q}_\varepsilon(t)$) represents the fluctuating bath variable that couples to the Δ (ε) terms. Since ε and Δ are physically different, $\hat{Q}_\Delta(t)$ and $\hat{Q}_\varepsilon(t)$ are supposed to be uncorrelated. Also note that all fluctuations discussed in this thesis, unless otherwise specified, are zero-mean.

The noise power spectral densities (PSD), $S_\Delta(f)$ and $S_\varepsilon(f)$, are defined as the symmetrized bilateral PSD:

$$S_\lambda(f) = (2\pi)^2 \int_{-\infty}^{\infty} dt \exp(-i2\pi ft) \frac{1}{2} \langle \lambda(0)\lambda(t) + \lambda(t)\lambda(0) \rangle \ , \tag{2.27}$$

where $\lambda \in \{x', y', z' \dots$ or $\Delta(= \hat{Q}_\Delta), \varepsilon(= \hat{Q}_\varepsilon) \dots \}$ indicates either the fluctuating part of system Hamiltonian or the axis to which those fluctuations couple. It is parametrized in units of frequency [Hz], e.g., for λ originally in unit of energy [J], it is reduced by a Planck constant, i.e., $\lambda \rightarrow \lambda/h$. The symmetrized autocorrelation function, $\frac{1}{2}\langle \lambda(0)\lambda(t) + \lambda(t)\lambda(0) \rangle$, is equivalent to the regular autocorrelation function $\langle \lambda(0)\lambda(t) \rangle$ for classical noise or quantum noise in the classical limit, i.e., $hf < k_{\mathrm{B}}T$, where k_{B} is Boltzmann's constant and T is the temperature. For quantum noise, the expectation value is taken over the environment's ensemble state, i.e., $\langle \hat{O} \rangle = \mathrm{Tr}_{\mathrm{E}}[\hat{O}\rho_{\mathrm{E}}]$, where ρ_{E} is the environment's density matrix. More discussion about the difference between the quantum and classical noise can be found in Appendix A.

When transformed into the qubit frame, the Hamiltonian in Eq. (2.26) becomes

$$
\begin{aligned}
\hat{\mathcal{H}}_I' &= \frac{h}{2}\left[(\hat{Q}_\Delta \cos\theta + \hat{Q}_\varepsilon \sin\theta)\hat{\sigma}_{z'} + (-\hat{Q}_\Delta \sin\theta + \hat{Q}_\varepsilon \cos\theta)\hat{\sigma}_{x'}\right] \\
&= \frac{h}{2}\left[\hat{Q}_{z'}\hat{\sigma}_{z'} + \hat{Q}_{x'}\hat{\sigma}_{x'}\right] .
\end{aligned}
\tag{2.28}
$$

The Δ and ε noise are assumed to be uncorrelated as their fluctuations have different physical origins (in the device we explored in this thesis), the PSD of the qubit-frame noise $\hat{Q}_{z'}(t)$ or $\hat{Q}_{x'}(t)$ is a (co)sinusoidally weighted sum of the PSD in the lab frame, namely,

$$
\begin{aligned}
S_{x'}(f) &= \sin^2\theta \, S_\Delta(f) + \cos^2\theta \, S_\varepsilon(f) , \\
S_{z'}(f) &= \cos^2\theta \, S_\Delta(f) + \sin^2\theta \, S_\varepsilon(f) .
\end{aligned}
\tag{2.29}
$$

Eq. (2.29) suggests that we are able to tune the sensitivity to lab-frame noise by varying θ or, physically, ε. In the special case when $\varepsilon = 0$, the laboratory frame and the qubit frame coincide and the z'-noise has no contribution from the ε noise.

The evolution of this open quantum system in the Markovian weak-coupling limit can be solved by the Bloch-Redfield theory. For a general open quantum system, $\hat{\mathcal{H}}_S + \hat{\mathcal{H}}_I + \hat{\mathcal{H}}_E$ ($\hat{\mathcal{H}}_S$, $\hat{\mathcal{H}}_I$ and $\hat{\mathcal{H}}_E$ stand for the system, interaction and environment Hamiltonian, respectively), the evolution of the combined system, $\hat{\rho}(t)$, in the interaction picture, $\hat{\rho}_{int} = \hat{U}^\dagger \hat{\rho} \hat{U}$ ($\hat{U} = e^{-i\hat{\mathcal{H}}_S t/\hbar}$), is governed by the interaction-picture Liouville-von Neumann equation,

$$
\frac{d\hat{\rho}_{int}}{dt} = \frac{-i}{\hbar}[\hat{\mathcal{H}}_{I,int}, \hat{\rho}_{int}] ,
\tag{2.30}
$$

where $\hat{\mathcal{H}}_{I,int}' = \hat{U}^\dagger \hat{\mathcal{H}}_I' \hat{U}$. In the rest, we omit the subscript "int" for more uncluttered expressions.

Next, making two major assumptions,

- **Born approximation:** the coupling is weak enough and the reservoir is big enough, so that the density matrix factorizes, $\hat{\rho} = \hat{\rho}_S \otimes \hat{\rho}_E$, and the environment

stays unperturbed, i.e., $\hat{\rho}_E$ is time-independent

- **Markovian approximation:** the correlation time of the noise in the rotating frame is much shorter than the relaxation time, or the system is "memoryless" over the time scale of the environment's fluctuation,

we obtain the Redfield equation,

$$\frac{d\hat{\rho}_S(t)}{dt} = -\frac{1}{\hbar^2} \int_{-\infty}^{0} d\tau\, \mathrm{Tr}_E[\hat{\mathcal{H}}_I(t), [\hat{\mathcal{H}}_I(t+\tau), \hat{\rho}_S(t) \otimes \hat{\rho}_E]] \,. \qquad (2.31)$$

Substituting the Hamiltonians in Eq. (2.15) and Eq. (2.28) into Eq. (2.31) and working out the algebra, we find

$$\hat{\rho}_S(t) = \begin{pmatrix} \rho_{uu}(t) & \rho_{ud}(t) \\ \rho_{du}(t) & \rho_{dd}(t) \end{pmatrix}$$

$$= \begin{pmatrix} \overline{\rho_{uu}} + (\rho_{uu}(0) - \overline{\rho_{uu}})\, e^{-\Gamma_1 t} & \rho_{ud}(0)\, e^{-(\Gamma_1/2 + \Gamma_\varphi)t} \\ \\ \rho_{du}(0)\, e^{-(\Gamma_1/2 + \Gamma_\varphi)t} & \overline{\rho_{dd}} + (\rho_{dd}(0) - \overline{\rho_{dd}})\, e^{-\Gamma_1 t} \end{pmatrix} . \qquad (2.32)$$

The decay rates are related to the qubit-frame noise PSDs by

$$\Gamma_1 = \frac{1}{2} S_{\perp z'}(\nu_q) = \frac{1}{2} S_{x'}(\nu_q) \,,$$

$$\Gamma_\varphi = \frac{1}{2} S_{z'}(0) \,,$$

$$\Gamma_2 = \frac{1}{2}\Gamma_1 + \Gamma_\varphi \,, \qquad (2.33)$$

The rate-PSD dependence can be further broken down to lab-frame noise by Eq. (2.29).

In the "south pole $\leftrightarrow$ ground state" convention, the lower right element of the density matrix corresponds to the ground state population. $\overline{\rho_{uu}}$ ($\overline{\rho_{dd}}$) is the excited (ground) state population in thermal equilibrium with the environment. Given an effective environment temperature T, the population ratio follows the Boltzmann distribution, i.e., $\overline{\rho_{uu}}/\overline{\rho_{dd}} = e^{-\bar{\beta}\nu_q}$, where $\bar{\beta} = h/k_B T$. When transformed back to the

qubit frame, Eq. (2.32) in the Bloch representation can be written as (Fig. 2-9)

$$\frac{d\mathcal{R}_{x'}}{dt} = -\Gamma_2 \mathcal{R}_{x'} - 2\pi\nu_q \mathcal{R}_{y'} ,$$
$$\frac{d\mathcal{R}_{y'}}{dt} = -\Gamma_2 \mathcal{R}_{y'} + 2\pi\nu_q \mathcal{R}_{x'} ,$$
$$\frac{d\mathcal{R}_{z'}}{dt} = -\Gamma_1 (\mathcal{R}_{z'} - \overline{\mathcal{R}}_{z'}) , \tag{2.34}$$

where $\overline{\mathcal{R}}_{z'} = \overline{\rho_{uu}} - \overline{\rho_{dd}} = -\tanh(\frac{\bar{\beta}\nu_q}{2})$ is the longitudinal equilibrium polarization. Eq. (2.34) is identical to the Bloch equation in Eq. (2.9).
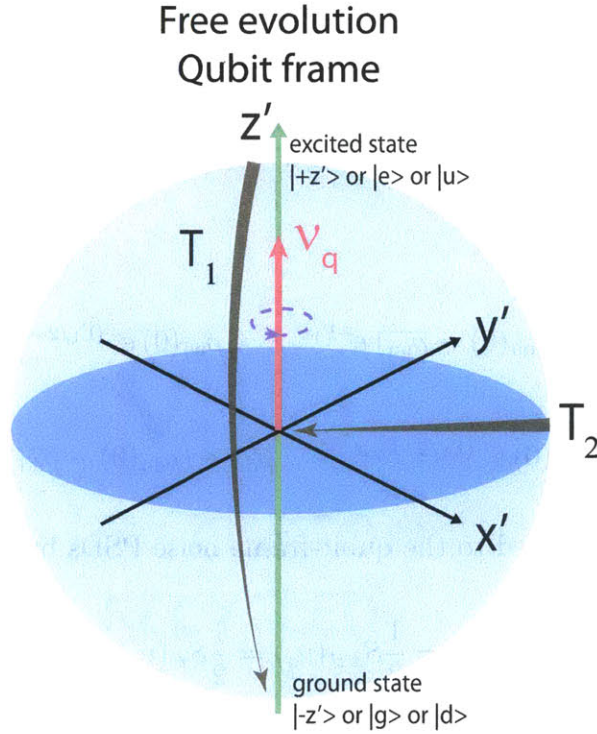
Figure 2-9: Free-evolution dynamics in the qubit frame. The red arrow indicates the quantizing field. The qubit undergoes Larmor precession (purple dashed line) around the longitudinal axis (green arrow), while depolarizes (grey arrows) both longitudinally (T_1) and transversely (T_2) at the same time.

We now make several comments on Eq. (2.34) to facilitate our understanding.

1. In Eq. (2.34), the x'- and y'-depolarization due to T_1 process share the same rate, $\Gamma_1/2$. One might ask the question: what leads to the symmetry of the transverse depolarization while the noise couples to the x' channel only. In fact, the effect of

x'-noise is similar to depolarization from the bit-flip channel [1], so there should be asymmetry in the rates, i.e., $\Gamma_{x'} = 0$ and $\Gamma_{y'} = \Gamma_1$ (ignoring pure dephasing). However, Eq. (2.34) is still valid, because we made the Markovian approximation during derivation which assumes that the noise correlation time is much shorter than the relaxation times. The assumption suggests that $\nu_q \gg \Gamma_1, \Gamma_2$, so that the qubit effectively mixes the x'- and y'-depolarization during fast precession. In Sec. 2.6.1, we will see a non-Markovian example.

2. The equilibrium population ratio is determined from the relaxation (Γ_-, not to be confused with Γ_1) and excitation rate (Γ_+) (see Appendix A for more details):

$$\frac{\overline{\rho_{uu}}}{\overline{\rho_{dd}}} = \frac{\Gamma_+}{\Gamma_-} , \tag{2.35}$$

and they are related to the unsymmetrized PSD at the positive and negative of the qubit frequency, respectively:

$$\Gamma_- = \frac{1}{2}S^U_{\perp z'}(\nu_q) ,$$
$$\Gamma_+ = \frac{1}{2}S^U_{\perp z'}(-\nu_q) . \tag{2.36}$$

$S^U_\lambda(f)$ is the Fourier transform of the unsymmetrized (regular) correlation function, $\langle \lambda(0)\lambda(t) \rangle$, and is different from its negative counterpart for general quantum fluctuations $\hat{\lambda}$, because the time-dependent quantum variables at symmetric times do not commute. It follows that $\Gamma_1 = \Gamma_- + \Gamma_+ = \frac{1}{2}S^U_{\perp z'}(\nu_q) + \frac{1}{2}S^U_{\perp z'}(-\nu_q) = S_{\perp z'}(\nu_q)$. For the quantum noise, $S^U_\lambda(-f)/S^U_\lambda(f) = e^{-\beta f}$ at an equilibrium temperature T. In the low-temperature limit which pertains to our experiment ($\nu_q \approx 5\,\text{GHz}$ and $T \approx 65\,\text{mK}$), the equilibrium approaches the ground state (Fig. 2-9).

3. We did not take into account any y- or y'-noise (physically, charge noise in our device) in the model, since it is negligible in our system and provides no more insight about the decohering dynamics. To incorporate the effect from y

noise is trivial, simply adding an extra term, $\hat{Q}_y\,\hat{\sigma}_y$, to Eq. (2.26). Assuming uncorrelated with other noise, the y-noise (equivalent to y'-noise) is included into the transverse noise, $S_{\perp z'}(\nu_q) = S_{x'}(\nu_q) + S_{y'}(\nu_q)$, and contributes to Γ_1 only.

Before further discussion, please bear in mind the fact that decoherence in superconducting qubits should be understood in a sense of time-ordered ensemble average. Unlike measuring an ensemble of spins in NMR experiments, here we only have single artificial spin and are required to repeat a same measurement, typically, several thousand times to improve population estimate.

Following Eq. (2.32), the free-evolution decohering processes are conveniently defined with respect to the quantization axis, z' (Fig. 2-9).

$T_1 = 1/\Gamma_1$ is the longitudinal depolarization/relaxation time, or often "relaxation time" for short. It describes how fast the longitudinal polarization (portion along z' or the diagonal matrix element) approaches equilibrium (Fig. 2-18a). Such longitudinal relaxation is the consequence of environmental modes at the qubit frequency (ν_q) transversely coupled ($\perp z'$) to the qubit. The inversion-recovery experiment (Sec. 2.5.2), which initializes the qubit at the excited state and records how it temporally relaxes along z' (Fig. 2-18a), is one of the standard methods for measuring T_1.

$T_2 = 1/\Gamma_2$ is the transverse depolarization/relaxation time, and often named "coherence time" or "dephasing time". It estimates how fast the transverse polarization (portion in the $x'-y'$ plane or the off-diagonal matrix element) decays. In the Markovian weak-coupling limit, the Bloch-Redfield theory [40, 41, 42] gives a simple description of the exponential dephasing rate (Eq. (2.32)): $1/T_2 = 1/2T_1 + 1/T_\varphi$, where $T_\varphi = 1/\Gamma_\varphi$ is the pure dephasing time. Unfortunately, in many realistic situations such as when the noise exhibits a $1/f$-type spectrum ($S(f) = 1/|f|^\alpha$, where $\alpha \sim 1$), the Bloch-Redfield approach does not apply, because the noise correlation times become enormous at low frequencies. However, the decay due to T_1 process and due to pure dephasing still factorize [43]. Pure dephasing is an ensemble-averaging effect over different realizations of the fluctuating qubit frequency [37], which is sensitive to

longitudinally coupled low-frequency noise.

Depending on the experiments, there are various types of T_2. T_2 usually means the transverse depolarization during bare free precession, like what we described previously in this section. However, for the rest, we would like to extend it as a general designation for any type of transverse depolarization. The simplest one is the free-induction or Ramsey decay (Sec. 2.5.3), which measures the associated coherence time T_{Ramsey} (usually seen as T_2^* in the literature) with bare equatorial precession (Fig. 2-18b). The measured pure dephasing is the result of ensemble averaging over the inhomogeneous broadening [44] (temporal inhomogeneity due to low-frequency noise), suggesting the process can be corrected for.

If a refocusing pulse is added in the middle of the free-evolution period as in the spin-echo or Hahn-echo experiment (Sec. 2.5.4), the effect from the low-frequency noise can be reduced. In superconducting qubits where the noise PSD is usually $1/f$-type, and we obtain the usually much longer echo decay time T_{Echo}. More advanced sequences such as the CP-like sequence (Sec. 2.5.4), a generalized version of the spin-echo sequence, may further improve coherence and, in addition, be utilized to extract the PSD through its noise-filtering properties.

2.5.2 Inversion Recovery

The inversion-recovery experiment is a method for measuring the longitudinal relaxation time, T_1. The value of T_1 provides information about environmental modes at the qubit frequency, ν_q (typically several gigahertz, categorized in the high-frequency regime). It is a technique originally used in NMR [35].

The pulse sequence (Fig. 2-10) consists of a single π-pulse and a certain delay τ before readout. The π-pulse brings the qubit from the thermal ground state $|-z'\rangle$ (we normalize the equilibrium polarization at the beginning) to the excited state $|+z'\rangle$. During the delay, the qubit undergoes longitudinal relaxation until thermal equilibrium ($|-z'\rangle$) is reached again. The polarization relaxes from $|+z'\rangle$ to $|-z'\rangle$ along the z'-axis in the process. By stepping τ, we thereby record how the qubit relaxes.

51

(a) Inversion-Recovery Seq.
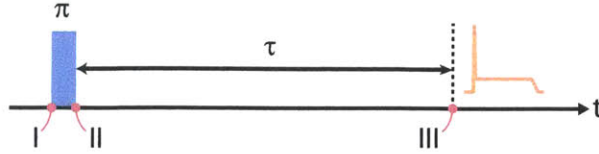
(b) Dynamics in Inversion-Recovery Seq.
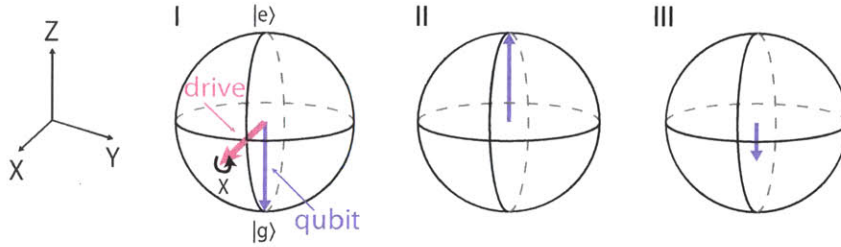
Figure 2-10: (a) Inversion-recovery pulse sequence. The readout pulse (orange) is delayed by a duration of τ after the π-pulse. (b) Bloch sphere representation of the rotating-frame qubit dynamics under the sequence in (a). The purple arrow is the qubit's state polarization, while the magenta arrow indicates the driving field. The qubit is initially prepared in its ground state ($|g\rangle = |-z'\rangle$) (I). The first π-pulse (not necessary to be an X-pulse) rotates the qubit by 180° to the excited state (II). During the delay, the qubit undergoes T_1 relaxation towards equilibrium. The instantaneous longitudinal polarization after the delay is read out (III).

The decay law is exponential (Eq. (2.34)), given that the correlation time of the transverse noise in the rotating frame is short. In the noise-filtering perspective, the assumption can be understood as that the transverse noise has a smooth spectrum around the qubit frequency over a width of $1/T_1$. The ground-state probability can be expressed as:

$$P_{\text{IR}}(\tau) = 1 - \exp\left(-\Gamma_1\tau\right) , \qquad (2.37)$$

where $\Gamma_1 = 1/T_1$ is the longitudinal relaxation rate, and is related to the qubit-

frequency noise transversely coupled to the system (Eq. (2.33) and Eq. (2.29)):

$$\Gamma_1 = \frac{1}{2} S_{\perp z'}(\nu_q) = \frac{1}{2} S_{x'}(\nu_q) \ . \tag{2.38}$$

Prefactors other than "$\frac{1}{2}$" in Eq. (2.38) might be spotted in other literatures. This is due to variation in the PSD definition Eq. (2.27). In this thesis, we follow the convention of using symmetrized bilateral PSD with type-I Fourier transform. We clarify the confusion in Appendix B.

2.5.3   Free Induction

The free-induction (FI) or Ramsey experiment is a method for measuring the transverse depolarization (loss of phase coherence, dephasing) time T_2, during bare free precession. Here, T_{Ramsey} denotes the characteristic decay time. However, as we discussed in Sec. 2.5.1, there might be neither a simple form for the decay law nor a well-defined T_{Ramsey}. In practice, the $1/e$-time, T_e, at which the normalized signal (starting from unity) drops to e^{-1}, is a universal figure of merit. The value of T_{Ramsey} provides valuable information about the low-frequency noise. This technique is used in NMR to characterize the evolution of the transverse magnetization [45], and is the basis of Fourier transform spectroscopy.

Before introducing the free-induction sequence, let us take a few minutes to illustrate the mechanism of dephasing. If the qubit starts with a superposition state, in the rotating frame and in the resonant case, the state vector is supposed to stay where it is permanently. However, if there is fluctuation of the precession frequency, the qubit precesses at different rates. One example is illustrated in Fig. 2-11c. For an ensemble of realizations, the state vectors, initially synchronized, continue to fan out due to their random precession rates. Over a characteristic time, their phases becomes totally random. As a result, we would observe the average transverse polarization to decay.

If the distribution of the fluctuating precession rate is known, the expectation value

of the transverse polarization can be computed by summing up all the realizations:

$$\mathcal{R}_Y = \int_{-\infty}^{\infty} d\Delta\nu \, \cos(2\pi\Delta\nu\tau) \, \mathcal{P}(\Delta\nu) \,, \qquad (2.39)$$

where $\mathcal{P}(\Delta\nu)$ is the probability density function of $\Delta\nu$. An important indication of Eq. (2.39) is that the time-domain signal is the Fourier transform of the fluctuator's spectral distribution. For the typical example of Gaussian distributed noise, the Fourier transform yields a Gaussian decay in the time-domain.

The pulse sequence (Fig. 2-11) applicable to the superconducting qubits consists of two $\pi/2$-pulses (both along X) spaced by τ. The experiment can be done with either on- or off-resonance pulses. For resonant pulses, the first $\pi/2$-pulse brings the qubit from the ground state ($|-Z\rangle$) to the superposition state ($|+Y\rangle$). During the free-evolution period between the pulses, the qubit undergoes transverse depolarization (diminishing of Y-polarization). The second $\pi/2$-pulse brings the remaining polarization back onto the Z-axis for readout. Here we have ignored the T_1 process, because the transverse depolarization is usually much faster. For off-resonance pulses, the dynamics is identical except that the qubit precesses at a rate equivalent to the frequency detuning $\Delta\nu$, while the transverse polarization continues to shrink. By stepping τ, we record how the qubit dephases.

Given short-correlated noise, the decay law is exponential (Eq. (2.34)):

$$P_{\mathrm{FI}}(\tau) = \frac{1}{2} + \frac{1}{2}\cos(2\pi\Delta\nu\tau) \times \exp\left(-(\Gamma_1/2 + \Gamma_\varphi)\tau\right) \,, \qquad (2.40)$$

where Γ_φ is the pure-dephasing rate. Pure dephasing is the consequence of ensemble averaging over the inhomogeneous broadening of the qubit frequency:

$$
\begin{aligned}
\Gamma_\varphi &= \frac{1}{2} S_{z'}(0) \\
&= \frac{1}{2}\left(\cos^2\theta \, S_\Delta(0) + \sin^2\theta \, S_\varepsilon(0)\right) \\
&\approx \frac{1}{2}\left(S_\Delta(0) + \frac{\varepsilon^2}{\Delta^2} S_\varepsilon(0)\right) \,.
\end{aligned}
\qquad (2.41)
$$

54

(a) Free-Induction Seq.
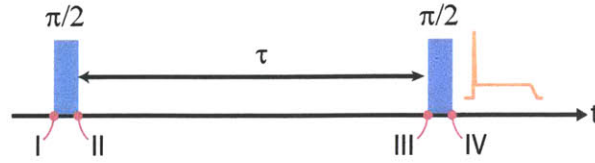
(b) Dynamics in Free-Induction Seq.
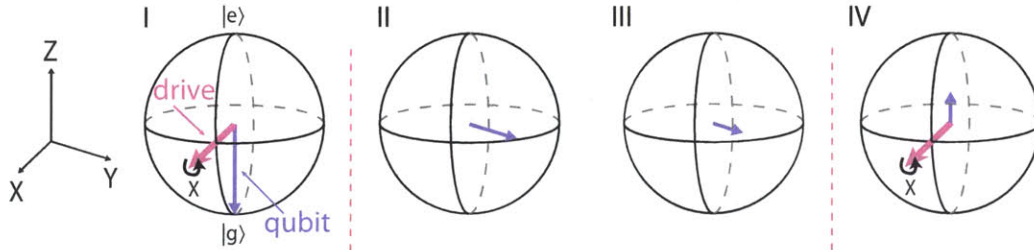
(c) Dephasing
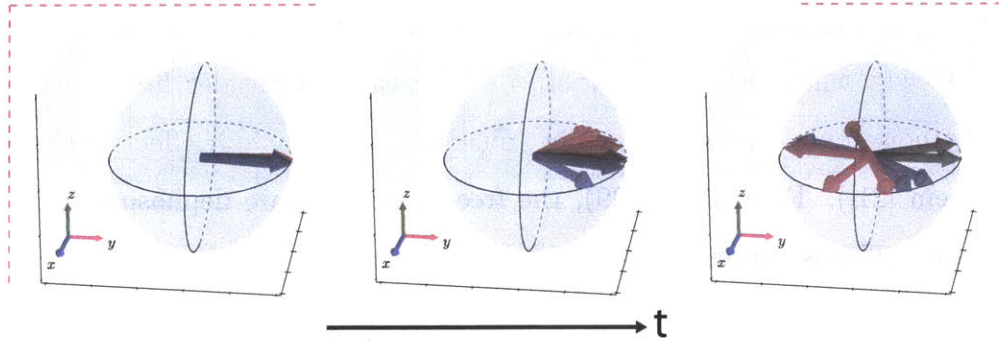
Figure 2-11: (a) Free-induction pulse sequence. The readout pulse (orange) is performed right after the second $\pi/2$-pulse. (b) Bloch sphere representation of the rotating-frame qubit dynamics under the sequence in (a). The purple arrow is the qubit's state polarization, while the magenta arrow indicates the driving field. The qubit is initially prepared in its ground state ($|g\rangle = |-z'\rangle = |-Z\rangle$) (I). The first $\pi/2$-pulse rotates the qubit by 90° into the equatorial plane (II). During the delay, the qubit undergoes transverse relaxation (III). The second $\pi/2$-pulse projects the remaining polarization onto Z ($=z'$) for readout (IV). (c) Illustration of the dephasing effect by tracking an ensemble of state vectors whose color indicates faster (red) or slower (blue) precession rate. From left to right: the vectors fan out along with the free-induction time.

The last line in Eq. (2.41) describes the situation when $\varepsilon \ll \Delta$, corresponding to the working range in our experiments. It indicates that the Δ noise dominates free-induction decay when biased at the so-called sweet spot, i.e., $\varepsilon = 0$. On the other

55

hand, the ε noise may overpower it, given that the working point is sufficiently away from the sweet spot.

However, the decay is usually not simply exponential. For example, in many solid-state structures, the low-frequency part of the noise spectrum exhibits a $1/f$-type power law. This will make the noise singular at zero frequency. Fortunately, the transverse relaxation due to T_1 process and due to pure dephasing still factorize [43] (ignoring the sinusoidal modulation from the detuning):

$$P(\tau) = \exp\left(-\frac{\Gamma_1}{2}\tau\right) h(\tau) . \tag{2.42}$$

Note that Eq. (2.42) is not restricted to free-induction decay, but any type of transverse decay.

The free-induction pure dephasing can be analyzed from the effect of quasistatic noise [46, 44], when the noise statistics is Gaussian. Consider first-order (linearly coupled) noise only (the second-order (quadratically coupled) effect is negligible in our system [21]). From Eq. (2.39), the free-induction pure dephasing for Gaussian distributed noise is expressed by

$$h_{\mathrm{FI}}(\tau) = \exp\left(-\frac{(2\pi)^2 \sigma_{z'}^2 \tau^2}{2}\right) , \tag{2.43}$$

where

$$\begin{aligned}
\sigma_{z'}^2 &= 2 \int_{1/t_{\mathrm{acq}}}^{1/2\tau} \mathrm{d}f\, \frac{S_{z'}(f)}{(2\pi)^2} \\
&\approx 2 \int_{1/t_{\mathrm{acq}}}^{1/2\tau} \mathrm{d}f\, \frac{S_\Delta(f) + \frac{\varepsilon^2}{\Delta^2} S_\varepsilon(f)}{(2\pi)^2}
\end{aligned} \tag{2.44}$$

is the total noise power (correlator parametrized in unit of frequency) effectively sampled by our measurement protocol, or the variance of z' fluctuation $\langle Q_{z'}^2 \rangle$ contributed by noise within the quasistatic frequency range $[1/t_{\mathrm{acq}}, 1/2\tau]$. The low-frequency cut-off is determined by the total acquisition time t_{acq} (typically $1 \sim 10\,\mathrm{s}$) of a repeated measurement, and the high-frequency cut-off is set by the free-induction time

τ (typically $0.01 \sim 10\,\mu s$). Noise in this range can be considered as static during each free-induction period, but varying over the longer time span between experimental realizations, so has the name "quasistatic". The prefactor "2" accounts for the integration in the negative branch. For a system of temporal ensemble, such noise effectively adds to the variation of the precession rates among experimental realizations. This is somewhat different from the NMR case, in which spatial variation created by field inhomogeneity dominates, and the expectation-valued measurement over an ensemble of spins is performed. On the other hand, fluctuation slower than t_{acq} does not add to the temporal inhomogeneity. Neither does fluctuation fast than τ, since it is averaged out during the free-induction time.

The result in Eq. (2.43) can also be derived by the filter function method [47, 48], in which the coherence function, i.e., the exponent in the pure-dephasing function, is a weighted integral over the noise spectrum:

$$h(\tau) = \exp\left(-\tau^2 \int_0^\infty \mathrm{d}f\, S_{z'}(f)\, F(f,\tau) \right) , \qquad (2.45)$$

The weighting function $F(f,\tau)$ is called the filter function, and is determined by the pulse sequence. The free-induction filter function is a sinc-squared function, $F_{\mathrm{FI}}(f,\tau) = \mathrm{sinc}^2(\pi f\tau)$, which has a main peak around zero frequency (Fig. 2-12). An infinite noise power, generated by the $1/f$ noise for example, can diverge the integral in Eq. (2.45), so the lower and upper bounds in the integration should be replaced with parameters corresponding to realistic experiments. Therefore, we have

$$h_{\mathrm{FI}}(\tau) = \exp\left(-\tau^2 \int_{f_{\mathrm{low}}}^{f_{\mathrm{high}}} \mathrm{d}f\, S_{z'}(f)\, \mathrm{sinc}^2(\pi f\tau) \right) . \qquad (2.46)$$

The sinc-squared function can be approximated by a window function which is unity for $|f| < 1/2\tau$, giving the same result as the quasistatic approach (Eq. (2.43)-(2.44)).

We now evaluate $h_{\mathrm{FI}}(\tau)$ in two typical cases, $1/f$ noise and white noise. For $1/f$ noise, $S_{z'}(f) = A/|f|$, Eq. (2.44) becomes $\sigma_{z'}^2 = 2A\ln\left[(1/2\tau)/(1/t_{\mathrm{acq}})\right]/(2\pi)^2$. The weak, logarithmic sensitivity to the cut-off frequencies effectively allows us to treat it as a time-independent constant, e.g., $\sigma_{z'}^2 \approx 26A/(2\pi)^2$ for $\tau = 1\,\mu s$ and $t_{\mathrm{acq}} = 1\,s$

57
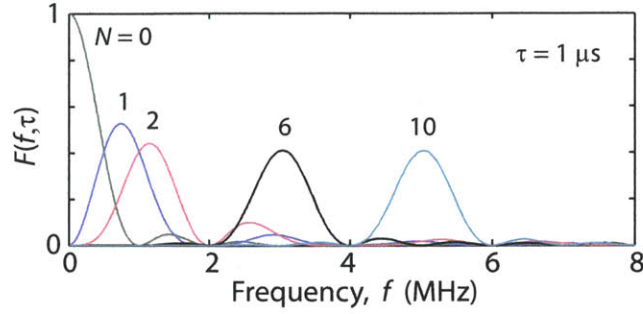
Figure 2-12: Filter functions of different sequences: $N = 0$ for free induction or Ramsey; $N = 1$ for spin echo; others for Carr-Purcell with N π-pulses. The total sequence (free-evolution) time τ is assumed to be $1\,\mu s$ in all cases.

(typical in our experiments), giving a Gaussian decay,

$$h_{\mathrm{FI}}(\tau) = \exp(-13A\,\tau^2) \ . \tag{2.47}$$

For white noise, $S_{z'}(f) = S_{\mathrm{w}}$, on the other hand, the integral is linearly sensitive to the upper cut-off frequency, so that $\sigma_{z'}^2 = S_{\mathrm{w}}/\tau/(2\pi)^2$, yielding an exponential decay,

$$h_{\mathrm{FI}}(\tau) = \exp(-\frac{1}{2}S_{\mathrm{w}}\tau) \ . \tag{2.48}$$

Here we find that $\Gamma_{\varphi} = S_{\mathrm{w}}/2 = S_{z'}(0)/2$, which returns the result as the Bloch-Redfield approach. The reason is that, for Gaussian noise, a white spectrum or a cut-off frequency higher than the threshold frequency relevant for the measurement protocol ($f = 1/\tau$) is almost equivalent to say that the noise is short-correlated. From the above examples, we see that the spectral shape around $f = 1/\tau$ is critical to the total inhomogeneities and hence the decay law.

2.5.4 Spin Echo and Carr-Purcell Sequence

The spin-echo (SE) or Hahn-echo experiment is a method for measuring the transverse depolarization time, T_2, with contribution from inhomogeneous or low-frequency noise removed. Often, the technique is capable of significantly extending the coherence

58

time from free-induction decay, and is considered as a simple but efficient technique to dynamically preserve phase coherence in a complex measurement protocol. In addition, the characteristic decay time, T_{Echo}, provides valuable information about the intermediate-frequency noise (to be defined later). Spin echo was used in NMR to distinguish the homogeneous decay from the inhomogeneous decay [49].

The pulse sequence is based on the free-induction sequence. Besides two $\pi/2$-pulses spaced by τ, an additional π-pulses is inserted right in the middle of the free-induction period. The π-pulses, also known as the refocusing pulse, makes the dynamics different from free induction. The refocusing condition only requires the driving axis of the π-pulse to be in the $X - Y$ plane, and the π-pulse phase can take an arbitrary value. Assume it has a same phase as the $\pi/2$-pulses. The first $\pi/2$-pulse brings the qubit from the ground state ($|-Z\rangle$) to the superposition state ($|+Y\rangle$). Next, during the first half of the free-evolution period, the qubit undergoes dephasing (vectors fanning out), same as in free induction. The π-pulse mirrors all the vectors against it. During the second half of free-evolution period, given that all vectors continue to precess at their own rates same as in the first half (quasistatic), they would coincide at $|-Y\rangle$ right before the last $\pi/2$-pulse. It illustrates a dynamical way to recover the loss of phase coherence from the low-frequency noise by using the refocusing pulse. In an ideal case where only noise below certain frequency or only spatial inhomogeneity exists, spin-echo pure dephasing is completely removed and we shall have a T_1-limited echo time, i.e., $T_{\text{Echo}} = 2T_1$.

However, the echo technique is not omnipotent against all types of noise. For example, if individual vector's precessing rate fluctuates appreciably between the first and second half of the free-induction periods, the vectors would not coincide as before. This suggests that, the spin-echo sequence becomes inefficient in refocusing noise at a frequency close to $1/\tau$, and the spin-echo decay should tell us related noise information.

In general, the spin-echo decay law shares many similarities with that of free-induction decay. The decay due to T_1 process and due to pure dephasing factorize.

(a) Spin-Echo Seq.
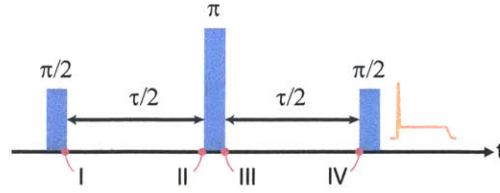
(b) Refocusing in Spin-Echo Seq.
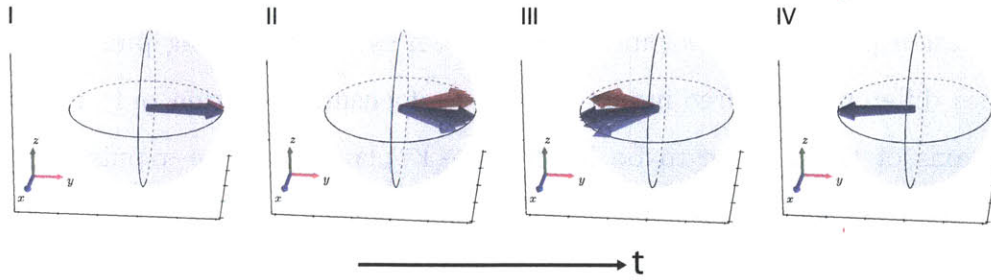
Figure 2-13: (a) Spin-echo pulse sequence. (b) Illustration of refocusing phase diffusion under the sequence in (a). The state vectors of all possible realizations are phase-synchronized right after the first $\pi/2$-pulse (I). During the first half of free-evolution period, they spread out in the same way of free-induction dephasing (II) until the (refocusing) π-pulse mirrors the state vector projects (III). The vectors then continue to precess at their own rate as before, and coincide again after the second half of free-evolution period (IV). The observed transverse polarization shows a revival signal at the time τ. Hereafter, the phenomenon has the name "echo".

Using the filter-function method, the spin-echo pure dephasing can be expressed by

$$h_{\mathrm{SE}}(\tau) = \exp\left(-\tau^2 \int_0^\infty \mathrm{d}f\, S_{z'}(f)\, \mathrm{sinc}^2(\frac{\pi f \tau}{2}) \sin^2(\frac{\pi f \tau}{2})\right) . \qquad (2.49)$$

It is easy to check that the spin-echo filter function, $F_{\mathrm{SE}}(f, \tau) = \mathrm{sinc}^2(\frac{\pi f \tau}{2}) \sin^2(\frac{\pi f \tau}{2})$ has a main peak at $f \approx 1/\tau$ (Fig. 2-12), so the spin-echo sequence does act as a noise filter which spectrally select the noise that contributes to observed dephasing.

We now evaluate $h_{\mathrm{SE}}(\tau)$ for the case of $1/f$ noise and white noise. For $1/f$ noise, $S_{z'}(f) = A/|f|$, Eq. (2.49) results in a Gaussian decay,

$$h_{\mathrm{SE}}(\tau) = \exp(-A \ln 2\, \tau^2) . \qquad (2.50)$$

60

Comparing with Eq. (2.47), the echo technique improves the Gaussian free-induction pure-dephasing time by a factor of ~ 4.3. For white noise, $S_{z'}(f) = S_{\mathrm{w}}$, Eq. (2.49) gives the same exponential decay as free induction,

$$h_{\mathrm{SE}}(\tau) = \exp(-\frac{1}{2}S_{\mathrm{w}}\tau) \,, \tag{2.51}$$

indicating that the refocusing fails to recover coherence against white noise. The result is obvious if one notices the fact that $S_{z'}(1/\tau) = S_{z'}(0) = S_{\mathrm{w}}$.

Inspired by the echo technique, the NMR community developed a generalized version of spin-echo sequence, which fills up a fixed free-induction period with multiple refocusing pulses so that the new sequence can filter out more low-frequency noise. The shorter the pulse spacing, the higher the filter frequency. As a result, we should expect to further improve the coherence time against the $1/f$-type noise.

The pulse sequence is known as the Carr-Purcell (CP) sequence [50]. Basically, it comprises N equally spaced π-pulses (Fig. 2-14a). Every two neighboring π-pulses and associated free-evolution periods can be considered as a repeated elementary cell which constructs a complete refocusing cycle and an overall identity operation. Consequently, the sequence is often implemented with an even number of π-pulses. The filter function (even N), $F_{\mathrm{CP}}^{(N)}(f,\tau) = 4\mathrm{sinc}^2(\pi f\tau)\sin^4(\frac{\pi f\tau}{2N})/\cos^2(\frac{\pi f\tau}{N})$ has a main peak almost at $f = N/2\tau$ (Fig. 2-12).

A modified version of the CP sequence, the Carr-Purcell-Meiboom-Gill (CPMG) sequence [51], is usually preferred in practice. In the CPMG sequence, the π-pulses are 90°-phase-shifted (Y-pulse), and this modification makes the sequence robust against pulse errors (Fig. 2-14b). Assume the pulse is not perfect and gives slightly bigger or smaller nutation angle than π. The CP sequence will accumulate the error coherently (second-order error), while CPMG has only fourth-order sensitivity. The modification can lead to dramatic improvement in experiments when pulse number becomes large. However, CP and CPMG belong to the same type of sequence, since they have the same filter function.

The CP-like sequence can effectively decouple the system from the noisy environ-
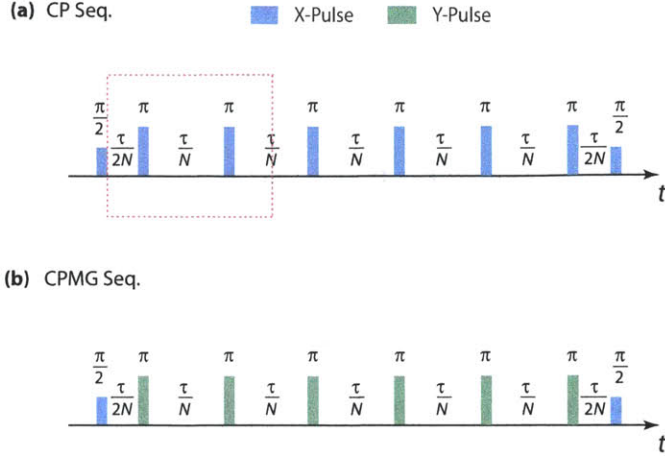
Figure 2-14: (a) Carr-Purcell pulse sequence. The cell included by the dashed box indicates a refocused identity. (b) Carr-Purcell-Meiboom-Gill pulse sequence.

ment during a measurement. Such technique is often called dynamical decoupling (DD) [52]. There are a variety of advanced dynamical-decoupling sequences, such as CP, PDD (periodic dynamical decoupling) [52, 53], UDD (Uhrig dynamical decoupling) [54] and CDD (concatenated dynamical decoupling) [55]. Each has a unique noise-suppressing protocol and might be an optimal solution to a certain noise model.

2.6 Driven Evolution and Related Experiments

Driven-evolution related experiments, like its free-evolution counterpart, does not necessarily mean that the qubit is driven by r.f. pulses all the time. It merely indicates that we only care about decohering phenomena during the driven-evolution periods in these experiments. In other words, noise information of our interest is encoded during certain driven periods.

We will show that there is a nice analogy between free and driven evolution, and their decohering dynamics share many similarities. Driven-evolution decoherence can be better described and understood via the analogy. Moreover, many driven-evolution related experiments can find their free-evolution counterparts. Several important ones

will be introduced in this section.

2.6.1 Driven Evolution and Its Decoherence

The qubit dynamics under a harmonic drive is discussed in Sec. 2.4. Assume resonant driving along the X-axis ($\Delta\nu = 0$, $\phi = 0$). The Hamiltonian in Eq. (2.24) is simplified as

$$\tilde{\tilde{\mathcal{H}}} = \frac{h}{2}\nu_{\mathrm{R}}\hat{\sigma}_X \ . \tag{2.52}$$

The Hamiltonian describes a two-level system in the rotating frame, which is quantized along X with a level splitting $h\nu_{\mathrm{R}}$. Regardless of issues like controllability, any well-defined two-level system can be considered as a qubit, so now we do have a new logical qubit, but in a different reference frame. We prefer to call it "fictitious qubit", when making the analogy with the original qubit described in Eq. (2.15).

The driven-evolution dynamics in the rotating frame is analogous to the free-evolution dynamics in the qubit frame. That is, the qubit precesses around the X-axis at the fictitious qubit frequency ν_{R}, and its subtended angle depends on the initial state. For example, if the qubit is prepared at either $|+X\rangle$ or $|-X\rangle$ state, its state vector will stick to that orientation, same as the corresponding free-evolution counterpart when the qubit is initialized in its excited ($|+z'\rangle$) or ground ($|-z'\rangle$) state. In this spirit, $|+X\rangle$ ($|-X\rangle$) is defined as the fictitious excited (ground) state. In another situation when the qubit is initialized at the "equatorial" states (in the $Y-Z$ plane), the state vector will precess around the $Y-Z$ plane just as its free-evolution counterpart precessing around the $x'-y'$ plane.

In a more general situation when $\Delta\nu \neq 0$, the effective quantization axis is the vector sum of the detuning field and the driving field (Fig. 2-6), and becomes tilted from $X-Y$ plane. The fictitious qubit is energized by a modified frequency ν_{R}' (Eq. (2.25)) along the Z'-axis. Pedagogically, we ought to define the new frame $\{X', Y', Z'\}$ which diagonalizes the rotating-frame Hamiltonian along Z' (a routine choice for the quantization axis). However, for most of the discussions in this thesis,

we do not necessitate the complication invoked by the finite detuning. To simplify the discussion and involve as few frames as possible, we keep the analogy between the qubit-frame quantization axis z' and the rotating-frame quantization axis X, unless otherwise specified.

As for the environmental noise, we can rewrite the same interaction Hamiltonian given in Eq. (2.28) in rotating-frame coordinates:

$$\begin{aligned}
\tilde{\tilde{\mathcal{H}}}_I &= \frac{h}{2} \left[\hat{Q}_{z'} \hat{\sigma}_Z + \hat{Q}_{x'} \cos(2\pi\nu_{\text{rf}} t)\hat{\sigma}_X - \hat{Q}_{x'} \sin(2\pi\nu_{\text{rf}} t)\hat{\sigma}_Y \right] \\
&= \frac{h}{2} \left[\hat{Q}_Z \hat{\sigma}_Z + \hat{Q}_X \hat{\sigma}_X + \hat{Q}_Y \hat{\sigma}_Y \right] .
\end{aligned} \tag{2.53}$$

Comparing the first and second line in Eq. (2.53), it is easy to see that the qubit-frame z'-noise is invariably transferred into the rotating-frame Z-noise. On the other hand, the x'-noise is separated into the X- and Y-noise with a frequency mixing of ν_{rf}, indicating that the rotating-frame noise $S_{X,Y}(f)$ is simply the frequency-modulated qubit-frame noise, derived from $S_{x'}(|f \pm \nu_{\text{rf}}|)$.

In the following discussion, the rotating-wave approximation and the weak-coupling assumption are still valid, but we will loose the Markovian constraint. The noise correlation time might be comparable to the relaxation times in the rotating frame, because the fictitious qubit frequency ν_{R} is much less than the original qubit frequency. Following the analogy to the free-evolution decoherence, we can derive the driven-evolution version of the Bloch equations, which is known as the generalized Bloch equations (GBE). GBE have been studied extensively in spin systems [56]. Here, we follow the recipe prescribed in [57] and obtain the non-Markovian GBE in the rotating frame,

$$\begin{aligned}
\frac{d\mathcal{R}_X}{dt} &= -\Gamma_X \mathcal{R}_X + v_X , \\
\frac{d\mathcal{R}_Y}{dt} &= -\Gamma_Y \mathcal{R}_Y - 2\pi\nu_{\text{R}} \mathcal{R}_Z + v_Y , \\
\frac{d\mathcal{R}_Z}{dt} &= -\Gamma_Z \mathcal{R}_Z + 2\pi\nu_{\text{R}} \mathcal{R}_Y + v_Z ,
\end{aligned} \tag{2.54}$$

where

$$\Gamma_X = \frac{1}{2} S_Y(\nu_{\mathrm{R}}) + \frac{1}{2} S_Z(\nu_{\mathrm{R}})$$

$$= \frac{1}{2} \left[\frac{1}{4} S_{x'}(\nu_{\mathrm{q}} + \nu_{\mathrm{R}}) + \frac{1}{4} S_{x'}(\nu_{\mathrm{q}} - \nu_{\mathrm{R}}) \right] + \frac{1}{2} S_{z'}(\nu_{\mathrm{R}}) \,,$$

$$\Gamma_Y = \frac{1}{2} S_X(0) + \frac{1}{2} S_Z(\nu_{\mathrm{R}})$$

$$= \frac{1}{2} \left[\frac{1}{2} S_{x'}(\nu_{\mathrm{q}}) \right] + \frac{1}{2} S_{z'}(\nu_{\mathrm{R}}) \,,$$

$$\Gamma_Z = \frac{1}{2} S_X(0) + \frac{1}{2} S_Y(\nu_{\mathrm{R}})$$

$$= \frac{1}{2} \left[\frac{1}{2} S_{x'}(\nu_{\mathrm{q}}) \right] + \frac{1}{2} \left[\frac{1}{4} S_{x'}(\nu_{\mathrm{q}} + \nu_{\mathrm{R}}) + \frac{1}{4} S_{x'}(\nu_{\mathrm{q}} - \nu_{\mathrm{R}}) \right] \qquad (2.55)$$

are the depolarization rates which can be further related to lab-frame noise by Eq. (2.29), and

$$v_X = -\frac{1}{8} J_{x'}(\nu_{\mathrm{q}} + \nu_{\mathrm{R}}) + \frac{1}{8} J_{x'}(\nu_{\mathrm{q}} - \nu_{\mathrm{R}}) - \frac{1}{2} J_{z'}(\nu_{\mathrm{R}}) \,,$$

$$v_Y = 0 \,,$$

$$v_Z = -\frac{1}{8} J_{x'}(\nu_{\mathrm{q}} + \nu_{\mathrm{R}}) - \frac{1}{8} J_{x'}(\nu_{\mathrm{q}} - \nu_{\mathrm{R}}) - \frac{1}{4} J_{x'}(\nu_{\mathrm{q}}) \,, \qquad (2.56)$$

where $J_\lambda(f) = S_\lambda(f) \tanh(\frac{\bar{\beta} f}{2})$, defines the steady-state polarization,

$$\overline{\mathcal{R}}_X = \frac{v_X}{\Gamma_X} \,,$$

$$\overline{\mathcal{R}}_Y = \frac{\Gamma_Z v_Y + \nu_{\mathrm{R}} v_Z}{\nu_{\mathrm{R}}^2 + \Gamma_Y \Gamma_Z} \,,$$

$$\overline{\mathcal{R}}_Z = \frac{\Gamma_Y v_Z - \nu_{\mathrm{R}} v_Y}{\nu_{\mathrm{R}}^2 + \Gamma_Y \Gamma_Z} \,. \qquad (2.57)$$

We now continue to comment on Eq. (2.54)-(2.57) and elucidate several important findings, which would help understand the underlying physics behind these equations and explain experimental observations.

1. Unlike the free-evolution Bloch equations in which we can mix the x'- and y'-depolarization during fast precession, we return to the asymmetric setting between Y- and Z-depolarization due to our dropping the Markovian approxi-

65
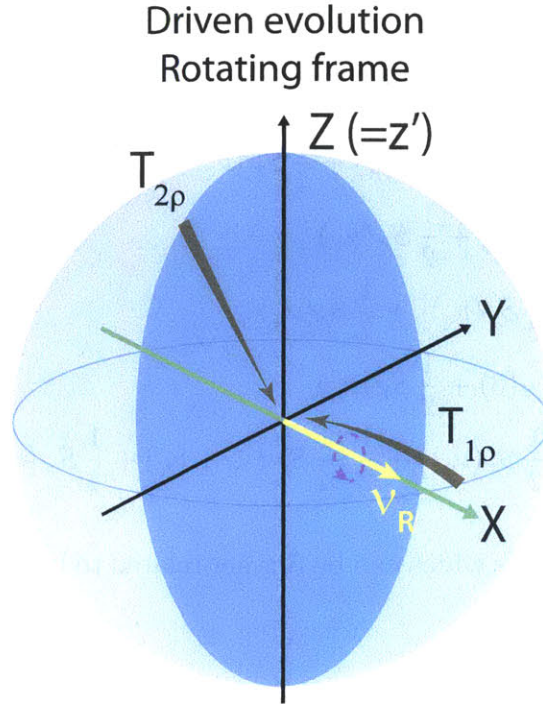
Figure 2-15: Driven-evolution dynamics in the rotating frame. The yellow arrow indicates the quantizing field. The qubit undergoes Rabi precession (purple dashed line) around the rotating-frame longitudinal axis (green arrow), while depolarizes (grey arrows) both longitudinally ($T_{1\rho}$) and transversely ($T_{2\rho}$) at the same time.

mation. From the first line of each equation in Eq. (2.54), we see that Γ_X results from the Y- and Z-channel bit flip; Γ_Y results from the X-channel phase flip and the Z-channel bit flip; Γ_Z results from the X-channel phase flip and the Y-channel bit flip.

However, in experiments, we are unable to precisely determine the depolarization solely along Y or Z, because of the simultaneous Rabi precession. The extracted transverse depolarization rate is effectively the average of Γ_Y and Γ_Z.

Therefore, we can define the driven-evolution analogue of Γ_1, Γ_φ and Γ_2 as

$$\Gamma_{1\rho} = \Gamma_X = \frac{1}{8}\left[S_{x'}(\nu_q + \nu_R) + S_{x'}(\nu_q - \nu_R)\right] + \frac{1}{2}S_{z'}(\nu_R)\,,$$

$$\Gamma^\dagger_{\varphi\rho} = \frac{1}{4}S_{x'}(\nu_q)\,,$$

$$\Gamma_{2\rho} = \frac{1}{2}\left(\Gamma_Y + \Gamma_Z\right) = \frac{1}{16}\left[S_{x'}(\nu_q + \nu_R) + S_{x'}(\nu_q - \nu_R)\right] + \frac{1}{4}S_{z'}(\nu_R) + \frac{1}{4}S_{x'}(\nu_q)$$

$$= \frac{1}{2}\Gamma_{1\rho} + \Gamma^\dagger_{\varphi\rho}\,. \tag{2.58}$$

As expected, the transverse depolarization due to longitudinal relaxation and due to pure dephasing add up in the same way as in the free-evolution case (Eq. (2.33)).

2. In our model, we only take into account noise from the internal parameters, i.e., the Δ and ε noise. However, additional noise could be introduced by the harmonic drive, e.g., instability of the microwave signal. In fact, low-frequency fluctuation of the drive amplitude A_{rf} is a parasitic effect in our device, and are proven to dominate the transverse depolarization in many instances [58]. The effect of the A_{rf} fluctuation, i.e., the ν_R fluctuation, can be understood via the analogy to its free-evolution counterpart, the free-induction pure dephasing. The temporal inhomogeneity of the fictitious qubit frequency contributes to the rotating-frame pure dephasing to first order, just like the linearly coupled noise to free induction. Therefore, we use the "$\dagger$" symbol in Eq. (2.58) to indicate that the rotating-frame pure dephasing is free from the ν_R fluctuation.

3. We now explain the origin of the terms in the second line of each equation in Eq. (2.55). To proceed, it will be helpful to review Eq. (2.53) and the followed discussion.

First, the z'-noise is invariantly transformed into the Z-noise, as it is the invariant coordinate between the two reference frames. As a consequence, $S_{z'}(\nu_R)$ directly contributes to the rotating-frame relaxation. Via the analogy to the free-evolution rate-PSD relation (Eq. (2.33) and Eq. (2.38), we have the same

67

prefactor "$\frac{1}{2}$".

Next, the Y-noise is derived from the x'-noise with a frequency mixing, so $S_Y(\nu_R)$ comes from $S_{x'}(\nu_q \pm \nu_R)$. The prefactor "$\frac{1}{4}$" can be understood as follows. Consider the time-domain realization of $S_{x'}(\nu_q + \nu_R)$ as a sinusoid, $A\cos(2\pi(\nu_q + \nu_R)t + \phi)$, where ϕ is randomized. In the rotating frame, the projection of this noise on the Y-axis noise is expressed as: $-A\cos(2\pi(\nu_q + \nu_R)t + \phi)\sin(2\pi\nu_q t) = \frac{A}{2}\sin(2\pi\nu_R t + \phi) - \frac{A}{2}\sin(2\pi(2\nu_q + \nu_R)t + \phi)$, where the first term on the r.h.s is the noise of our interest and the second term is the ineffective counter-rotating wave. Clearly, the amplitude of the noise is halved due to the branching into the rotating and counter-rotating wave. Hence the quartered power.

Similarly, the pure dephasing noise $S_X(0)$ is derived from $S_{x'}(\nu_q)$, but the power reduction factor due to frequency mixing is "$\frac{1}{2}$" instead of "$\frac{1}{4}$". Still take the sinusoidal example, $A\cos(2\pi\nu_q t + \phi)$. The corresponding symmetrized bilateral PSD over a differential bandwidth δf is $S_{x'}(\nu_q) = \frac{A^2}{4\delta f}$. The sinusoid's projection on the X-axis in the rotating frame becomes $\frac{A}{2}\cos\phi$, and the corresponding PSD is $S_X(0) = \frac{A^2}{4}\langle\cos^2\phi\rangle\frac{1}{\delta f} = \frac{A^2}{8\delta f} = \frac{1}{2}S_{x'}(\nu_q)$. Therefore, it is the particularity of the symmetrized bilateral PSD at zero frequency that makes the difference. We may also obtain the result in the viewpoint of limit. For symmetrized bilateral PSD, we know that $S_X(\pm f) = \frac{1}{4}S_{x'}(f + \nu_q)$, when $f \neq 0$. If we approach f to zero, $S_X(0+)$ and $S_X(0-)$ finally add up.

Overall, the driven-evolution decoherence is indeed a free-evolution analogue but with a frequency down-conversion for qubit-frame transverse noise. For example, in the free-induction experiment, pure dephasing originates from the z'-noise close to zero frequency. On the driven side, the effective noise associated with Rabi becomes the near-zero-frequency X-noise which is derived from the x'-noise whose frequency is close to ν_q. Therefore, we can think of the difference between free induction and Rabi as a shift of the filter function from $F_{FI}(f, \tau)$ to $F_{RB}^{\dagger}(f, \tau) = F_{FI}(f - \nu_q, \tau)$ ("$\dagger$" indicates that the filter function applies to

the frequency-mixed x'-noise). The effect in other experiments can be analyzed accordingly.
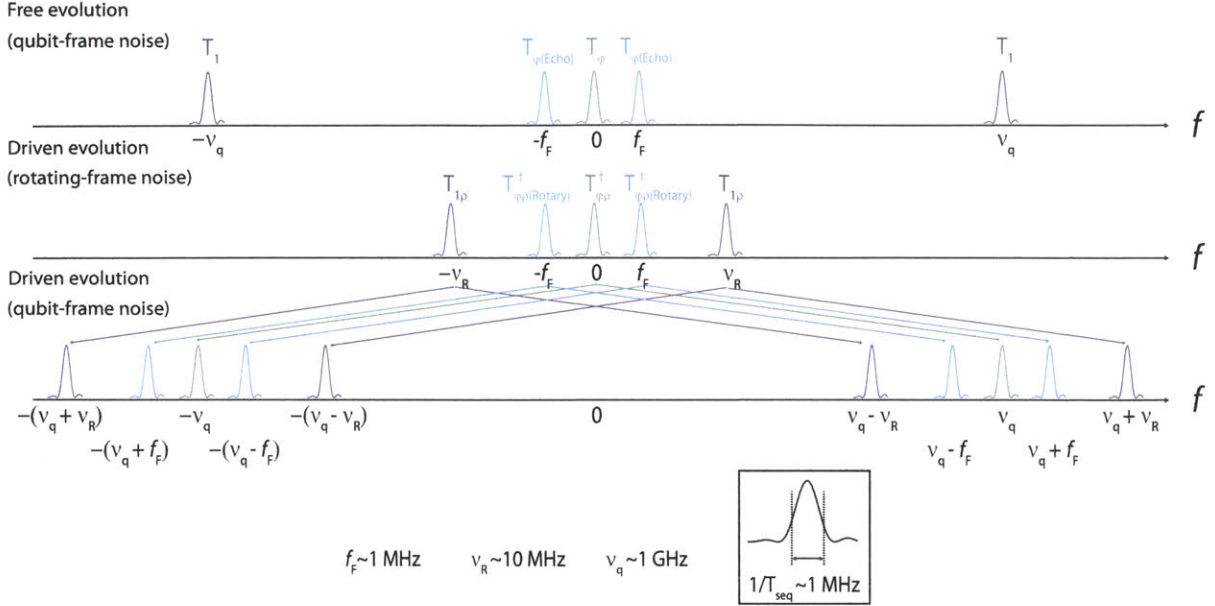
Figure 2-16: Noise selectivity of analogous experiments between free and driven evolution and noise frequency conversion between the qubit frame and the rotating frame for driven-evolution experiments. At the bottom are typical values of several relevant frequencies and also the noise filter's width. f_F stands for the filter frequency of the spin-echo or rotary-echo filter. T_{seq} is the total length of pulse sequence .

This perspective helps us understand why the pure dephasing associated with $\Gamma^\dagger_{\varphi\rho}$ is always exponential. Fig. 2-17 illustrates the free-induction and Rabi pure-dephasing filter on a $1/f$ spectrum. The free-induction sequence acts as a $1/\tau$-width bandpass noise filter at $f = 0$, so the decay law has depends crucially on the spectral shape over this small band (compared to ν_q). When the harmonic drive is on as in Rabi precession, for the x'-noise, the filter band (still $1/\tau$-width) is shifted to be around $f = \nu_q$. Given that the noise spectrum is smooth at this high frequency (mostly the case), the qubit effectively sees a white or short-correlated noise.

4. If we further assume that the noise spectrum is smooth over a bandwidth of ν_R around ν_q, we can make the approximation, $S_{x'}(\nu_q \pm \nu_R) \approx S_{x'}(\nu_q)$. This is
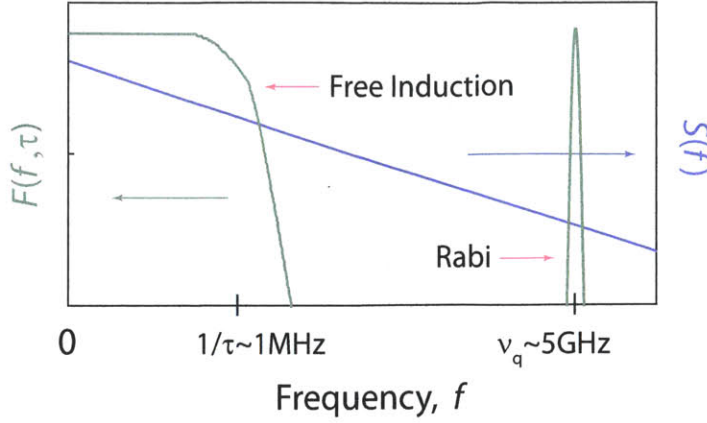
Figure 2-17: Sketch of the free-induction and Rabi (green) pure-dephasing filter function and a $1/f$ noise spectrum (blue) in log-log scale. The free-induction filter is for the z'-noise and related to Γ_φ; the Rabi filter is for the x'-noise and related to $\Gamma_{\varphi\rho}^\dagger$. The two filters have the same bandwidth (typically 1 MHz), but different center frequency, 0 for free induction and ν_q (~ 5 GHz in our device) for Rabi.

usually true, since we operate in the weak-driving limit (RWA). Eq. (2.58) is then simplified to

$$
\begin{aligned}
\Gamma_{1\rho} &= \frac{1}{4}\, S_{x'}(\nu_q) + \frac{1}{2}\, S_{z'}(\nu_R) = \frac{1}{2}\Gamma_1 + \Gamma_\nu \;, \\
\Gamma_{\varphi\rho}^\dagger &= \frac{1}{4}\, S_{x'}(\nu_q) = \frac{1}{2}\Gamma_1 \;, \\
\Gamma_{2\rho} &= \frac{3}{8}\, S_{x'}(\nu_q + \nu_R) + \frac{1}{4}\, S_{z'}(\nu_R) = \frac{3}{4}\Gamma_1 + \frac{1}{2}\Gamma_\nu \;,
\end{aligned}
\tag{2.59}
$$

where we define

$$
\begin{aligned}
\Gamma_\nu &= \frac{1}{2}\, S_{z'}(\nu_R) \\
&\approx \frac{1}{2}\left(S_\Delta(\nu_R) + \frac{\varepsilon^2}{\Delta^2}\, S_\varepsilon(\nu_R) \right)
\end{aligned}
\tag{2.60}
$$

as the relaxation rate contributed by the Rabi-frequency noise. The second line of Eq. (2.60) shows its ε-dependence (sensitivity) to the ε noise when close to the sweet spot.

It can be inferred from Eq. (2.59) that, regardless of the Rabi-frequency noise, the driven-evolution longitudinal and transverse relaxation times are upper-

limited by $2T_1$ and $4T_1/3$, respectively.

5. At first glance, the steady-state longitudinal polarization (X) in Eq. (2.57) seems not in thermal equilibrium. One would expect the steady-state polarization to be related to the Boltzmann distribution of the $\nu_{\rm R}$ mode, i.e., $\overline{\mathcal{R}}_X = -\tanh(\frac{\beta\nu_{\rm R}}{2})$. However, the impression is wrong, because of the negligence of the frequency-mixing effect when convert noise into the rotating frame. Note that the unsymmetrized rotating-frame Y-noise, $S_Y^{\rm U}(\nu_{\rm R})$ and $S_Y^{\rm U}(-\nu_{\rm R})$, are derived from both $S_{x'}(\nu_{\rm q}+\nu_{\rm R})$ and $S_{x'}(\nu_{\rm q}-\nu_{\rm R})$, and thus equal. The correct equilibrium should be computed from the rotating-frame relaxation and absorption rates, $\overline{\mathcal{R}}_X = \frac{\Gamma_+-\Gamma_-}{\Gamma_++\Gamma_-} = \frac{S_{\perp X}^{\rm U}(-\nu_{\rm R})-S_{\perp X}^{\rm U}(\nu_{\rm R})}{S_{\perp X}^{\rm U}(-\nu_{\rm R})+S_{\perp X}^{\rm U}(\nu_{\rm R})}$, where $S_{\perp X}^{\rm U}(\pm\nu_{\rm R}) = S_Z^{\rm U}(\pm\nu_{\rm R}) + S_Y^{\rm U}(\pm\nu_{\rm R}) = S_{z'}^{\rm U}(\pm\nu_{\rm R}) + \frac{1}{4}S_{x'}(\nu_{\rm q}+\nu_{\rm R}) + \frac{1}{4}S_{x'}(\nu_{\rm q}-\nu_{\rm R})$. There we obtain the result in Eq. (2.57).

Unlike the free-evolution case, the steady-state transverse polarization during driven evolution does vanish. This is another effect brought by the drop of Markovian approximation. If we let $\nu_{\rm R} \gg \Gamma_Y, \Gamma_Z$, the steady-state solution will return to 0.

6. In the NMR literature, we often see that the rotating-frame Bloch equations are written with free-evolution decohering processes [22]:

$$\frac{\mathrm{d}\mathcal{R}_X}{\mathrm{d}t} = -\Gamma_2\mathcal{R}_X \ ,$$
$$\frac{\mathrm{d}\mathcal{R}_Y}{\mathrm{d}t} = -\Gamma_2\mathcal{R}_Y - 2\pi\nu_{\rm R}\mathcal{R}_Z \ ,$$
$$\frac{\mathrm{d}\mathcal{R}_Z}{\mathrm{d}t} = -\Gamma_1\mathcal{R}_Z + 2\pi\nu_{\rm R}\mathcal{R}_Y \ . \tag{2.61}$$

This phenomenological approach of writing the equation of motion is questionable in principle, although it does show agreement with experiments, especially in weak-driving liquid-state NMR experiments.

Note that, in the NMR case, the coordinates in the Hamiltonian correspond to the real 3D space, and the noisy environment becomes isotropic in liquid state.

71

Assuming that the quantizing field is along the z-axis (the laboratory frame coincides with the qubit frame) and the nutation axis of low driving field is X, we have $S_x(f) = S_y(f) = S_z(f) = S(f)$, $S(0) \approx S(\nu_R)$ and $S(\nu_q \pm \nu_R) \approx S(\nu_q)$. Therefore $\Gamma_1 = \frac{1}{2} S_x(\nu_q) + \frac{1}{2} S_y(\nu_q) = S(\nu_q)$ and $\Gamma_2 = \frac{1}{2}\Gamma_1 + \frac{1}{2} S_z(0) = \frac{1}{2}S(\nu_q) + \frac{1}{2} S(0)$. The rotating-frame longitudinal and transverse depolarization rates obtained by the formal GBE theory can be related to Γ_1 and Γ_2:

$$
\begin{aligned}
\Gamma_{1\rho} = \Gamma_X &= \frac{1}{2} S_Y(\nu_R) + \frac{1}{2} S_Z(\nu_R) \\
&= \frac{1}{2} \left(\frac{1}{2} S_x(\nu_q) + \frac{1}{2} S_y(\nu_q) \right) + \frac{1}{2} S_z(\nu_R) \\
&= \frac{1}{2} S(\nu_q) + \frac{1}{2} S(0) \\
&= \Gamma_2 \, , \\
\Gamma_{2\rho} &= \frac{1}{2} \Gamma_{1\rho} + \frac{1}{2} S_X(0) \\
&= \frac{1}{2} \Gamma_2 + \frac{1}{2} \left(\frac{1}{2} S_x(\nu_q) + \frac{1}{2} S_y(\nu_q) \right) \\
&= \frac{1}{2} \Gamma_2 + \frac{1}{2} S(\nu_q) \\
&= \frac{1}{2} (\Gamma_2 + \Gamma_1) \, .
\end{aligned}
\tag{2.62}
$$

Therefore, the formalism in Eq. (2.61) gives the right result in terms of experimental observation, though it is not applicable to an arbitrary system.

Now, it is more clear that almost every aspect between free and driven evolution is analogous. More details about the analogy can be found in Table. 2.1 in the end of this chapter. Imitating the free-evolution case, we can define driven-evolution decohering processes with respect to the new quantization axis, X.

$T_{1\rho} = 1/\Gamma_{1\rho}$ is the rotating-frame longitudinal depolarization/relaxation time, i.e. relaxation in the rotating frame, which corresponds to depolarization along the X-axis (Fig. 2-18a). The responsible environmental noise is the transversely coupled ($\perp X$) Rabi-frequency (ν_R) fluctuation. To measure $T_{1\rho}$, we resort to the $T_{1\rho}$ or spin-locking experiment (Sec. 2.6.2), which prepares the qubit at either $|\pm X\rangle$ state, and then records how it depolarizes during continuous driving.

$T_{2\rho} = 1/\Gamma_{2\rho}$ is the rotating-frame transverse depolarization/relaxation time. Similar to the free-evolution argument, this transverse depolarization can also be divided into a $T_{1\rho}$-induced part and a pure dephasing part $T_{\varphi\rho}$, all with respect to the new quantization axis. As discussed before, $T_{\varphi\rho}$ can be further factorized into a high-frequency-noise-induced part $T_{\varphi\rho}^{\dagger} = 1/\Gamma_{\varphi\rho}^{\dagger}$, which decays exponentially, and a part associated with low-frequency ν_{R} fluctuation, $T_{\varphi\rho}^{\ddagger}$, whose decay law can be derived by the filter function approach.

$T_{2\rho}$, like its free-evolution counterpart, also varies in different experiments. $T_{2\rho}$ usually means the transverse depolarization during bare Rabi precession, like the instance we previously discussed in this section. However, in the rest of this section, we would like to extend it as a general designation for any type of rotating-frame transverse depolarization. The simplest one is Rabi decay from the Rabi experiment (Sec. 2.6.3), which measures the decaying oscillatory signal (characteristic time T_{Rabi}) by resonantly driving the qubit starting from its ground state (Fig. 2-18b). Note that the Rabi experiment in a general sense corresponds to nutation starting from an arbitrary state, so even the $T_{1\rho}$ experiment is just a special case of Rabi. In this thesis however, unless otherwise specified, we denote Rabi as its most original version, in which the qubit starts from its ground state $|-z'\rangle$ $(=|-Z\rangle)$. Rabi is the driven-evolution analogue of the free-induction experiment (Sec. 2.5.3), since both characterize the transverse decay during bare equatorial precession. In our device, the Rabi decay is mostly affected by the ν_{R} inhomogeneity (linear coupling, first order), i.e., the low-frequency fluctuation of the effective microwave amplitude seen by the qubit [58]. Depending on the working point, it may also be sensitive to $\Delta\nu$ inhomogeneity (quadratic coupling, second order), which can also modify the fictitious qubit frequency, i.e., the effective Rabi frequency ν_{R}'.

If the second half of the Rabi pulse is 180°-phase-shifted as in the rotary-echo experiment (Sec. 2.6.4), the Rabi field in the rotating frame is reversed to point to $-X$ instead of X, and the Rabi precession is executed in the opposite way. Therefore, during the second half, variation of the fictitious qubit frequency can be refocused, just like how it is done in spin echo (Sec. 2.5.4). Rotary echo is a "close" driven-evolution

analogue of spin-echo, and the decay (characteristic time T_{Rotary}) can be analyzed in a similar way. It is only "close" because the refocusing action is not executed with π-pulses as in spin echo. Instead, we reverse the Hamiltonian while keeping the state unchanged. However, the phase-accumulation scheme is still the same. Furthermore, the analogy to the CP-like sequence would be the multiple-phase-shift generalization of the rotary-echo sequence.
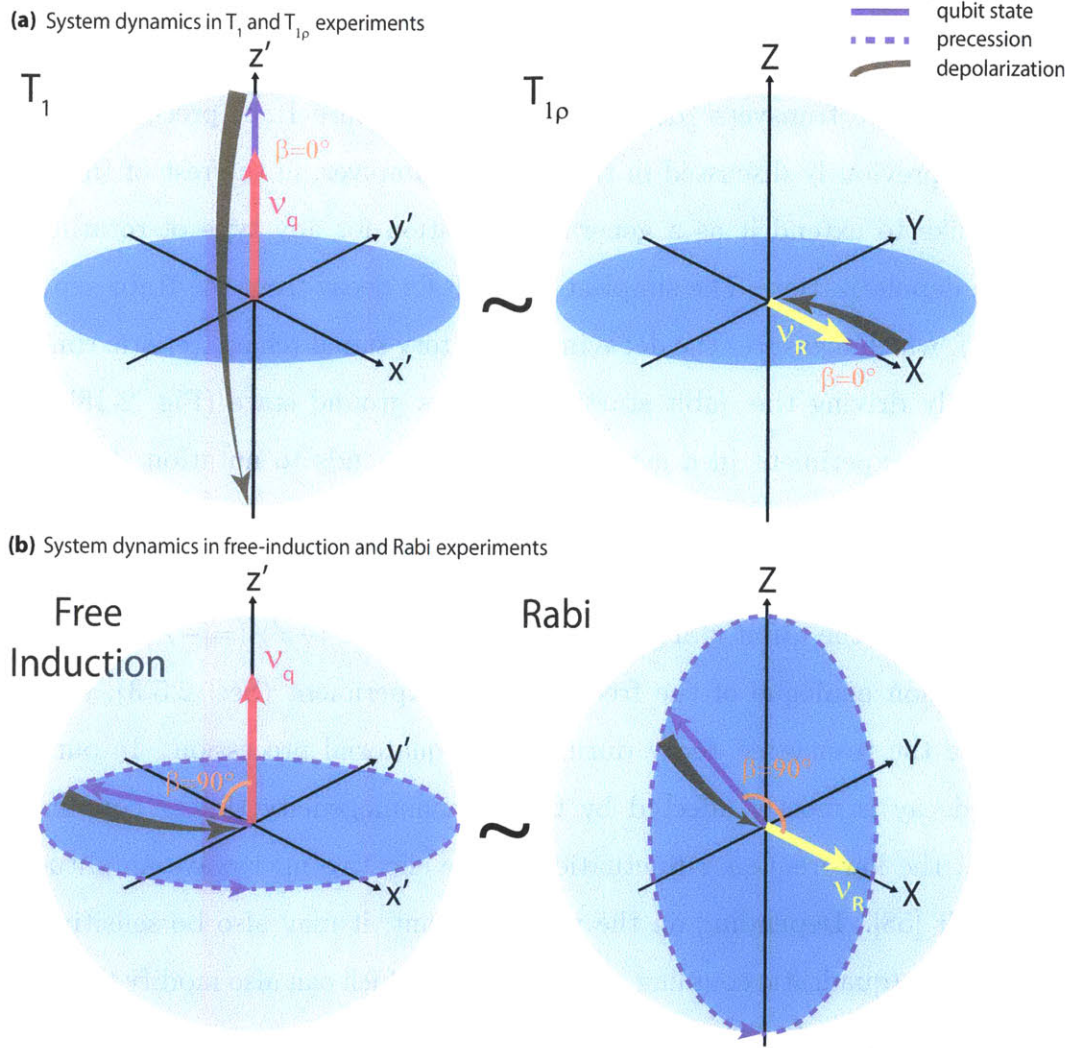
Figure 2-18: Schematic diagram of system dynamics in analogous experiments between free and driven evolution. (a) T_1 versus $T_{1\rho}$. The figures represent the typical case when the initial qubit state is parallel with the quantizing field ($\beta = 0$). Depolarization shown is based on the condition, $\nu_{\text{R}} \ll k_{\text{B}}T/h \ll \nu_{\text{q}}$, so that, at the steady state, $\mathcal{R}_{z'} \approx -1$ for the T_1 process, and $\mathcal{R}_X \approx 0$ for the $T_{1\rho}$ process. (b) Free induction versus Rabi. Precession is indicated by the dashed line, while depolarization happens simultaneously. The process shown ignores the longitudinal relaxation.

2.6.2 Spin Locking

The spin-locking (SL) or $T_{1\rho}$ experiment is a method for measuring the rotating-frame longitudinal relaxation time, $T_{1\rho}$. Its free-evolution counterpart is the inversion-recovery (IR) experiment. $T_{1\rho}$ is able to provide information about environmental modes at the Rabi frequency $\nu_{\rm R}$ (Eq. (2.59)), aside from the qubit-frequency noise accessible from T_1 already. Because the Rabi frequency can be tuned, and ranges over $0.1 - 100\,\mathrm{MHz}$ in our device, we may utilize the $T_{1\rho}$ experiment as a noise spectrum analyzer in the intermediate-frequency regime. Spin locking is a technique originally used in NMR to study atomic motion with long correlation time [59, 60, 61].

The original pulse sequence applicable to superconducting qubits consists of two $\pi/2$-pulses and a $90°$-phase-shifted continuous driving pulse in between. In order to make the discussion consistent, we assume that the phase order is $\overline{Y}$-X-$\overline{Y}$. This is equivalent to the X-Y-X order in [62], since only the relative phase is important (Sec. 2.4.3). The first $\pi/2)_{\overline{Y}}$ pulse brings the qubit from its ground state ($|-Z\rangle = |-z'\rangle$) to $|+X\rangle$ on the equator. The continuous driving field is then applied along X and thereby parallel with the qubit state, so that the qubit is effectively locked in this orientation and experiences longitudinal relaxation $\Gamma_{1\rho}$ only. After a finite duration τ, the remaining polarization along X is projected, by the last $\pi/2)_{\overline{Y}}$ pulse, back along Z for readout. By stepping τ, we thereby record how the qubit relaxes in the rotating frame.

Note that, in the high-temperature regime, $h\nu_{\rm R} \ll k_{\rm B}T$, the steady-state X-polarization should approach zero (Eq. (2.57)). This is generally true for our experiments, since $T \approx 65\,\mathrm{mK}$ is the effective device temperature, obtained by measuring the SQUID's switching-current distribution [37], and we usually measure at $\nu_{\rm R} < 100\,\mathrm{MHz}$.

The decay law is exponential (Eq. (2.54)), and the ground-state probability in the high-temperature regime can be expressed as

$$P_{\rm SL}(\tau) = \frac{1}{2} - \frac{1}{2}\exp\left(-\Gamma_{1\rho}\tau\right) , \qquad (2.63)$$

(a) Spin-Locking Seq.

X-Pulse   Y-Pulse
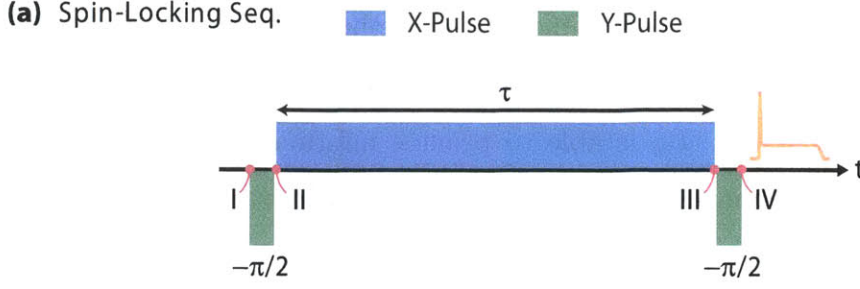
(b) Dynamics in Spin-Locking Seq.
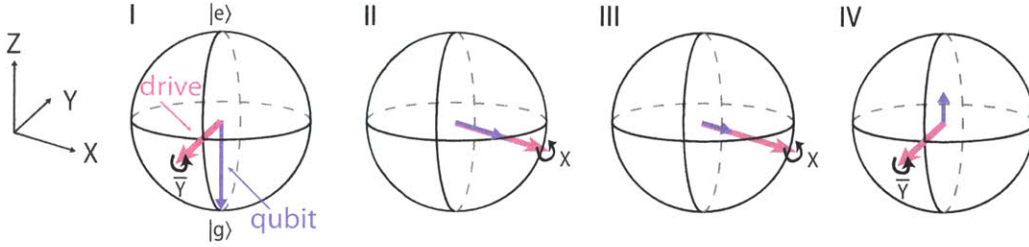
Figure 2-19: (a) Spin-locking pulse sequence. Ideally, neighboring pulses are immediately concatenated. (b) Bloch sphere representation of the rotating-frame qubit dynamics under the sequence in (a). The purple arrow is the qubit's state polarization, while the magenta arrow indicates the driving field. The qubit is initially prepared in its ground state (I). The first $\pi/2)_{\overline{Y}}$ pulse rotates the qubit by 90° into the equatorial plane (II). The second 90°-phase-shifted continuous driving pulse of duration τ, is then aligned with the qubit state, effectively locking the qubit along X. During the pulse, the qubit undergoes rotating-frame relaxation towards its steady state (III). The final $\pi/2)_{\overline{Y}}$ pulse projects the remaining polarization onto Z $(=z')$ for readout (IV).

where $\Gamma_{1\rho} = 1/T_{1\rho}$ is the rotating-frame longitudinal relaxation rate, and is related to both the qubit-frequency and Rabi-frequency noise (Eq. (2.59) and Eq. (2.29)):

$$
\begin{aligned}
\Gamma_{1\rho} &= \frac{1}{2}\Gamma_1 + \Gamma_\nu = \frac{1}{4}S_{x'}(\nu_\mathrm{q}) + \frac{1}{2}S_{z'}(\nu_\mathrm{R}) \\
&= \frac{1}{2}\Gamma_1 + \frac{1}{2}\left(\cos^2\theta\, S_\Delta(\nu_\mathrm{R}) + \sin^2\theta\, S_\varepsilon(\nu_\mathrm{R})\right) \\
&\approx \frac{1}{2}\Gamma_1 + \frac{1}{2}\left(S_\Delta(\nu_\mathrm{R}) + \frac{\varepsilon^2}{\Delta^2}S_\varepsilon(\nu_\mathrm{R})\right) .
\end{aligned}
\tag{2.64}
$$

76

The last line in Eq. (2.64) describes the situation when $\varepsilon \ll \Delta$. It indicates that Γ_ν is mostly contributed by the Δ noise at the sweet spot ($\varepsilon = 0$), and by the ε noise when sufficiently away from it.

2.6.3 Rabi Precession

The Rabi (RB) experiment [39], named after I.I. Rabi, is a method for measuring the rotating-frame transverse depolarization time $T_{2\rho}$, with bare rotating-frame (Rabi) precession. It is the driven-evolution analogue of the free-induction (FI) experiment. T_{Rabi} denotes the characteristic decay time, and the decay, like its free-evolution counterpart, might not have a simple form for the decay law. The $1/e$ time is a good measure. Besides the noise that contributes to $T_{1\rho}$, the value of T_{Rabi} provides additional information about the low-frequency ν_{R} and $\Delta\nu$ noise, i.e., slow fluctuation of the drive amplitude and the qubit frequency (z' noise), respectively. The former modifies the effective Rabi frequency to first order, and the latter to second order. They constitute the second part of the rotating-frame pure dephasing $T_{\varphi\rho}^{\ddagger}$. The weighting of each source's contribution depends on the working point of ε and ν_{R}. In most occasions for our device, the low-frequency ν_{R} noise dominates the Rabi decay. The Rabi experiment sets the simplest example of driven evolution, and is widely used in NMR and atomic physics for driving transitions. The technique also becomes popular in quantum information science for its usefulness in building quantum gates.

The pulse sequence is simply a single continuous driving pulse, say X-pulse. As described in Sec. 2.4.1 and Sec. 2.6.1, the qubit, initialized at its ground state $|-Z\rangle$, undergoes precession around the $Y-Z$ plane, while depolarize at the same time. The depolarization due to the pure-phasing part can be understood in the same way as in the free-induction pure dephasing illustrated in Sec. 2.5.3. It is an ensemble effect from the variation of the Rabi-precession rate. By stepping the pulse duration τ, we thereby record the damping Rabi cycles.

The general-sense $T_{2\rho}$, like its free-evolution counterpart, also factorizes into two parts, one induced by high- and intermediate-frequency (ν_{q} and ν_{R}) noise and the

77

(a) Rabi Seq.
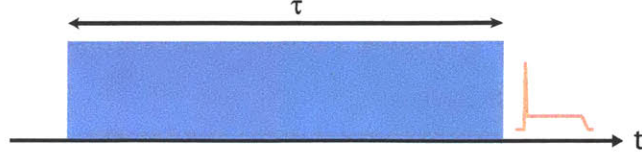
(b) Rabi dephasing
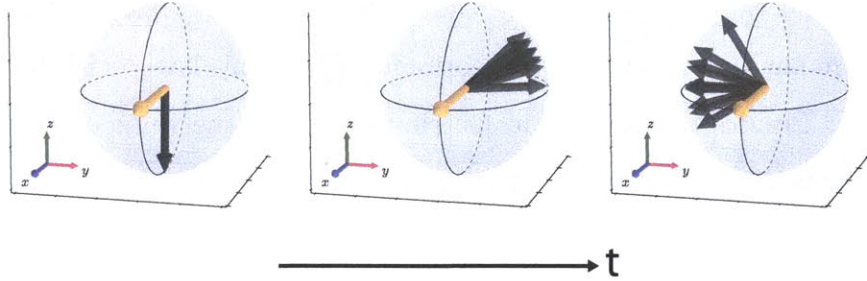
Figure 2-20: (a) Rabi pulse sequence. It is simply a single duration-varying driving pulse. (b) Illustration of the rotating-frame (Rabi) dephasing by tracking an ensemble of state vectors with fluctuating Rabi frequencies. From left to right: starting from the ground state, the vectors continue to fan out, while their mean nutation speed is given by a nominal Rabi frequency (yellow).

other by low-frequency noise:

$$P(\tau) = \exp\left(-(\frac{\Gamma_{1\rho}}{2} + \Gamma_{\varphi\rho}^{\ddagger})\tau\right) h(\tau) , \qquad (2.65)$$

where $h(\tau)$ is the pure-dephasing function, which corresponds to the second part of pure dephasing associated with $T_{\varphi\rho}^{\ddagger}$.

In the Rabi case, based on Eq. (2.59) and the quasistatic or filter function approach prescribed in Sec. 2.5.3, we obtain the approximated Rabi decay law for $1/f$-like ν_{R}

and $\Delta\nu$ noise,

$$P_{\mathrm{RB}}(\tau) = \cos(2\pi\nu_{\mathrm{R}}\tau) \times \exp\left(-(\frac{3}{4}\Gamma_1 + \frac{1}{2}\Gamma_\nu)\tau\right)$$

$$\times \exp\left(-\frac{(2\pi)^2\sigma_\nu^2\tau^2}{2}\right) \times \left(1 + \left(\frac{2\pi\sigma_{z'}^2}{\nu_{\mathrm{R}}}\tau\right)^2\right)^{-1/4}, \qquad (2.66)$$

where σ_ν^2 and $\sigma_{z'}^2$ are the variance of ν_{R} and $\Delta\nu$ fluctuation sampled by the measurement protocol (Eq. (2.44)), respectively. The second line in Eq. (2.66) represents $h_{\mathrm{RB}}(\tau)$.

In Eq. (2.66), the exponential part results from the qubit-frequency and Rabi-frequency noise as derived in the GBE theory. Noise at these relatively high frequencies usually has a smooth spectrum over the critical bandwidth $1/\tau$ (short-correlated in the rotating frame), and thus gives exponential decay which cannot be corrected for by dynamic decoupling (irreversible). Close to the sweet spot, Γ_ν has a quadratic ε-dependence on $S_\varepsilon(\nu_{\mathrm{R}})$ (Eq. (2.64)), suggesting that we can tune the sensitivity to this noise by biasing ε. The Gaussian decay is the consequence of the $1/f$ drive-amplitude noise. The effect is analogous to the linearly coupled (first-order) noise in free-induction decay (Eq. (2.43)). For linearly coupled noise with an arbitrary spectrum, we can also use the filter function method (Eq. (2.45) and Eq. (2.46)). Since the phase-accumulation scheme is identical to that of free induction, Rabi shares the same filter functions, i.e., $F_{\mathrm{RB}}^{\ddagger}(f,\tau) = F_{\mathrm{FI}}(f,\tau)$ ("$\ddagger$" indicates that the filter function is for the low-frequency noise without frequency mixing. The drive-amplitude noise in our device is proved to be a parasitic effect from instability in a current line which fluctuates the effective microwave field seen by the qubit [58]. σ_ν^2 is independent of ε, but scales with ν_{R}. The polynomial function represents the effect of quadratically coupled (second-order) $\Delta\nu$ noise (see [37] for detailed derivation). As shown in Eq. (2.44), it also has a quadratic ε-dependence on the ε noise.

2.6.4 Rotary Echo

The rotary-echo (RE) or Hahn-echo experiment is a method for measuring the transverse depolarization time, $T_{2\rho}$, with contribution from inhomogeneous or low-frequency noise removed. It can be considered as a driven-evolution analogue of the spin-echo (SE) experiment. The characteristic decay time, T_{Rotary}, provides information about the rotating-frame longitudinal relaxation, as well as the drive-amplitude noise at the rotary-echo filter frequency. Rotary echo was developed in NMR to mitigate the driven-evolution dephasing from the r.f. field inhomogeneity [63].

The pulse sequence consists of two continuous driving pulse next to each other with the same amplitude and duration but a 180°-phase difference, say the $X-\overline{X}$ combination. During the first pulse, the qubit, starting from its ground state $|-Z\rangle$, undergoes Rabi precession for a duration of $\tau/2$ around the $Y - Z$ plane counter-clockwise as viewed from the X-axis. The 180°-phase shift of the second pulse effectively reverses the driving axis to be along $\overline{X}$, so that the qubit precesses in the opposite direction during the second pulse. If the precession rate is the same between the first and second half (quasistatic), the qubit would end up at the ground state $|-Z\rangle$, no matter how the rate varies among different realizations. Therefore, inhomogeneities or low-frequency fluctuation of the effective Rabi frequency (fictitious qubit frequency) can be refocused by this technique. Indeed, rotary echo is a driven-evolution analogue of spin echo. It sets the simplest example of driven-evolution dynamical decoupling.

Similar to the spin-echo sequence, rotary-echo is also susceptible to noise at a frequency close to $1/\tau$. Therefore, rotary-echo could be utilized to extract noise information at this particular frequency. To linearly coupled Gaussian noise, both sequences share the same filter function, i.e., $F_{\mathrm{RE}}(f,\tau) = F_{\mathrm{SE}}(f,\tau)$ (Eq. (2.49).

Following the extension of the spin-echo sequence to the CP-like sequence, we can also generalize the rotary-echo sequence to a multiple-refocusing version, which is a series of pulses with uniform amplitude and duration but in an alternate phase setting (Fig. 2-22). As the total driving period is chopped into finer cells, the sequence becomes sensitive to higher-frequency noise.

(a) Rotary-Echo Seq.
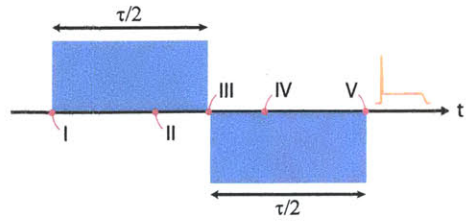
(b) Refocusing of Rabi Dephasing in Rotary-Echo Seq.
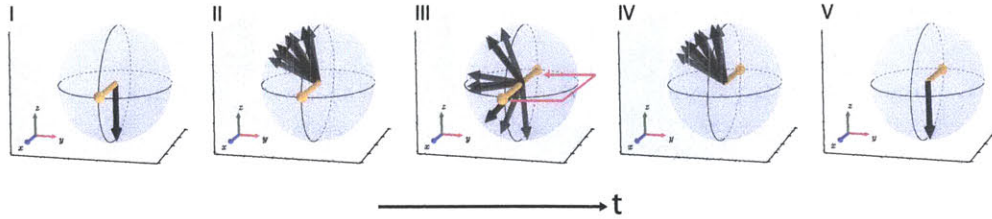
Figure 2-21: (a) Rotary-echo pulse sequence. (b) Illustration of the rotating-frame phase refocusing under the sequence in (a). The qubit, initialized at the ground state (I), nutates and dephases during the first pulse (II). At the transition to the second pulse (III), the orientation of driving field (yellow) reverses (red arrow), and starts to nutate the qubit in the opposite direction during the second pulse. Since the Rabi precession rate of each realization is unchanged throughout the sequence, the dynamics is completely reversed in the second half (IV) and all the phases echo in the end (V).

CP-like Rotary-Echo Seq.
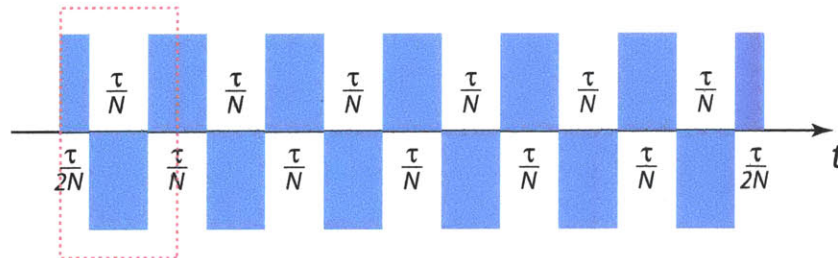
Figure 2-22: The CP-like generalization of the rotary-echo pulse sequence. The cell included by the dashed box indicates a refocused identity.

In this spirit, all the dynamical-decoupling sequences can be implemented by their driven-evolution counterparts. The grandest experimental challenge would be to fight against pulse imperfection introduced by waveform distortion from electronics and by

noise from the system itself, e.g., the $\Delta\nu$ fluctuation.

2.7 Summary

In this chapter, we discuss the qubit dynamics both during free and driven evolution in a theoretical perspective. Table. 2.1 summaries the analogy between the two types of evolution.

	Decoherence during free evolution	Decoherence during driven evolution
Working frame	Qubit frame	Rotating frame
Quantization axis	z'-axis	X-axis
Nutation freq.	level splitting ν_q	Rabi frequency ν_R
Longitudinal relaxation		
Method	Inversion recovery [64, 65]	Spin locking - $T_{1\rho}$ ([46])
Process	$T_1\ (=1/\Gamma_1)$	$T_{1\rho}\ (=1/\Gamma_{1\rho})$
Longitudinal decay	z'-axis	X-axis
Starting state	$|+z'\rangle$	$|\pm X\rangle$
Steady state	$|-z'\rangle$	$\mathcal{R}_X \approx 0$
Decay rate	Γ_1 (exponential)	$\Gamma_{1\rho}$ (exp.)
Decay law	$\exp\{-\Gamma_1\tau\}$, where $\Gamma_1 = \frac{1}{2}S_{x'}(\nu_q)$	$\exp\{-(\frac{1}{2}\Gamma_1+\Gamma_\nu)\tau\}$, where $\Gamma_\nu = \frac{1}{2}S_{z'}(\nu_R)$
Noise susceptibility		
• in general	$S_{\perp z'}(\nu_q)$	$S_{\perp X}(\nu_R)$
• flux qubit	$S_{x'}(\nu_q)$	$S_{x'}(\nu_q \pm \nu_R \approx \nu_q),\ S_{z'}(\nu_R)$
Noise of interest	$S_{x'}(\nu_q)$	$S_{z'}(\nu_R)$
Transverse decoherence		
Method	Free induction, Spin echo, CPMG [64, 66, 21]	Rabi [21, 67], Rotary echo [58]
Process	$T_2\ (=1/\Gamma_2)$	$T_{2\rho}\ (=1/\Gamma_{2\rho})$
Transverse decay	$x'-y'$ plane	$Y-Z$ plane
Starting state	e.g., $|\pm x',\pm y'\rangle$	$|-Z\rangle\ (=|-z'\rangle)$
Steady state	$\mathcal{R}_{x',y'}=0$	$\mathcal{R}_{Y,Z}\approx 0$
Decay rate		
• Bloch-Redfield	$\Gamma_2 = \frac{1}{2}\Gamma_1 + \Gamma_\varphi$ (exp.)	$\Gamma_{2\rho} = \frac{1}{2}\Gamma_{1\rho} + \Gamma_{\varphi\rho}$ (exp.)
• $1/f$-type noise	exp.×Gaussian (linear)	exp.×Gaussian×algebraic (quadratic)
Decay law (FI/RB)	$\exp\{-\frac{1}{2}\Gamma_1\tau - \frac{1}{2}(2\pi)^2\sigma_{z'}^2\tau^2\}$ $\times \cos(2\pi\Delta\nu\tau)$	$\exp\{-(\frac{3}{4}\Gamma_1+\frac{1}{2}\Gamma_\nu)\tau-\frac{1}{2}(2\pi)^2\sigma_\nu^2\tau^2\}$ $\times[1+(\frac{2\pi\sigma_{z'}^2}{\nu_R}\tau)^2]^{-1/4}\cos(2\pi\nu_R\tau)$
Noise susceptibility		
• in general	Γ_1: $S_{\perp z'}(\nu_q)$; Γ_φ: $\Delta\nu$ inhom.	$\Gamma_{1\rho}$: $S_{\perp X}(\nu_R)$; $\Gamma_{\varphi\rho}$: ν_R' inhom.
• flux qubit	Γ_1: $S_{x'}(\nu_q)$; Γ_φ: $\Delta\nu$ inhom.	$\Gamma_{1\rho}$: $S_{x'}(\nu_q\pm\nu_R\approx\nu_q),\ S_{z'}(\nu_R)$; $\Gamma_{\varphi\rho}$: $S_{x'}(\nu_q),\ \nu_R$ and $\Delta\nu$ inhom.
Noise of interest	$\sigma_{z'}^2$	$\Gamma_\nu = \frac{1}{2}S_{z'}(\nu_R)$

Table 2.1: Comparison of decohering properties during free evolution and driven evolution (weak and resonant).

Chapter 3

A Superconducting Qubit: The Persistent-Current Qubit

3.1 Introduction

There are various candidates for physical realization of a quantum two-level system (qubit). These range from systems provided by nature, like nuclear spins [24], to man-made systems, like quantum dots [10]. Among them, the superconducting qubits are considered as the leading candidate for scalable quantum computing [11, 12, 13]. They are based on modern lithography which patterns solid-state structures on chip, providing scalability and enormous engineering flexibility.

The superconducting qubits are fabricated superconducting circuits that use Josephson junctions [16] as the elements that creates well-defined two-level system [68, 69, 70]. There are numerous designs of superconducting qubits, and in this thesis we will only focus on one, the persistent-current qubit [14]. It is a state-of-art design of the superconducting flux qubit, so, by saying flux qubit, we mean the persistent-current qubit unless otherwise specified.

In this chapter, we will review the flux qubit and how it is measured. We will also briefly discuss how the device was fabricated and the experimental setup used to measure the qubit.

3.2 The Persistent-Current Qubit

To start with, a brief review of quantum harmonic oscillator would help us understand the construction of superconducting qubits. The superconducting LC resonator is an ideal example of quantum harmonic oscillator.

Consider a non-dissipative LC resonator (Fig. 3-1). It is one of the simplest circuits, which consists of an inductor with inductance L and a capacitor with capacitance C. It is a electrical analogue of a one-dimensional mechanical harmonic oscillator, in which the mechanical quantities, position x and momentum p, are replaced by the electromagnetic ones:

$$x \to \Phi = LI$$
$$p \to Q = CV \ , \tag{3.1}$$

where Φ is the branch flux on the inductor (through current I), and Q is the branch charge on the capacitor (crossing voltage V). Analogously, the kinetic energy K and potential energy U are the capacitive energy and inductive energy, respectively:

$$K = \frac{1}{2}CV^2 = \frac{Q^2}{2C}$$
$$U = \frac{1}{2}LI^2 = \frac{\Phi^2}{2L} \ . \tag{3.2}$$

By Legendre transformation, the classical Hamiltonian is equivalent to the total energy:

$$H = \frac{1}{2C}Q^2 + \frac{1}{2L}\Phi^2 \ . \tag{3.3}$$

In the quantum regime, the Hamiltonian is quantized by first replacing the variables Q and Φ by quantum operators $\hat{Q}$ and $\hat{\Phi}$. $\hat{Q}$ and $\hat{\Phi}$ form a pair of canonical conjugates, which obey the canonical commutation relation,

$$\left[\hat{\Phi}, \hat{Q}\right] = i\hbar \ . \tag{3.4}$$
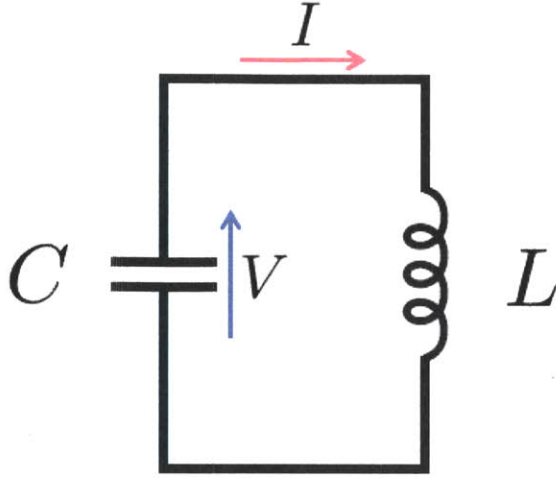
Figure 3-1: Schematic diagram of an *LC* circuit.

The quantum Hamiltonian reads

$$\hat{H} = \frac{1}{2C}\hat{Q}^2 + \frac{1}{2L}\hat{\Phi}^2 \ ,$$ (3.5)

which can be expressed in either flux or charge representation. If we choose the flux representation, the operators are given by

$$\hat{\Phi} = \Phi$$
$$\hat{Q} = -i\hbar\frac{\partial}{\partial\Phi} \ .$$ (3.6)

The solution of Eq. (3.5) can be found in many textbooks. The most significant result is that the eigenvalues of quantum harmonic oscillator (E_n^{LC}) corresponds to a series of uniformly spaced energy levels (Fig. 3-2):

$$E_n^{LC} = \left(n + \frac{1}{2}\right)\hbar\omega_r \ ,$$ (3.7)

where $\omega_r = 1/\sqrt{LC}$ is the oscillator's resonant frequency.

In this energy structure, all transitions are degenerate. Therefore, it is impossible to construct a qualified two-level system, the subspace of which is well protected from
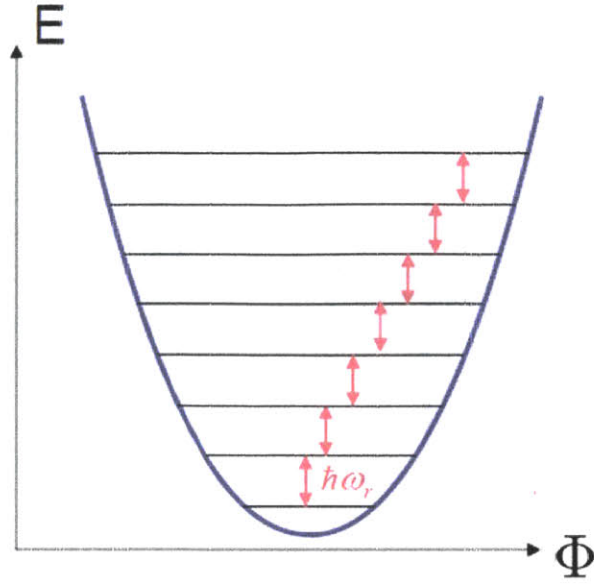
Figure 3-2: Energy diagram of a quantum harmonic oscillator.

leakage. Also, an arbitrary transformation is not feasible in this structure. In order to construct a well-defined two-level system based on the LC resonator, we need to introduce anharmonicity into the system, which can "stretch" the energy levels to a non-uniform structure. To that end, we may blend some nonlinear ingredient into the circuit.

3.2.1 Josephson Junction

Many materials are observed to have zero electrical resistance when cooled below a critical temperature, e.g., $1.2\,\mathrm{K}$ for Aluminum. This phenomenon is called superconductivity. In conventional superconductors like many metals, it is explained by the BCS theory [71, 72, 73]. Below a critical temperature, electrons start to form bound pairs, known as the Cooper pairs, by an attraction mediated by lattice phonons. If the minimum energy to excite the Cooper pairs is larger than the thermal energy of the lattice, the cooper pair fluid is a superfluid, meaning that it can flow without energy dissipation. All the Cooper pairs in a superconductor can be described by a wave function with a single phase parameter, $\Psi = \sqrt{n_{\mathrm{s}}}\,e^{i\varphi_{\mathrm{s}}}$, where n_{s} is the density of Cooper pairs and φ_{s} is the superconducting phase.
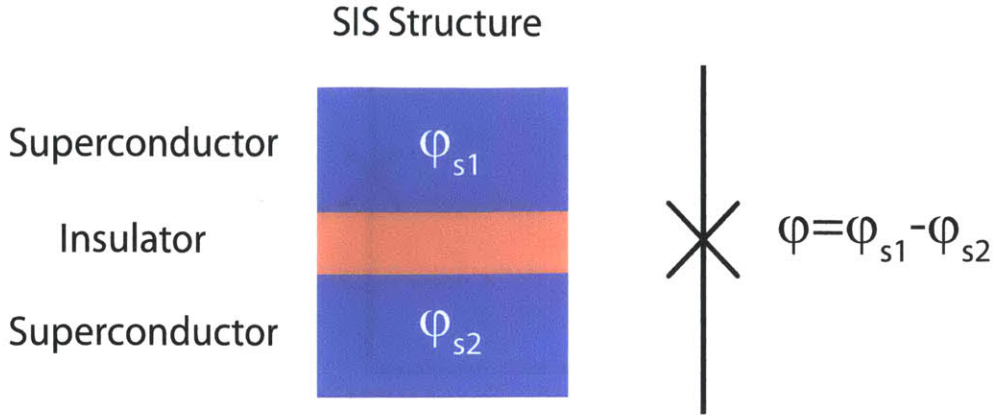
SIS Structure

Figure 3-3: Schematic diagram of the Josephson junction with the Superconductor-Insulator-Superconductor (SIS) structure. The cross is the circuit symbol for the Josephson junction, which is described by the gauge-invariant phase difference (φ) between the two superconducting electrodes..

What is more remarkable is that these Cooper pairs can tunnel through a potential barrier without dissipation. The barrier can be constructed by sandwiching a nanometer-thick insulator with two superconducting electrodes. Such structure is the most common type of the Josephson junction. The current and voltage between the two electrodes can be related to the their gauge-invariant phase difference, $\varphi = \varphi_{s1} - \varphi_{s2}$ [74]:

$$I = I_c \sin \varphi \qquad (3.8)$$

$$V = \frac{\Phi_0}{2\pi} \frac{d\varphi}{dt} , \qquad (3.9)$$

where I_c is known as the junction's critical current, which depends on the materials and junction width, and $\Phi_0 = h/2e$ is the superconducting flux quantum. The gauge-invariant phase difference is related to the branch flux for the junction by $\Phi = \frac{\varphi}{2\pi}\Phi_0$.

The non-dissipative Josephson junction can be modeled as an inductor L_J shunted by a capacitor C (Fig. 3-4). Eq. (3.8) and Eq. (3.9) are known as the current-phase and voltage-phase relations, respectively, and, when combined with the voltage-current
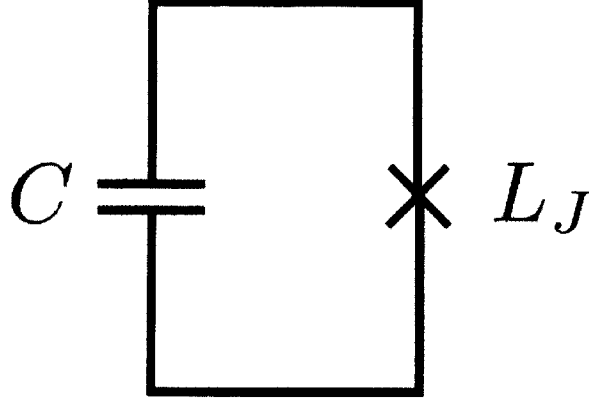
Figure 3-4: Schematic diagram of the equivalent circuit of a Josephson junction.

relation of an inductor, $V = L_{\mathrm{J}}\frac{\mathrm{d}I}{\mathrm{d}t}$, yield a phase-dependent inductance,

$$L_{\mathrm{J}} = \frac{\Phi_0}{2\pi I_{\mathrm{c}} \cos\varphi} \,. \tag{3.10}$$

The Josephson junction behaves like a nonlinear inductor, in which the stored energy becomes anharmonic:

$$U = -E_{\mathrm{J}} \cos\varphi \,, \tag{3.11}$$

where $E_{\mathrm{J}} = \frac{\Phi_0 I_{\mathrm{c}}}{2\pi}$ is known as the Josephson energy. By introducing the Josephson junction, we now have an anharmonic energy-level structure from the sinusoidal potential (E_n^{JJ}) and the lowest two states may be utilized as the qubit space (Fig. 3-5).

Note that the capacitive (kinetic) energy (Eq. (3.2)) is quantified by the junction's charging energy, $E_{\mathrm{C}} = e^2/2C$, while the inductive (potential) energy by the Josephson energy, E_{J} (Eq. (3.11)). The associated variables, Φ and Q, are subject to Heisenberg's uncertainty principle (Eq. (3.4)), so the working regime of the junction varies. On the one hand, when $E_{\mathrm{J}} \gg E_{\mathrm{C}}$, Φ is well defined, and Q has large quantum fluctuations. Therefore, the junction's Josephson (nonlinear) behavior dominates. One can expect stronger anharmonicity in the system. On the other hand, when $E_{\mathrm{J}} \ll E_{\mathrm{C}}$, Q is well defined, and Φ has large quantum fluctuations. The charging (linear) behaviour of the capacitor dominates. The system is close to the harmonic circuit.
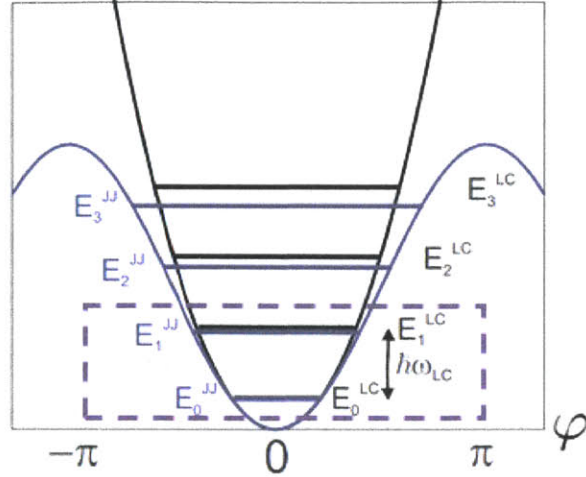
Figure 3-5: Energy diagram (blue) of the nonlinear circuit in Fig. 3-4, compared to the harmonic one (black). The lowest two levels in the dashed-box can be treated as a closed two-level system. $\omega_{LC} = \omega_r$ is the resonant frequency of the harmonic LC resonator.

3.2.2 The Persistent-Current Qubit

There are a variety of designs of superconducting qubits. Depending on the relative significance between the Josephson energy and the charging energy, E_J/E_C, super-conducting qubits are categorized into three primitive types, namely, charge [18], phase [75, 76] and flux qubit [77, 14].

The original design of the flux qubit is the RF SQUID quantum system first proposed by Leggett and Caldeira [78], from which the persistent-current qubit is improved. The RF SQUID, a superconducting loop interrupted by a single junction, can form a double well potential when biased by an external magnetic field of nearly half a flux quantum. These wells correspond to different fluxoid quantizations, with zero or one fluxoid quanta in the loop. These two states have circulating currents in opposite directions. When biased at exactly half a flux quantum, the wells are aligned. Thus the two lowest energy eigenstates are the symmetric and antisymmetric combination of both wells. When biased slightly off of half a flux quantum, one well is lower than the other. Thus the two lowest energy eigenstates are almost the two fluxoid quantization states, corresponding to current circulating in one direction or the other. This forms a measurable quantum system, as a magnetometer can detect

91

the flux in the loop and distinguish the circulating current of the two states.

The major problem with the RF SQUID design is that in order to have a potential energy landscape with two well-defined minima, both the inductance of the SQUID loop and the Josephson energy must be large [79]. First, this suppresses the tunneling, making it difficult to produce coherent superpositions between the lowest states in the wells. Second, the large inductance produces large magnetic fields (one flux quantum difference between the two circulating-current states), so any minute deviation from the optimal point will lead to strong coupling to the environment and fast decoherence.

The problem is solved by the design of the persistent-current qubit, which is now widely used in the community [14, 15]. The persistent-current qubit is a superconducting loop interrupted by three or four Josephson junctions (Fig. 3-6) with $E_J/E_C \sim 50$. In the three-junction design, one junction is smaller in cross-sectional area and thus has a smaller Josephson energy and capacitance than the other two by a factor α ($0.5 < \alpha < 1$). The potential energy of the system can be taken as the sum of each junction's inductive energy:

$$U = -E_J(\cos\varphi_1 + \cos\varphi_2 + \alpha\cos\varphi_3) \,, \tag{3.12}$$

where E_J is the Josephson energy of the larger junction. Due to the boundary condition in a closed loop, the gauge-invariant phases are constrained by the magnetic flux threading the loop:

$$\varphi_1 - \varphi_2 + \varphi_3 = 2\pi f_e \,, \tag{3.13}$$

where $f_e = \Phi_e/\Phi_0$ and Φ_e is the applied magnetic flux piercing the qubit loop.

Using the boundary condition, the energy in Eq. (3.12) represents a two-dimensional potential landscape, a function of φ_1 and φ_2. For a range of magnetic frustration close to $f_e = 1/2$, there are two stable solutions, which correspond to the energy minima in the two-dimensional potential. They also correspond to the loop currents flowing in opposite directions. It is easy to check that the solutions is periodic with period $f_e = 1$ and is symmetric about $f_e = 1/2$.
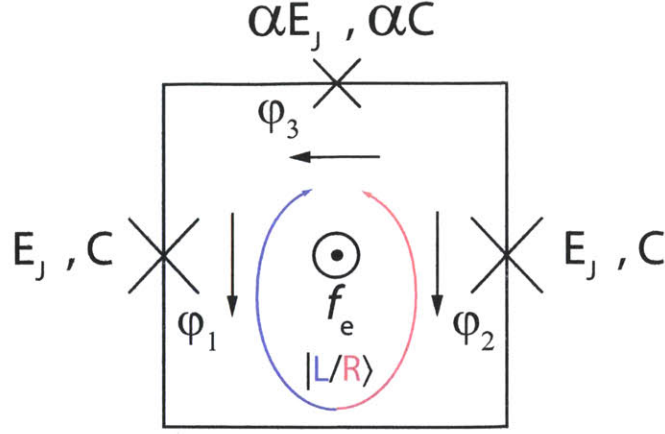
Figure 3-6: Schematic diagram of the persistent-current or flux qubit. The flux qubit is a superconducting loop of interrupted by three Josephson junctions, where the third junction is smaller in the Josephson energy and capacitance than the other two junctions by a factor of α. f_e is the applied magnetic flux threading the qubit loop (out of the plane), in units of a flux quantum Φ_0. The blue (red) arrow indicates the clockwise (anticlockwise) loop current, which also corresponds to the diabatic state $|\mathrm{L}\rangle$ ($|\mathrm{R}\rangle$).

The minima of Eq. (3.12) forms a two-dimensional square lattice pattern with lattice vectors, $\mathbf{a_1}$ and $\mathbf{a_2}$ (Fig. 3-7). The nearest neighbors, $(\varphi^* + 2k_1\pi, -\varphi^* + 2k_2\pi)$ and $(-\varphi^* + 2k_1\pi, \varphi^* + 2k_2\pi)$, where $\cos\varphi^* = 1/2\alpha$ and $k_{1,2}$ is an integer, construct a unit cell (figure-eight-shaped contour in Fig. 3-7). The barrier between the intra-cell double wells can be engineered by changing α. In general, smaller α results in lower intra-cell barrier, thus stronger intre-cell tunneling, which is important for allowing quantum superposition. This implies that, for the four-junction design where three junctions are identical and the third is smaller in size by a factor of α, the relevant tunneling is still the intra-cell tunneling between the double-well, which is tuned by α, despite that the potential landscape becomes three-dimensional.

Let $\varphi_p = (\varphi_1 + \varphi_2)/2$ and $\varphi_m = (\varphi_1 - \varphi_2)/2$, the quantum-mechanical Hamiltonian can be written as

$$\hat{H} = \frac{\hat{P}_p^2}{2M_p} + \frac{\hat{P}_m^2}{2M_m} + E_\mathrm{J}(-2\cos\varphi_p\cos\varphi_m - \alpha\cos(2\pi f_\mathrm{e} + 2\varphi_m))\,, \tag{3.14}$$

where $\hat{P}_p = -i\hbar\,\partial/\partial\varphi_p$ and $\hat{P}_m = -i\hbar\,\partial/\partial\varphi_m$. In the mass terms, $M_p = (\Phi_0/2\pi)^2 2C$

93
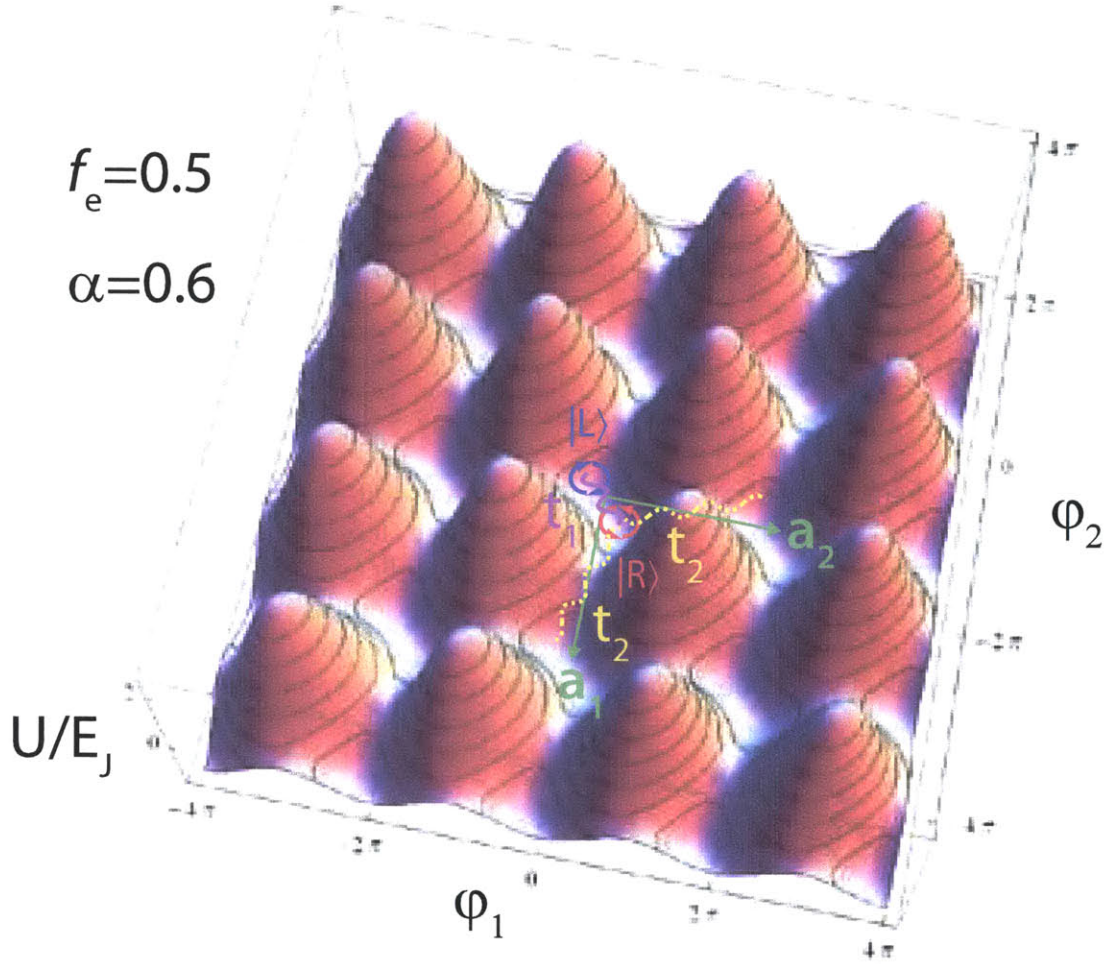
Figure 3-7: Contour plot of the 2D potential energy for the persistent-current qubit at $f_e = 0.5$ and $\alpha = 0.6$. The nearest two wells form a unit cell repeated in this two-dimensional centered cubic lattice, with lattice vectors, $\mathbf{a_1}$ and $\mathbf{a_2}$ (green arrows). The local ground states of the two wells are the diabatic circulating-current states, $|L\rangle$ and $|R\rangle$, respectively. By designing for negligible inter-cell tunneling (yellow dashed line; strength quantified by t_2), the potential can be viewed as a single double-well where only intra-cell tunneling is considered (purple solid line; strength quantified by t_1). Therefore, the potential energy can be treated as a one-dimensional double-well along the direction of intra-well coupling.

and $M_m = (\Phi_0/2\pi)^2 2C(1 + 2\alpha)$.

3.2.3   Tight-Binding Model and Two-Level Approximation

We use the tight-binding model, which approximates the system's wave function by a linear combination of the localized wave functions located at each individual

potential well. In addition, because the junctions are designed within the Josephson (anharmonic) regime $(E_J/E_C \gg 1)$, we can safely narrow our consideration to the ground states of the isolated wells.

These two approximations dramatically simplifies the problem. Let $|L\rangle$ denote the wave function for the ground state on one side of the double potential wells, and $|R\rangle$ be the wave function on the other side. The wave function of the system is their superposition, $|\psi\rangle = c_L |L\rangle + c_R |R\rangle$, and the Hamiltonian in Eq. (3.14) can be rewritten in this basis set as

$$\hat{\mathcal{H}} = \begin{pmatrix} H_{LL} & H_{LR} \\ H_{RL} & H_{RR} \end{pmatrix} = \frac{1}{2} \begin{pmatrix} \varepsilon & \Delta \\ \Delta & -\varepsilon \end{pmatrix} , \tag{3.15}$$

where the zero-energy offset is set by the ground state energy when $|L\rangle$ and $|R\rangle$ are in degeneracy, e.g., when $f_e = 1/2$. The energy difference between the two states of opposite circulating currents is given by $\varepsilon = 2(\partial U/\partial f_e)(f_e - 1/2) = 2I_p\Phi_0(f_e - 1/2)$, where I_p is the circulating current. ε is known as the flux detuning or energy flux bias. Δ is the tunnel-coupling matrix element between the two circulating-current states. Considering tunnel-coupling within the nearest cells only, $\Delta = t_1 + t_2 e^{i\mathbf{k}\cdot\mathbf{a_1}} + t_2 e^{i\mathbf{k}\cdot\mathbf{a_2}}$, where t_1 is the intra-cell tunneling matrix element, tunable by α, and t_2 is the inter-cell tunneling matrix element. $\mathbf{k}$ is the crystal momentum. Because $t_2/t_1 \propto e^{-E_J/E_C} \ll 1$, we can restrict our attention to intra-cell tunneling only, i.e., $\Delta = t_1$. Note that t_2 is related to gate voltage and offset charges. In the flux qubit, the gate-voltage fluctuation or charge noise has little influence to the energy levels, and thus is usually neglected.

The reduced Hamiltonian represented by Pauli matrices reads

$$\hat{\mathcal{H}} = \frac{h}{2}\left[\varepsilon\hat{\sigma}_z + \Delta\hat{\sigma}_x\right] , \tag{3.16}$$

where we express ε and Δ in terms of their corresponding frequency, i.e., making the substitution $\varepsilon \to h\varepsilon$ and $\Delta \to h\Delta$ in Eq. (3.15). Also note that, since only the intra-cell tunneling is considered, $\Delta = t_1$ is a real number, so there is no σ_y term. However,

even if there is, we can always renormalize the σ_x and σ_y components to retain the form in Eq. (3.16). The energy diagram associated with Eq. (3.16) is sketched in Fig. 3-8. The eigenvalues of the two-level system are

$$E_{\pm} = \pm \frac{h}{2}\sqrt{\varepsilon^2 + \Delta^2} \tag{3.17}$$

with eigenstates given by

$$|\psi_-\rangle = \sin\frac{\vartheta}{2}|\mathrm{L}\rangle - \cos\frac{\vartheta}{2}|\mathrm{R}\rangle$$
$$|\psi_+\rangle = \cos\frac{\vartheta}{2}|\mathrm{L}\rangle + \sin\frac{\vartheta}{2}|\mathrm{R}\rangle \ , \tag{3.18}$$

where $\vartheta = \tan^{-1}(\Delta/\varepsilon)$ and the codomain of $\tan^{-1}$ takes $[0, \pi]$.
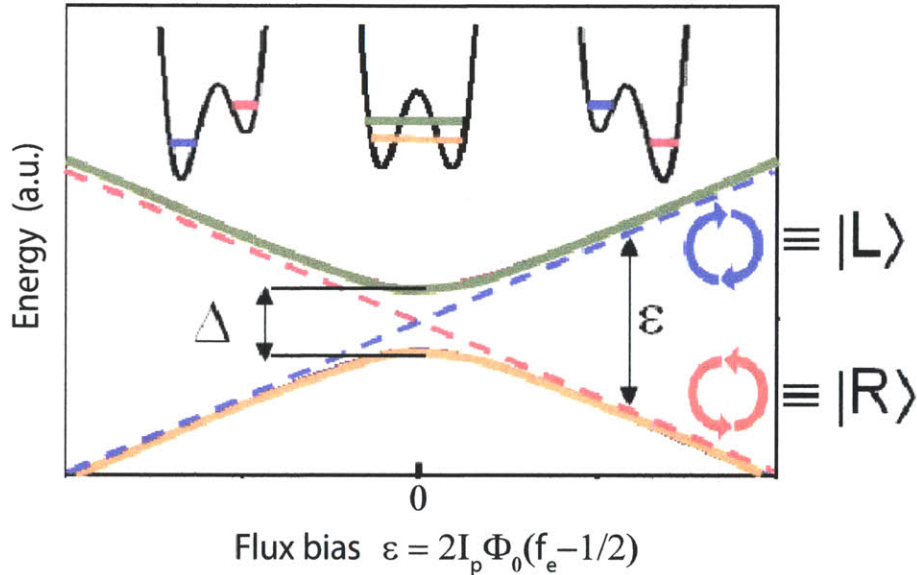
Figure 3-8: Two-level approximated energy diagram of the flux qubit. The ground state energy of the double-well follows the lower orange curve, while the excited state energy follows the upper green curve. When the system is tuned sufficiently away from $\varepsilon = 0$, the double-well tilts and the eigenstates are just the diabatic states, $|\mathrm{L}\rangle$ and $|\mathrm{R}\rangle$. At $\varepsilon = 0$, the double-well is symmetric and the eigenstates are the symmetric and anti-symmetric combinations of $|\mathrm{L}\rangle$ and $|\mathrm{R}\rangle$. The energies of the diabatic states are represented by dashed lines.

The physical picture of this system is illustrated in Fig. 3-8. When biasing the external flux far away from the half flux quantum point, i.e. $|\varepsilon| \gg \Delta$, the double-well

potential is tilted and the energy eigenstates become the diabatic circulating-current states. The energy difference $\Delta E = E_+ - E_-$ is approximately $h|\varepsilon|$. At $\varepsilon = 0$, i.e., exactly half a flux quantum threading the loop, the two wells are aligned (degeneracy), and the energy eigenstates become the symmetric and anti-symmetric combination of the two diabatic states, i.e., $\frac{1}{\sqrt{2}}(|L\rangle + |R\rangle)$ and $\frac{1}{\sqrt{2}}(|L\rangle - |R\rangle)$. The energy splitting is $h\Delta$. Such hybrid states are the consequence of the tunnel coupling between the two wells, which introduces an avoided crossing in the energy diagram. The remarkableness of such states is the quantum superposition of opposite circulating-current states, meaning the simultaneous existence of classically contradictive currents. These currents are formed by millions of electron pairs that behave coherently, so it is a true macroscopic quantum phenomenon [29]!

In experiments, we usually operate close to $\varepsilon = 0$, because the sensitivity to flux noise $(\partial \Delta E / \partial \varepsilon)$ is small. Therefore, it is more convenient to express the Hamiltonian in the orthogonal bases corresponding to the eigenbases at degeneracy. That is,

$$\hat{\mathcal{H}} = \frac{h}{2}\left[\Delta \hat{\sigma}_z + \varepsilon \hat{\sigma}_x\right] . \tag{3.19}$$

This is the same Hamiltonian as in Eq. (2.10).

3.2.4 The SQUID Detector

The diabatic circulating-current states can generate different magnetic flux. This suggests a natural way to measure these states by inductively coupling the flux qubit to a magnetometer, which is a DC Superconducting Quantum Interference Device (DC SQUID)[80].

A DC SQUID is a superconducting loop interrupted by two Josephson junctions, which are larger than those in the qubit loop (Fig. 3-9a) and described by phase differences $\varphi_{1,sq}$ and $\varphi_{2,sq}$. They are designed to have the same critical current $I_{c,sq}$ and shunt capacitor C_{sh}. Two lines are connected to manipulate the SQUID by applying a current line (I_{sq}), and to measure the voltage (V_{sq}) across the SQUID. Due to the same boundary condition on the gauge-invariant phase difference as in

Eq. (3.13) but with one less variable, the current through the SQUID (I_{sq}) depends on the magnetic flux ($f_{e,sq} = \Phi_{e,sq}/\Phi_0$) threading its loop:

$$I_{sq} = 2I_{c,sq}|\cos(\pi f_{e,sq})|\sin\varphi_{1,sq} \,, \tag{3.20}$$

whose form is analogous to the current-phase relation of a single junction (Eq. (3.8)). Thus, the DC SQUID can be treated as a single junction with tunable critical current, i.e., $I'_{c,sq} = 2I_{c,sq}|\cos(\pi f_{e,sq})|$ (Fig. 3-9b).

From the RCSJ model [74], when a current I_b is added to the SQUID, ideally, the SQUID will be operating in either mode:

- Non-switching: when $I_b < I'_{c,sq}$, there is no voltage across the SQUID (zero-voltage state).

- Switching: when $I_b > I'_{c,sq}$, a non-zero voltage occurs (finite-voltage state).

Therefore, $I'_{c,sq}$ is known as the switching current. The exact switching-current distribution of a DC SQUID can be quantitatively calculated by the macroscopic quantum tunneling (MQT) theory, and depends on the SQUID parameters and temperature [81].

When the qubit is embedded inside the DC SQUID, its magnetization, resulting from the persistent currents, modulates the flux threading the SQUID loop (a modulation of $\pm\,\delta f_{e,sq}$, depending on the current direction) and thus the switching current (Fig. 3-9b). In this spirit, the device is often designed such that, an externally applied magnetic flux, which biases the qubit around half flux quantum, also sets the working point of the SQUID around $f_{e,sq} = k + 1/2$, where k is an integer. Around these points, the SQUID is most sensitive (enhanced $\partial I_{c,sq}/\partial f_{e,sq}$) to flux variation.

To read out the qubit's state (or more precisely, the probability in one of the energy eigenstates), we apply to the SQUID a rapid readout pulse, which consists of a sample-and-hold current (Fig. 3-9c) [21]. The output voltage, after room-temperature amplification, is threshold-detected to register the presence (absence) of a voltage corresponding to the qubit being (not being) in state $|L\rangle$. We determine the switching
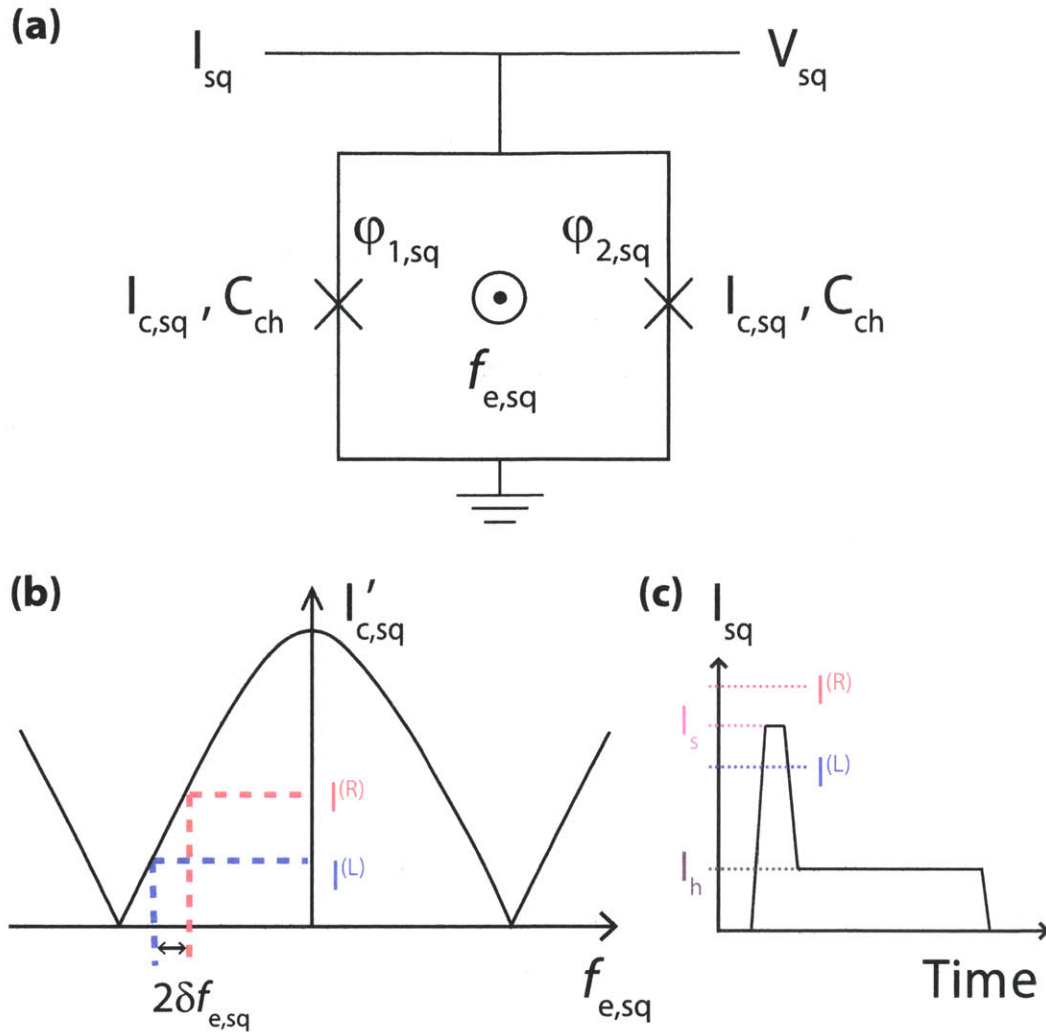
Figure 3-9: (a) Schematic diagram of the DC SQUID. The DC SQUID is a supercon-
ducting loop interrupted by two Josephson junctions, with additional leads attached
to pulse the SQUID (I_{sq}) and to measure the SQUID voltage (V_{sq}). $f_{e,sq}$ is the mag-
netic flux piercing the SQUID loop, in units of a flux quantum Φ_0. (b) The SQUID
switching current's dependence on the applied flux. Dashed lines illustrate how the
qubit state can be differentiated by the switching current in a sensitive regime of the
lobe. $I^{(L)}$ ($I^{(R)}$) is the switching current for the diabatic state $|L\rangle$ ($|R\rangle$). Note that,
the symmetry point in the figure is not necessarily $f_{e,sq} = 0$. (c) Rapid readout pulse.
The sample current I_s is calibrated to sit between $I^{(L)}$ and $I^{(R)}$ for state differentia-
tion. The hold current I_h is for room-temperature electronics to register the SQUID
output.

probability, P_{sw}, statistically by repeating this measurement several thousand times.

Due to enhanced relaxation when a current is flowing through the SQUID, a rapid

sample pulse is desirable for good readout visibility. A hold current is necessary for

room-temperature electronics to register the voltage signal before retrapping occurs. The repetition rate is limited, as a sufficient delay ($\sim 1\,\text{ms}$ in our device) between measurements is required for the readout-induced quasiparticles to relax back to the ground state.

One might ask how we can differentiate the state at degeneracy, where both eigenstates have 50% probability to be in either circulating-current state. We are fortunate to have a parasitic effect to solve this problem. Besides sampling the SQUID's switching current, the readout pulse also couples flux into the qubit, effectively shifting the flux bias adiabatically, $|\psi_-\rangle \rightarrow |\text{L}\rangle$ and $|\psi_+\rangle \rightarrow |\text{R}\rangle$, before the measurement takes place [82, 64]. The adiabatic shift is essential, since it conserves the eigenstates' population while shifting the eigenbases to those that can be distinguished.

3.3   Device Description and Measurement Setup

The device explored in this thesis is fabricated at NEC, Japan, by using the standard Niemeyer-Dolan angle-evaporation deposition process of Al–AlO$_x$–Al on a SiO$_2$/Si wafer (Fig. 3-10a). All the experiments are performed at MIT.

Our persistent-current qubit [66, 21] consists of a superconducting loop with diameter $d \sim 2\,\mu\text{m}$, interrupted by four Josephson junctions (Fig. 3-10). Three of the junctions each have the Josephson energy $E_\text{J} = h \times 210\,\text{GHz}$, and charging energy $E_\text{C} = h \times 4\,\text{GHz}$; the fourth is smaller by a factor $\alpha = 0.54$. The ratio of energy scales puts the device in the flux limit, $E_\text{J}/E_\text{C} \approx 50$, thus making the gauge-invariant phases well defined. The geometric (L_g) and kinetic (L_k) loop inductances are negligible compared to the Josephson inductance (L_J):

$$L_\text{g} \sim \mu_0 d \sim 2\,\text{pH}, \quad L_\text{k} = \mu_0 \lambda_\text{L}^2 \, l/S \sim 30\,\text{pH}, \quad L_\text{J} = \Phi_0/2\pi I_\text{c} \sim 10\,\text{nH},$$

where we used $\lambda_\text{L} = 100\,\text{nm}$, $l = 10\,\mu\text{m}$, and $S = 20 \times 250\,\text{nm}^2$.

The four-junction design shares the similar tight-binging solutions with the three-junction one (Sec. 3.2). However, the extra junction usually provides better coherence
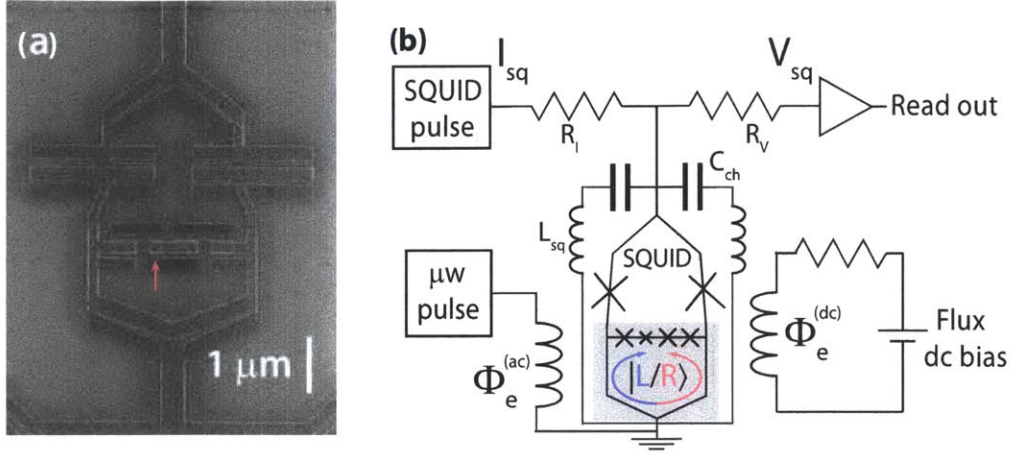
Figure 3-10: (a) Scanning electron micrograph (SEM) of a device (qubit and SQUID shown) with identical design parameters as the one measured in the experiments. The arrow indicates the smaller junction. (b) Schematic diagram of device and measurement circuitry. The qubit loop (shaded) is magnetically controlled by dc flux bias from a coil mounted in the box and microwave irradiation from an on-chip antenna. The coupled DC SQUID is shunted by a capacitor C_{sh} and loop inductance L_{sq}. A current line and a voltage line are connected for bias and readout.

properties in that it restores the symmetry that is lost in the three-junction circuit due to the double-layer structure [83]. Such structure will always produce an even number of junctions in the circuit, so to enclose only three into the loop unavoidably undermines the symmetry between the two branch lines shared by the qubit and SQUID, transferring fluctuation of the SQUID's bias current to the qubit.

In experiments, we operate the qubit by an external magnetic flux, $\Phi_e \approx -\Phi_0/2$, threading the loop. Around half a flux quantum, the qubit's potential energy assumes a double-well profile. The wells are associated with clockwise and counterclockwise circulating currents of magnitude $I_p \approx 180\,\text{nA}$ and energies $\pm h\varepsilon/2 = \pm I_p \Phi_b$, where $\Phi_b = \Phi_e + \Phi_0/2$, tunable by the applied flux, so we have the sensitivity $\kappa_\varepsilon = \partial\varepsilon/\partial\Phi \approx 1.1\,\text{MHz}/\mu\Phi_0$. These diabatic circulating-current states tunnel-couple with a strength $\Delta = 5.4\,\text{GHz}$. Because the interface between the superconductor and the oxide is never perfectly smooth, the effective contact surface could be changing on a microscopic scale, fluctuating E_J or I_c, and thus Δ. The sensitivity in this device is calculated to be $\kappa_\Delta = \partial\Delta/\partial i_c \approx 3.2\,\text{GHz}$ [21] (∂i_c is normalized critical-current

fluctuation, i.e., $\partial i_c = \partial I_c / I_c$).

The simulated energy diagram (Fig. 3-11) shows that the device is a good approximation to a two-level system, as the transition between the second and third level is about 30 GHz, way above the level splitting between the lowest two levels.
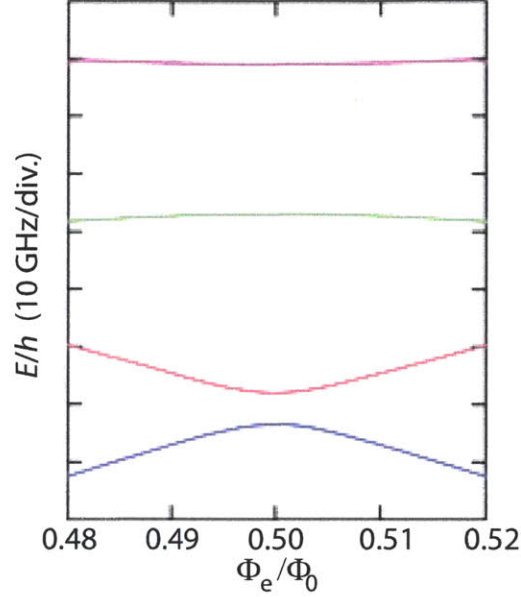
Figure 3-11: Simulated energy structure.

The qubit is embedded in a hysteretic DC SQUID, a sensitive magnetometer which serves as the qubit readout. It has critical current $I_{c,sq} = 4.5\,\mu\text{A}$; normal resistance $R_N = 0.25\,\text{k}\Omega$; mutual qubit–SQUID inductance $M_{Q-S} = 21\,\text{pH}$; on-chip shunt capacitors $C_{sh} \approx 10\,\text{pF}$, inductors $L_{sq} \approx 0.1\,\text{nH}$, and bias resistors $R_I = 1\,\text{k}\Omega$ and $R_V = 1\,\text{k}\Omega$. The shunt capacitors bring the plasma frequency down to $f_p/2\pi = 2.1\,\text{GHz}$. The size of the SQUID loop is about three times that of the qubit loop. Therefore, when half a flux quantum threads the qubit loop, approximately three halves threads the SQUID loop, optimizing the state distinguishability (Fig. 3-9c).

The rapid readout is calibrated for an optimized visibility of 79 % between the qubit's ground and excited state (Fig. 3-12), which is limited primarily by the much faster relaxation when the sample current biases the SQUID away from the bias-current sweet spot [66]. The adiabatic flux shift induced by the readout pulse is about $30\,\text{m}\Phi_0$ in magnitude (in terms of ε, $\sim 30\,\text{GHz} \gg \Delta$) and to the left hand

side in Fig. 3-8 or Fig. 3-11 due to the realistic geometry in our device. Therefore, the ground-state population is registered by that of $|L\rangle$ after the shift. The diabatic state $|L\rangle$ corresponds to a smaller switching current for the working point we choose (Fig. 3-9b), implying a higher (lower) switching probability for the ground (excited) state (Fig. 3-12b).
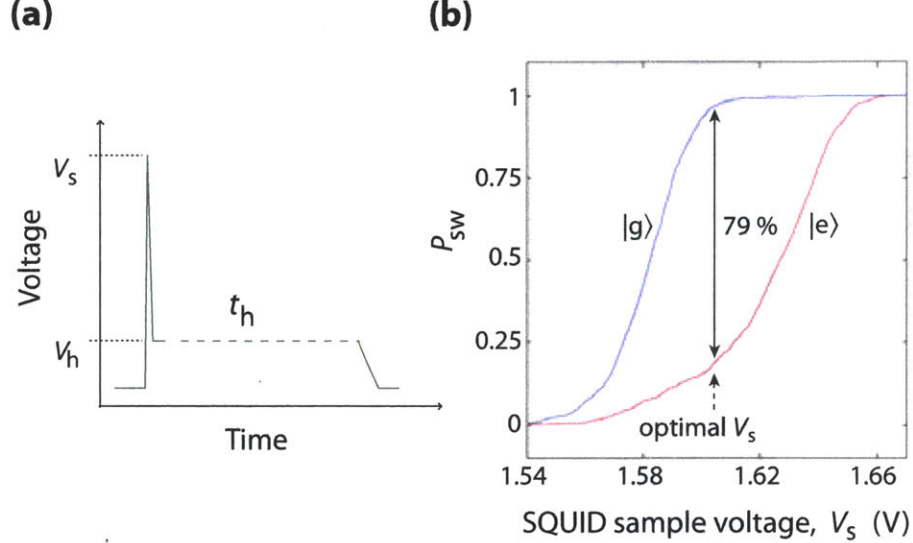
Figure 3-12: (a), Readout pulse (voltage pulse generated from a waveform generator). The pulse is properly attenuated and then goes across a 1-kΩ bias resistance. The optimized pulse shape is programmed to have a 5 ns sample pulse, including 1.5 ns rise, 2 ns sample, and 1.5 ns fall times, followed by a 4 μs hold plateau at $20 \sim 30\%$ of the sample voltage. (b), Readout visibility at $\Phi_b = 0$. Scans of the SQUID's switching probability, P_{sw}, versus the height of the sampling pulse. We obtain 79% readout visibility between the qubit's ground and excited states. Relaxation during read out leads to an imperfect determination of the excited state (17% dark counts at the optimal V_s). Note that, for such nanosecond sample pulse, the effective sample voltage is much lower than the nominal value due to electronics' bandwidth limitation.

The chip containing the qubit and surrounding SQUID is mounted in a closed microwave package (Fig. 3-13). Two SSMB lines (I_{sq} and V_{sq}) connect to the chip via microstrip lines and wirebonds for SQUID bias and readout. A niobium coil, a solenoid in the shape of a bobbin, with mutual coupling $M_{dc} = 0.6$ pH to the qubit loop is mounted to the lid to provide the dc magnetic field, i.e., $\Phi_e^{(dc)}$ ($\varepsilon^{(dc)}$) and $\Phi_{e,sq}^{(dc)}$. The qubit loop is also coupled to an on-chip microwave antenna (aluminum loop

launched from a coplanar waveguide towards ground) with designed mutual inductance $M = 0.02\,\mathrm{pH}$ ($R = 50\,\Omega$ termination), which provides r.f microwave irradiation, i.e., $\Phi_e^{(\mathrm{ac})}$ ($\varepsilon^{(\mathrm{ac})}$), for qubit manipulation.
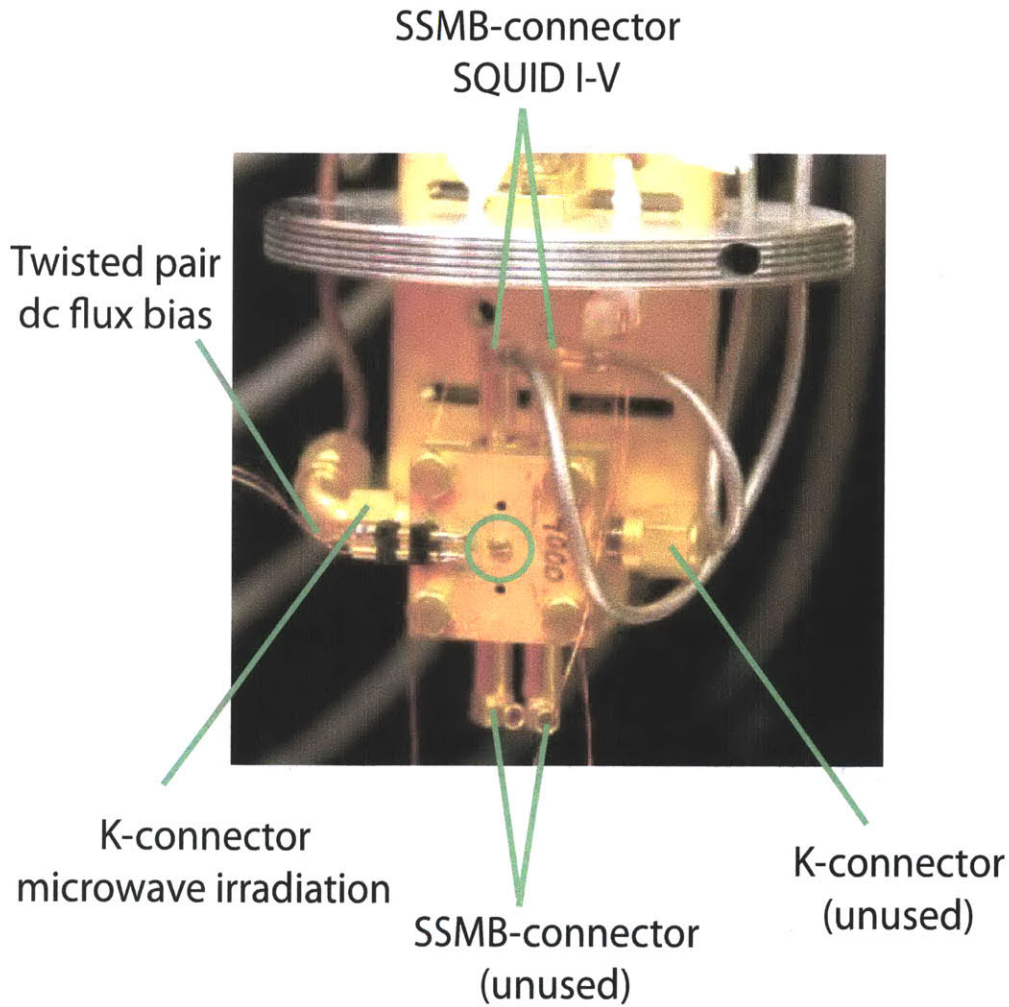
Figure 3-13: Microwave package mounted on a cold finger. The chip is embedded at the center of the package (unseen). Readout electronics are connected via two SSMB connectors, and r.f. control is applied via a K-connector which is connected to a co-planar waveguide and then an on-chip antenna. The dc flux bias is provided by a niobium wire coil mounted on the lid (indicated by the circle, but on the other side), which is connected to room-temperature electronics via a twisted pair.

The package is placed within an aluminum can to shield it from magnetic flux noise as well as 50 mK blackbody radiation, and is thermally anchored to the mixing chamber of an Oxford Kelvinox 400 dilution refrigerator, which provides a typical

base temperature of 12 mK (not necessarily the effective device temperature) (Fig. 3-14). Four layers of cryoperm-10 μ-metal shielding were installed in the Kelvinox to provide magnetic shielding
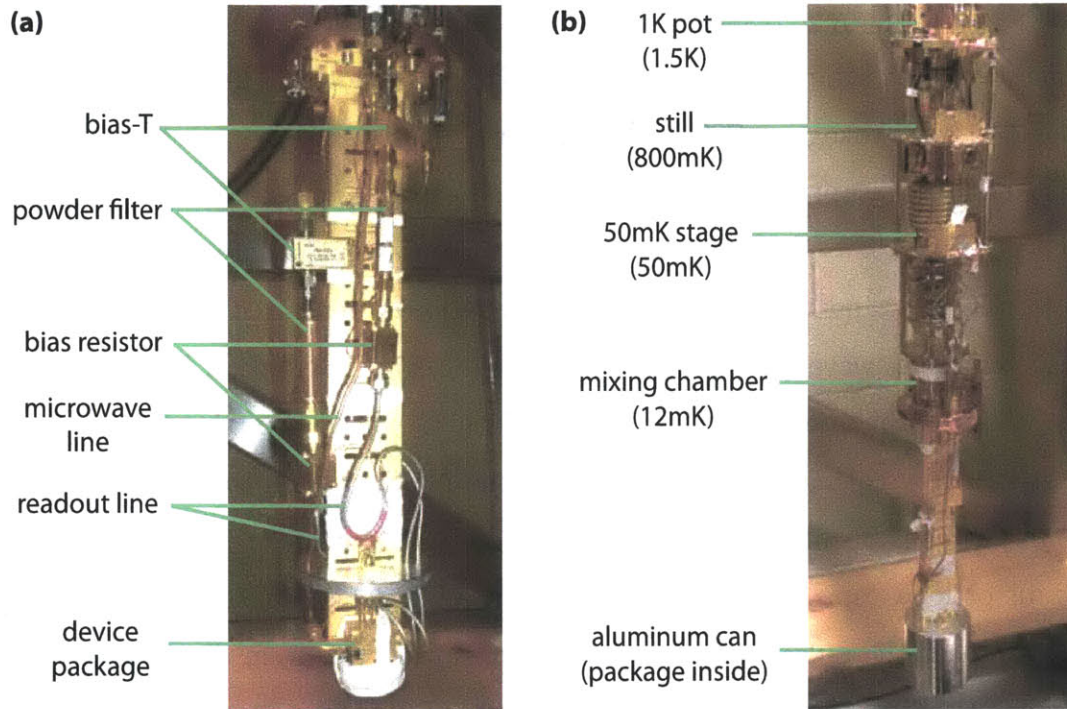
Figure 3-14: (a) Electronics below the mixing chamber. (b) Dilution refrigerator insert and temperature at each stage.

The SQUID lines (I_{sq} and V_{sq}) go through copper powder filters (low-pass) and 1 kΩ resistor boxes (impedance match) below the mixing chamber. The voltage line goes through a twisted pair and an RC filter (50 kHz cutoff) at the 1K pot. The current line combines two lines by a bias-T before the powder filter. One fast line ($I_{sq}^{(ac)}$) with 40 dB attenuation at the 1K pot and 10 dB attenuation at the mixing chamber is used for the rapid readout. The other dc line ($I_{sq}^{(dc)}$) goes through a similar setup as in the voltage line to provide dc current bias.

The dc flux line made of twisted pair is filtered at the 1K pot, and thermally anchored at every stage before passing through a powder filter below the mixing chamber and then reaching the solenoid mounted on the package. The microwave line has 20 dB attenuation at the 1K pot and no additional filtering.

Outside the refrigerator, the SQUID voltage line goes to a homemade low-noise

battery-powered amplifier and an SR560 low-noise preamplifier. An Agilent 53132A Universal Counter is then used to perform threshold detection and accumulate the total number of switches within an allotted gate time. The fast SQUID current signal is generated by a Tektronix 5014 Arbitrary Waveform Generator (AWG) (four channels, 1.2 GHz sampling rate and $\sim$ 300 MHz bandwidth). The SQUID bias signal is provided by a Yokogawa 7651 Programmable DC Source.

The dc flux bias, provided by another same Yokogawa, passes though a homemade RC filter box (2 kΩ, $\sim$1 kHz cutoff). The r.f. microwave pulses are created by mixing the in-phase (A_I) and quadrature (A_I) pulse envelopes, generated by the same AWG, with a continuous wave, provided by an Agilent E8267D PSG Vector Signal Generator Vector. We use the internal I/Q mixer of the PSG for envelope mixing. The pulses are further gated by gating pulses generated by the AWG in order to eliminate leakage.

Imperfections in the electronics and coaxial cables outside the cryostat will cause pulse distortions, especially for those few-nanosecond-long (Gaussian) shaped pulses. To ensure that the pulses we send to the cryostat are free from distortions, we first determine the transfer function H_{ext}, the frequency-domain representation of the systems impulse response, with a high-speed oscilloscope and then use H_{ext}^{-1} to correct for imperfections in the AWG and in the I/Q mixers. This setup allows us to create well-defined Gaussian-shaped microwave pulses with pulse widths as short as 2.5 ns.

The pulses may be further improved by taking into account signal distortions occurring inside the cryostat, e.g., from bonding wires or impedance mismatches on the chip. The associated transfer function H_{int} can be derived indirectly by measuring amplified response of the qubit's evolution due to pulse distortions [84]. However, this second-step calibration technique was not used in the experiments explored in this thesis.

Chapter 4

Basic Coherence Characterization Methods

4.1 Introduction

In this chapter, we present several coherent characterization methods introduced in Chap. 2 in an experimental perspective. The device and measurement setup from which all the data are taken is the same one described in Sec.3.3.

4.2 Qubit Spectrum

In almost all of our experiments, we need to first find out the qubit frequency for calibrating r.f. pulses. The routine is to measure the qubit's spectrum prior to other measurements. The spectrum will also help identify the flux bias we are going to operate in further measurements.

The qubit frequency versus external dc flux bias $\Phi_b = \Phi_e + \Phi_0/2$ (the qubit is biased around $\Phi_e = -\Phi_0/2$) is measured through saturated frequency spectroscopy (Fig. 4-1) [85]. That is, driving the qubit with a sufficiently long (longer than any relaxation times, about five times T_1 in our experiment) and low-power r.f. pulse, whose frequency, ν_{rf}, is the scanned parameter.

The measured spectroscopy (Fig. 4-1a) confirms the qubit frequency's depen-
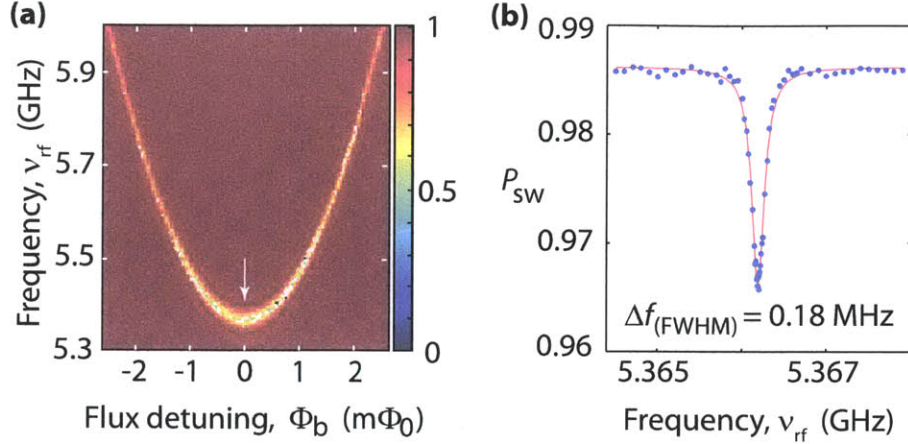
Figure 4-1: (a) Frequency spectroscopy of the qubit measured by a weak saturation pulse. (b) Spectroscopy at $\Phi_b = 0$, i.e., the degeneracy point or the sweet spot (arrow in (a)).

dence on the flux detuning (Eq. (2.16)), and reaches the minimum $\Delta \approx 5.366\,\mathrm{GHz}$ at the sweet spot. The Lorentzian full-width-at-half-maximum (FWHM) linewidth $\Delta f_{(\mathrm{FWHM})} = 0.18\,\mathrm{MHz}$ (Fig. 4-1b) is slightly larger than that inferred from the time-domain free-induction decay, indicating slight power broadening.

4.3 Free-Evolution Coherence Characterization

The inversion recovery, free induction (Ramsey) and spin echo are routinely a basic combination of free-evolution coherence characterization experiments. Their results, when combined, provides valuable noise information over a wide frequency range.

4.3.1 Inversion Recovery and High-Frequency Noise Spectroscopy

The pulse sequence and dynamics is described in Sec. 2.5.2. In fact, since the longitudinal depolarization rate is independent of the qubit's initial state, an arbitrary nutation angle besides π is basically feasible. Even a saturation (long driving) pulse can do the job. However, the π-pulse inversion maximizes the visibility, making it a more efficient experiment. An example of measured T_1 relaxation at the sweet spot

$(\Phi_b = 0)$ is shown in Fig. 4-2. The fitting model is

$$P_{sw}(\tau) = -A \exp\left(-\Gamma_1 \tau\right) + C , \qquad (4.1)$$

where A and C are constants. Statistically, $T_1 = 1/\Gamma_1 = 12 \pm 1\,\mu s$, and is remarkably long among superconducting qubits[13], about six times longer than a similarly designed and fabricated device[66]. T_1 also varies among different thermal cycles. In several new cool-downs, we do observe longer T_1. For example, $T_1 \sim 15\,\mu s$ for the experiment discussed in Chap. 6. The use of lower repetition rate $\sim 500\,\mathrm{Hz}$ (before, $1\,\mathrm{kHz}$) and new configuration of noise sources after thermal cycling are part of the reason.
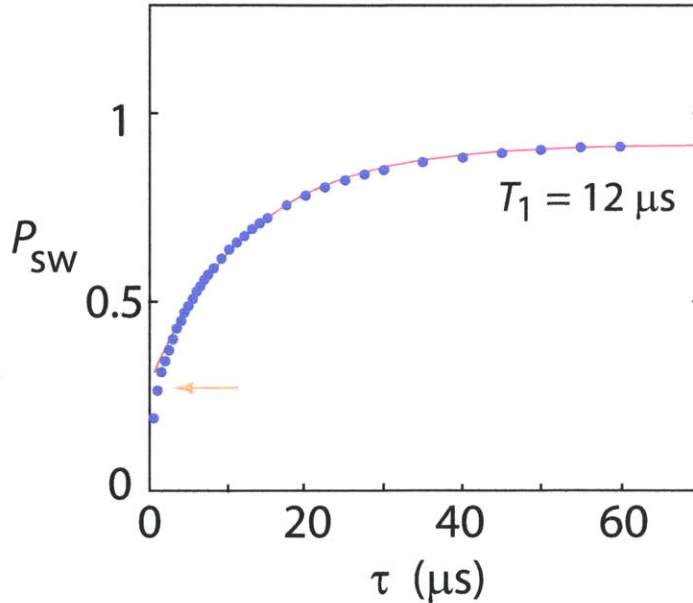
Figure 4-2: An example of measured inversion recovery showing T_1 relaxation at $\Phi_b = 0$ with an exponential decay time of $12\,\mu s$ from fit. The arrow indicates a faster decay at the beginning. The repetition rate is $1\,\mathrm{kHz}$.

It is often seen that the measured relaxation exhibits a faster decay during the beginning $1 \sim 2\,\mu s$ (arrow in Fig. 4-2). The behavior depends on the qubit frequency. It is absent in measured relaxation at some other ν_q, so to be related to some specific environmental modes. We think that the non-equilibrium dynamics of a localized

spin bath leads to the varying relaxation rate over time.

The flux-detuning dependence of T_1 is shown in Fig. 4-3 (black dots). The rates are symmetric about the sweet spot, as expected from Eq. (2.29). Despite small random variations due to inhomogeneity in environmental modes, T_1 is generally independent of flux bias in the vicinity of the degeneracy point. This agrees with Eq. (2.29), since the first-order dependence on the ε noise is flat in this region ($\cos^2 \theta \approx 1$), and the Δ noise (possibly from charge or critical-current fluctuation) is relatively small and thus negligible.

Note that the π-pulse we use to excite the qubit is a resonant pulse which could possibly influence the same environmental modes related to the qubit's relaxation. To measure the true relaxation at certain flux bias, we can modify the protocol. Bias the qubit at a different frequency and excite it, and then adiabatically shift to the working point. However, the meaning of the true relaxation rate is ambiguous. A pulsed experiment is usually made up of many resonant pulses, so the relaxation rate corresponding to unperturbed environment might not be practical.

High-frequency spectroscopy is performed by measuring relaxation over a wider range of flux detuning. The PSD can be inferred from Eq. (2.38), for $f > \Delta$. Since there are two noise sources (ε and Δ), we are unable to decompose individual contributions. Shown in Fig. 4-7 is the combined x'-noise PSD done by the saturation pulse. Distinguishing between the two sources is possible with the tunable-Δ persistent-current qubit [86]. There we can change the energy splitting while keeping the sensitivity fixed. A similar experiment has been demonstrated in the charge qubit where an ohmic charge noise is observed [65].

4.3.2 Free Induction Decay and Quasistatic Noise

The pulse sequence and dynamics is described in Sec. 2.5.3. An example of measured free-induction decay at the sweet spot is shown in Fig. 4-4. To be more general, both
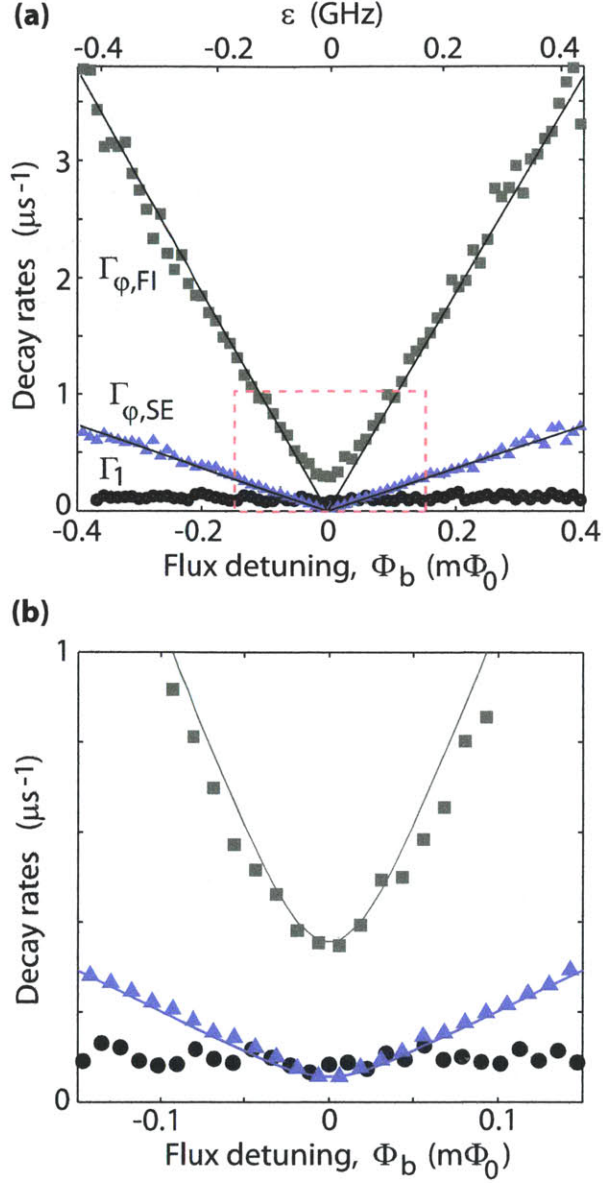
Figure 4-3: (a) Energy-relaxation rate, Γ_1, Gaussian pure-dephasing rates for free-induction (Ramsey) decay, $\Gamma_{\varphi,\text{FI}}$, and the spin-echo decay, $\Gamma_{\varphi,\text{SE}}$, after subtracting the Γ_1 contribution. Straight, black lines are fits to $\Gamma_{\varphi,\text{FI/SE}}(\Phi_b)$ with the ε noise considered only. (b) Blow up of the data in the dashed-box region in (a), along with simulated free-induction and spin-echo decay rates including both the ε and Δ noises.

exponential and Gaussian decay modes are included in the fitting model:

$$P_{\text{sw}}(\tau) = A\cos(2\pi\Delta\nu\tau + B)\exp\left(-\Gamma_1\tau/2 - \Gamma_{\varphi,\text{FI}}^{(\text{E})}\tau - (\Gamma_{\varphi,\text{FI}}^{(\text{G})}\tau)^2\right) + C\,, \qquad (4.2)$$

111

where Γ_1 is known from previously measured T_1 relaxation, and $\Gamma_{\varphi,\mathrm{FI}}^{(\mathrm{E})}$ ($\Gamma_{\varphi,\mathrm{FI}}^{(\mathrm{G})}$) is the free-induction exponential (Gaussian) pure-dephasing rate. At base temperature, the pure-dephasing component is Gaussian-dominated, indicating the noise to be $1/f$-type. Therefore, we assume only the Gaussian part is present for analysis related to this section. However, as we will see in Sec. 4.3.4, the exponential decay could be comparable to even overrides the Gaussian decay at higher temperatures.
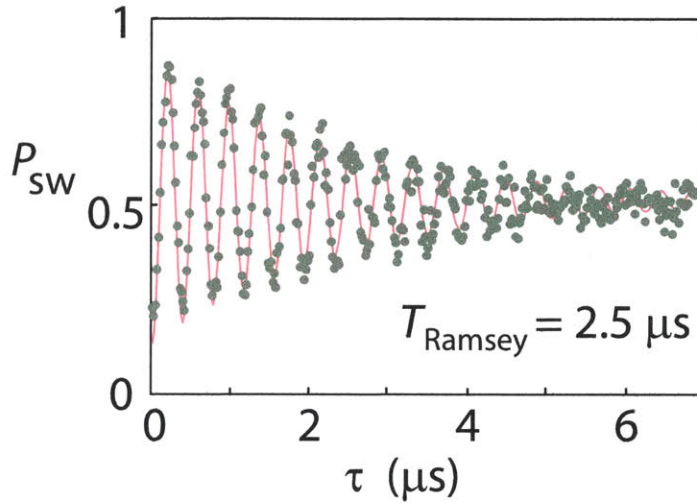
Figure 4-4: An example of measured free-induction decay or Ramsey fringe at $\Phi_{\mathrm{b}} = 0$ and $\Delta\nu = 2.5\,\mathrm{MHz}$ with a $1/e$ time of $2.5\,\mu s$ from fit.

The flux-detuning dependence of $\Gamma_{\varphi,\mathrm{FI}}^{(\mathrm{G})}$ is shown in Fig. 4-3 (green squares). The sensitivity to ε noise grows with increasing flux detuning. The Gaussian decay rates are proportional to $|\varepsilon|$, in agreement with Eq. (2.29) and Eq. (2.44) for $1/f$ noise, except for a small vicinity of the degeneracy point ($|\varepsilon| < 100\,\mathrm{MHz}$). We calculated the second-order effect [46] from ε noise. The decay rate from quadratically coupled noise, which scales with $\sigma_{x'}^2/\nu_{\mathrm{q}}$, where $\sigma_{x'}^2$ is the total transverse quasistatic noise that equals to σ_ε^2 at degeneracy, fails to explain the measured free-induction decay. Thus when close to the sweet spot, dephasing is dominated by the Δ noise. By fitting the extracted decay rates to their ε dependence, the resultant quasistatic noise is

$\sigma_\varepsilon \approx 11$ MHz for the quasistatic ε noise, and $\sigma_\Delta \approx 65$ kHz for the quasistatic Δ noise. Modeled by the $1/f$ noise, $S_\lambda(f) = A_\lambda/|f|$, we have $A_\varepsilon \approx 2.0 \times 10^{14}$ (rad/s)^2 and $A_\Delta \approx 6.0 \times 10^9$ (rad/s)^2. The equivalent flux and critical-current noise are $A_\Phi = (1.7\,\mu\Phi_0)^2$ and $A_{i_c} = (4.0 \times 10^{-6})^2$ (i_c is normalized critical current) [21].

4.3.3 Spin Echo and Carr-Purcell-Meiboom-Gill Spectroscopy

The pulse sequence and dynamics is described in Sec. 2.5.4. An example of measured spin-echo decay at the sweet spot is shown in Fig. 4-5. For generality, we also include both exponential and Gaussian decay in the fitting model,

$$P_{\text{sw}}(\tau) = A \exp\left(-\Gamma_1 \tau/2 - \Gamma_{\varphi,\text{SE}}^{(\text{E})}\,\tau - (\Gamma_{\varphi,\text{SE}}^{(\text{G})}\,\tau)^2\right) + C \,, \qquad (4.3)$$

where Γ_1 is known from previously measured T_1 relaxation, and $\Gamma_{\varphi,\text{SE}}^{(\text{E})}$ ($\Gamma_{\varphi,\text{SE}}^{(\text{G})}$) is the spin-echo exponential (Gaussian) pure-dephasing rate. At degeneracy, the decay is almost exponential, and approaches the $2T_1$ limit. Therefore, the majority of the dephasing noise is long-correlated, and thereby effectively refocused by the echo technique. Away from degeneracy, a Gaussian pure dephasing becomes prominent due to the introduction of the stronger $1/f$ ε noise extending to the high-frequency cutoff ($f = 1/\tau$) of the quasistatic regime.

The flux-detuning dependence of $\Gamma_{\varphi,\text{SE}}^{(\text{G})}$ is shown in Fig. 4-3 (blue triangles). The Gaussian decay rates are proportional to $|\varepsilon|$, and the dependence is in accordance with what we found from the free-induction results (Sec. 4.3.2). Both experiments are well explained by the $1/f$ model for the ε noise. At the sweet spot, because the decay time is already close to the $2T_1$-limit, extracting the decay envelope requires a much finer measurement and analysis. More results and discussions are shown in Sec. 4.3.4.

Next, we apply the CPMG dynamical-decoupling sequences introduced in Sec. 2.5.4. The pure-dephasing component is still Gaussian. Fig. 4-6a shows the flux-detuning dependence of the $1/e$ decay rates for CPMG dynamical-decoupling sequences with $N = 2\ldots 48$ π-pulses along with the free induction ($N = 0$) and spin echo ($N =$
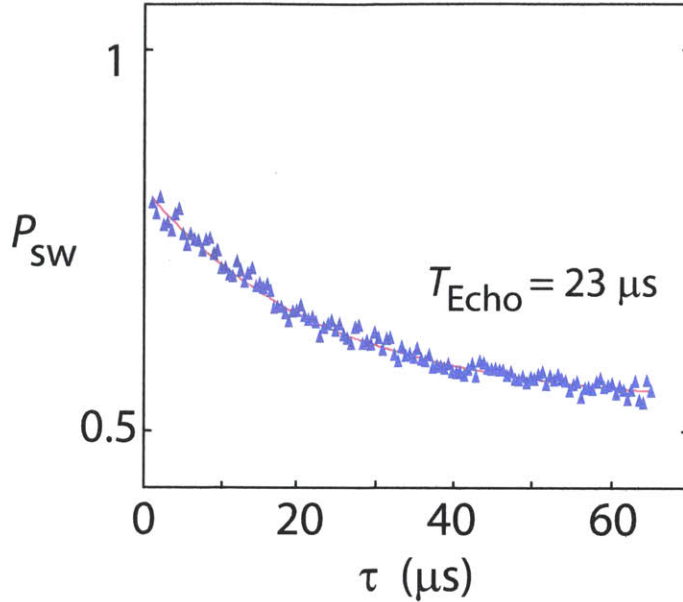
Figure 4-5: An example of measured spin-echo decay at $\Phi_b = 0$ with a $1/e$ time of $23\,\mu s$ (best case) from fit.

1) [21]. The rates monotonically improve towards the $1/2T_1$-limit when the number of π-pulses increases, extending the range around $\Phi_b = 0$ for which pure dephasing is negligible. We explicitly demonstrate the improvement in detail for each N out to $|\varepsilon| = 400\,\text{MHz}$, corresponding to a change in the qubit frequency of $15\,\text{MHz}$. However, the dynamical-decoupling method is not fundamentally limited to this range. Although the coherence times generally decrease as $|\varepsilon|$ is increased due to the qubit's increased sensitivity to the ε (flux) noise, the fractional improvement in coherence is essentially constant over the entire range.

At a specific flux bias $\Phi_b = -0.4\,\text{m}\Phi_0$, where the qubit is highly sensitive to the ε noise, the CPMG sequence gives a marked improvement in the decay time up to $N \approx 200$ π-pulses, beyond which pulse errors begin to limit the CPMG efficiency (Fig. 4-6b). We achieve a 50-fold enhancement of T_{CPMG} over the free induction T_{FI}, and well over 100-fold improvement in the Gaussian pure dephasing time. We have also performed CP and UDD dynamical-decoupling sequences. The CPMG sequence performs about 5% better than UDD, and dramatically outperforms CP,

despite having the same filter function. This shows that we have pulse errors in our system and CPMG is a robust sequence against pulse non-idealities.
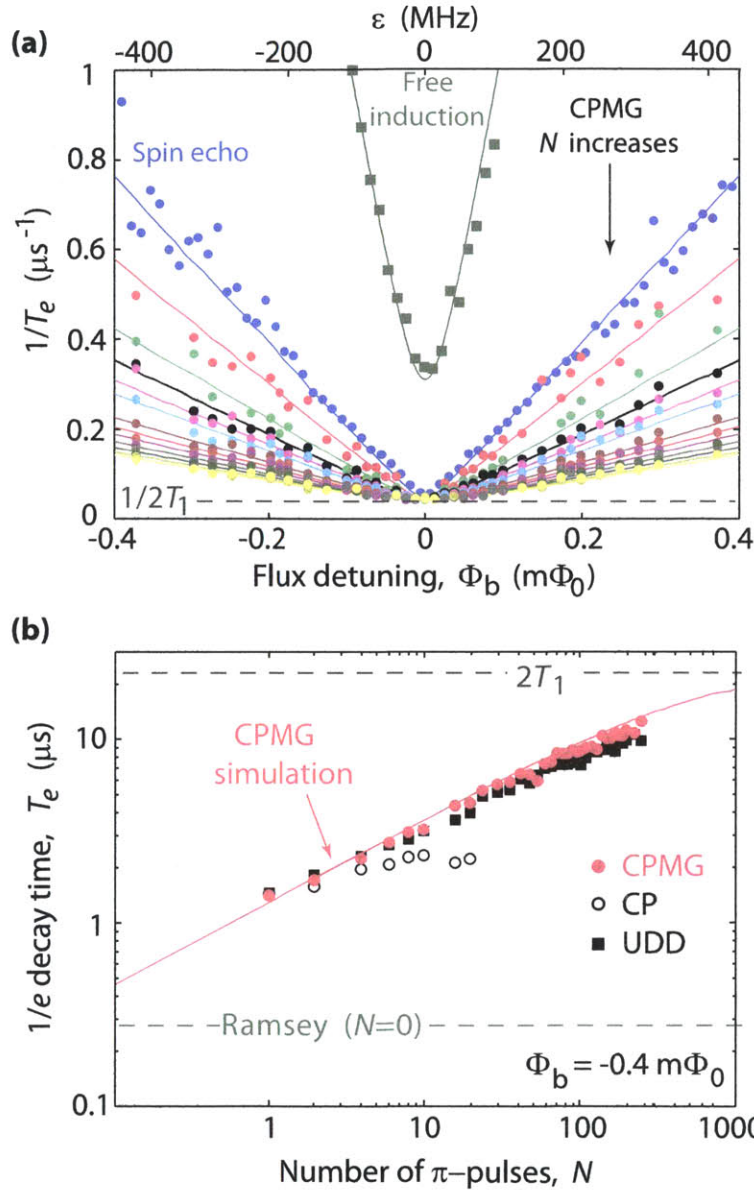
Figure 4-6: (a) $1/e$ decay rates versus flux detuning: Free induction ($N = 0$, green squares) and CPMG (coloured dots) with $N = 1, 2, 4, 6, 8, 10, 16, 20, 24, 30, 36, 42, 48$. Solid lines are calculations by the filter function method (Sec. 2.5.4) with parameters extracted from the free-induction and spin-echo results (Sec. 4.3.2 and Sec. 4.3.3). (b) $1/e$ decay time under N-pulse CPMG, CP, and UDD sequences at $\Phi_b = -0.4 \, \text{m}\Phi_0$ ($\varepsilon = 430 \, \text{MHz}$). The simulation (red line) assumes ideal pulses and noise.

Given its superior performance mitigating noise, we in turn use the filtering prop-

erty of the CPMG sequence to characterize the ε-noise spectrum. The main peak of the N-π-pulse CP filter function $F_{\mathrm{CP}}^{(N)}(f,\tau)$ (Sec. 2.5.4) becomes narrower about $f = N/2\tau$ when N increases, so we can treat the noise as a constant and approximate Eq. (2.45) as

$$h_{\mathrm{CP}}(\tau) \approx \exp\left(-\tau^2 \int_0^\infty \mathrm{d}f\, S_{z'}(N/2\tau)\, F_{\mathrm{CP}}^{(N)}(f,\tau)\right)$$
$$= \exp\left(-\frac{1}{2} S_{z'}(N/2\tau)\,\tau\right)\,. \tag{4.4}$$

The noise PSD for each N and τ can thus be extracted from the pure-dephasing signal. There are three types of decay involved in the measured CPMG decay: pure dephasing ($\Gamma_{\varphi,\mathrm{CP}}$) and exponential relaxation ($\Gamma_1/2$) during the total free-evolution time τ, and pulse-induced decay (Γ_{p}) during the r.f. driven periods. Using a recursive method explained in detail in the supplementary information of [21], we effectively divide out the Γ_1 and Γ_{p} components from the raw data and compute the noise PSD $S_\varepsilon(f)$ without presuming a functional form for the decay function or the spectrum. This procedure yields a $1/f$-type PSD over the region $0.2-20\,\mathrm{MHz}$ in Fig. 4-7, with a slight increase in the measured PSD above $2\,\mathrm{MHz}$. Interestingly, by fitting the lower-frequency, linear portion we find that the PSD can be approximated by a $1/f^\alpha$ power law [87] with $\alpha \approx 0.9$ (solid, red line) and noise amplitude $A_\Phi = (0.8\,\mu\Phi_0)^2$.

Remarkably, dynamical decoupling techniques are not only restricted to recover coherence within the Hilbert space of individual two-level systems, but also applicable to a broader range of quantum phenomena. For example, in the same device, we successfully implement a generalized version of the refocusing technique to a hybrid system, a flux qubit couple to an unknown microscopic two-level system, where the fluctuating coupling parameter leads to fast decoherence between the entangled states [88]. The coupling coherence is further enhanced when applying multiple refocusing pulses.

116
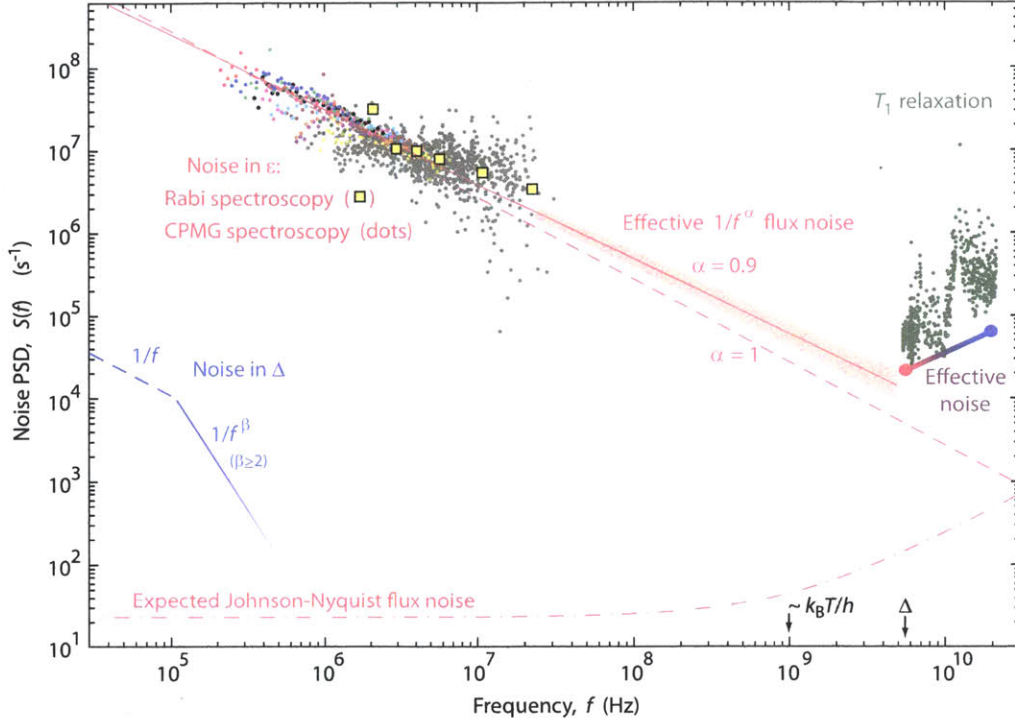
Figure 4-7: **Multi-coloured dots**, Extracted ε-noise PSD $(0.2 - 20\,\mathrm{MHz})$ by CPMG spectroscopy data at $\Phi_\mathrm{b} = -0.4\,\mathrm{m}\Phi_0$. Colours correspond to the various N in Fig. 4-6a; grey dots for data up to $N = 250$. **Yellow squares**, Extracted ε-noise PSD $(2 - 20\,\mathrm{MHz})$ by Rabi spectroscopy. **Diagonal, dashed lines**, Estimated $1/f$ ε (red) and Δ (blue) noise inferred from the free-induction and spin-echo measurements. **Solid, red line**, Power-law dependence, $S_\varepsilon(f) = (2\pi\,\kappa_\varepsilon)^2 A_\Phi / [|f/1\,\mathrm{Hz}|^\alpha\,1\,\mathrm{Hz}]$, extrapolated beyond the qubit's frequency, Δ. Fitting the low-frequency, linear portion of the CPMG noise spectrum (before the slight upturn beyond $2\,\mathrm{MHz}$) yields the parameters $A_\Phi = (0.8\,\mu\Phi_0)^2$ and $\alpha = 0.9$. The shaded area covers $\alpha \pm 0.05$. **Green dots**, High-frequency transverse noise is predominantly from the ε noise at $f = \Delta$. **Dotted line**, Expected Johnson-Nyquist flux noise due to $50\,\Omega$ environment mutually coupled with strength $M = 0.02\,\mathrm{pH}$ to the qubit.

4.3.4 Temperature Dependence

Next, we measure the temperature dependence of T_1, T_FI and T_SE, in order to better understand the noise sources. All the experiments are performed at a sequence repetition rate of $500\,\mathrm{Hz}$ to remove the effect from quasiparticles generated during SQUID switching. In a single trace, we average 5000 times per sampled point, and further improve statistics by recalibrating and measuring ten identical traces for more averaging. Such two-step averaging scheme help reduce the signal distortion from slow

117

flux drift and noise below the quasistatic low-frequency cutoff ($500/5000 = 0.1\,\mathrm{Hz}$). We deliberately heat the mixing-chamber temperature from the base temperature (nominal mixing-chamber temperature: $T_{\mathrm{M.C.}} \approx 12\,\mathrm{mK}$; effective device temperature: $T_{\mathrm{Esc.}} \approx 65\,\mathrm{mK}$) to characterize coherence at various temperatures up to $250\,\mathrm{mK}$. There was a 4K warm-up between the experiments in this section and those in Sec. 4.3.1– 4.3.3.

Example traces of inversion recovery, free induction and spin echo are shown in Fig. 4-8 – 4-10. All the traces show increasing smoothness with improved averaging. In the free-induction measurement, we use resonant pulses, on one hand, for avoiding complication brought by the deviated nutation from detuned pulses [37], and on the other hand, for more fitting efficiency. Given that we are only interested in the behavior of the decay envelope and that fitting a fringed trace would spend too much weighting on the oscillating component, the resonant free induction enhances fitting efficiency and accuracy. Also note that the second $\pi/2$-pulse is replaced by $-\pi/2$-pulse for the trace in Fig. 4-9.
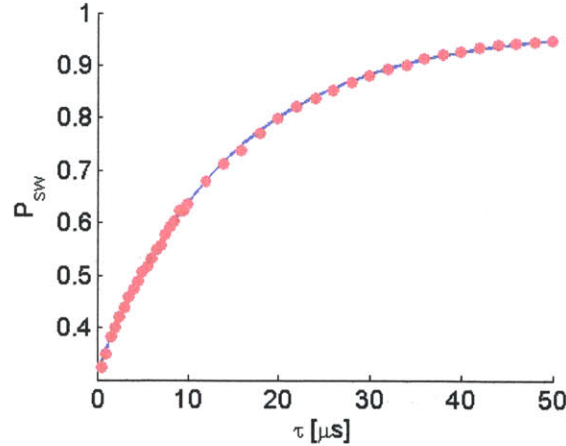
Figure 4-8: An example of the raw data (dots) from which relaxation time T_1 is extracted. Data are measured at $\Phi_{\mathrm{b}} = 0$ and at the base temperature. The fit (solid line) to Eq. (4.1) gives an exponential decay time is $T_1 = 14.7\,\mu s$.

Decay rates are obtained by fitting the data to Eq. (4.1)-(4.3). In particular, both exponential ($\Gamma_{\varphi,\mathrm{FI}}^{(\mathrm{E})}$ and $\Gamma_{\varphi,\mathrm{SE}}^{(\mathrm{E})}$) and Gaussian ($\Gamma_{\varphi,\mathrm{FI}}^{(\mathrm{G})}$ and $\Gamma_{\varphi,\mathrm{SE}}^{(\mathrm{G})}$) decay rates are now set as fitting parameters. With improved statistics, we are able to distinguish between
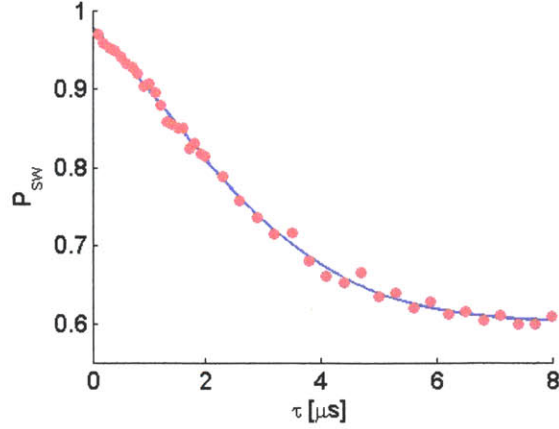
Figure 4-9: An example of the raw data (dots) from which free-induction pure-dephasing time $\Gamma_{\varphi,\mathrm{FI}}$ is extracted. Data are measured at $\Phi_b = 0$ and at the base temperature. The fit (solid line) to Eq. (4.2) gives a Gaussian pure-dephasing time $\Gamma_{\varphi,\mathrm{FI}}^{(G)} = 4.3\,\mu s$ and an exponential pure-dephasing time $\Gamma_{\varphi,\mathrm{FI}}^{(E)} = 6.4\,\mu s$.
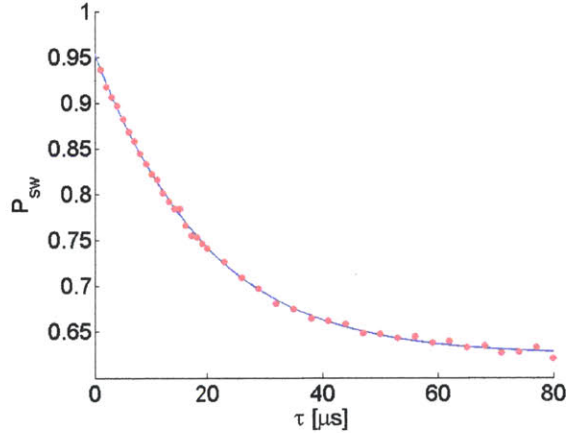
Figure 4-10: An example of the raw data (dots) from which spin-echo pure-dephasing time $\Gamma_{\varphi,\mathrm{SE}}$ is extracted. Data are measured at $\Phi_b = 0$ and at the base temperature. The fit (solid line) to Eq. (4.3) gives a Gaussian pure-dephasing time $\Gamma_{\varphi,\mathrm{SE}}^{(G)} = 102\,\mu s$ and an exponential pure-dephasing time $\Gamma_{\varphi,\mathrm{SE}}^{(E)} = 62\,\mu s$.

their individual contribution. The extracted rates are shown in Fig. 4-11 − 4-16. The nominal mixing-chamber temperature $T_{\mathrm{M.C.}}$ measured by an in-fridge thermometer is related to the effective device temperature, which is supposedly equivalent to the SQUID's escape temperature $T_{\mathrm{Esc.}}$ obtained from measuring the SQUID's switching-current distribution, by $T_{\mathrm{Esc.}} = \sqrt{(65\,\mathrm{mK})^2 + T_{\mathrm{M.C.}}^2}$.
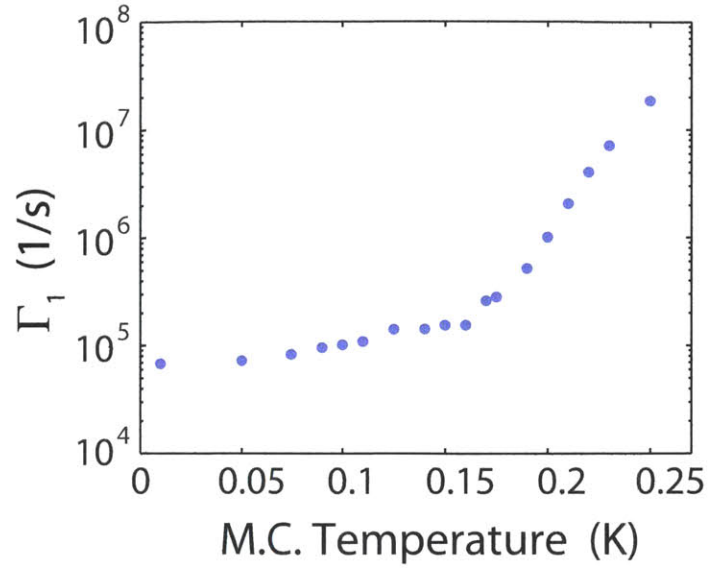
Figure 4-11: Temperature (mixing-chamber) dependence of T_1 relaxation rate measured at $\varepsilon = 0$ (predominantly Δ noise).
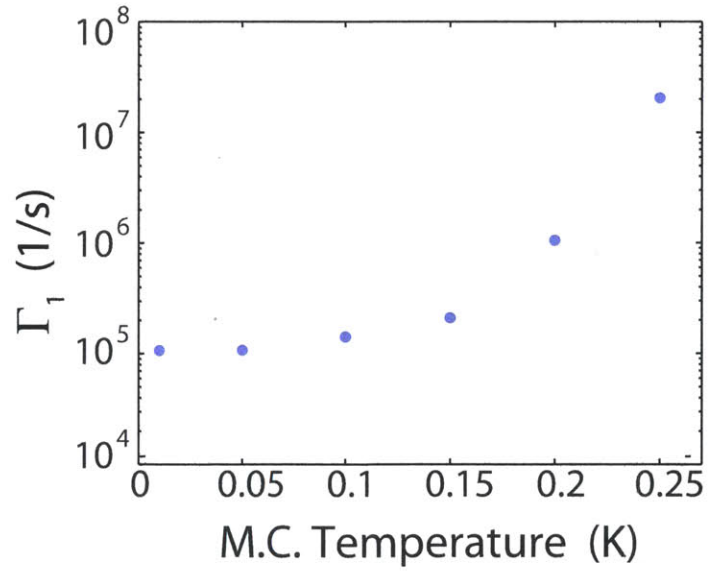
Figure 4-12: Temperature (mixing-chamber) dependence of T_1 relaxation rate measured at $\varepsilon = 640\,\mathrm{MHz}$. (predominantly ε noise).
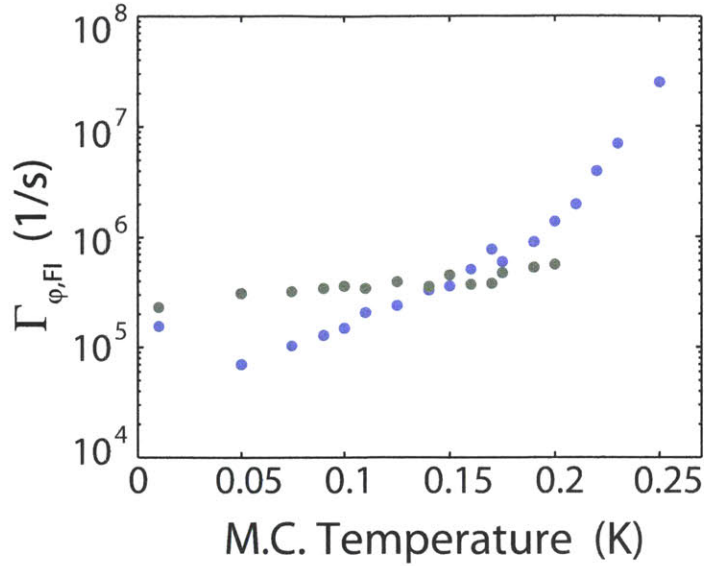
Figure 4-13: Temperature (mixing-chamber) dependence of free-induction pure-dephasing rate measured at $\varepsilon = 0$ (predominantly Δ noise). Blue dots correspond to the exponential decay component $\Gamma_{\varphi,\mathrm{FI}}^{(\mathrm{E})}$, and green dots correspond to the Gaussian decay component $\Gamma_{\varphi,\mathrm{FI}}^{(\mathrm{G})}$ (same for Fig. 4-14). Above $T_{\mathrm{M.C.}} = 200\,\mathrm{mK}$, the exponential decay dominates over the Gaussian decay, so that the Gaussian fit becomes undependable (same argument for Fig. 4-14 − 4-16).
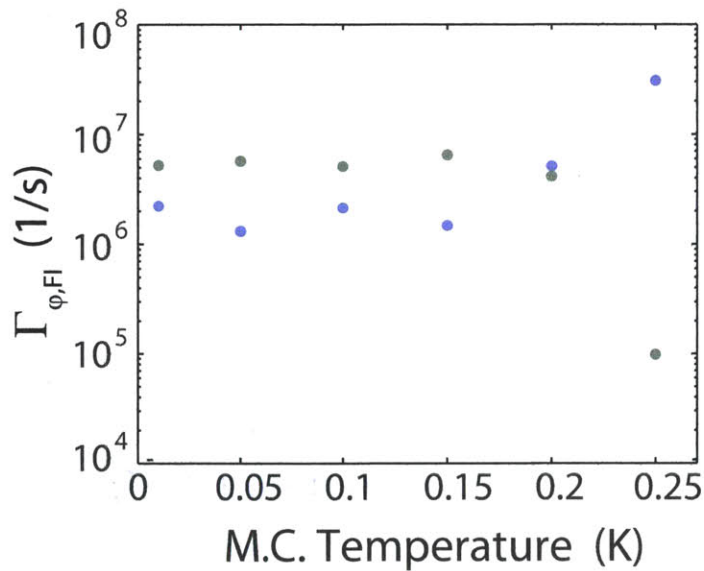
Figure 4-14: Temperature (mixing-chamber) dependence of free-induction pure-dephasing rate measured at $\varepsilon = 640\,\mathrm{MHz}$ (predominantly ε noise).
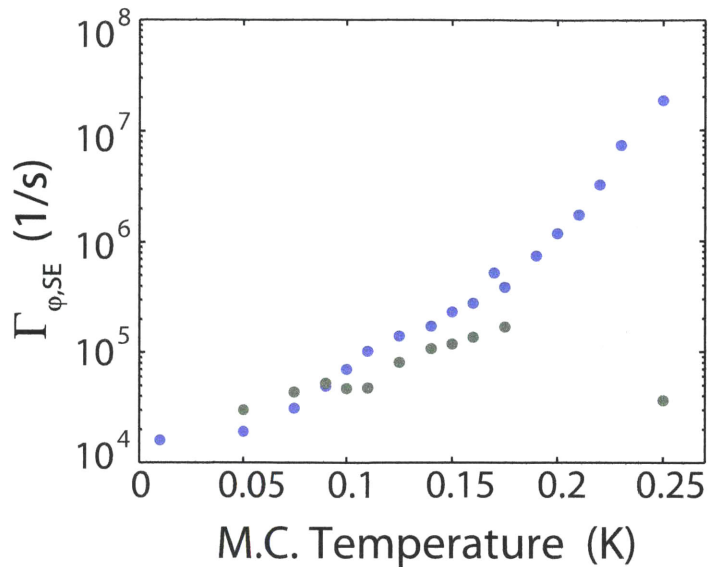
Figure 4-15: Temperature (mixing-chamber) dependence of spin-echo pure-dephasing rate measured at $\varepsilon = 0$ (predominantly Δ noise). Blue dots correspond to the exponential decay component $\Gamma_{\varphi,\text{SE}}^{(\text{E})}$, and green dots correspond to the Gaussian decay component $\Gamma_{\varphi,\text{SE}}^{(\text{G})}$ (same for Fig. 4-16).
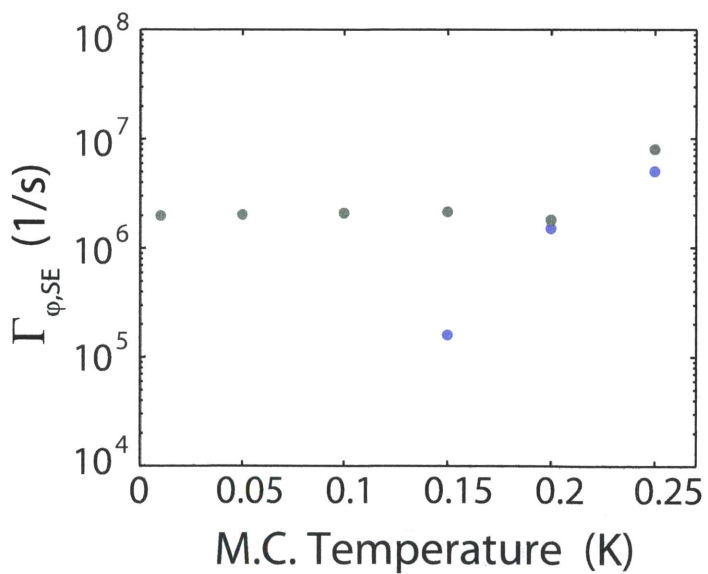
Figure 4-16: Temperature (mixing-chamber) dependence of spin-echo pure-dephasing rate measured at $\varepsilon = 640\,\text{MHz}$ (predominantly ε noise).

Now we discuss several observations and conclusions from the temperature results:

1. The relaxation rate Γ_1 measured both at and away from degeneracy grows slowly with temperature until $T_{\text{M.C.}} \approx 160\,\text{mK}$, above which a faster than exponential growth occurs. This could be due to quasiparticle-induced relaxation [89, 90], in which the quasiparticle density scales as $\sqrt{T}\,e^{-\Delta_{\text{g}}/T}$ (Δ_{g} is the gap parameter and T is the temperature). However, at lower temperatures, the relaxation rate cannot be explained by quasiparticles alone, and is saturated by some other mechanism.
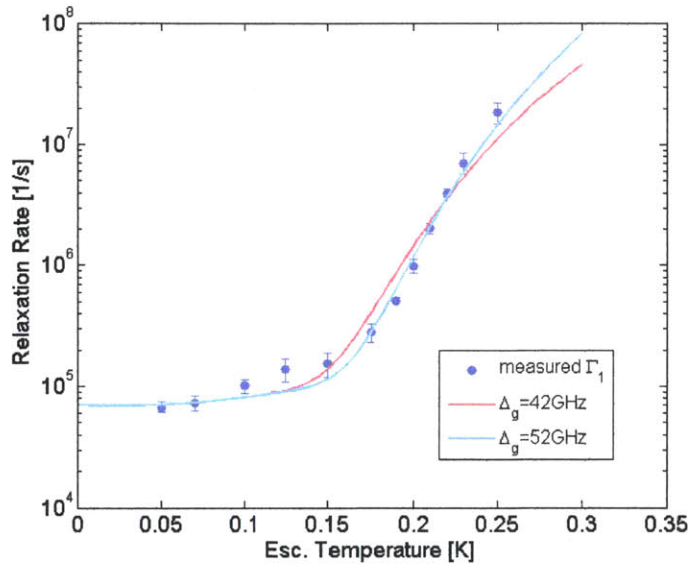
Figure 4-17: Temperature dependence of Γ_1 with fit to the quasipartical model $A\sqrt{T/\Delta_{\text{g}}}\,e^{-\Delta_{\text{g}}/T} + C$, where A and C are constants and Δ_{g} is the gap parameter. For aluminum, $\Delta_{\text{g}} = 42\,\text{GHz}$ (red). However, $\Delta_{\text{g}} = 52\,\text{GHz}$ (cyan) gives a better fit.

2. The free-induction and spin-echo Gaussian decay rates at degeneracy have slight increase with temperature. Because Gaussian decay is more prominent in free induction than in spin echo, we focus on $\Gamma_{\varphi,\text{FI}}^{(\text{G})}$ only. We find that the quasistatic noise power ($\sim (\Gamma_{\varphi,\text{FI}}^{(\text{G})})^2$) fits to a temperature-squared dependence plus a low-temperature saturation. This agrees with the T^2-dependence from the $1/f$ critical-current noise model [91].

3. The free-induction and spin-echo exponential decay rates at degeneracy exhibits

123
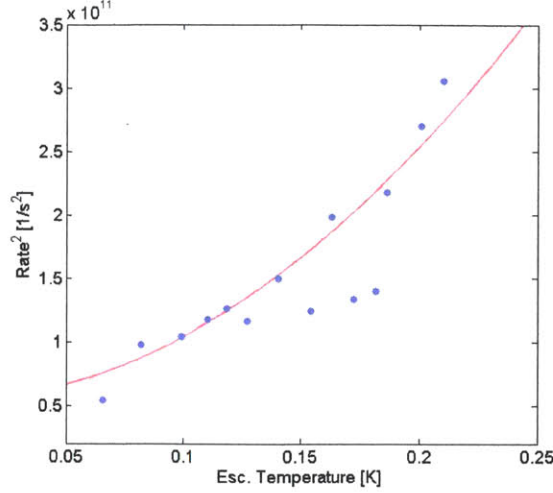
Figure 4-18: Temperature dependence of $(\Gamma^{(G)}_{\varphi,\mathrm{FI}})^2$ measured at $\varepsilon = 0$. The red line shows the dependence: $AT^2 + C$, where A and C are constants.

a consistent faster-than-exponential increase with temperature, implying a rising white noise level. The finding is separately confirmed in the intermediate-frequency spectroscopy by the $T_{1\rho}$ method (Sec. 6.6). The rising trend is similar to that of Γ_1 in Fig. 4-11. Note that the free-induction exponential decay rates are subject to larger error bars at lower temperatures $< 150\,\mathrm{mK}$, because the decay in this regime is Gaussian-dominated. In addition, the range of the echo filter frequency is a better matching to the measured $T_{1\rho}$-spectroscopy range in Fig. 6-11 than the free-induction threshold frequency ($1/\tau > 5\,\mathrm{MHz}$ in general). This tells why the $T_{1\rho}$ result is more consistent with the spin-echo result. The mechanism of such temperature dependence is still unknown.

4. Γ_1 measured at $\varepsilon = 640\,\mathrm{MHz}$ agrees with that at $\varepsilon = 0$, implying no substantial increase for the high-frequency Δ noise. For the Gaussian component, both $\Gamma^{(G)}_{\varphi,\mathrm{FI}}$ and $\Gamma^{(G)}_{\varphi,\mathrm{SE}}$ at $\varepsilon = 640\,\mathrm{MHz}$ are almost independent of temperature below $200\,\mathrm{mK}$. The datapoint at $250\,\mathrm{mK}$ is erroneous due to dominating exponential decay, so not to be trusted. In general, the result agrees with the low-frequency ε noise spectroscopy (Sec. 5.3.2) and the flux noise measured in SQUID [87]. For the exponential component, $\Gamma^{(E)}_{\varphi,\mathrm{FI}}$ and $\Gamma^{(SE)}_{\varphi,\mathrm{E}}$ at $\varepsilon = 640\,\mathrm{MHz}$ exceed the Gaussian part above $200\,\mathrm{mK}$. It is due to the same white noise increase observed

124
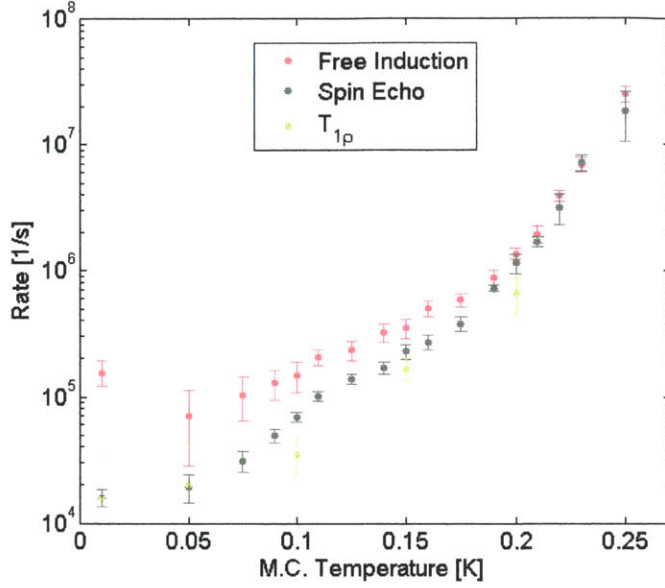
Figure 4-19: Temperature dependence of $\Gamma^{(E)}_{\varphi,\mathrm{FI}}$, $\Gamma^{(E)}_{\varphi,\mathrm{SE}}$ and $\Gamma_\nu = \Gamma_{1\rho} - \Gamma_1/2$ obtained in Sec. 6.6.

at degeneracy, so, above $200\,\mathrm{mK}$, decay at this flux bias becomes dominated by the white Δ noise.

From the above discussions, we propose an simplified model of the temperature dependence for the Δ and ε noise,

$$S_\Delta(f) = (A_1 + B_1 T^2)/f^{\alpha_1} + C_1 \mathcal{E}(T) + D_1 f^{\beta_1} \tag{4.5}$$

and

$$S_\Delta(f) = (A_2)/f^{\alpha_2} + C_2 + (D_2 + E_2 \mathcal{E}(T))f^{\beta_2} , \tag{4.6}$$

where $A_1, B_1, \ldots, E_2$ are constants, and $\mathcal{E}(T)$ is an increasing function of temperature. In the model, we have assumed an ohmic noise spectrum (colored by $\beta_{1,2} \sim 1$) for the high-frequency behavior.

The naive Gaussian plus exponential fitting model neglects other possibilities and detailed spectral dependence of noise, so our conclusion on temperature dependence is not to high accuracy. However, several important features are still captured semi-

125

quantitatively.

4.4 Driven-Evolution Coherence Characterization

We now turn to the driven-evolution coherence characterization methods, including the Rabi and rotary-echo experiments.

4.4.1 The Rabi Spectroscopy

The pulse sequence and dynamics is described in Sec. 2.6.3. An example of measured Rabi decay at the sweet spot is shown in Fig. 4-20.
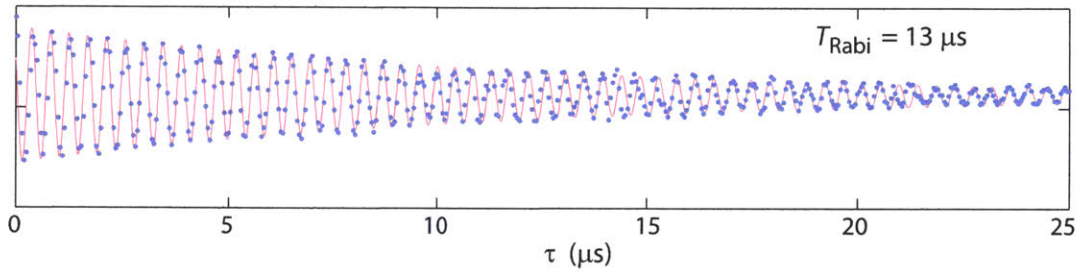
Figure 4-20: An example of measured Rabi decay at $\Phi_b = 0$ and $\nu_R = 2.3\,\mathrm{MHz}$. The $1/e$ time is about $13\,\mu s$.

We aim to extract the ε-noise PSD at the Rabi frequency, $S_\varepsilon(\nu_R)$, from the Rabi decay, whose sensitivity to the noise depends on the flux bias (Eq. (2.60)). To improve accuracy, we measure at various flux bias, and then fit to the dependence to obtain $S_\varepsilon(\nu_R)$. The simplified fitting model for the Rabi trace (Fig. 4-21a) is

$$P_{sw}(\tau) = A\cos(2\pi\nu_R\tau + B)\exp\left(-\Gamma_R\tau\right) \times \left(1 + \left(\frac{2\pi\sigma_{z'}^2}{\nu_R}\tau\right)^2\right)^{-1/4} + C, \qquad (4.7)$$

where $\sigma_{z'}^2 \approx \sigma_\Delta^2 + (\frac{\varepsilon}{\Delta})^2\sigma_\varepsilon^2$ is the longitudinal quasistatic noise, which is known from the free-induction results. Γ_R is the exponential decay rate which depends on the flux bias, and is further fit to $\Gamma_R(\varepsilon) = \frac{3}{4}\Gamma_1 + \frac{1}{2}\Gamma_\nu = D + \frac{1}{4}(\frac{\varepsilon}{\Delta})^2 S_\varepsilon(\nu_R)$ (from Eq. (2.60)) to

obtain $S_\varepsilon(\nu_R)$ (Fig. 4-21b). Note that, close to the sweet spot, decay from other noise sources are generally ε-independent, so we group them in to a single fitting parameter D. The extracted noise PSD ranging over $2-20\,\mathrm{MHz}$ are shown in Fig. 4-7, which generally agrees with the $1/f$ dependence in the CPMG spectroscopy.
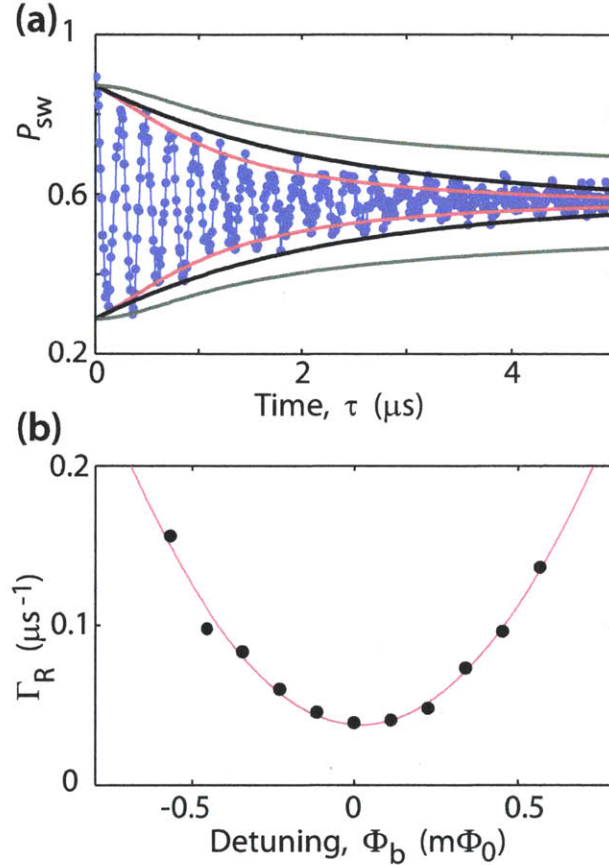
Figure 4-21: (a) Rabi oscillations at $\nu_R = 2\,\mathrm{MHz}$ and $\varepsilon = 225\,\mathrm{MHz}$. The red envelope is a fitting using Eq. (4.7). The black line shows the Γ_R decay only, and the green line is decay from the $\sigma_{z'}^2$ noise only. (b) Γ_R versus flux detuning at $\nu_R = 2\,\mathrm{MHz}$, with a parabolic fit.

There are a few shortcomings in this Rabi-spectroscopy approach. First, the complex Rabi decay law naturally leads to an inaccurate fit. As illustrated in Fig. 4-21a, it is difficult to determine the decay envelope from the fragile oscillating signal. Second, the detuning fluctuation $\sigma_{z'}^2$ has the same ε-dependence as Γ_ν, so any inaccuracy in determining the longitudinal quasistatic noise will directly affect the extracted PSD. The effect is more significant at small ν_R, explaining the inconsistent data at

2 MHz (first datapoint of the Rabi spectroscopy in Fig. 4-7). Third, compared to (Eq. (2.66)), we ignored the low-frequency fluctuation of the drive amplitude, σ_ν^2, in the Rabi fitting model. Its effect is relatively weak for the Rabi frequencies involved in this experiment. In addition, σ_ν^2 is ε-independent so that can be grouped into the parameter D. This is a rough approximation. However, it has little effect as the errors from the first two shortcomings are already overwhelming. Fourth, the experiment becomes inefficient for large ν_R, as too many datapoints need to be taken to fit the oscillation. This is also the reason that limits our spectroscopy up to 20 MHz. This problem can be solved by measuring the decay envelope only, an approach illustrated in Fig. 4-22a. Note that all these shortcomings are solved in the rotating-frame relaxation $T_{1\rho}$ experiment [92].

4.4.2 Rotary Echo

In our device, it is found that the Rabi decay at degeneracy is limited by slow fluctuation in the drive amplitude [58]. Such fluctuation is a parasitic effect in this type of circuit. The qubit loop, which is directly coupled to the microwave antenna, also experiences an oscillating field mediated by off-resonant driving of a resonator formed by the SQUID and shunt capacitor (known as the plasma mode, corresponding to the loop formed by the SQUID junction, C_{sh} and L_{sq} in Fig. 3-10), leading to strong modifications of the Rabi frequency. Since the indirect coupling is tunable by the SQUID's bias current $I_{sq}^{(dc)}$ which fluctuates slowly even zero-biased, the effective Rabi frequency is subject to low-frequency noise, reducing of the coherence time during driven evolution. The noise can be mitigated with the rotary-echo pulse sequence, which, for driven systems, is analogous to the spin-echo sequence.

The pulse sequence and dynamics is described in Sec. 2.6.4. An example of measured rotary-echo decay at the sweet spot is shown in Fig. 4-22a, along with the Rabi decay with the same drive amplitude. A nearly 3-fold improvement of coherence time is achieved by this rotating-frame echo technique. The experiments are performed in a slightly different way as their free-evolution counterparts (free induction and spin echo). For Rabi, we obtain the oscillation amplitude at a certain τ (sampled less

densely) by sweeping the pulse length in the vicinity of τ to obtain one Rabi cycle or two for fit. For rotary echo, we fix the amplitude of the first pulse at A_{rf} and sweep the second one to ensure we have the same amplitude (regardless of the sign) in both halves, since the effective driving amplitude could be slightly different between the positive- and negative-amplitude pulses.

(a)　　　　　　　　　　　**(b)**
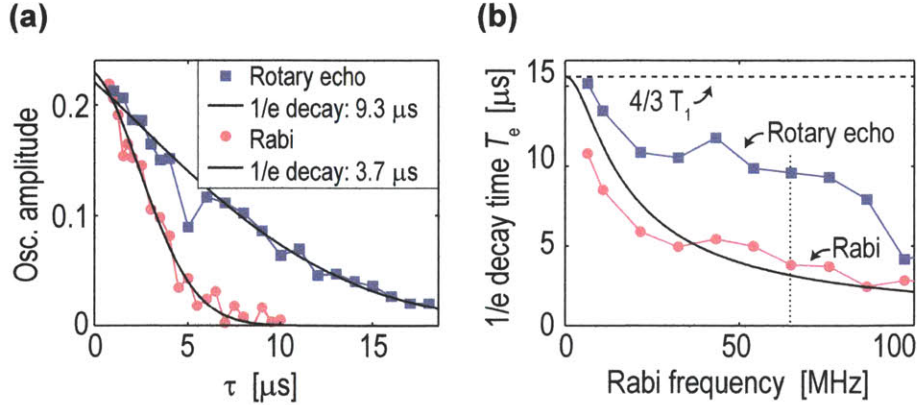
Figure 4-22: (a) Envelopes of the Rabi and rotary-echo decay, measured at $\nu_{\mathrm{R}} = 65\,\mathrm{MHz}$ and $I_{\mathrm{sq}} = 0$. (b) $1/e$ decay times versus the Rabi frequency for Rabi and rotary echo, extracted from the traces shown in (a). The dashed line shows the upper limit set by the T_1 relaxation. The solid line shows a fit to the model of resonator-mediated $I_{\mathrm{sq}}^{(\mathrm{dc})}$ fluctuation, where the standard ν_{R} deviation $\sigma_\nu/\nu_{\mathrm{R}} = 0.06\%$ [58]. The dotted line marks the position for the decay envelope shown in (a).

Fig. 4-22b shows the capability of extending coherence by the rotary-echo technique over the Rabi-frequency range $5 - 100\,\mathrm{MHz}$. In addition, the rotary-echo sequence has the similar noise-filter property as the spin-echo sequence. To extract high-accuracy noise information, a CP-like generalization of RE may be used.

4.5　Summary

By using the collection of methods shown above, we successfully characterize various aspects of the coherence properties in our device, and then integrate the results to perform the noise spectroscopy in different frequency regimes (Fig. 4-7). These methods set the basic tools for characterizing a quantum system, and can be easily adapted for implementation in other qubit modalities.

Chapter 5

Repeated Fixed-Time Free Induction and Low-Frequency Noise Spectroscopy

5.1 Introduction

A major remaining obstacle to implementing fault-tolerant quantum computation with superconducting qubits is the insufficient coherence time T_2 compared to the gate-operation time. The ultimate goal is to mitigate and eliminate the noise leading to decoherence. To this end, a more detailed understanding of the noise processes – such as magnetic-flux, critical-current, and charge fluctuations – would expedite materials science, device engineering, and the development of coherent-control methods.

Effective surface spins have recently been identified as one dominant source of low-frequency magnetic-flux noise [93, 94], detrimental to several types of superconducting qubits; however, open questions remain regarding the nature of these spins. Their noise is known to be due to local fluctuators [95, 96, 97, 86] and the spectrum exhibits a $1/f^\alpha$ power-law dependence from a few hertz to tens of megahertz with $0.5 < \alpha < 1$ [98, 87, 46, 66, 99, 100]. Its dependence on the device geometry [101, 102] merits further study.

In the flux qubit [15, 14], the noise in the tunnel coupling Δ between the circulating-current states shows a $1/f$-type spectrum from a few Hertz to hundreds of kilohertz [21]. This noise may originate in the critical-current fluctuations of the Josephson junctions [91, 103, 104, 105], and/or fluctuating offset charges, due to, e.g., charge traps located in the oxides of the junction, metal–insulator interfaces, or surfaces. Charge noise can lead to dephasing even in the flux qubit, even though the junctions have a relatively high ratio of Josephson-tunneling to Coulomb-charging energies $(E_J/E_C \approx 50$ in our device).

In this chapter, we introduce a measurement technique for low-frequency noise. A distinguishing feature of our technique is that it enables the measurement of noise spectra up to frequencies limited only by the achievable measurement repetition rate. This is important, because noise measured in this manner resides (at least in part) within the relevant measurement bandwidth of time-domain experiments, e.g., free-induction decay, that use the standard ensemble-averaging (that is, the averaging of multiple trials acquired at the same repetition rate) to estimate the qubit-state occupation probability.

We present a direct characterization of the $1/f$ noise PSD in our superconducting flux qubit. We distinguish between the ε noise, which is effective flux noise, and the Δ noise, which can be parametrized as effective critical-current noise or effective charge noise. Interestingly, we find that the same $1/f^\alpha$ power laws, measured at much higher frequencies (Sec. 4.3), extend down to the $10^{-2} - 10^2$ Hz range nearly unchanged. Over the temperature range $65 - 200$ mK, both the ε and Δ noise are independent of temperature, and any $\Delta - \varepsilon$-noise correlations are very small or nonexistent.

5.2 Low-Frequency Noise Spectroscopy

Over decades, researchers have been studying low-frequency noise in superconducting quantum circuits. For example, flux noise spectroscopy was performed on superconducting quantum interference devices (SQUIDs) cooled to milli-Kelvin tempera-

tures [98, 87]. A series of experiments displayed a flux noise with a power spectrum which scales like $1/f^\alpha$, where α roughly ranges from 0.6 to 1. The magnitude of the noise was found to have only a weak dependence on device parameters such as loop inductance, geometry, material, etc. Defining the power-law dependence as $S_\Phi(f) = A_\Phi/[|f/1\,\mathrm{Hz}|^\alpha\,1\,\mathrm{Hz}]$, we have a canonical value of the noise amplitude at $1\,\mathrm{Hz}$, $\sqrt{A_\Phi} = 1 \sim 4\,\mu\Phi_0/\sqrt{\mathrm{Hz}}$ (see Appendix B for clarifying the confusion in the definition of A_Φ). The origin and mechanism of this noise is still unknown, and no experiments have indisputably shown it, despite various theories. Now it seems clear that this excess noise is intimately associated with the decohering phenomena of superconducting qubits.

It is only in recent years that the capability to directly measure the noise from the qubit's response has become feasible [99, 101, 44, 106, 107], due to improved coherence and readout fidelity. The pioneering work [99] done with a superconducting phase qubit presents a technique which measures the low-frequency flux fluctuation from the spectroscopic response of the qubit, connecting the results to previous measurements in SQUID devices for the first time. Though generally applicable to other qubit systems, the technique has relatively low sensitivity and largely depends on the cleanness of the qubit's resonance spectrum. Also, the frequencies accessible in this spectroscopy method is outside the relevant range of the dephasing noise which constitutes the integrated quasistatic noise (Sec. 2.5.3 and Sec. 4.3.2).

In the rest of this chapter, we will introduce a new low-frequency spectroscopy method, which, instead of measuring the qubit's frequency spectroscopically, utilizes the free-induction sequence as an encoder of low-frequency fluctuations in the precession frequency. This method, also explored in [106, 107], outperforms the spectroscopic response one in terms of better signal-to-noise ratio (SNR). Note that here "signal" means the $1/f$ noise we aim to resolve, and "noise" means the undesired errors due to any measurement imperfection. In addition, we work out both theoretical and experimental challenges, extending the upper limit of this noise spectroscopy up to the achievable measurement repetition rate. The significance of this improvement lies in the fact that we are able to probe noise relevant for the dephasing of the

time-domain experiments, e.g., free-induction decay. From Sec. 2.5.3, we see that the free-induction decay is an integral behavior of the noise within the quasistatic range. Knowing the spectral dependence of these noise would help us identify the noise origin and facilitate our understanding of the underlying mechanism. The method can be applied to any two-level system.

5.3 The Repeated Fixed-Spacing Free-Induction Experiment

The method is based on a modified protocol of the free-induction experiment. In the regular free-induction experiment (Sec. 2.5.3 and Sec. 4.3.2), the diffusion of an ensemble of Bloch vectors due to precession-frequency variation leads to a shrinking average polarization (dephasing), and the influential noise is spectrally upper-limited by the inverse of the pulse spacing, $1/\tau$ and lower-limited by the inverse of the total acquisition time t_{acq} (typically $1 \sim 10\,\mathrm{s}$). Therefore, if only these noise sources are present, the qubit frequency is zero-mean. However, noise slower than t_{acq} could fluctuate the mean qubit frequency from zero at a longer time scale. This suggests the capability of the free-induction sequence to encode noise slower than the total acquisition time for a repeated measurement (noise frequency below $1/t_{\mathrm{acq}}$).

Ensemble-Averaged Scheme

Inspired by this mechanism, we developed a measurement protocol based on free induction, to record the time evolution of the qubit frequency. We repeatedly let the qubit undergo free induction, two $\pi/2$-pulses of the same phase. Instead of scanning the pulse separation τ, we fix it at a value τ_0. We also fix the nominal detuning $\Delta\nu^{(0)}$ of the applied microwave frequency ν_{rf} from the average qubit frequency $\bar{\nu}_{\mathrm{q}}$ to $\Delta\nu^{(0)} \equiv \bar{\nu}_{\mathrm{q}} - \nu_{\mathrm{rf}} = -1/4\tau_0$, so that the qubit fulfills a $\pi/2$ rotation around the $X - Y$ plane (both $\Delta\nu^{(0)} = 1/4\tau_0$ and $\Delta\nu^{(0)} = -1/4\tau_0$ will work, but we choose $\Delta\nu^{(0)} = -1/4\tau_0$ for presentational convenience).

As for the data-collecting scheme, we first introduce the scheme proposed in [106,

107] and also part of [44], and then show the optimized technique of extending noise spectroscopy over the $1/t_{acq}$ limit. We call the former the ensemble-averaged scheme, and the latter the single-shot scheme. It will be seen that, regardless of the difference in experimental implementation, the ensemble-averaged scheme is just a trivial modification by pre-processing the single-shot data, which provides less information than the single-shot scheme.

In the ensemble-averaged scheme, the binary data from projection measurements are automatically averaged over a collection time t_{acq} by a counter, which threshold-detects the SQUID's switching event from its output voltage. Assume that the sequence repetition rate is $1/t_{rep}$ (typically $1 \sim 2\,\text{ms}$). Then, $M = t_{acq}/t_{rep}$ trials will be counted and averaged to improve the switching-probability estimate. Repeating this measure-count cycle every t_{acq} (the realistic cycle time is always slightly larger, because of unavoidable delay in pulse generation and cable transmission), we end up collecting a time series $\{p_j\}$ at a sampling frequency $1/t_{acq}$, i.e., $t_{j+1} - t_j = t_{acq}$, where t_j is the time when p_j is recorded. $\{p_j\}$ is processed and Fourier transformed to produce the noise spectroscopy, and the whole process will be repeated a few more times for better PSD estimate.

Assuming small fluctuations in the qubit frequency, $\nu_q(t) = \bar{\nu}_q + \delta\nu_q(t)$, and the above sequence, $\delta\nu_q(t)$ will translate into fluctuation of the precession phase, i.e., $\delta\varphi = \delta\nu_q \tau_0$, which in turn translates into fluctuation of the Z-polarization and is read out as a fluctuation of the SQUID's switching probability. The transfer function between the mean switching probability and $\delta\nu_q$ is a sinusoid, $p_{sw}(t, \tau_0) = p_{sw}^{(0)} + a(\tau_0) \sin(2\pi\, \delta\nu_q(t)\, \tau_0)$, where $p_{sw}^{(0)}$ is the offset switch-probability corresponding to the qubit's 50%-superposition state, and $a(\tau_0)$ is the amplitude of the free-induction decay at the pulse separation τ_0.

The transfer function can be experimentally obtained by performing the mapping between p_{sw} and $\Delta\nu^{(0)}$. The recipe for finding the transfer function and the working point is

1. Perform the τ_0-spaced free-induction sequence and scan the r.f. frequency around the resonance frequency (Fig. 5-1). Because increasing the r.f. fre-

quency is equivalent to decreasing the detuning, so we obtain the dependence of p_{sw} on $\Delta\nu^{(0)}$.

2. Fit the dependence to a sinusoidal function. Among the obtained fitting parameters are the offset $p_{sw}^{(0)}$, the amplitude $a(\tau_0)$ and the oscillation frequency τ_0.

3. The working point of $\Delta\nu^{(0)}$ for the repeated measurements is chosen to be the $90°$-rotated point, indicated by the green dashed line in Fig. 5-1. Because the first-order derivative of a sinusoid is largest at this point, the sensitivity of p_{sw} to $\delta\varphi$ is maximized.

Next, performing the repeated measurements discussed above at this working point and then converting p_j back to $\delta\nu_q(t_j)$ using the extracted transfer function, we obtain the time-evolution of the qubit frequency.
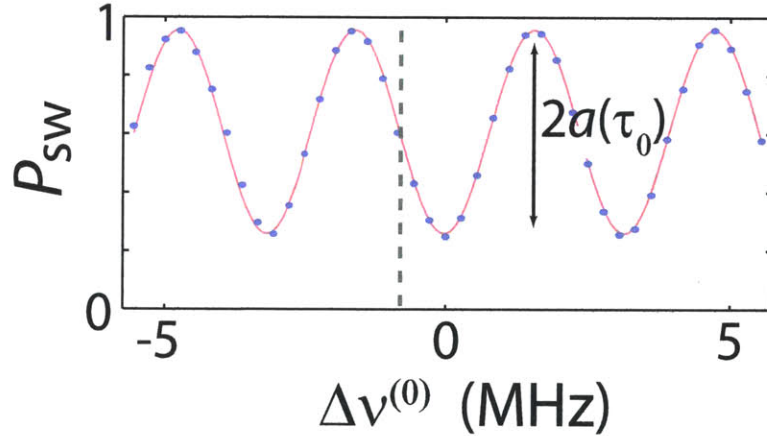
Figure 5-1: Measured dependence of p_{sw} on $\Delta\nu^{(0)} = \bar{\nu}_q - \nu_{rf}$ at $\tau_0 = 0.3\,\mu s$ and $\varepsilon = 0$. The solid line is a sinusoidal fit and the dashed line indicates the $\Delta\nu^{(0)} = -1/4\tau_0$ working point.

There are two shortcomings in this scheme. First, it only records noise below the sampling frequency (more precisely, the Nyquist frequency $1/2t_{acq}$), out of the quasistatic range related to decoherence (Fig. 5-2). In spite of the possibility to extrapolate to the desired range from certain presumed dependence, the scheme is not a direct measurement after all. Second, we have to pay attention to the dynamic

range of the precession-phase fluctuation $\delta\varphi$, restricting the majority of the sampled points within $[-\pi/2, \pi/2]$ where the p_{sw}-$\Delta\nu^{(0)}$ mapping is monotonic. Otherwise, we would collect too many undistinguishable "bad" datapoints which distort the spectroscopy results.
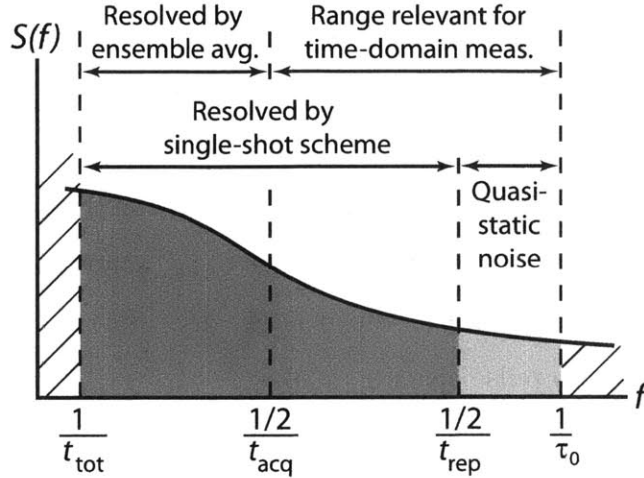
Figure 5-2: Sketch of the PSD, indicating the frequency intervals resolved by the ensemble-averaging and single-shot schemes. Here t_{tot} is the total length of the recorded time-evolution trace (can be several minutes to hours); $t_{\text{acq}} = 1 \sim 10\,\text{s}$ is the acquisition time per measured point in time-domain experiments such as free-induction decay; $t_{\text{rep}} = 1 \sim 2\,\text{ms}$ is the repetition time (the acquisition/collection/sampling time in the single-shot scheme); and $\tau_0 \sim 1\,\mu\text{s}$ is the typical pulse spacing.

Single-Shot Scheme

To exploit the repeated-free-induction method, we proposed an improved sampling and data-processing scheme. We successfully implemented the scheme and justified our approach from the theoretical side. In the so-called single-shot scheme, the sequence repetition rate $1/t_{\text{rep}}$ is taken as the sampling rate of the time series (Fig. 5-2). That is, we directly Fourier transform the raw data of the time evolution of the SQUID's switching events (a binary time series) without any time-domain averaging beforehand. In other words, the acquisition time in the single-shot scheme is reduced

to t_{rep} (the smallest possible value). Therefore, the ensemble-averaged scheme is a simple modification of the single-shot scheme by rearranging the data and averaging over the subgroups at the pre-processing step. Noise information between $1/t_{\mathrm{acq}}$ and $1/t_{\mathrm{rep}}$ is unfortunately smeared out.

Let $\{z_k\}$ ($z_k = 0$ or 1 and $z_{j+1} - z_j = t_{\mathrm{rep}}$) denote the binary time series. z_k is the Bernoulli-trial outcome with a success probability equal to the switching probability at the time $\{z_k\}$ is taken, i.e., $p_{\mathrm{sw}}(t_k, \tau_0) = p_{\mathrm{sw}}^{(0)} + a(0) \sin(2\pi\, \delta\nu_{\mathrm{q}}(t_k)\, \tau_0)$. Note that, the sinusoid's amplitude is replaced by $a(0)$ (before is $a(\tau_0)$). This is because, in the single-shot scheme, each observation consists of only one realization and no ensemble average involved, taking the dephasing effect out of the transfer function (T_1 process is ignored, since $T_1 \gg \tau_0$). The dynamic range of p_{sw} spans the full visibility bounded by the ground and excited state, which is exactly twice the amplitude of the free-induction decay at zero pulse spacing, $a(0)$.

At first glance, it seems that we might obtain very "noisy" noise spectrum based on these "inaccurate" binary outcome. However, as we shall see in Sec. 5.3.1, the single-shot scheme is of the same accuracy and efficiency as the ensemble-averaged one, while providing more information. The SNRs are equal in both cases, and the background shot noise caused by random trials can be further eliminated by preforming a cross-correlated spectroscopy. These equivalences can be intuitively understood as follows. Because PSD is a statistical (expectation-valued) estimate of a stochastic process, the way of (uniformly) rearranging and averaging the outcome data does not affect the result. For the same reason, the unwanted background shot noise is the same in both schemes. From the perspective of estimated error, p_j is better than z_k in terms of reduced variance by a factor of $1/M$, but such improvement is paid off by the less averaging at the Fourier-transform step (the number of elements in $\{z_k\}$ is M times that of $\{p_j\}$). Therefore, the final PSD estimate always takes same statistical accuracy, given the same sample volume.

5.3.1 Method and Analysis

Single-Shot Readout

Instead of the regular way of using a counter to automatically accumulate the SQUID's switching events, we use the oscilloscope (LeCroy WaveRunner 204Xi) to save the time-evolution of the SQUID's output voltage for a certain duration t_{tot} (limited by the oscilloscope's memory). An example is shown in Fig. 5-3. The voltage data is immediately converted to a binary series by a specially written program which threshold-detects the switching events. Then, repeat for more traces to improve the PSD estimate.
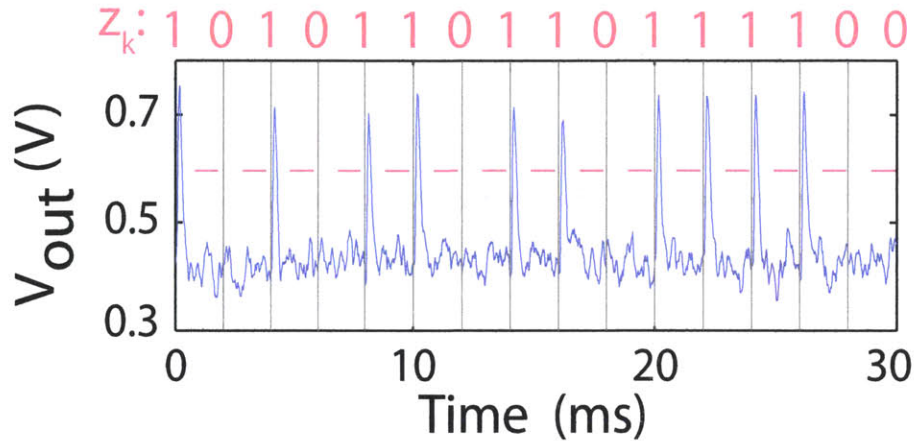
Figure 5-3: Individual SQUID-switching events measured on an oscilloscope. The dashed, horizontal line is a software threshold detector, which converts the time evolution to a binary time series shown on top.

There are a few technical issues to be clarified for this readout approach:

- The sampling frequency of the output voltage should be high enough to resolve the quick burst at the switching event, but is also preferred to be as low as possible to reduce the number of sampled points so as to minimize the delay time from data transferring and processing.

- Depending on the sampling frequency of the output voltage, t_{tot} is limited by the oscilloscope's memory ($t_{tot} \leq 100\,\text{s}$ in our case), so the lower limit of the noise spectroscopy for a single-shot trace is limited. However, lower frequencies can still be obtained by performing the ensemble-averaged scheme on multiple repeated single-shot traces.

139

- One might ask why not use the counter to do single-shot readout. This is because, by setting the repetition time t_{rep} as the counting cycle, data transferring between the counter and computer (usually tens of milliseconds per transfer) becomes inefficient. If we count and transfer at every measurement, the actual sampling period is much longer than the expected repetition period ($t_{\mathrm{rep}} = 1 \sim 2\mathrm{ms}$).

Power Spectral Density Estimator

The Wiener-Khinchin theorem states that the (bilateral) PSD of a wide-sense-stationary random process $w(t)$ is given by the (type-I) Fourier transform of its autocorrelation function $R(\tau) = \langle w(t)w(t+\tau)\rangle$:

$$S(f) = \int_{-\infty}^{\infty} d\tau\, e^{-i2\pi f\tau} R(\tau) \ . \tag{5.1}$$

The expectation value in the definition of the autocorrelation function can be taken by averaging over t. Therefore, by the autocorrelation theorem, we can write the PSD estimator for a finite sample time T_{s} as

$$S(f) = \frac{W(f)^* W(f)}{T_{\mathrm{s}}} \ , \tag{5.2}$$

where $W(f)$ is the Fourier transform of $w(t)$:

$$W(f) = \int_{-\infty}^{\infty} d\tau\, e^{-i2\pi ft} w(t) \ . \tag{5.3}$$

For the discrete version of $w(t)$, i.e., w_n, $n = 1, 2, \ldots, N$, the calculation of PSD is done by discrete Fourier transformation (DFT). Eq. (5.2) is rewritten as

$$S(f_k) = \frac{W_k^* W_k \Delta t}{N} \ , \tag{5.4}$$

where $\Delta t = t_{n+1} - t_n$ is the spacing between neighboring points, $f_k = k/N\Delta t$, $k =$

$0, 1, \ldots, N/2$ and $\{W_k\}$ is the discrete Fourier transform of $\{w_n\}$:

$$W_k = \sum_{n=1}^{N} w_n e^{-i2\pi(n-1)k/N} , \tag{5.5}$$

which is consistent with the fast Fourier transform (FFT) defined in MATLAB. We then take the statistical average of L traces measured in succession:

$$\langle S(f_k) \rangle = \frac{1}{L} \sum_{l=1}^{L} S^{(l)}(f_k) . \tag{5.6}$$

Nonlinear Effect and Correction Factor

Let $y_n = p_{sw}(t_n)$, where t_n is the time at which the measurement of z_n is taken. Therefore, each element of the binary time series $\{z_n\}$ is an independent Bernoulli random variable with expectation value given by y_n. We will show later that the PSD of $\{z_n\}$, $S_{zz}(f_k)$, is equivalent to that of $\{y_n\}$, $S_{yy}(f_k)$, except for an additional white noise level resulting from the shot noise, and the shot noise can be eliminated by the cross-PSD technique. We thus can assume $S_{zz}(f_k) = S_{yy}(f_k) + S_s$, where S_s is a constant. $S_{zz}(f_k)$ can be computed from Eq. (5.4).

If the precession-phase fluctuation $\delta\varphi$ is small so that $p_{sw}(t_n)$ only fluctuates in the vicinity of $p_{sw}^{(0)}$, we can linearize about it, i.e., $\delta p_{sw} = 2\pi a(0)\tau_0\,\delta\nu_q(t)$. Hence, the PSD of the qubit-frequency fluctuation (correlator in unit of angular frequency, to be consistent with the PSD definition in Eq. (2.27)) can be expressed as

$$S_{\nu_q}(f_k) = \frac{S_{yy}(f_k)}{(a(0)\tau_0)^2} = \frac{S_{zz}(f_k)}{(a(0)\tau_0)^2} - \frac{S_s}{(a(0)\tau_0)^2} , \tag{5.7}$$

where $a(0)$ and τ_0 are known parameters, and the constant subtrahend can be eliminated by a technique introduced later. Eq. (5.7) says that we are able to compute the noise PSD from the inconvertible binary series $\{z_n\}$, given that τ_0 is small enough to restrict the phase fluctuation within the linear-approximation regime. Note that the noise strength is independent of the measurement protocol and considered as fixed, so τ_0 acts as a noise amplifier when encoding the qubit-frequency fluctuation into the

141

accumulated precession phase.

On the other hand, we want to make τ_0 large enough, so that the desired $1/f$ noise gets amplified relative to the shot noise. Otherwise, the obtained spectroscopy would have substantial data scattering, especially at high frequencies, where the white noise dominates over the $1/f$ noise. It will be seen that there is a trade-off between the noise amplification and the nonlinear effect of the sinusoidal transfer function, and we can find an optimal spacing τ_0^* which optimizes SNR. However, τ_0^* is presumably large enough to undermine the linear approximation. How can we perform an both accurate and efficient experiment?

We solve this problem by working out a correction factor which accounts for the nonlinear effect under looser restriction on τ_0. We present the proof in Appendix C The correction factor is found to be simply the square of the ratio $(a(\tau_0)/a(0))^2$, which is exactly the normalized decay amplitude. Hence, we can write a generalized version of Eq. (5.7) by dividing the correction factor:

$$\frac{S_{zz}(f_k)}{(a(\tau_0)\tau_0)^2} = S_{\nu_q}(f_k) + S_n \, , \tag{5.8}$$

where $S_n = S_s/(a(\tau_0)\tau_0)^2$ is the white shot noise. Examples of computed PSD (l.h.s. of Eq. (5.8)) for both the ε and Δ noise and using both ensemble-averaged and single-shot sampling schemes are shown in Fig. 5-4. Now, the method is almost complete except for eliminating the white noise term.

Shot Noise and Cross-PSD

To understand the annoying white noise, let us turn to the autocorrelation function of $\{z_n\}$ and $\{y_n\}$. For m-th autocorrelation term, $m \neq 0$,

$$R_{zz}(m) = \langle z_n z_{n+m} \rangle = \langle y_n y_{n+m} \rangle = R_{yy}(m) \, . \tag{5.9}$$

The second equality relation holds, because the Bernoulli trials are independent from each other. The expectation value also averages out this randomness. If $m = 0$, the autocorrelation term becomes the mean square value, and it is different between $\{z_n\}$

and $\{y_n\}$:

$$\Delta R(0) = R_{zz}(0) - R_{yy}(0) = \langle z^2 \rangle - \langle y^2 \rangle = \sigma_z^2 - \sigma_y^2 . \tag{5.10}$$

where $\sigma_\lambda^2 = \langle \lambda^2 \rangle - \langle \lambda \rangle^2$ ($\lambda = y, z$) is the variance. The last equality holds, because $\langle z \rangle = \langle y \rangle = p_{\mathrm{sw}}^{(0)}$. Eq. (5.10) says that the difference between the zero-delay autocorrelation term of $\{z_n\}$ and $\{y_n\}$ is exactly the difference of their variance.

Since PSD is just the Fourier transform of the autocorrelation function, the difference in their PSD is then

$$S_{\mathrm{s}} = S_{zz}(f_k) - S_{yy}(f_k) = \Delta R(0)e^{-i2\pi f_k \cdot 0}t_{\mathrm{rep}} = (\sigma_z^2 - \sigma_y^2)t_{\mathrm{rep}} . \tag{5.11}$$

In the discrete case, the integration is replaced by a summation, and a differential time step $\Delta t = t_{\mathrm{rep}}$ in the single-shot scheme. Eq. (5.11) shows that, for the finite case, the zero-delay term in the frequency domain becomes a constant. This explains the origin the white noise level, which is analogous to the electronic shot noise [108]. Here, the discrete nature of projective readout raises the variance of the original process, which is reflected as a white noise in the frequency domain. For practical parameters, $\sigma_z \gg \sigma_y$, so we can approximate the white noise as

$$\begin{aligned} S_{\mathrm{s}} &\approx \sigma_z^2 t_{\mathrm{rep}} \\ &= \langle p_{\mathrm{sw}}(1 - p_{\mathrm{sw}}) \rangle t_{\mathrm{rep}} \\ &\approx p_{\mathrm{sw}}^{(0)}(1 - p_{\mathrm{sw}}^{(0)})t_{\mathrm{rep}} , \end{aligned} \tag{5.12}$$

where $p_{\mathrm{sw}}^{(0)} \approx 0.5 \sim 0.6$ typically. Substituting Eq. (5.12) into Eq. (5.8) gives the white noise level in the final noise spectrum.

In the ensemble-averaged scheme, the Bernoulli statistics is replaced by the binomial one. That is, in Eq. (5.12), σ_z^2 is replaced by the variance of $\{p_j\}$, σ_p^2. Note that $M * p_j$ is M-trial-binomially distributed, so $\sigma_p^2 \approx p_{\mathrm{sw}}^{(0)}(1 - p_{\mathrm{sw}}^{(0)})/M$. On the other hand, the time step t_{rep} is also changed to t_{acq} in the ensemble-averaged scheme. Recall that $M = t_{\mathrm{acq}}/t_{\mathrm{rep}}$. Therefore, the white shot noise has the same level in either

143

scheme. This suggests that SNR is not affected by the way of rearranging data and the averaging procedures.

The undesired white noise can be automatically eliminated by a cross-PSD technique. The recipe is:

1. Split $\{z_n\}$ into the two interleaved time series, $z_n' = z_{2n-1}$ and $z_n'' = z_{2n}$.

2. Calculate the cross-correlated PSD of $\{z_n'\}$ and $\{z_n''\}$,

$$S_{Z'Z''}(f_k) = \frac{Z_k'^* Z_k'' \, e^{i2\pi f_k t_{\mathrm{rep}}} \, 2t_{\mathrm{rep}}}{N/2} \, , \tag{5.13}$$

where $f_k = k/N t_{\mathrm{rep}}$, $k = 0, 1, \ldots, N/4$. The term $e^{i2\pi f_k t_{\mathrm{rep}}}$ is added to account for the additional phase introduced by a real-time delay (t_{rep}) between two interleaved series.

Since $\{z_n'\}$ and $\{z_n''\}$ are essentially from the same realization $\{z_n\}$ of a random process. Their cross-correlation terms are the same as the original autocorrelation ones (Eq. (5.9)). So are their PSDs. However, the white noise is eliminated in this step, because now the zero-delay cross-correlation term no longer suffers from shot noise: $R_{z'z''}(0) = \langle z_n' z_n'' \rangle = \langle z_n z_n + 1 \rangle$.

3. The cross-PSD obtained from a single trace is subject to substantial errors and is generally an complex number. The average over multiple traces should be executed in a coherent way, namely,

$$\langle S_{Z'Z''}(f_k) \rangle = \frac{1}{L} \sum_{l=1}^{L} S_{Z'Z''}^{(l)}(f_k) \, . \tag{5.14}$$

4. Further smooth the results by a sliding average in the frequency domain before taking the norm as the final PSD. This step is particularly useful to $1/f$-type noise, because SNR scales with $1/f$. That means that more averaging is needed at high frequencies to resolve the true noise. If we perform a sliding average by scaling the width of the sliding window (Δf) with f, more averaging will be taken at higher frequencies. Meanwhile, the effective weight of data number in

144

each decade ($\sim f/\Delta f$) is the same. This is important for the analysis of the $1/f$ noise, which is routinely plotted in linear-log scale.

Notably, it can be inferred from the second step that, any white noise (not only the shot noise) will be eliminated in the cross-correlated PSD, so this sets a limitation to this technique. If the noise we want to resolve is white itself, we would have no way to decompose or disentangle it from the shot noise. The cross-PSD technique is efficient when the desired noise has a non-flat spectrum such as $1/f$-type.

Even with the cross-PSD technique and a decent number (~ 1000) of repeated traces, high-frequency PSDs could still be quite noisy. To optimize SNR, i.e., to minimize the shot-noise level, we look for a best choice for τ_0. From Eq. (5.8), the white noise level can only be tuned by τ_0 (S_s is fixed). If the free-induction decay is Gaussian, i.e., $a(\tau_0) = \exp(-(\tau_0/T^{(G)})^2)$, where $T^{(G)}$ denotes the Gaussian-decay time constant, the denominator in From Eq. (5.8) reaches its maximum at $\tau_0^* = T^{(G)}/\sqrt{2}$. If the decay is exponential, i.e., $a(\tau_0) = \exp(-\tau_0/T^{(E)})$, where $T^{(E)}$ denotes the Exponential-decay time constant, $\tau_0^* = T^{(E)}$.

5.3.2 Temperature Results

We performed the same spectroscopy at different temperatures. The ε- and Δ-noise PSDs are plotted in Fig. 5-4(b) for several temperatures. For the Δ noise, the base-temperature spectroscopy falls perfectly on the $1/f$ power law extracted in Sec. 4.3.2. For the ε noise, there is also striking agreement with the $1/f^{0.9}$ power law, measured at considerably higher frequencies, $0.2 - 20\,\mathrm{MHz}$ (Sec. 4.3.3).

Figure 5-5 shows the integrated noise powers Π_λ versus temperature T in the $65 - 200\,\mathrm{mK}$ range, where our readout visibility is sufficient. We observe in essence temperature independence for both noises. For the ε (flux) noise, this is consistent with previous observations in SQUIDs [87, 94];

In order to analyze the Δ noise, we parametrize it as an effective critical-current noise with critical current $I_c = 0.4\,\mu\mathrm{A}$, in a Josephson junction with area $\mathcal{A} = (0.2\,\mu\mathrm{m})^2$. Van Harlingen et al. [91] found a "canonical" value for the $1/f$ I_c-noise

145
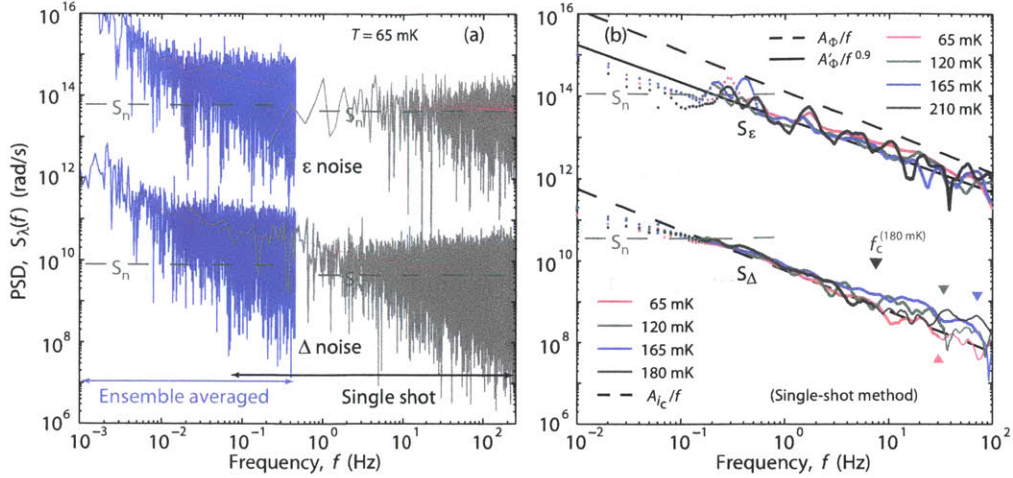
Figure 5-4: Bilateral noise PSDs. (a) Standard PSDs computed by the time series of switching probabilities $\{p_j\}$ in the ensemble-averaged scheme (blue data, on left) and of the binary time series $\{z_n\}$ in the single-shot scheme (gray, on right), measured at base temperature. The red points (thin line) are averages of hundreds of traces. ($S_\varepsilon(f)$ measured at $\varepsilon = 450\,\mathrm{MHz}$.) (b) Cross-PSDs of interleaved time series $S_\lambda(f)$ at different device temperatures ($S_\varepsilon(f)$ measured at $\varepsilon = 640\,\mathrm{MHz}$). The data were smoothed by a sliding average with a triangular weight function of width $\Delta f = f/4$. The dashed, diagonal lines are the $1/f$ noises $S_\lambda(f) = (2\pi)^2 \kappa_\lambda^2 A_{\Phi,i_c}/|f|$, derived in Sec. 4.3.2; the sensitivities are $\kappa_\Delta \equiv \partial\Delta/\partial i_c = 3.2\,\mathrm{GHz}$ (i_c is normalized critical current) and $\kappa_\varepsilon \equiv \partial\varepsilon/\partial\Phi = 1.1\,\mathrm{MHz}/\mu\Phi_0$, and the noise strengths are $A_\Phi = (1.7\,\mu\Phi_0)^2$ and $A_{i_c} = (4.0 \times 10^{-6})^2$. The solid, diagonal line is $S_\varepsilon(f) = (2\pi)^2 \kappa_\varepsilon^2 A'_\Phi/(|f/1\,\mathrm{Hz}|^{0.9}\,1\,\mathrm{Hz})$, with $A'_\Phi = (0.8\,\mu\Phi_0)^2$. The horizontal, green, dashed lines are the shot-noise levels S_n at low temperature; the triangles represent an upper cut-off frequency f_c for sufficient averaging, above which the data are not dependable.

power at $1\,\mathrm{Hz}$ and $4.2\,\mathrm{K}$: $A_{I_c}^{\mathrm{can}} \approx 144\,(\mathrm{pA})^2(I_c/\mu\mathrm{A})^2/(\mathcal{A}/\mu\mathrm{m}^2)$ in several SQUIDs and qubits of various sizes, made of different materials. The authors hypothesized a quadratic temperature dependence, consistent with certain plausible models for the noise sources below $100\,\mathrm{mK}$, while noting that other models suggest a linear dependence. The bilateral normalized noise-PSD then becomes $S_{i_c}^{\mathrm{can}}(f) = A_{I_c}^{\mathrm{can}}I_c^{-2}\,(T/4.2\,\mathrm{K})^2/|f|$, which, for $T = 65\,\mathrm{mK}$, is considerably lower (almost 20 times) than our measured value. On the other hand, Eroms et al. [105] measured resistance fluctuations in aluminum tunnel junctions: they found about 100 times lower noise power at $4.2\,\mathrm{K}$, a linear temperature dependence, and saturation below $0.8\,\mathrm{K}$, i.e.,
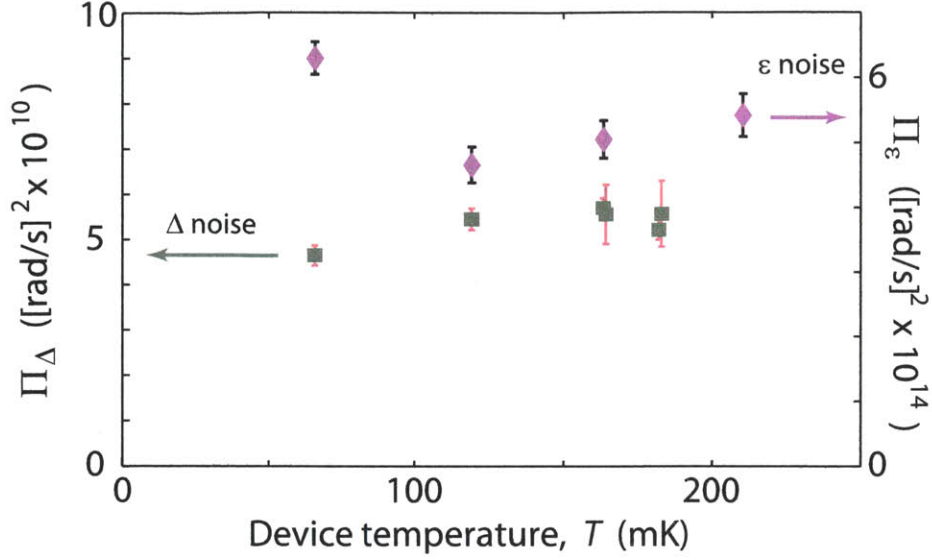
Figure 5-5: $\Pi_\lambda(T) = (2\pi)^2 \int_{F_\lambda} df \, S_\lambda(f;T)$ in the frequency intervals $F_\varepsilon = 0.02 - 50\,\text{Hz}$ and $F_\Delta = 0.02 - 2\,\text{Hz}$, cf. Fig. 5-4b. It is possible to measure the ε noise up to somewhat higher temperatures and frequencies than the Δ noise. Note that the Π_λ values depend on the integration limits although the choice of F_λ does not make any significant difference in the trends. (The double data points for the 165 and 180 mK Δ noise were measured with different pulse spacings τ_0.) The error bars are derived only from the fit error of the read-out visibility $a(\tau_0)$.

$S_{i_c}(f) = (1/100) \times A_{I_c}^{\text{can}} I_c^{-2} (T/4.2\,\text{K})/|f|$. With $T = 0.8\,\text{K}$, this gives a value about 2.5 times lower than what we observe. We also note that recently, contrary to these findings, Paik et al. [109] reported no evidence for $1/f$ I_c noise in a Josephson junction.

An alternative source of the Δ noise is the fluctuating offset charges, known to exhibit $1/f$ noise [110, 65, 111]; these charges effectively supply a gate voltage to each island. The charge-noise power typically observed in single-electron tunnelling (SET) devices is proportional to temperature [112] (although quadratic dependencies have also been observed [65]) and saturates below about 200 mK, due to self heating of the SET, at a "canonical" value A_Q of about $(1 \sim 10\,\text{m}e)^2$ at 1 Hz. We estimate our qubit's maximum sensitivity to charge fluctuations, $\kappa_{\Delta,Q} \equiv \partial\Delta/\partial Q$, to be in the range $0.1 \sim 1\,\text{MHz}/e$. We can then parametrize the Δ noise as charge noise and estimate the free-induction pure-dephasing time $T_\varphi = (2\pi\,\kappa_{\Delta,Q})^{-1} A_Q^{-1/2} (\ln[t_{\text{acq}}/2\,\tau])^{-1/2} \approx 4 \sim 400\,\mu\text{s}$. The lower end of this range is not far from our observed value. Moreover, the

147

tunneling of charged quasiparticles between the small islands constituting our device may displace offset charges and contribute to dephasing at $\varepsilon = 0$.

5.3.3 $\Delta - \varepsilon$ Correlation

Last, we turn to possible $\Delta - \varepsilon$ noise correlations. Fig. 5-6 shows how we repeatedly measured the switching probability $p_{sw}^{\pm}$ at alternating flux biases $\pm\varepsilon^{(0)}$, with $\pm\varepsilon^{(0)}$ chosen such that the effects of the two sources of noise on $\delta\nu_q$ were similar in magnitude, i.e., $|\partial\nu_q/\partial\varepsilon|\sigma_\varepsilon \approx |\partial\nu_q/\partial\Delta|\sigma_\Delta$. We set the pulse separation τ_0 and nominal frequency detuning $\Delta\nu^{(0)}$ for repeated measurements. At the bias points $\varepsilon = \pm\varepsilon^{(0)}$, $\delta\varepsilon$ fluctuations induce negatively correlated $\delta\nu_q$ fluctuations, whereas $\delta\Delta$ fluctuations induce positively correlated $\delta\nu_q$ fluctuations. Based on the free-induction decay law, $p_{sw}^{\pm}$ can be expressed as a function of $\delta\varepsilon$ and $\delta\Delta$,

$$\begin{aligned}
p_{sw}^{\pm}(\delta\varepsilon, \delta\Delta) = p_0 - a_0 \exp\left(-\tau_0/2T_1\right) \\
\times \exp\left(-\left[\tau_0/T_\varphi(\pm\varepsilon^{(0)}+\delta\varepsilon)\right]^2\right) \cos\left(2\pi\,\delta\nu_q^{\pm}(\delta\varepsilon, \delta\Delta)\,\tau_0\right),
\end{aligned} \tag{5.15}$$

where $[1/T_\varphi(\varepsilon)]^2 = A + B\,\varepsilon^2$ is associated with the Gaussian pure dephasing induced by the ε-dependent quasistatic noise, and $\delta\nu_q^{\pm}(\delta\varepsilon, \delta\Delta) = \nu_q - \nu_q^{(0)} = \left[(\pm\varepsilon^{(0)} + \delta\varepsilon)^2 + (\Delta + \delta\Delta)^2\right]^{-1/2} - \left[(\varepsilon^{(0)})^2 + \Delta^2\right]^{-1/2}$. In Eq. (5.15), T_1, $\varepsilon^{(0)}$ and Δ are known from other measurements. All the other parameters can be determined in a pre-measurement (inset of Fig. 5-6b), which maps out the function by scanning ε and ν_{rf} ($\delta\nu_{rf} = -\delta\Delta$).

At each time step, the measurement of $p_{sw}^{\pm}$ for $\varepsilon = \pm\varepsilon^{(0)}$ yields two non-linear equations in the two unknowns $\delta\varepsilon$ and $\delta\Delta$. We solve this system numerically: Fig. 5-6(a) shows the raw $p_{sw}^{\pm}$ data and extracted time evolution of $\delta\varepsilon$ and $\delta\Delta$. We then calculate the cross-PSD $S_{\varepsilon\Delta}(f)$ and the normalized magnitude of the correlation function,

$$|\gamma_{\varepsilon\Delta}(f)| = \frac{|S_{\varepsilon\Delta}(f)|}{[S_\varepsilon(f)S_\Delta(f)]^{1/2}}, \tag{5.16}$$

as shown in Fig. 5-6(b). Within the range of $10^{-3} - 10^{-1}$ Hz, the correlation is upper-bounded by 0.2, which possibly suggests that the two noise sources are uncorrelated.
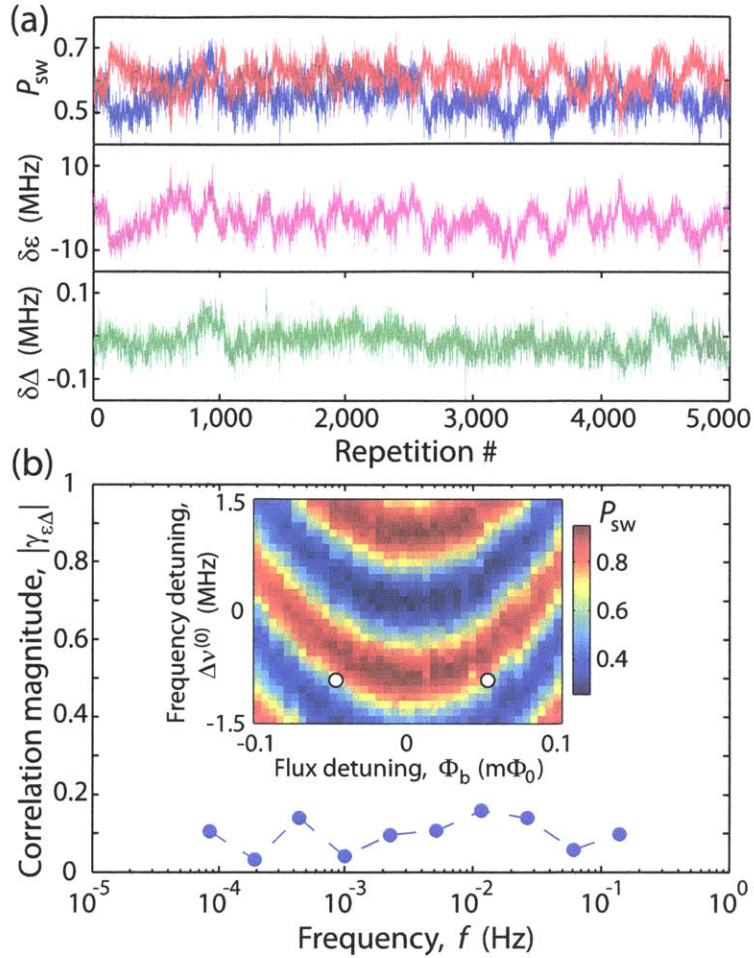
Figure 5-6: $\delta\varepsilon - \delta\Delta$-noise correlations measured at base temperature. (a) **Top panel:** Time series of $p_{sw}^{\pm}$ with fixed $\tau_0 = 0.3\,\mu$s, nominal $\Delta\nu^{(0)} = -0.8\,$MHz, and 1,000 averages per measured point. The flux-bias polarity was alternated between positive (blue) and negative (red) $\varepsilon^{(0)}$ ($\pm\Phi_b = \pm 0.058\,$mΦ_0, see inset in (b)), with a 2-second repetition period. **Middle and bottom panels:** Differential ($\delta\varepsilon$) and common-mode ($\delta\Delta$) noise inferred from the data in the top panel. (b) Normalized correlation magnitude (Eq. 5.16); the smaller the magnitude, the more indeterminate the correlation phase, and therefore we cannot discriminate between possible correlation and anticorrelation. **Inset:** Fixed-spacing Ramsey fringes by scanning r.f. frequency, measured over a vicinity of the sweet spot. White circles indicate the bias points used in the top panel of (a).

5.4   Summary

In conclusion, our spectroscopy of both the ε noise (flux) and Δ (critical-current or charge noise) noise, facilitated by single-shot measurements and thorough data

149

analysis, shows that the very same $1/f^\alpha$ dependencies, measured at higher frequencies, extend down to millihertz frequencies. This apparently indicates that the same noise mechanisms are active and dominant over some ten orders of magnitude or more for the ε noise and at least eight orders of magnitude for the Δ noise. The ε noise may extend, with roughly constant slope (on a logarithmic scale), up to the qubit's transition frequency at several gigahertz [21]: there, this noise is nearly transverse to the flux qubit's energy eigenbasis, and would therefore also contribute to energy relaxation. Moreover, both noises are temperature independent in the $65-200\,\text{mK}$ range, which suggests that the microscopic mechanisms are dominated by even lower energy scales than that. This is useful information for the development of noise models. It also calls for further studies of the reproducibility of the device properties, and, in particular, of the Δ noise, as it limits the coherence time in superconducting flux and transmon qubits. The small, if not negligible, $\Delta-\varepsilon$ noise correlations show that the noises are due to distinct underlying mechanisms.

Chapter 6

A Better Noise Spectroscopy Method: The $T_{1\rho}$ Experiment

6.1 Introduction

Within the gate-based model of quantum computation, a quantum algorithm may be efficiently implemented on a quantum information processor by decomposing it into a finite and discrete set of coherent gate operations [113]. Their realization, although in detail dependent on the particular physical-qubit modality, may be broadly divided into two categories, free-evolution and driven-evolution, indicating the period(s) during which the desired gate operates on the system. For example, in the case of superconducting qubits considered here, a phase gate (e.g., Z-gate) may be implemented by free evolution in combination with a static offset field, whereas a bit-flip gate (e.g., X-gate or Y-gate) may be realized with pulsed microwaves at the qubit frequency. During these two types of evolution, unwanted environmental noise acts to decohere the system and increase the gate error rate. While process tomography may provide the complete map of the action of a gate operation, it does not characterize the noise sources which cause fidelity degradation and which, in principle, may differ under free- and driven-evolution conditions. In contrast, the noise sensitivity of the quantum device itself, in conjunction with tailored pulse sequences, may be used to identify spectral features of the noise, "noise spectroscopy," and thereby elucidate the

underlying noise mechanisms [22, 114].

Dynamical decoupling protocols, e.g., spin echo and its multi-pulse extensions, have been applied to mitigate dephasing during free evolution in numerous qubit modalities, including atomic ensembles [115, 116] and single atoms [117], spin ensembles [118], diamond nitrogen–vacancy centres [119, 120], semiconductor quantum dots [121, 122], and superconducting qubits [21]. The spectral filtering properties [123] of these and related sequences have proven a useful tool for performing free-evolution noise spectroscopy with superconducting qubits over a wide range of frequencies spanning millihertz [44, 106] to over 20 MHz [21]. Several groups have also made progress characterizing [46, 21, 107, 67] and mitigating [58] decoherence during driven evolution. This case is more difficult in practice, however, because driven-evolution decoherence may be highly correlated with the operational errors that occur while implementing a particular protocol. Such correlations pose challenges for fault-tolerant quantum information processing, and it motivates the importance of characterizing the noise processes which are manifest while the qubit is under external drive.

Noise spectroscopy during driven evolution has been studied most extensively via Rabi nutation of the qubit between its ground and excited states, achieved by continuously driving the qubit with an oscillating field. Noise power at the Rabi frequency is inferred from the Rabi-oscillation-decay envelope, and the noise spectrum is reconstructed over the achievable range of Rabi frequencies by varying the field amplitude [46, 21, 107, 67]. There are several drawbacks to this approach, however, including the Rabi experiment's associated transverse decay, its sensitivity to low-frequency fluctuations of the Rabi frequency, the interpretation of the resultant non-exponential decay law, and the practical consideration of sampling sufficiently many points to resolve and fit accurately a decaying sinusoid oscillating at the Rabi frequency. This type of Rabi-based noise spectroscopy can, however, be generalized by preparing the qubit in an arbitrary initial state. One unique case, originating within the NMR community, is the so-called $T_{1\rho}$ experiment [59, 60, 61, 46, 124, 92], which measures the driven-evolution analogue to T_1 relaxation. In $T_{1\rho}$, the driving field is applied along an axis collinear with the qubit's state-vector in the rotating frame, re-

sulting in a condition called "spin locking." The main advantages of $T_{1\rho}$-based noise spectroscopy are that the qubit decays longitudinally from the spin-locked state with a straightforward exponential decay law (no oscillations), it is much less sensitive to low-frequency noise, and it can have higher accuracy over a wider frequency range than the standard Rabi-based approach.

In this chapter, we demonstrate a modified $T_{1\rho}$ pulse sequence to perform noise spectroscopy during the driven evolution of a superconducting flux qubit. The modified pulse sequence addresses several non-idealities due primarily to 1/f-type noise that may pollute the spin-locking dynamics when using the conventional $T_{1\rho}$ sequence. Using this improved sequence, we measure both the flux and tunnel-coupling noise spectra during driven evolution over the frequency range $0.1 - 200 \, \text{MHz}$. The observed flux-noise power spectral density (PSD) generally agrees with the $1/f$ dependence found independently using free-evolution noise spectroscopy [21]. Notably, between the experiments in [21] and those presented here, we thermal-cycled the device from 12 mK to 4 K and back again. With the higher accuracy afforded by the $T_{1\rho}$ measurement, we resolved two additional "bump"-like features in the spectrum, possibly due to a set of two-level systems (TLSs), e.g., electron spins, that were apparently activated by the thermal cycling. We further demonstrate that the underlying noise mechanisms associated with these particular spectral features are also active during free evolution by observing their signature in a time-domain echo experiment.

6.2   The Spin-Locking Dynamics

We follow the example discussed in Sec. 2.6.2, in which the continuous driving pulse is a resonant X-pulse. The measurement of the rotating-frame relaxation time $T_{1\rho}$ begins by preparing the qubit state to be either parallel or anti-parallel with X (collinear with the driving field), corresponding to the fictitious qubit's excited ($|+X\rangle$) and ground state ($|-X\rangle$), respectively (Fig. 6-1). This results in the so-called "spin-locking" condition, a reference to the fictitious state remaining aligned in the absence of noise with the static driving field ν_{R} in Eq. (2.52). The measurement of the

153

relaxation time from the spin-locked condition to a depolarized steady-state is the so-called $T_{1\rho}$ experiment. Just as T_1 depends on the noise at the qubit frequency ν_q that is transverse to the z'-axis, so is $T_{1\rho}$ determined by the noise at the fictitious level splitting ν_R that is transverse to the X-axis. This suggests the potential of using it as a noise detector operated at achievable Rabi frequencies.
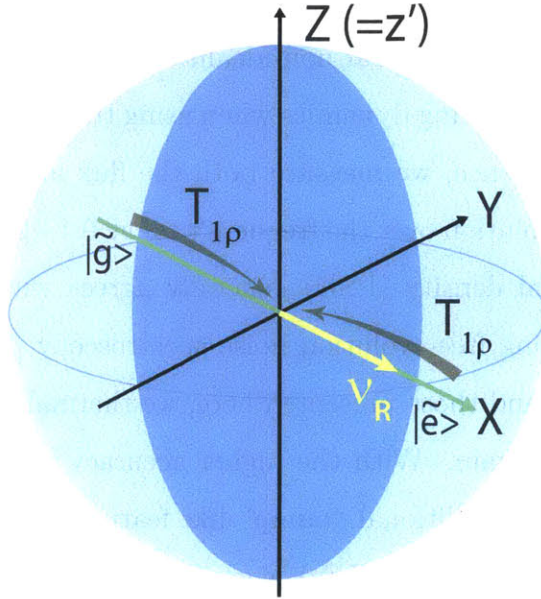
Figure 6-1: Spin locking and $T_{1\rho}$ process in the rotating frame. The green axis indicates the rotating-frame quantization axis.

Spin locking was originally an NMR technique used for producing high-resolution spectrum and studying slow atomic motion. In this section, we will introduce a prototype spin-locking sequence as applied in superconducting qubits, and then explain why it can be a better noise spectrum analyzer.

6.2.1 The Original Sequence and System Dynamics

The original $T_{1\rho}$ sequence applied to superconducting qubits was a three-pulse sequence [62], two $\pi/2$ pulses separated by a 90°-phase-shifted continuous driving pulse (labelled here "SL-3", see Fig. 6-2a). For presentational convenience, we set the phase

order as $\overline{Y}$-X-$\overline{Y}$, but it is effectively the same as the X-Y-X one in [62], since only the relative phase is important. The phase shift is implemented by altering the driving-field phase ϕ via standard IQ mixing techniques. The dynamics can be visualized with the assistance of the Bloch sphere within the rotating frame (Fig. 6-2b). The first $\pi/2)_{\overline{Y}}$ (bar indicates a 180-degrees-shifted or opposite orientation) pulse brings the qubit from its ground state to the equator, parallel with X (step I). The driving field is then applied along X and thereby aligned with the qubit state, so that the qubit is effectively locked in this orientation and experiences relaxation $\Gamma_{1\rho}$ only (steps II and III). Note that, in the classical regime ($\nu_{\mathrm{R}} \ll k_{\mathrm{B}}T/h = 1.3\,\mathrm{GHz}$, where $T \approx 65\,\mathrm{mK}$ is the effective device temperature, obtained by measuring the SQUID's switching-current distribution), the steady-state population should approach the state of near-zero X-polarization. After a finite duration τ, the remaining polarization along X is projected, by the last $\pi/2)_{\overline{Y}}$ pulse, back along Z for readout (step IV).

The connection between the $T_{1\rho}$ decay and the underlying noise is given in Eq. (2.63) and Eq. (2.64). There we see that, if we manage to obtain $\Gamma_{1\rho}$ and Γ_1 from $T_{1\rho}$ and T_1 measurements, respectively, the noise PSD at the Rabi frequency is known. This provides a direct method to perform noise PSD, as the Rabi frequency can be easily tuned.

6.2.2   Comparison with other Methods

Several groups have applied Rabi-based techniques to extract the noise PSD [21, 107, 67]. However, the $T_{1\rho}$ experiment, when utilized as a noise spectrum analyzer, has inherent advantages. The main advantages of $T_{1\rho}$-based noise spectroscopy are that the qubit decays longitudinally from the spin-locked state with a straightforward exponential decay law (no oscillations); the decay is dominated by noise at the spin-locking frequency and, like its T_1 analogue, is relatively insensitive to broadband low-frequency noise; and it can therefore have higher accuracy over a wider frequency range than the standard Rabi-based approach.

First, the Rabi frequency is first-order sensitive to fluctuations of the driving-field amplitude $\delta\nu_{\mathrm{R}}$, whose RMS fluctuation is found in this case proportional to ν_{R}

(a) SL-3 Seq.

X-Pulse   Y-Pulse

τ

$-\pi/2$ $-\pi/2$

I   II   III   IV

(b) Dynamics in SL-3 Seq.

I $|e\rangle$ II   III   IV

Z   Y   X

drive

$\bar{Y}$ X   X $\bar{Y}$

$|g\rangle$ qubit
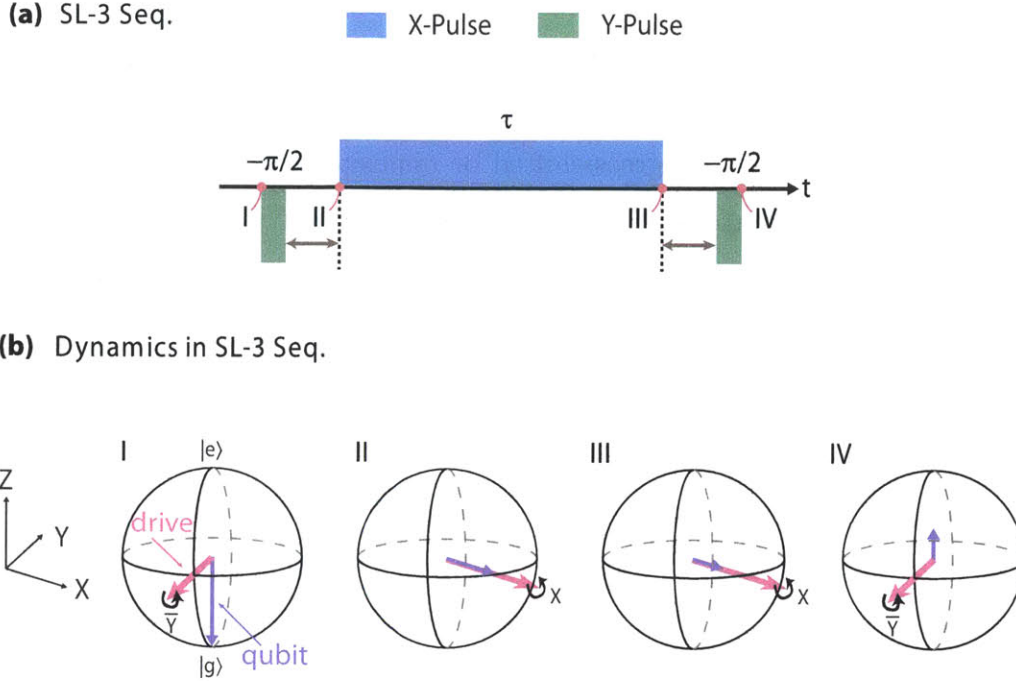
Figure 6-2: (a) Standard three-pulse spin-locking sequence (SL-3). Blue and green indicate X- and Y-pulse, respectively. Double-headed arrows indicate effective free-evolution periods (usually $30 \sim 50\,\mathrm{ns}$) between adjacent pulses. (b) Bloch sphere representation of the rotating-frame qubit dynamics under SL-3. The purple arrows are the qubit's state polarization, while the magenta arrows indicate the driving-field orientation. The qubit is initially prepared in its ground state ($|g\rangle = |-z'\rangle$) (I). The first $\pi/2)_{\bar{Y}}$ pulse rotates the qubit by 90° into the equatorial plane (II). The second 90°-phase-shifted continuous driving pulse of duration τ, is then aligned with the qubit state, effectively locking the qubit along X. During the pulse, the qubit undergoes relaxation in this rotating frame towards its steady state (III). The final $\pi/2)_{\bar{Y}}$ pulse projects the remaining polarization onto Z (=z') for readout (IV).

($\sim 0.06\% \, \nu_\mathrm{R}$) [58]. Hence, the temporal ν_R inhomogeneity becomes important when the driving is strong (large ν_R). In addition, low-frequency fluctuation of the qubit's level splitting ($\delta\nu_\mathrm{q}$) modulates the effective Rabi frequency to second order, adding to the inhomogeneous broadening [21]. The effect dominates the Rabi decay when the driving is weak enough (small ν_R, as the second-order contribution $\sigma_{z'}^2/\nu_\mathrm{R}$ exceeds decay rates from other sources) (Sec. 2.6.3 and Table. 2.1). The decay law under

these two effects for $1/f$-type noise is given in Eq. (2.66). They are analogous to the scenarios of free-evolution dephasing due to low-frequency noise via linear and quadratic coupling, respectively [46]. In contrast, the locking dynamics in the $T_{1\rho}$ experiment largely reduces its sensitivity to these fluctuations, and thus substantially improves the accuracy of extracted noise PSD, especially at both high- and low-frequency regimes.

In addition, $T_{1\rho}$ has a simple exponential decay law (Eq. (2.63)), whereas the Rabi decay law (Eq. (2.66)) can be complicated by its sinusoidal nutation in conjunction with a non-exponential decay envelope related to its sensitivity to low-frequency noise (see Sec. 2.6.3 and Sec. 4.4.1), both of which pose a challenge to high-precision fitting. A $T_{1\rho}$ measurement requires far fewer datapoints than would a Rabi decay envelope on a sinusoid oscillating at the Rabi frequency. These properties make the $T_{1\rho}$ method more accurate and experimentally efficient.

The $T_{1\rho}$ method also, in regard to accuracy and resolution, excels over the free-evolution version of noise spectroscopy, e.g. using dynamical decoupling pulse sequences, over the similar frequency range [21]. Such free-evolution methods depend on the noise filtering property of a multiple-pulse sequence, whose performance is undermined by pulse imperfection. Decoherence during pulses limits the achievable pulse number, thus the filter's resolution. The resolvable range is also comparatively narrow. Above certain frequencies, neighboring pulses start to overlap due to the finite rise and fall time, causing indistinct free-evolution periods. On the other hand, at low frequencies, pulses are so sparsely distributed that there could be very few pulses, making the sequence a coarse filter. In addition, an evident disadvantage in the CPMG spectroscopy is its data scattering. Because of the exponential transfer function between the normalized signal and the PSD (Eq. (2.45)), errors get amplified when taking logarithm to extract PSD, especially at high and low frequencies.

157

6.3 Robust Sequences

The recorded $T_{1\rho}$ decay signal using the original (SL-3) sequence may still suffer from several types of system imperfection, in particular, signal distortion due to low-frequency noise via other channels. In this section, we will show two major types of signal distortion observed in experiments. With the help of specially designed robust sequences, we succeed in recovering the $T_{1\rho}$ decay from them.

6.3.1 5-Pulse Sequence and Cancellation of Dephasing Effect

One example of a measured $T_{1\rho}$ trace is shown in Fig. 6-3b (brown trace). Another example can be found in [62], an early demonstration of spin-locking implemented on a quantronium qubit. A prominent feature in these examples is the presence of unwanted Rabi-frequency oscillations on the back of an otherwise exponential decay function. We excluded the possibility of a constant frequency detuning in our experiment, which could effectively separate the driving field and qubit state during the locking period and lead to oscillations. Rather, we determined that the oscillations were due to dephasing during the intervals between adjacent pulses. In our experiments, we use Gaussian pulses with $\sim 10\,\mathrm{ns}$ width for the $\pi/2$ pulses and Gaussian rise-and-fall for the long driving pulse. To clearly separate pulses, there is a practically unavoidable duration of free evolution between pulses (Fig. 6-2d). Depending on the length τ of the second pulse, phase diffusion accumulated during the first interval will sometimes be doubled (for $\nu_{R}\tau = 1, 2, 3 \ldots$), and sometimes be refocused (for $\nu_{R}\tau = \frac{1}{2}, 1\frac{1}{2}, 2\frac{1}{2} \ldots$), producing those oscillations. In the presence of this noise, the locking protocol is compromised to a differing degree for the temporal ensemble elements, making the observed decay a complicated combination of precession, relaxation and decoherence processes. To correct for it, we developed a modified five-pulse sequence (labelled "SL-5a," see Fig. 6-3a), which adds one $\pi)_{x}$ pulse in the middle of each interval in SL-3. The added pulses refocus the phase diffusion as is done in a spin-echo sequence [64]. Relaxation obtained using SL-5a is shown in Fig. 6-3b, and it shows a clear improvement (no oscillation) over SL-3.

(a) SL-5a Seq.

X-Pulse   Y-Pulse

(b) Comparison between SL-3 and SL-5a
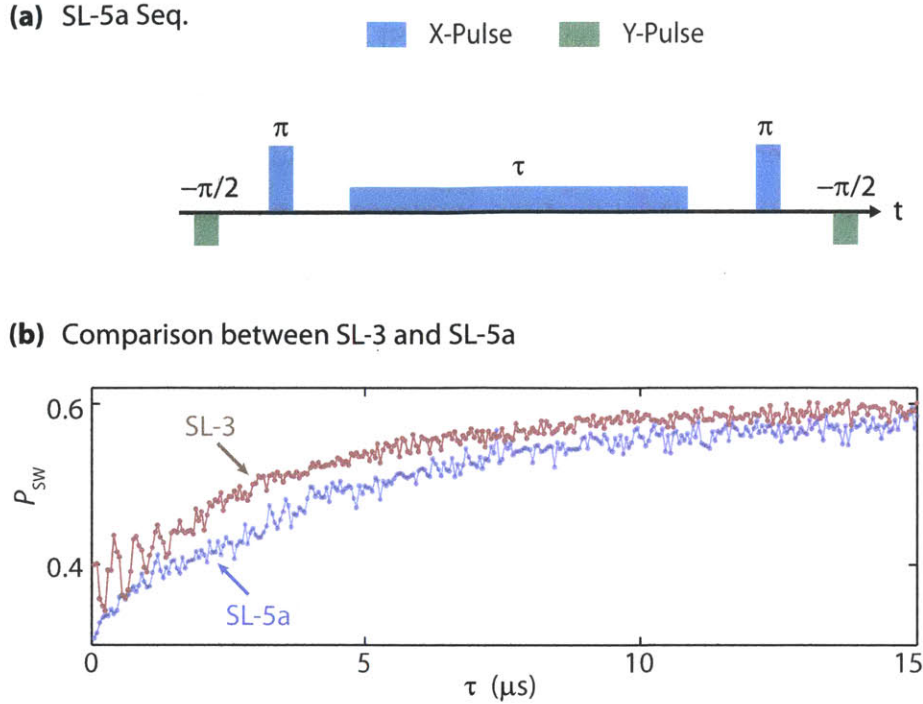
Figure 6-3: (a) Modified five-pulse sequences SL-5a, robust against dephasing between the $\pi/2$-pulse and the continuous driving pulse. (b) Comparison of measured signals by SL-3 (brown) and SL-5a (blue). Both traces are taken at $\varepsilon = 192\,\mathrm{MHz}$ and $\nu_\mathrm{R} = 3\,\mathrm{MHz}$. P_SW is the measured switching probability of the readout SQUID, and is linear with the qubit's state population.

6.3.2 Twin Sequence and Recovery from Ultra-Low-Frequency Signal Distortion

In several measured traces, we observe a second type of signal distortion—random fluctuations at the few-percent level on the exponential signal, and at a time scale of minutes or tens of minutes—e.g., Fig. 6-4b (blue trace). As we describe in detail below, low-frequency fluctuations of the frequency detuning result in the "shivering" of the effective Rabi field and, thereby, fluctuations in the observed decay signal. We first describe how we corrected the distortion, and then explain its origin. The solution is to use a complementary pulse sequence (labelled "SL-5b," see Fig. 6-4a) together with SL-5a. The new sequence is nominally identical to SL-5a, except that

we replace the two $\pi/2)_{\overline{Y}}$ pulses with two $\pi/2)_Y$ pulses, such that the qubit Bloch vector is anti-parallel with the driving axis for SL-5b. Ideally, both sequences should give the same decay function. However, when we apply the sequences in an interleaved sampling order (inner loop: alternate between SL-5a and SL-5b; outer loop: step τ), the anti-symmetry of the signal fluctuation, slow compared with the collection time at each value τ, is captured by the twin sequences, as shown by the example in Fig. 6-4b. We then recover the smooth exponential decay by taking the average of the two traces.

The reason is closely related to the ultra-slow ($\sim$minutes) fluctuation of frequency detuning $\delta\nu$. First, the occurrence of the signal distortion at large τ indicates a deviation of the steady-state population from zero X-polarization. Assuming small detuning ($\Delta\nu \ll \nu_{\mathrm{R}}$), to first order, the steady-state X-polarization [56], in the practical limit $\nu_{\mathrm{R}} \ll k_{\mathrm{B}}T/h \ll \nu_{\mathrm{q}}$, is

$$\langle \hat{\sigma}_X \rangle^{\mathrm{ss}} = -\frac{\sin\eta\, S_{x'}(\nu_{\mathrm{q}})}{\frac{1}{2} S_{x'}(\nu_{\mathrm{q}}) + S_{z'}(\nu_{\mathrm{R}})} \,, \tag{6.1}$$

where $\eta = \arctan(\Delta\nu/\nu_{\mathrm{R}})$ is the angle of the driving field with respect to X due to frequency detuning (see Fig. 6-4c). Eq. (6.1) is applicable to both SL-5a and SL-5b, but the difference in the last back-projection pulse gives rise to a differential signal response to the non-zero X-polarization. Therefore, fluctuation of the frequency detuning, to first order, causes fluctuation of the steady-state longitudinal polarization and the anti-symmetric feature of the traces in Fig. 6-4b. The relaxation dynamics in both sequences with finite detuning are sketched in the right panel of Fig. 6-4c. Ignoring the process at small τ where the much faster $T_{2\rho}$ process is involved, the normalized decay signal, to first order of η, can be approximated as $P_{\mathrm{a}}(\tau) = \frac{1}{2}(1 - \overline{\mathcal{R}}_X)(1 - e^{-\Gamma_{1\rho}\tau})$ for SL-5a, and $P_{\mathrm{b}}(\tau) = \frac{1}{2}(1 + \overline{\mathcal{R}}_X)(1 - e^{-\Gamma_{1\rho}\tau})$ for SL-5b. The average $P(\tau) = \frac{1}{2}(P_{\mathrm{a}}(\tau) + P_{\mathrm{b}}(\tau)) = \frac{1}{2}(1 - e^{-\Gamma_{1\rho}\tau})$ becomes independent of detuning, and recovers the underlying relaxation signal.

(a) SL-5b Seq.

(b) Comparison between SL-3 and SL-5a

(c)
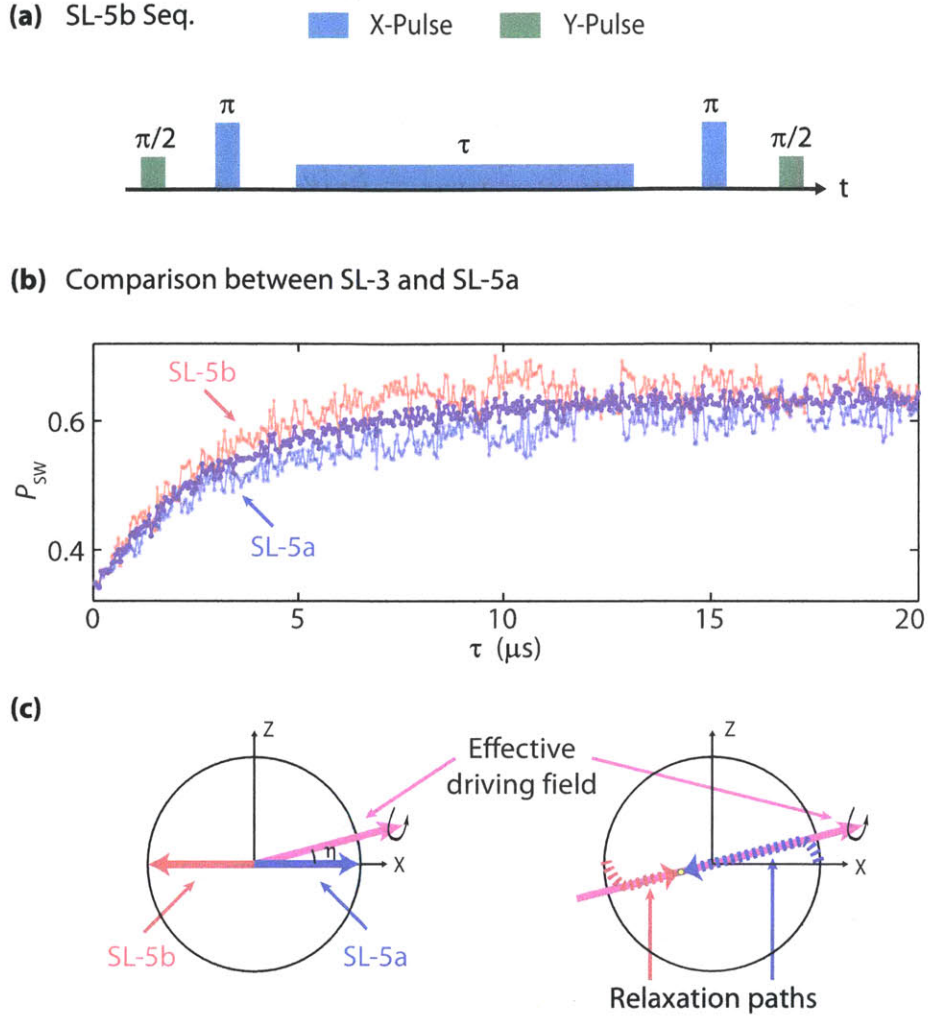
Figure 6-4: (a) Modified five-pulse sequences SL-5b. By alternatively applying SL-5a and SL-5b in experiments, the signal distortion due to low-frequency steady-state fluctuation can be corrected for at a data pre-averaging step. (b) Comparison of measured signals by SL-5a (blue), SL-5b (red) and their average (purple). Both traces are taken at $\varepsilon = 960\,\mathrm{MHz}$ and $\nu_\mathrm{R} = 24\,\mathrm{MHz}$. The data are taken in an interleaved order between blue and red traces. (c) Cross-section sketch of the qubit dynamics under the SL-5a and SL-5b protocols, with the driving field (magenta arrow) tilted by an angle η ($\eta > 0$ in this example) due to slow fluctuations of the frequency detuning. On the left are the qubit states right before the locking pulse; on the right, their relaxation paths during the locking period are indicated by the dashed lines. The steady-state solution (the contacting point of blue and red dash lines) deviates away from $\overline{\mathcal{R}}_X = 0$ when $\eta \neq 0$.

6.4 Results

We use the modified $T_{1\rho}$ pulse sequence to implement noise spectroscopy during driven evolution. To derive the Δ-noise PSD, we perform a driven-evolution $T_{1\rho}$ measure-

161

ment for various ν_R at $\varepsilon = 0$, where the qubit is first-order insensitive to the ε noise, as well as the standard (free-evolution) inversion-recovery T_1-measurement. Both T_1 and $T_{1\rho}$ traces are fit to extract the exponential decay rates Γ_1 and $\Gamma_{1\rho}$, which, from Eq. (2.64), give the Δ-noise PSD by $S_\Delta(\nu_R) = S_{z'}(\nu_R) = 2\Gamma_{1\rho} - \Gamma_1$ (Fig. 6-5 and Fig. 6-6).

For the ε-noise PSD, we perform the same experiments at $\varepsilon \neq 0$, where the qubit becomes predominantly sensitive to the ε noise. From Eq. (2.64), we have $S_\varepsilon(\nu_R) = [S_{z'}(\nu_R) - \cos^2\theta S_\Delta(\nu_R)]/\sin^2\theta = [2\Gamma_{1\rho} - \Gamma_1 - \cos^2\theta S_\Delta(\nu_R)]/\sin^2\theta$, where $S_\Delta(\nu_R)$ is previously measured (Fig. 6-7 and Fig. 6-8). In Fig. 6-7, it can be seen that the flux bias we choose as the working point generally increase with the Rabi frequency. In the noise-sensitivity point of view, it is always better to bias further away from the sweet spot, so that the flux noise is more dominant. However, greater flux bias also leads to stronger fluctuation of the qubit frequency, and thus worse locking condition (alignment between the qubit state and the drive field), especially for small ν_R. The best solution is to reduce the flux bias at weaker driving, because having the locking protocol well-performed is a priority. The loss of sensitivity can be compensated by more averaging.

The locking Rabi frequency, ν_R, is determined by measuring Rabi oscillations with the same driving-field amplitude. The lower limit ($\sim 100\,\text{kHz}$) of the spectrum is determined by the $\Delta\nu$ inhomogeneity $\sigma_{z'}^2$, which breaks the locking condition when driving is too weak. On the other hand, an undetermined effect (presumably heating due to strong driving) which distorts the SQUID's switching-current distribution prevents us from probing frequencies higher than $\sim 200\,\text{MHz}$.

The spectroscopy results are presented in Fig. 6-9. In this device, the measured Δ-noise spectrum is generally white. Since the extrapolated $1/f$ Δ-noise from low-frequency measurements crosses the white noise level around the lower limit, we are unable to determine whether the $1/f$ noise extends to this regime or has a cut-off [44]. The noise could be due to Johnson noise from charge or critical current fluctuations, or due to thermal photon noise [125] originating from the LC resonator associated with the readout SQUID which inductively couples to the qubit.

Figure 6-5: Rates measured at $\varepsilon = 0$ at base temperature. Blue dots with error bars: measured driven-evolution relaxation rate, $\Gamma_{1\rho}$; red dots: half of measured free-evolution relaxation rate, $\frac{1}{2}\Gamma_1$. Since we operate at the same bias point, Γ_1 is single valued.

The ε-noise spectrum exhibits a $1/f^\alpha$ dependence with $\alpha = 0.9$, a value that generally agrees with independently measured free-evolution noise spectroscopy using a Ramsey ($1\,\mathrm{mHz} - 100\,\mathrm{Hz}$) [44] and CPMG ($0.1 - 20\,\mathrm{MHz}$) approach [21]. Although not necessarily a universal result, this suggests that driven evolution does not activate ε-noise sources for this device. In general, the $T_{1\rho}$ spectroscopy confirms these results with better accuracy and extends the frequency range by 5x (limited in this device by a heating effect at high drive). Note that measuring at higher frequency ($0.1 - 1\,\mathrm{GHz}$) is feasible in principle by using this technique.

In contrast to previous free-evolution measurements, we observe on the $1/f$ trend two clear "bump"-like features, one around $1\,\mathrm{MHz}$ and the other around $20\,\mathrm{MHz}$. These features appear after thermal-cycling the device from base temperature to $4.2\,\mathrm{K}$ and back again, which likely activated the fluctuators. The one at $1\,\mathrm{MHz}$ has a
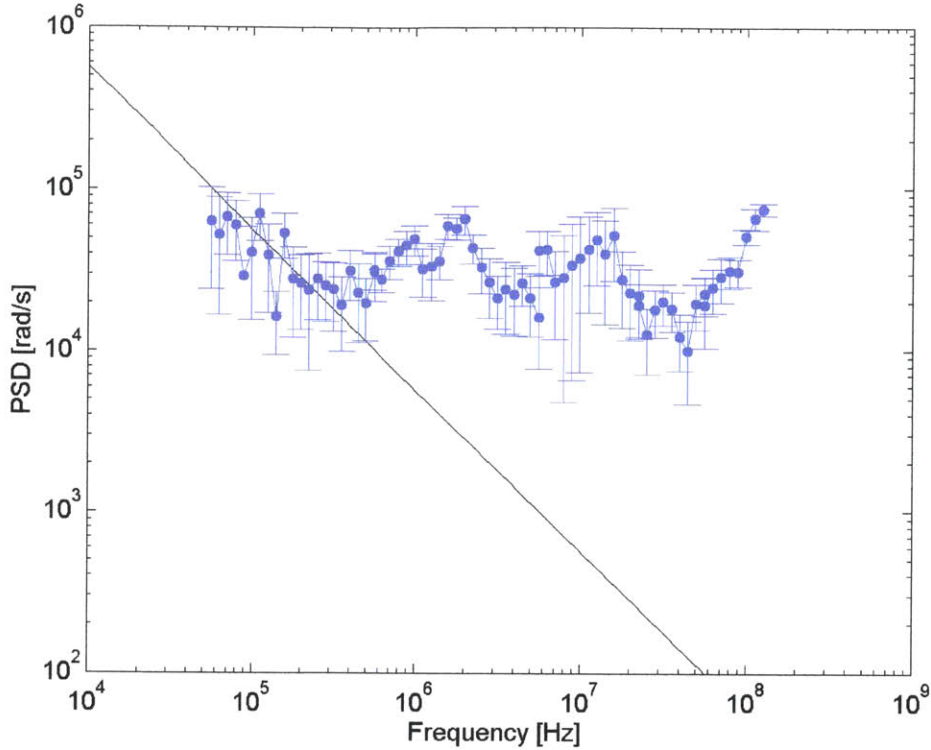
Figure 6-6: Δ-noise PSD (blue dots) from 60 kHz to 125 MHz. Black line is the extracted $1/f$ Δ noise from coherence characterization measurements (Sec. 4.3.2 and Sec. 4.3.3).

clear peak above the general $1/f$ background. This excludes the possibility of random telegraph noise (RTN), possibly generated by some microscopic two-level fluctuators (TLFs), as the cause of this bump, since RTN would produce a Lorentzian spectrum centered at zero frequency [126, 127]. To fit the main features, we assume that the ε-noise PSD is a combination of the $1/f^{0.9}$ line and two Lorentzians. Both bumps are better fit to Lorentzians centered around 1 MHz and 20 MHz than those centered at zero frequency. One example is shown by the black line in Fig. 6-9.

The thermal cycling is required for changing sample and electronics or power shutdown. The qubits properties can change with time, and in particular after thermal cycling, due to microscopic rearrangements in the material and its surroundings (e.g. in the tunnel-junctions oxide). From our observation, the device described in this thesis shows negligible variation of its energy relaxation time T_1 and spin echo time T_{Echo} at the degeneracy point over different cooldowns. However, the free-induction
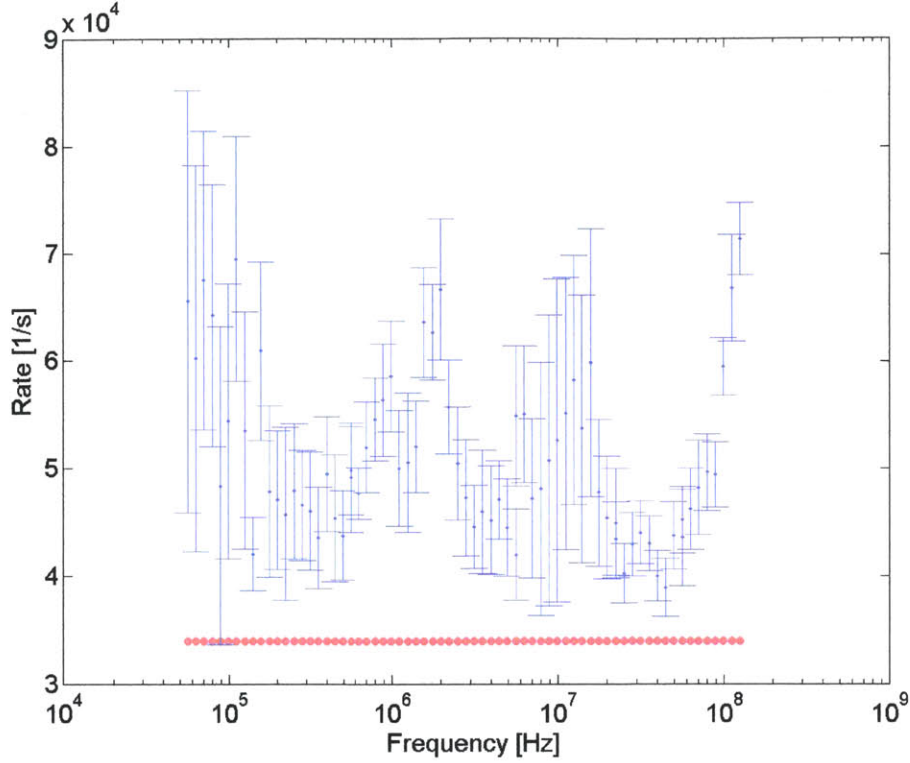
164
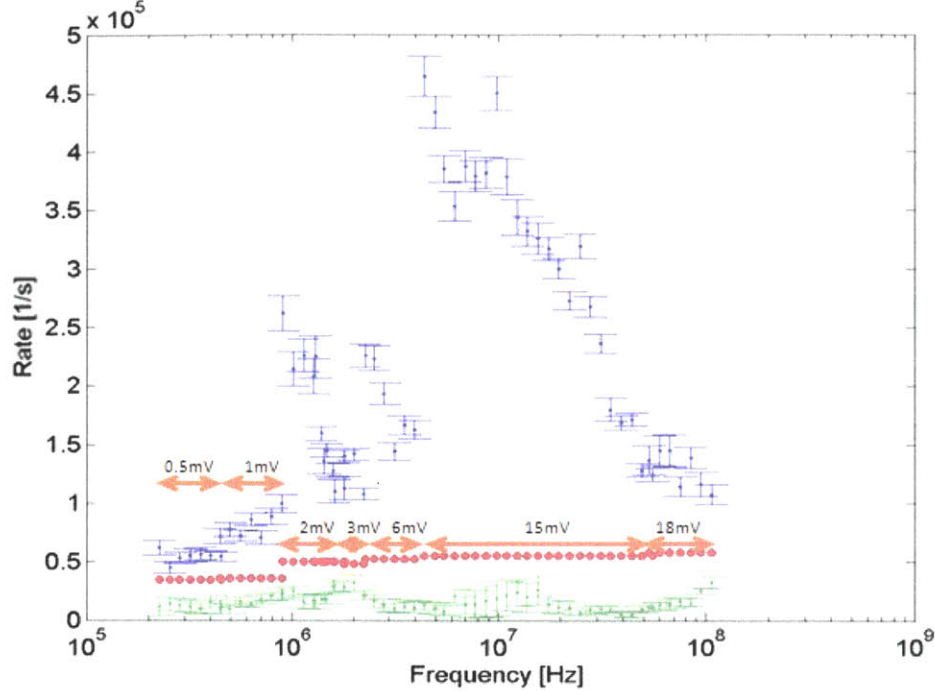
Figure 6-7: Rates measured at $\varepsilon > 0$ at base temperature. Blue dots with error bars: measured driven-evolution relaxation rate, $\Gamma_{1\rho}$; red dots: half of measured free-evolution relaxation rate, $\frac{1}{2}\Gamma_1$. Green dots are the Δ-noise contribution, $\frac{1}{2}\cos^2\theta\, S_\Delta(\nu_R)$, as derived in Fig. 6-6. Orange arrows and above texts indicate the flux bias where corresponding data are taken. The bias is denoted by the voltage applied through a DC bias line ($1\,\mathrm{mV} \approx 64\,\mathrm{MHz}$ in terms of ε). Γ_1 has slight variation between different bias points.

time measured at the degeneracy point may exhibit variations up to 50% on different cooldowns, indicating a change of low-frequency Δ noise. The low-frequency ε noise is generally consistent. However, the bump features are mercurial. For example, the $1\,\mathrm{MHz}$ bump shown in the $T_{1\rho}$ results was absent during the cycle when the CPMG experiments was done (Sec. 4.3.3).

6.5 Time-Domain Confirmation

We find a signature of the $1\,\mathrm{MHz}$ bump feature in a free-evolution, time-domain spin-echo experiment. Fig. 6-10 shows the phase-decay during spin-echo as measured at several flux-bias points where the qubit coherence is mostly limited by the ε noise.
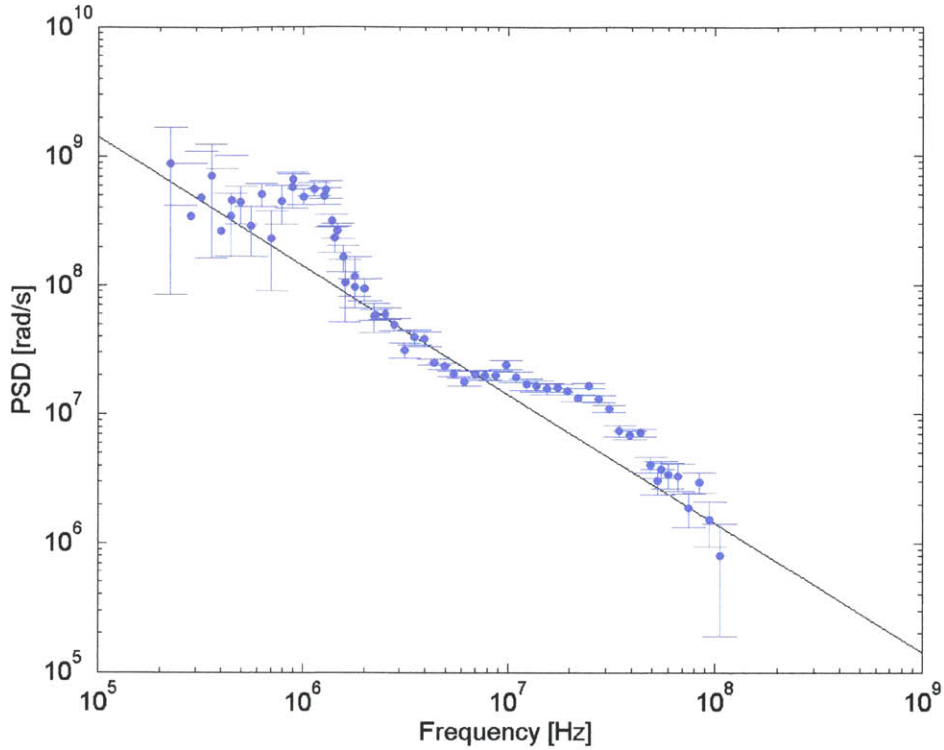
Figure 6-8: ε-noise PSD (blue dots) from $200\,\mathrm{kHz}$ to $100\,\mathrm{MHz}$. Black line is extracted $1/f\ \varepsilon$ noise from coherence characterization measurements (Sec. 4.3.2 and Sec. 4.3.3).

Under a Gaussian-noise assumption, the spin-echo sequence is most sensitive to the noise whose frequency is about the inverse of the total free-evolution time of the sequence. The spin-echo decay functions all exhibit a clear "dip" feature around $1\,\mu\mathrm{s}$, corresponding to the spectral feature around $1\,\mathrm{MHz}$. To model this result, we use the previously assumed PSD function $S'(f)$ ($1/f^{0.9}$ plus two Lorentzians) with tunable parameters to reproduce the echo-decay signal by the filter function method [46, 48, 21]. The agreement is good, and bump parameters estimated from the temporal spin-echo measurement are within 30% of a direct fit to the driven-evolution spectral data. In general, we are able to predict the phase decay from the $T_{1\rho}$ spectroscopy results, and, in turn, justify the performance of the $T_{1\rho}$ spectroscopy method on a superconducting qubit.

In the case of the $20\,\mathrm{MHz}$ bump, simulations indicate that the echo signature corresponding to this broad, relatively small feature in the noise spectrum would yield
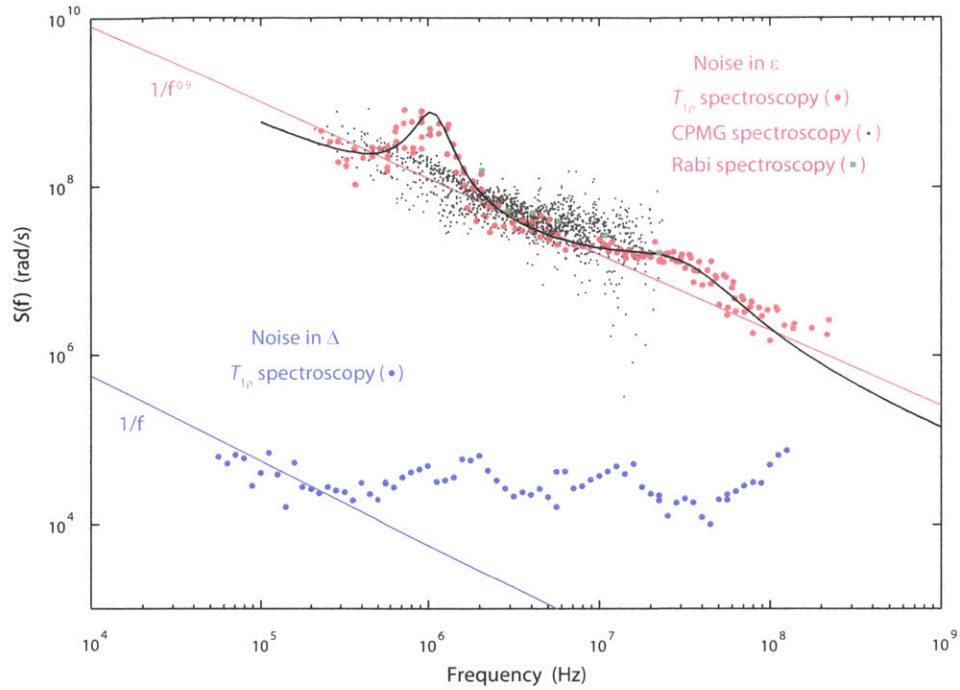
Figure 6-9: ε (red dots) and Δ (blue dots) noise spectroscopy by the $T_{1\rho}$ method. Here, previous results on the ε noise by the CPMG (grey dots) and Rabi (green dots) methods measured on the same device are plotted for comparison. From the fitting results, the error rate in the worst case is about 30% for the ε noise, and 70% for the Δ noise. Previous experiments and the $T_{1\rho}$ experiment were separated by six months and a 4K warm-up. The red and blue solid lines are the $1/f^\alpha$ power laws, extrapolated from separate low-frequency noise measurements [44]. The black line represents the function $S'(f) = A/f^{0.9} + S_1\mathcal{L}(f; F_1, W_1) + S_2\mathcal{L}(f; F_2, W_2)$, where $\mathcal{L}(f; F, W) = W^2/((f - F)^2 + W^2)$, and $A = (2\pi\, 0.65 \times 10^6)^2\, (\text{rad/s})^2$, $S_1 = 7.0 \times 10^8\,\text{rad/s}$, $F_1 = 1.05\,\text{MHz}$, $W_1 = 0.25\,\text{MHz}$, $S_2 = 1.2 \times 10^7\,\text{rad/s}$, $F_2 = 20\,\text{MHz}$, $W_2 = 25\,\text{MHz}$.

only a small deviation from the spin-echo phase-decay function with no discernable "dip". The temporal resolution in Fig. 6-10 is furthermore insufficient to resolve such a deviation.

It is possible that the observed Lorentzian bumps are generated by two sets of coherent TLSs [128], such as electron spins. In a magnetic environment, each spin executes Larmor precession at a frequency proportional to its local field. Its transverse component, via a coupling depending on geometric relations among the device, the field and the spin [95], adds to a net fluctuating flux whose PSD reflects the spectral
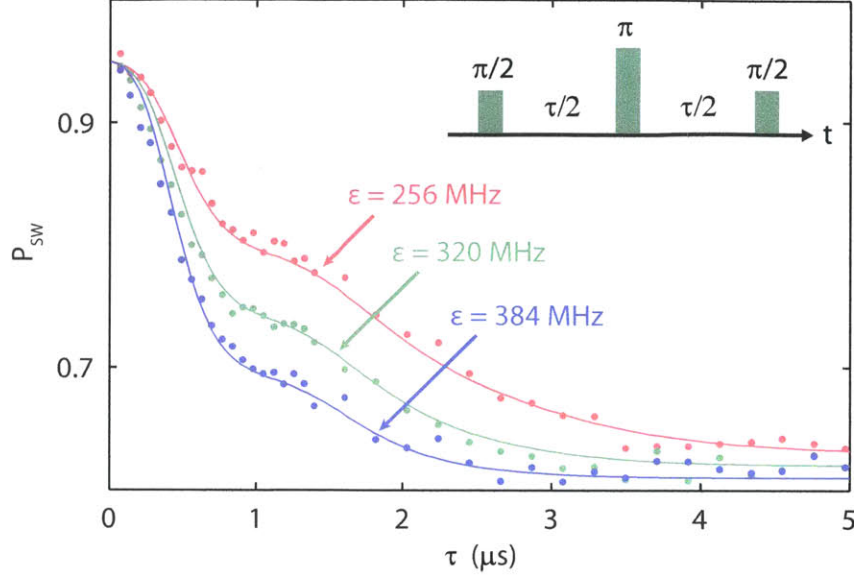
Figure 6-10: Temporal signature of TLS during free-evolution. Echo phase-memory decay (dots) measured at $\varepsilon = 256\,\mathrm{MHz}$ (red), $320\,\mathrm{MHz}$ (green) and $384\,\mathrm{MHz}$ (blue), and corresponding simulation (solid lines) with assumed flux noise PSD function, $S'(f) = A/f^{0.9} + S_1\mathcal{L}(f; F_1, W_1)$, where $A = (2\pi\,0.9 \times 10^6)^2\,(\mathrm{rad/s})^2$, $S_1 = 9.0 \times 10^8\,\mathrm{rad/s}$, $F_1 = 1.25\,\mathrm{MHz}$, $W_1 = 0.35\,\mathrm{MHz}$. Inset is the echo pulse sequence. Here, τ is the total free evolution time in the sequence. Note that the $20\,\mathrm{MHz}$ bump has little influence at these bias points.

(Larmor-frequency) distribution of spins, even though the ensemble has already lost its coherence. The width of the Lorentzian indicates in part the field inhomogeneity. Assuming uncorrelated surface electron spins and an average coupling strength of $2.7 \times 10^{-8}\Phi_0/\mu_B$ from simulation, both Lorentzian bumps correspond to $\sim 10^6$ spins. The number scales down in the presence of a high degree of spin order [94]. Moreover, if we assume the spins feel the same magnetic field as the qubit, about $0.5\,\mathrm{mT}$ ($B_0 = \Phi_e/A_q$, where $\Phi_e = \Phi_0/2$ is the flux through the qubit loop and $A_q \approx 2\,\mu\mathrm{m}^2$ is the loop size), the corresponding electron-spin Larmor frequency is $14\,\mathrm{MHz}$. This is only a rough estimate, as screening due to superconducting metal may lead to a large variation of the field at various locations in the vicinity of the metal surface, and other locations for these spins, e.g., superconductor insulator boundary [100] and substrate, are also possible. Nonetheless, the crude estimate is consistent with our

observations.

6.6   Temperature Dependence

We also measured the Δ-noise spectrum at different temperatures (Fig. 6-11 and Fig. 6-12). The results clearly shows a white noise floor increasing with temperature. The observation is consistent with independently extracted white noise level from free-induction and spin-echo experiments. The average noise power in Fig. 6-11 is plotted in Fig. 4-19 for comparison. The reason is yet to be understood.
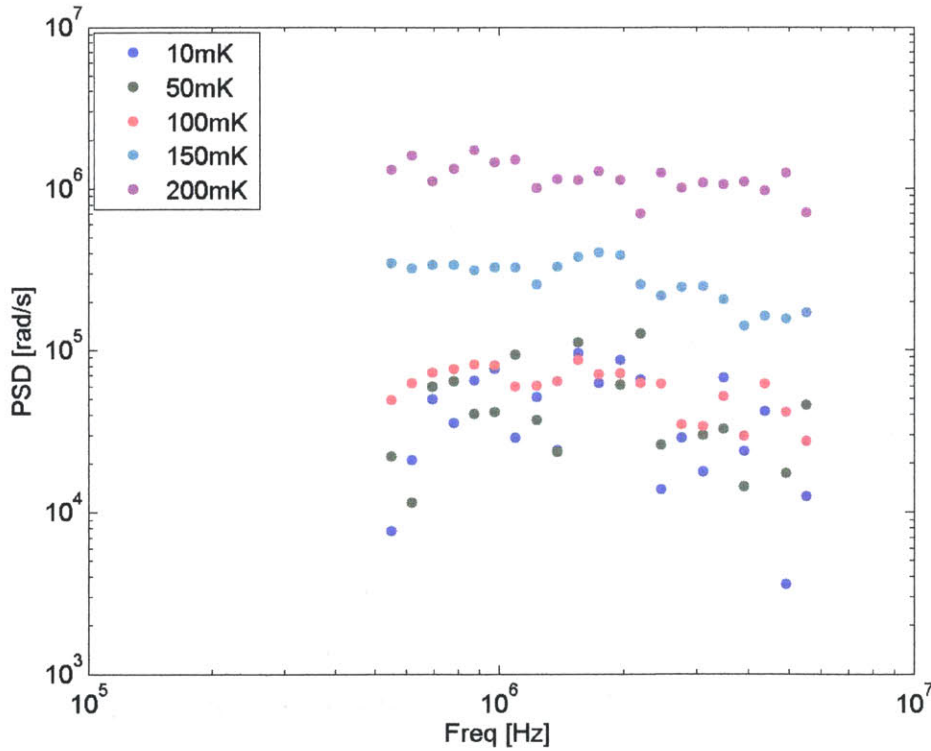
Figure 6-11: Δ-noise PSD $(0.5 - 5\,\mathrm{MHz})$ measured at different temperatures. Temperatures indicated in the legend are the nominal mixing-chamber temperature $T_{\mathrm{M.C.}}$ measured by a thermometer. The effective device temperature, obtained from the SQUID's escape temperature, $T_{\mathrm{Esc.}}$, generally follows the formula: $T_{\mathrm{Esc.}} = \sqrt{(65\mathrm{mK})^2 + T_{\mathrm{M.C.}}^2}$.
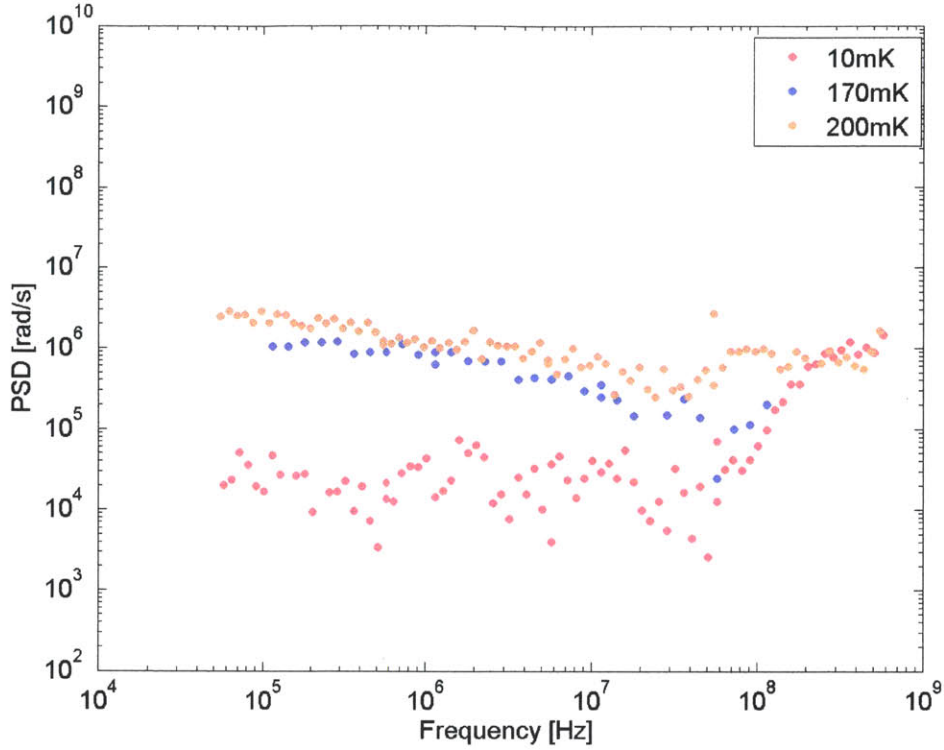
Figure 6-12: Δ-noise PSD ($50\,\mathrm{kHz} - 500\,\mathrm{MHz}$) measured at different temperatures. Temperatures indicated in the legend are the nominal mixing-chamber temperature $T_{\mathrm{M.C.}}$. Note that the spectroscopy exceeds the dependable range at higher temperatures, which is set by the inhomogeneous noise (lower limit, $\sim 1\,\mathrm{MHz}$) and heating effect (upper limit, $\sim 30\,\mathrm{MHz}$).

6.7   Summary

The modified $T_{1\rho}$ method presented here, in conjunction with existing free-evolution spectroscopy methods, enables the characterization of the noise sources relevant for both driven- and free-evolution quantum control methods. Although many noise sources may be manifest similarly during both driving conditions, in principle, the noise in these two cases need not be identical. For example, driven evolution may activate certain noise sources that are otherwise dormant during free-evolution. In this demonstration with a flux qubit, the flux and tunnel-coupling noise spectra reveal more detailed information and cover a wider frequency range, a 10x increase in this device, as compared with our previous free-evolution (CPMG spectroscopy) and driven evolution (Rabi spectroscopy) methods [21]. We observed the spectral features

170

of two sets of coherent TLSs in the environment, possibly due to effective electron spins on the metal surface, which are active during driven evolution. We could furthermore observe a temporal signature of one of these fluctuators in a free-evolution echo experiment, indicating that it is active during both driven- and free evolution. This type of noise characterization serves as an important first step towards the engineered mitigation of decoherence through improved materials, fabrication, control sequences, and qubit design. Our modifications to the $T_{1\rho}$ pulse sequence target the unwanted effects of low-frequency noise, opening this method to the multiple qubit modalities that are subject to such noise.

.

Chapter 7

Summary and Future Work

7.1 Summary

The work presented in this thesis can be summarized by a single picture, Fig. 7-1. The spirit is that any noise that contributes to observable decoherence phenomenon is basically resolvable. Sometimes, we need to unravel it from other contributing noise by combining results of other experiments.

- In the low-frequency regime, free induction (Sec. 4.3.2) and spin echo (Sec. 4.3.3) reveal the integrated noise in the quasistatic range (1 Hz−1 MHz). The repeated fixed-time free-induction technique with the single-shot readout scheme (Chap. 5) enables us to resolve the spectrum below a upper cutoff (1 kHz) which is only limited by achievable repetition rates of the measurements.

- In the intermediate-frequency regime (1 MHz−100 MHz), both free-evolution CP-like sequence (Sec. 4.3.3) and driven-evolution Rabi (Sec. 4.3.2) or $T_{1\rho}$ (Chap. 6) can be utilized to extract the noise PSD. The $T_{1\rho}$ spectroscopy is a more accurate method due to its intrinsic properties.

- In the high-frequency regime, noise information at the qubit frequency ($>$ 5 GHz) is obtainable by measuring the T_1 relaxation (Sec. 4.3.1).

173

The combined results construct a noise spectrum over 13 decades with a few gaps (Fig. 7-1).
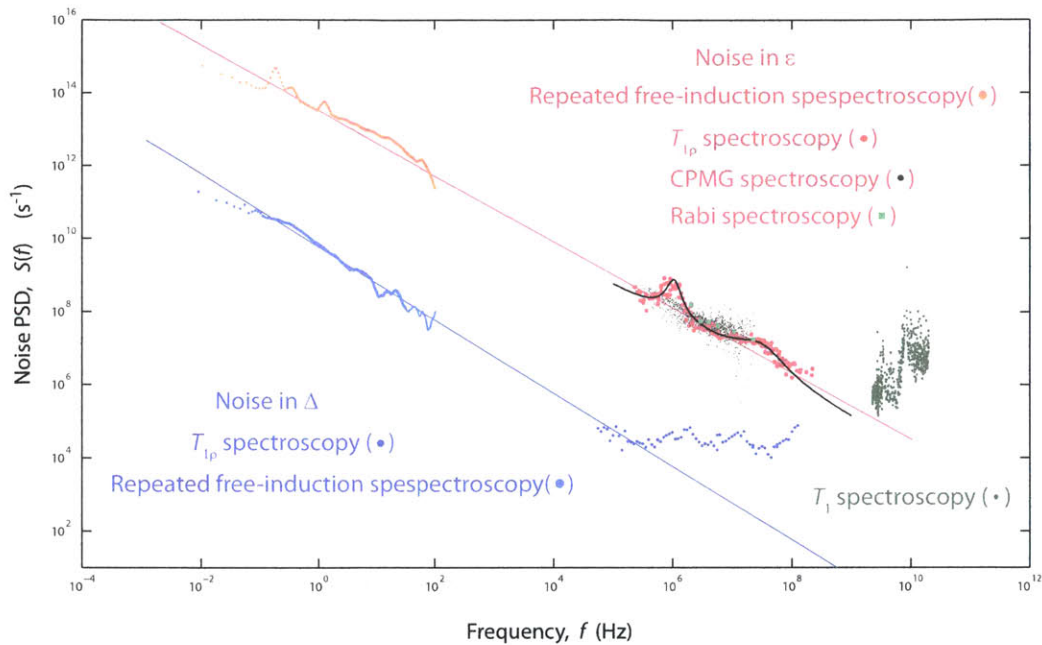
Figure 7-1: Noise spectroscopy by various methods at base temperature. **Orange dots**, Extracted ε-noise PSD by repeated free-induction spectroscopy. **Grey dots**, Extracted ε-noise PSD by CPMG spectroscopy. **Green squares**, Extracted ε-noise PSD by Rabi spectroscopy. **Red dots**, Extracted ε-noise PSD by $T_{1\rho}$ spectroscopy. **Cyan dots**, Extracted Δ-noise PSD by repeated free-induction spectroscopy. **Blue dots**, Extracted Δ-noise PSD by $T_{1\rho}$ spectroscopy. **Green dots**, Extracted combined noise PSD by T_1 spectroscopy. **Solid, red line**, $1/f^{0.9}$ power-law dependence derived in Chap. 4. **Solid, blue line**, $1/f$ power-law dependence derived in Chap. 4.

By learning from NMR, we are equipped with a handful of universal tools to manipulate and characterize our system. As the microwave engineering continues to improve, this notion will have substantial impact on the study of solid-state quantum systems, and may eventually contribute to the realization of scalable quantum computing.

7.2 Future Work

7.2.1 In-Plane dc Field

The "bump"-like features in the $T_{1\rho}$ spectroscopy shown in Chap. 6 are possibly due to surface electron spins. An experiment to verify this speculation is to add an in-plane (parallel with the loop plane) dc magnetic field, which is able to modify the spin's Zeeman frequency while keeps the through-loop flux unchanged. The field may be realized by wrapping an additional coil around the device package.

One challenge of this experiment is to prevent excessive heating from the coil, provided that a large enough dc field is applied. The line need to be properly thermally anchored at each stage. Another challenge is more a random phenomenon. As we mentioned, the "bump"-like feature is mercurial, since thermal cycling can possibly rearrange the configuration of noise sources. Therefore, whether to spot again such a strong "bump" depends on luck.

7.2.2 The Modified Two-Dimensional Exchange Experiment

To continue exploring coherence characterization methods by NMR techniques, there is another example called the two-dimensional (2D) exchange experiment [23], originally developed for studying chemical exchange processes. The experiment can be used to extract low-frequency noise information unobtainable by methods previously described in the thesis. We have an idea for implementing a more efficient 1D version of this experiment and expect to see signatures of slow (switching rate below 100 kHz) two-level fluctuators in the experimental observation. The challenge is that whether the fluctuators are strong enough to be visible in the measurement signal, when many other noise mechanisms are active at the same time.

7.2.3 The ρ-Qubit

Another field to explore is to utilize the fictitious qubit (ρ-qubit) in the rotating frame (Sec. 2.6.1) as the logic qubit for building a quantum computer. The ρ-qubit satisfies

every criteria for quantum computing. It is a well-defined two-level system, but just in another reference frame. The state initialization and readout can be achieved by using the spin-locking protocol. Gate operation can be done by modulating the drive amplitude for Z-gates (a more straightforward way), and by applying another harmonic drive which resonates with the ρ-qubit for X- and Y-gates. Most remarkably, the ρ-qubit is likely to have better decohering properties than the regular qubit. As shown in Chap. 4 and Chap. 6, $T_{1\rho}$ and $T_{2\rho}$ in this device are generally better than T_1 and T_2. This is also true for many solid-state qubits, because the low-frequency noise is what limits coherence times in these systems and by working in the rotating frame, sensitivity to the noise degrades from first order to second order. With specifically designed devices for utilizing the ρ-qubit as the computational unit, we might have a new type of architecture which allows more engineering flexibility and outperforms the regular qubit.

Besides quantum computing, the ρ-qubit is considered advantageous for many other fields of study. For example, the ρ-qubit might favor the study of strongly coupled systems. The ρ-qubit, as discussed above, is a well-initialized quantum two-level system but with relatively small energy splitting. In a solid-state system where qubit coupling is fixed and limited, we are still able to create a strong coupling by bringing the qubit frequency down in this ρ-scheme, even beyond the rotating-wave approximation. Also, with more flexibility in design and control, the ρ-qubit might help perform complicated quantum simulations in a more efficient way.

Appendix A

Quantum Noise

The standard description of quantum fluctuations is given by the autocorrelation function of the quantity in question ($\hat{\lambda}$). For stationary process,

$$R^{\mathrm{U}}(\tau) = \langle \hat{\lambda}(0)\hat{\lambda}(\tau) \rangle = \mathrm{Tr}[\hat{\lambda}(0)\hat{\lambda}(\tau)\rho] \, . \tag{A.1}$$

In the context of a quantum system, $\hat{\lambda}(0)$ does not commute with $\hat{\lambda}(\tau)$ in general, but the positive- and negative-delay autocorrelation functions form a pair of complex conjugate, i.e., $\langle \hat{\lambda}(0)\hat{\lambda}(\tau) \rangle = \langle \hat{\lambda}(\tau)\hat{\lambda}(0) \rangle^*$ [129], their average gives the symmetrized autocorrelation function,

$$R(\tau) = \frac{1}{2}\langle \hat{\lambda}(0)\hat{\lambda}(\tau) + \hat{\lambda}(\tau)\hat{\lambda}(0) \rangle \, , \tag{A.2}$$

which is equivalent to the unsymmetrized (regular) autocorrelation function in the classical limit ($R(\tau) = R^{\mathrm{U}}(\tau)$ when λ is a scalar), and is a Hermitian related to a directly measurable quantity, the symmetrized (classical) power spectral density, by Fourier transform,

$$S(f) = \int_{-\infty}^{\infty} \mathrm{d}\tau \, \exp(-i2\pi f\tau) \frac{1}{2}\langle \hat{\lambda}(0)\hat{\lambda}(\tau) + \hat{\lambda}(\tau)\hat{\lambda}(0) \rangle \, , \tag{A.3}$$

where $S(-f) = S(f)$. Accordingly, Fourier transform of the unsymmetrized autocorrelation function gives the unsymmetrized (quantum) power spectral density,

$$S^{\mathrm{U}}(f) = \int_{-\infty}^{\infty} d\tau \; \exp(-i2\pi f\tau) \, \langle \hat{\lambda}(0)\hat{\lambda}(\tau) \rangle \; . \tag{A.4}$$

Since the $\langle \hat{\lambda}(0)\hat{\lambda}(\tau) \rangle$ is in general a complex number, $S^{\mathrm{U}}(-f) \neq S^{\mathrm{U}}(f)$. $S^{\mathrm{U}}(f)$ $(S^{\mathrm{U}}(-f))$ is spectral density of the positive (negative) mode, which can be related to the absorption (emission) spectra by the noise sources. Therefore, the relaxation and excitation rates of the two-level system in consideration are related to them,

$$\Gamma_- \propto S^{\mathrm{U}}(\nu_{01}) \; ,$$

$$\Gamma_+ \propto S^{\mathrm{U}}(-\nu_{01}) \; , \tag{A.5}$$

where ν_{01} is the frequency splitting between the two levels. In the fluctuation-dissipation theorem [130, 34], for an environment at an equilibrium temperature of T,

$$\frac{S^{\mathrm{U}}(-f)}{S^{\mathrm{U}}(f)} = \exp\left(-\frac{hf}{k_{\mathrm{B}}T}\right) \; . \tag{A.6}$$

Therefore, it can be derived that

$$S(f) = \frac{1}{2}(S^{\mathrm{U}}(f) + S^{\mathrm{U}}(-f)) = J(f)\coth(-\frac{hf}{2k_{\mathrm{B}}T}) \; , \tag{A.7}$$

where $J(f) = \frac{1}{2}(S^{\mathrm{U}}(f) - S^{\mathrm{U}}(-f)) = \int_{-\infty}^{\infty} d\tau \; \exp(-i2\pi f\tau) \frac{1}{2}\langle \hat{\lambda}(0)\hat{\lambda}(\tau) - \hat{\lambda}(\tau)\hat{\lambda}(0) \rangle$ is the Fourier transform of the anti-symmetrized autocorrelation function (average commutator, anti-Hermitian), which represents an imaginary part of the a heat bath susceptibility, $J(f) = \chi''(f)$ [22, 131].

Appendix B

Definition

In this appendix, i clarify several confusions arising from different definitions of power spectral density (PSD). The definition followed in this thesis is the symmetrized bilateral PSD, i.e., type-I Fourier transform of the symmetrized autocorrelation function, in which the correlator $\omega(t)$ is expressed in unit of angular frequency:

$$S(f) = \int_{-\infty}^{\infty} dt \, \exp(-i2\pi f t) \frac{1}{2} \langle \omega(0)\omega(t) + \omega(t)\omega(0) \rangle , \qquad (B.1)$$

where $R(t) = \frac{1}{2}\langle \omega(0)\omega(t) + \omega(t)\omega(0) \rangle$ is the symmetrized autocorrelation function, and simplifies to the regular autocorrelation function $\langle \omega(0)\omega(t) \rangle$ for classical noise.

By using the angular-frequency correlator, the PSD is in unit of rad/s and we would have a concise and universal rate-PSD relation,

$$\Gamma_\lambda = \frac{1}{2} S(f_\lambda) , \qquad (B.2)$$

where we have matched pairs such as

$$\lambda = 1, \, f_\lambda = \nu_q; \quad \lambda = \varphi, \, f_\lambda = 0; \quad \lambda = 1\rho, \, f_\lambda = \nu_R . \qquad (B.3)$$

Therefore, it is naturally convenient to use the definition in Eq. (B.1). We will take it as the standard definition.

B.1 Confusion about Correlator

If we keep the standard definition unchanged, but express the correlator by another corresponding physical quantity λ, a prefactor of $(\partial\omega/\partial\lambda)^2$ (sensitivity) should be attached. For example, if the correlator in the statistical-average brackets is a quantity in unit of frequency, ν, we then have

$$S(f) = (2\pi)^2 \int_{-\infty}^{\infty} \mathrm{d}t \, \exp(-i2\pi f t) \frac{1}{2}\langle \nu(0)\nu(t) + \nu(t)\nu(0)\rangle \,, \qquad (B.4)$$

which is the same as Eq. (2.27), and widely used in this thesis. Similarly, if the correlator is an energy term, a prefactor is then $1/\hbar^2$. Also, $(\partial\omega/\partial\Phi)^2$ for magnetic flux.

After all, no matter what correlator is used in the correlation function, a sensitivity-squared prefactor should be multiplied to translate into a PSD equivalent to the one in Eq. (B.1), so that it can be directly related to the measured decay rates (Eq. (B.3)).

B.2 Confusion about Fourier Transform

There are usually two types of Fourier transform (from t to f), type-I,

$$X(f) = \int_{-\infty}^{\infty} \mathrm{d}t \, \exp(-i2\pi f t)\, x(t) \,, \qquad (B.5)$$

and type-II,

$$X(f) = \frac{1}{2\pi} \int_{-\infty}^{\infty} \mathrm{d}t \, \exp(-i2\pi f t)\, x(t) \,. \qquad (B.6)$$

Type-I is more widely used. Some examples are found in [57, 48, 115, 44]. However, sometimes type-II is also used, as in [65, 46, 66, 21]. The PSD defined with type-II Fourier transform is related to the standard one by $S^{\mathrm{II}}(f) = \frac{1}{2\pi}S(f)$. Since the measured decay rates always have the same value, the rate-PSD relation (Eq. (B.2))

for type-II PSD becomes

$$\Gamma_\lambda = \pi S^{\mathrm{II}}(f_\lambda) \, , \qquad\qquad (B.7)$$

an expression often seen in many literatures.

If unilateral PSD is used (doubling the PSD), another "$\frac{1}{2}$" factor should be added on the r.h.s. of the rate-PSD relations (Eq. (B.2) and Eq. (B.7)). The variation is summarized in Table. B.1.

	Type-I F.T.	Type-II F.T.
bilateral	$\Gamma_\lambda = \frac{1}{2}S(f_\lambda)$	$\Gamma_\lambda = \pi S(f_\lambda)$
unilateral	$\Gamma_\lambda = \frac{1}{4}S(f_\lambda)$	$\Gamma_\lambda = \frac{\pi}{2}S(f_\lambda)$

Table B.1: Rate-PSD relation for different definitions of Fourier transform (F.T.).

B.3   Confusion about Frequency Representation

Sometimes the PSD function is expressed by the angular-frequency argument, $S(\omega)$, as did in [46, 115, 21]. However, no matter how the argument changes, one should keep in mind that the PSD is always equivalent to that defined in Eq. (B.1).

For the example of $1/f$ noise, assume $S(f) = A/f$. If expressed by $\omega = 2\pi f$, $S(\omega) = A'/\omega$, where $A' = 2\pi A$. Usually, people in the community report A or A' inexplicitly. In addition, if the PSD is also defined with type-II Fourier transform, $S^{\mathrm{II}}(\omega) = A'/\omega/2\pi = A/\omega$. Therefore, the type-II $1/f$-noise PSD in argument of ω coincidently gives the same "A" as the standard PSD (type-I, in argument of f). An example of this coincidence can be found between [66, 21] and [44].

When reporting or comparing the result, one should be careful about the definition in use. Otherwise, a factor of 2π might easily kick in.

Appendix C

Correction Factor from Quasistatic Noise

Sec. 2.5.3 described how quasistatic noise determines the free-induction pure dephasing. Now we turn to its effect on the repeated fixed-time (τ_0) free-induction spectroscopy.

With our single-shot scheme, each element of the binary time series $\{z_n\}$ is a Bernoulli random variable z_n with expectation value given by the switching probability p_{sw}, which we now denote as

$$y_n = p^{(0)} + a(0)\sin x_n. \tag{C.1}$$

This function has a non-linear dependence on $x_n = 2\pi\delta\nu_n\tau_0$, the phase accrued during τ_0, where $\delta\nu_n$ is the average fluctuation of the transition frequency at time step n. This phase x_n, in turn, has noise contributions from two distinct frequency intervals, "1" and "2."

We denote as "interval 1" the frequencies which we can resolve by taking the Fourier transform of the series $\{z_n\}$, of total length Nt_{rep} and step size $t_{\mathrm{rep}} \approx 2\,\mathrm{ms}$, i.e. from $1/t_{\mathrm{tot}} = 1/Nt_{\mathrm{rep}} \approx 10^{-2}\,\mathrm{Hz}$ to $1/2t_{\mathrm{acq}} = 1/2t_{\mathrm{rep}} \approx 250\,\mathrm{Hz}$ (or with the interleaving method up to $1/4t_{\mathrm{rep}} \approx 125\,\mathrm{Hz}$). The noise within this interval has zero mean and variance σ_1^2.

In addition, there is a contribution from the quasistatic noise in "interval 2," which is the range from $1/2t_{\text{acq}}$ to $1/\tau_0$; see Fig. C-1. This noise cannot be resolved, but acts in aggregate and leads to dephasing, e.g. in a Ramsey-fringe experiment. It has zero mean and variance σ_2^2.

At each time step n, the element x_n is subject to noise contributions from both intervals, and their variances add up to $\sigma^2 = \sigma_1^2 + \sigma_2^2$. We write $x_n = u_n + v_n$, where u and v refer to the noise originating in intervals 1 and 2, respectively. Here u_n has correlations between the different time steps n due to the memory effect of the $1/f$ noise; on the other hand, v_n is incoherent and can be taken as a Gaussian i.i.d. random variable.

While it is impossible to unequivocally infer x_n from the measured z_n at each instance n, we can infer statistical properties of $\{x_n\}$, such as its correlations and spectral density, up to the frequency $f = 1/2t_{\text{rep}}$, which can approach $1/\tau_0$. This is advantageous compared to the ensemble-averaging method, which has a longer acquisition time $t_{\text{acq}} = Mt_{\text{rep}}$.

We can write the $m \neq n$ autocovariance function for $\Delta z_n = z_n - \langle z_n \rangle$ as

$$\langle \Delta z_m \, \Delta z_n \rangle = \langle \Delta y_m \, \Delta y_n \rangle = a_0^2 \langle \sin x_m \sin x_n \rangle \simeq \qquad (\text{C.2})$$

$$\simeq a_0^2 \langle x_m \, x_n \rangle = a_0^2 \langle u_m \, u_n \rangle.$$

The first equality holds because the Bernoulli trials are independent, and the last equality is the consequence of v_n being i.i.d., which implies $\langle u_m \, v_n \rangle = \langle v_m \, v_n \rangle = 0$. The third step is an equality only when $|x_n| \ll 1$; when σ_2 is large, e.g. at higher temperatures, or when we use a larger free-induction time τ_0 to decrease the statistical noise level, the variation of x_n can be large, and then this is not a good approximation. Instead of approximating, however, we can compensate the result for the sine nonlinearity. Expanding the correlator $\langle \Delta y_m \Delta y_n \rangle$, we obtain

$$\langle \sin x_m \sin x_n \rangle = \langle \sin(u_m + v_m) \sin(u_n + v_n) \rangle = \qquad (\text{C.3})$$
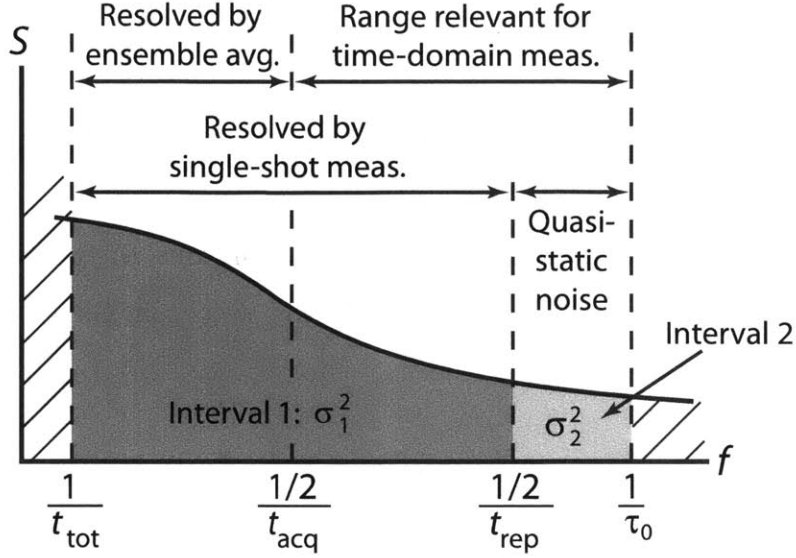
Figure C-1: Sketch of the PSD, indicating the frequency intervals resolved by the ensemble-averaging and single-shot schemes. Here t_{tot} is the total length of the recorded time-evolution trace (can be several minutes to hours); $t_{\mathrm{acq}} = 1 \sim 10\,\mathrm{s}$ is the acquisition time per measured point in time-domain experiments such as free-induction decay; $t_{\mathrm{rep}} = 1 \sim 2\,\mathrm{ms}$ is the repetition time (the acquisition/collection/sampling time in the single-shot scheme); and $\tau_0 \sim 1\,\mu s$ is the typical pulse spacing.

$$= \langle (\sin u_m \cos v_m + \cos u_m \sin v_m)(m \to n) \rangle.$$

Since sine is an odd function and v_n is a zero-mean, Gaussian i.i.d. variable, $\langle \sin v_{m,n} \rangle = 0$, and (C.3) becomes

$$\langle \sin u_m \cos v_m \sin u_n \cos v_n \rangle = \qquad (\mathrm{C.4})$$

$$= \langle \cos v_m \rangle \langle \cos v_n \rangle \langle \sin u_m \sin u_n \rangle.$$

The cosine factors depend on noise in interval 2, i.e., above the sampling frequency. This is similar to dephasing due to quasi-static noise, which acts uniformly on all the samples in time (incoherent averaging over a distribution of the noise), and leads to

185

Gaussian decay functions

$$\langle \cos v_{m,n} \rangle = \exp(-\sigma_2^2 \tau_0^2 / 2).$$ (C.5)

For the sine factor, the noise is from interval 1, i.e., it is resolved by our sampling, and therefore is not uniform. The process is a combination of ensemble-averaged incoherent noise and a frequency-dependent filtering due to the $(m - n)t_{\rm rep}$ time difference in the correlator. Evaluating this factor, we obtain Gaussian damping of a hyperbolic-sine function of the correlator,

$$\langle \sin u_m \sin u_n \rangle =$$ (C.6)

$$= \iint \mathrm{d}u_m \mathrm{d}u_n \, \sin u_m \sin u_n \, N(0, \sigma) =$$

$$= \exp(-\sigma_1^2 \tau_0^2) \sinh(\langle u_m u_n \rangle),$$

where the integral is taken over a two-dimensional normal distribution $N(0, \sigma)$ with zero mean and correlation matrix $\sigma = \{\sigma_m, \sigma_n, \sigma_{mn}\}$. (The distribution widths are equal, $\sigma_m = \sigma_n$, and $\sigma_{mn} = \langle u_m u_n \rangle$ is the correlation function.)

The correlator (C.2) finally becomes

$$\langle \Delta z_m \Delta z_n \rangle =$$ (C.7)

$$= a_0^2 \exp(-\sigma_1^2 \tau_0^2) \exp(-\sigma_2^2 \tau_0^2) \sinh(\langle u_m u_n \rangle).$$

Note that no approximation has been made so far. If the noise correlation due to $1/f$-type noise is small, as in our case where $\exp(\sigma_1^2 \tau_0^2) < 10$, we can neglect the frequency-dependent filtering effect and approximate $\sinh(\langle u_m u_n \rangle) \approx \langle u_m u_n \rangle$.

Now remains only the determination of the correction factors, which we know from the calibration measurement, $\exp\left[(\sigma_1^2 + \sigma_2^2)\tau_0^2\right] = (a_0/a(\tau_0))^2$, where we identify $a(\tau_0)/a_0 = h(\tau_0)$ (Eq. 2.43), so that, finally,

$$\langle u_m u_n \rangle \approx \langle \Delta z_m \Delta z_n \rangle / \left(a(\tau_0)\right)^2 .$$ (C.8)

We note that it resembles the signal damping due to dephasing in a Ramsey fringe. Therefore, the correction factor is $(a(\tau_0)/a(0))^2$.

Appendix D

Publications

[1] Jonas Bylander, Simon Gustavsson, Fei Yan, Fumiki Yoshihara, Khalil Harrabi, George Fitch, David G. Cory, Yasunobu Nakamura, Jaw-Shen Tsai, and William D. Oliver, "Noise spectroscopy through dynamical decoupling with a superconducting flux qubit", *Nature Phys.*, 7:565, 2011.

[2] Simon Gustavsson, Jonas Bylander, Fei Yan, William D. Oliver, Fumiki Yoshihara, and Yasunobu Nakamura, "Noise correlations in a flux qubit with tunable tunnel coupling", *Phys. Rev. B*, 84:014525, 2011.

[3] S. Gustavsson, J. Bylander, F. Yan, P. Forn-Díaz, V. Bolkhovsky, D. Braje, G. Fitch, K. Harrabi, D. Lennon, J. Miloshi, P. Murphy, R. Slattery, S. Spector, B. Turek, T. Weir, P. B. Welander, F. Yoshihara, D. G. Cory, Y. Nakamura, T. P. Orlando, and W. D. Oliver, "Driven Dynamics and Rotary Echo of a Qubit Tunably Coupled to a Harmonic Oscillator", *Phys. Rev. Lett.*, 108:170503, 2012.

[4] Fei Yan, Jonas Bylander, Simon Gustavsson, Fumiki Yoshihara, Khalil Harrabi, David G. Cory, Terry P. Orlando, Yasunobu Nakamura, Jaw-Shen Tsai, and

William D. Oliver, "Spectroscopy of low-frequency noise and its temperature dependence in a superconducting qubit", *Phys. Rev. B*, 85:174521, 2012.

[5] Simon Gustavsson, Fei Yan, Jonas Bylander, Fumiki Yoshihara, Yasunobu Nakamura, Terry P. Orlando, and William D. Oliver, "Dynamical Decoupling and Dephasing in Interacting Two-Level Systems", *Phys. Rev. Lett.*, 109:010502, 2012.

[6] Simon Gustavsson, Olger Zwier, Jonas Bylander, Fei Yan, Fumiki Yoshihara, Yasunobu Nakamura, Terry P. Orlando, and William D. Oliver, "Improving Quantum Gate Fidelities by Using a Qubit to Measure Microwave Pulse Distortions", *Phys. Rev. Lett.*, 110:040502, 2013.

[7] Fei Yan, Simon Gustavsson, Jonas Bylander, Xiaoyue Jin, Fumiki Yoshihara, David G. Cory, Yasunobu Nakamura, Terry P. Orlando, and William D. Oliver, "Rotating-frame relaxation $T_{1\rho}$ as a noise spectrum analyzer of a superconducting qubit undergoing driven evolution", Accepted for *Nature Commun.*, 2013.

Bibliography

[1] M. A. Nielsen and I. L. Chuang. *Quantum Computation and Quantum Information*. Cambridge University Press, 1st edition, 2000.

[2] R. P. Feynman. Simulating physics with computers. *Int. J. Theor. Phys.*, 21:467, 1982.

[3] P.W. Shor. Algorithms for quantum computation: discrete logarithms and factoring. In *Foundations of Computer Science, 1994 Proceedings., 35th Annual Symposium on*, pages 124–134, 1994.

[4] Peter W. Shor. Scheme for reducing decoherence in quantum computer memory. *Phys. Rev. A*, 52:R2493–R2496, Oct 1995.

[5] D. J. Griffith. *Introduction to Quantum Mechanics*. Pearson Prentice Hall, 2nd edition, 2004.

[6] E. Knill, R. Laflamme, and G. J. Milburn. A scheme for efficient quantum computation with linear optics. *Nature*, 409:46, 2001.

[7] Q. A. Turchette, C. J. Hood, W. Lange, H. Mabuchi, and H. J. Kimble. Measurement of conditional phase shifts for quantum logic. *Phys. Rev. Lett.*, 75:4710–4713, Dec 1995.

[8] David P. DiVincenzo. Two-bit gates are universal for quantum computation. *Phys. Rev. A*, 51:1015–1022, Feb 1995.

[9] J. I. Cirac and P. Zoller. Quantum computations with cold trapped ions. *Phys. Rev. Lett.*, 74:4091–4094, May 1995.

[10] Daniel Loss and David P. DiVincenzo. Quantum computation with quantum dots. *Phys. Rev. A*, 57:120–126, Jan 1998.

[11] Yuriy Makhlin, Gerd Schön, and Alexander Shnirman. Quantum-state engineering with josephson-junction devices. *Rev. Mod. Phys.*, 73:357–400, May 2001.

[12] Michel H. Devoret and John M. Martinis. Implementing qubits with superconducting integrated circuits. *Quantum Information Processing*, 3(1-5):163–203, 2004.

[13] John Clarke and Frank K. Wilhelm. Superconducting quantum bits. *Nature*, 453:1031, 2008.

[14] J. E. Mooij, T. P. Orlando, L. Levitov, Lin Tian, Caspar H. van der Wal, and Seth Lloyd. Josephson persistent-current qubit. *Science*, 285(5430):1036–1039, 1999.

[15] T. P. Orlando, J. E. Mooij, Lin Tian, Caspar H. van der Wal, L. S. Levitov, Seth Lloyd, and J. J. Mazo. Superconducting persistent-current qubit. *Phys. Rev. B*, 60:15398–15413, Dec 1999.

[16] B. D. Josephson. The discovery of tunnelling supercurrents. *Rev. Mod. Phys.*, 46:251–254, Apr 1974.

[17] David P. DiVincenzo. The physical implementation of quantum computation. *Fortschritte der Physik*, 48(9-11):771–783, 2000.

[18] Y. Nakamura, Yu. A. Pashkin, and J. S. Tsai. Coherent control of macroscopic quantum states in a single-cooper-pair box. *Nature*, 398:786, 1999.

[19] Chad Rigetti, Jay M. Gambetta, Stefano Poletto, B. L. T. Plourde, Jerry M. Chow, A. D. Córcoles, John A. Smolin, Seth T. Merkel, J. R. Rozen, George A. Keefe, Mary B. Rothwell, Mark B. Ketchen, and M. Steffen. Superconducting qubit in a waveguide cavity with a coherence time approaching 0.1 ms. *Phys. Rev. B*, 86:100506, Sep 2012.

[20] Matthias Steffen. Superconducting qubits are getting serious. *Physics*, 4:103, Dec 2011.

[21] Jonas Bylander, Simon Gustavsson, Fei Yan, Fumiki Yoshihara, Khalil Harrabi, George Fitch, David G. Cory, Yasunobu Nakamura, Jaw-Shen Tsai, and William D. Oliver. Noise spectroscopy through dynamical decoupling with a superconducting flux qubit. *Nature Phys.*, 7:565–570, 2011.

[22] C. P. Slichter. *Principles of Magnetic Resonance*. Springer, New York, 3rd edition, 1990.

[23] R.R Ernst. *Principles of Nuclear Magnetic Resonance in One and Two Dimensions*. Oxford University Press, USA, 1990.

[24] David G. Cory, Amr F. Fahmy, and Timothy F. Havel. Ensemble quantum computing by nmrspectroscopy. *Proceedings of the National Academy of Sciences*, 94(5):1634–1639, 1997.

[25] Isaac L. Chuang, Neil Gershenfeld, and Mark Kubinec. Experimental implementation of fast quantum searching. *Phys. Rev. Lett.*, 80:3408–3411, Apr 1998.

[26] D. G. Cory, M. D. Price, W. Maas, E. Knill, R. Laflamme, W. H. Zurek, T. F. Havel, and S. S. Somaroo. Experimental quantum error correction. *Phys. Rev. Lett.*, 81:2152–2155, Sep 1998.

[27] S. Somaroo, C. H. Tseng, T. F. Havel, R. Laflamme, and D. G. Cory. Quantum simulations on a quantum computer. *Phys. Rev. Lett.*, 82:5381–5384, Jun 1999.

[28] Lieven M. K. Vandersypen, Matthias Steffen, Gregory Breyta, Costantino S. Yannoni, Mark H. Sherwood, and Isaac L. Chuang. Experimental realization of shor's quantum factoring algorithm using nuclear magnetic resonance. *Nature*, 414(6866):883, 2001.

[29] Caspar H. van der Wal, A. C. J. ter Haar, F. K. Wilhelm, R. N. Schouten, C. J. P. M. Harmans, T. P. Orlando, Seth Lloyd, and J. E. Mooij. Quantum superposition of macroscopic persistent-current states. *Science*, 290(5492):773–777, 2000.

[30] William D. Oliver, Yang Yu, Janice C. Lee, Karl K. Berggren, Leonid S. Levitov, and Terry P. Orlando. Mach-zehnder interferometry in a strongly driven superconducting qubit. *Science*, 310(5754):1653–1657, 2005.

[31] Sergio O. Valenzuela, William D. Oliver, David M. Berns, Karl K. Berggren, Leonid S. Levitov, and Terry P. Orlando. Microwave-induced cooling of a superconducting qubit. *Science*, 314(5805):1589–1592, 2006.

[32] David M. Berns, Mark S. Rudner, Sergio O. Valenzuela, Karl K. Berggren, William D. Oliver, Leonid S. Levitov, and Terry P. Orlando. Amplitude spectroscopy of a solid-state artificial atom. *Nature*, 455:51, 2008.

[33] M. W. Johnson et al. Quantum annealing with manufactured spins. *Nature*, 73:194, 2011.

[34] A. M. Zagoskin. *Quantum Engineering: Theory and Design of Quantum Coherent Structures*. Cambridge University Press, 1st edition, 2011.

[35] M. H. Levitt. *Spin Dynamics*. Wiley, 2nd edition, 2008.

[36] F. Bloch. Nuclear induction. *Phys. Rev.*, 70:460–474, Oct 1946.

[37] G. Ithier. Manipulation, readout and analysis of the decoherence of a superconducting quantum bit. Doctoral thesis, Université Paris VI, 2005.

[38] D. M. Berns. Large amplitude driving of a persistent current qubit. Doctoral Thesis, Massachusetts Institute of Technology, 2008.

[39] I. I. Rabi. Space quantization in a gyrating magnetic field. *Phys. Rev.*, 51:652–654, Apr 1937.

[40] R. K. Wangsness and F. Bloch. The dynamical theory of nuclear induction. *Phys. Rev.*, 89:728–739, Feb 1953.

[41] F. Bloch. Generalized theory of relaxation. *Phys. Rev.*, 105:1206–1222, Feb 1957.

[42] A. G. Redfield. On the theory of relaxation processes. *IBM Journal of Research and Development*, 1:19, Jan 1957.

[43] Yu Makhlin. Dephasing of qubits by transverse low-frequency noise. *JETP Letters*, 78:497, 2003.

[44] Fei Yan, Jonas Bylander, Simon Gustavsson, Fumiki Yoshihara, Khalil Harrabi, David G. Cory, Terry P. Orlando, Yasunobu Nakamura, Jaw-Shen Tsai, and William D. Oliver. Spectroscopy of low-frequency noise and its temperature dependence in a superconducting qubit. *Phys. Rev. B*, 85:174521, May 2012.

[45] Norman F. Ramsey. A molecular beam resonance method with separated oscillating fields. *Phys. Rev.*, 78:695–699, Jun 1950.

[46] G. Ithier, E. Collin, P. Joyez, P. J. Meeson, D. Vion, D. Esteve, F. Chiarello, A. Shnirman, Y. Makhlin, J. Schriefl, and G. Schön. Decoherence in a superconducting quantum bit circuit. *Phys. Rev. B*, 72:134519, Oct 2005.

[47] Götz S. Uhrig. Exact results on dynamical decoupling by pulses in quantum information processes. *New Journal of Physics*, 10(8):083024, 2008.

[48] Lukasz Cywiński, Roman M. Lutchyn, Cody P. Nave, and S. Das Sarma. How to enhance dephasing time in superconducting qubits. *Phys. Rev. B*, 77:174509, May 2008.

[49] E. L. Hahn. Spin echoes. *Phys. Rev.*, 80:580–594, Nov 1950.

[50] H. Y. Carr and E. M. Purcell. Effects of diffusion on free precession in nuclear magnetic resonance experiments. *Phys. Rev.*, 94:630–638, May 1954.

[51] S. Meiboom and D. Gill. Modified spin echo method for measuring nuclear relaxation times. *Review of Scientific Instruments*, 29(8):688–691, 1958.

[52] Lorenza Viola and Seth Lloyd. Dynamical suppression of decoherence in two-state quantum systems. *Phys. Rev. A*, 58:2733–2744, Oct 1998.

[53] Pochung Chen. Dynamical decoupling-induced renormalization of non-markovian dynamics. *Phys. Rev. A*, 75:062301, Jun 2007.

[54] Götz S. Uhrig. Keeping a quantum bit alive by optimized π-pulse sequences. *Phys. Rev. Lett.*, 98:100504, Mar 2007.

[55] K. Khodjasteh and D. A. Lidar. Fault-tolerant quantum dynamical decoupling. *Phys. Rev. Lett.*, 95:180501, Oct 2005.

[56] E. Geva, R. Kosloff, and J. L. Skinner. On the relaxation of a two-level system driven by a strong electromagnetic field. *J. Chem. Phys.*, 102:8541, 1995.

[57] Anatoly Yu. Smirnov. Decoherence and relaxation of a quantum bit in the presence of rabi oscillations. *Phys. Rev. B*, 67:155104, Apr 2003.

[58] S. Gustavsson, J. Bylander, F. Yan, P. Forn-Díaz, V. Bolkhovsky, D. Braje, G. Fitch, K. Harrabi, D. Lennon, J. Miloshi, P. Murphy, R. Slattery, S. Spector, B. Turek, T. Weir, P. B. Welander, F. Yoshihara, D. G. Cory, Y. Nakamura, T. P. Orlando, and W. D. Oliver. Driven dynamics and rotary echo of a qubit tunably coupled to a harmonic oscillator. *Phys. Rev. Lett.*, 108:170503, Apr 2012.

[59] Charles P. Slichter and David Ailion. Low-field relaxation and the study of ultraslow atomic motions by magnetic resonance. *Phys. Rev.*, 135:A1099–A1110, Aug 1964.

[60] David C. Ailion and Charles P. Slichter. Observation of ultra-slow translational diffusion in metallic lithium by magnetic resonance. *Phys. Rev.*, 137:A235–A245, Jan 1965.

[61] D. C. Look and I. J. Lowe. Nuclear magnetic dipoledipole relaxation along the static and rotating magnetic fields: Application to gypsum. *J. Chem. Phys.*, 44:2995, 1966.

[62] E. Collin, G. Ithier, A. Aassime, P. Joyez, D. Vion, and D. Esteve. Nmr-like control of a quantum bit superconducting circuit. *Phys. Rev. Lett.*, 93:157005, Oct 2004.

[63] I. Solomon. Rotary spin echoes. *Phys. Rev. Lett.*, 2:301–302, Apr 1959.

[64] I. Chiorescu, Y. Nakamura, C. J. P. M. Harmans, and J. E. Mooij. Coherent quantum dynamics of a superconducting flux qubit. *Science*, 299(5614):1869–1871, 2003.

[65] O. Astafiev, Yu. A. Pashkin, Y. Nakamura, T. Yamamoto, and J. S. Tsai. Quantum noise in the Josephson charge qubit. *Phys. Rev. Lett.*, 93(26):267007, Dec 2004.

[66] F. Yoshihara, K. Harrabi, A. O. Niskanen, Y. Nakamura, and J. S. Tsai. Decoherence of flux qubits due to $1/f$ flux noise. *Phys. Rev. Lett.*, 97:167001, Oct 2006.

[67] Fumiki Yoshihara. in preparation, 2013.

[68] Richard F. Voss and Richard A. Webb. Macroscopic quantum tunneling in 1-μm nb josephson junctions. *Phys. Rev. Lett.*, 47:265–268, Jul 1981.

[69] John M. Martinis, Michel H. Devoret, and John Clarke. Energy-level quantization in the zero-voltage state of a current-biased josephson junction. *Phys. Rev. Lett.*, 55:1543–1546, Oct 1985.

[70] R. Rouse, Siyuan Han, and J. E. Lukens. Observation of resonant tunneling between macroscopically distinct quantum levels. *Phys. Rev. Lett.*, 75:1614–1617, Aug 1995.

[71] Leon N. Cooper. Bound electron pairs in a degenerate fermi gas. *Phys. Rev.*, 104:1189–1190, Nov 1956.

[72] J. Bardeen, L. N. Cooper, and J. R. Schrieffer. Microscopic theory of superconductivity. *Phys. Rev.*, 106:162–164, Apr 1957.

[73] J. Bardeen, L. N. Cooper, and J. R. Schrieffer. Theory of superconductivity. *Phys. Rev.*, 108:1175–1204, Dec 1957.

[74] M. Tinkham. *Introduction to Superconductivity.* Dover Publications, 2nd edition, 2004.

[75] Yang Yu, Siyuan Han, Xi Chu, Shih-I Chu, and Zhen Wang. Coherent temporal oscillations of macroscopic quantum states in a josephson junction. *Science*, 296(5569):889–892, 2002.

[76] John M. Martinis. Superconducting phase qubits. *Quantum Information Processing*, 8(2-3):81–103, 2009.

[77] Jonathan R. Friedman, Vijay Patel, W. Chen, S. K. Tolpygo, and J. E. Lukens. Quantum superposition of distinct macroscopic states. *Nature*, 406:43, 2000.

[78] A. J. Leggett and Anupam Garg. Quantum mechanics versus macroscopic realism: Is the flux there when nobody looks? *Phys. Rev. Lett.*, 54:857–860, Mar 1985.

[79] D. S. Crankshaw. Measurement and on-chip control of a niobium persistent current qubit. Doctoral Thesis, Massachusetts Institute of Technology, 2008.

[80] J. Clarke and A. I. Braginski. *The SQUID Handbook: Fundamentals and Technology of SQUIDs and SQUID Systems Vol. I.* Wiley, Weinheim, 2004.

[81] Shao-Xiong Li, Yang Yu, Yu Zhang, Wei Qiu, Siyuan Han, and Zhen Wang. Quantitative study of macroscopic quantum tunneling in a dc squid: A system with two degrees of freedom. *Phys. Rev. Lett.*, 89:098301, Aug 2002.

[82] L. Tian. A superconducting flux qubit: Measurement, noise and control. Doctoral Thesis, Massachusetts Institute of Technology, 2002.

[83] Guido Burkard, David P. DiVincenzo, P. Bertet, I. Chiorescu, and J. E. Mooij. Asymmetry and decoherence in a double-layer persistent-current qubit. *Phys. Rev. B*, 71:134504, Apr 2005.

[84] Simon Gustavsson, Olger Zwier, Jonas Bylander, Fei Yan, Fumiki Yoshihara, Yasunobu Nakamura, Terry P. Orlando, and William D. Oliver. Improving quantum gate fidelities by using a qubit to measure microwave pulse distortions. *Phys. Rev. Lett.*, 110:040502, Jan 2013.

[85] L. Allen and Eberly J. H. *Optical Resonance and Two-Level Atoms.* Dover Publications, 1987.

[86] Simon Gustavsson, Jonas Bylander, Fei Yan, William D. Oliver, Fumiki Yoshihara, and Yasunobu Nakamura. Noise correlations in a flux qubit with tunable tunnel coupling. *Phys. Rev. B*, 84:014525, Jul 2011.

[87] Frederick C. Wellstood, Cristian Urbina, and John Clarke. Low-frequency noise in dc superconducting quantum interference devices below 1 K. *Appl. Phys. Lett.*, 50:772–774, 1987.

[88] Simon Gustavsson, Fei Yan, Jonas Bylander, Fumiki Yoshihara, Yasunobu Nakamura, Terry P. Orlando, and William D. Oliver. Dynamical decoupling and dephasing in interacting two-level systems. *Phys. Rev. Lett.*, 109:010502, Jul 2012.

[89] G. Catelani, J. Koch, L. Frunzio, R. J. Schoelkopf, M. H. Devoret, and L. I. Glazman. Quasiparticle relaxation of superconducting qubits in the presence of flux. *Phys. Rev. Lett.*, 106:077002, Feb 2011.

[90] G. Catelani, R. J. Schoelkopf, M. H. Devoret, and L. I. Glazman. Relaxation and frequency shifts induced by quasiparticles in superconducting qubits. *Phys. Rev. B*, 84:064517, Aug 2011.

[91] D. J. Van Harlingen, T. L. Robertson, B. L. T. Plourde, P. A. Reichardt, T. A. Crane, and John Clarke. Decoherence in josephson-junction qubits due to critical-current fluctuations. *Phys. Rev. B*, 70:064517, Aug 2004.

[92] Fei Yan, Simon Gustavsson, Jonas Bylander, Xiaoyue Jin, Fumiki Yoshihara, David G. Cory, Yasunobu Nakamura, Terry P. Orlando, and William D. Oliver. Rotating-frame relaxation $T_{1\rho}$ as a noise spectrum analyzer of a superconducting qubit undergoing driven evolution. Accepted for *Nature Commun.*, 2013.

[93] S. Sendelbach, D. Hover, A. Kittel, M. Mück, John M. Martinis, and R. McDermott. Magnetism in squids at millikelvin temperatures. *Phys. Rev. Lett.*, 100:227006, Jun 2008.

[94] S. Sendelbach, D. Hover, M. Mück, and R. McDermott. Complex inductance, excess noise, and surface magnetism in dc squids. *Phys. Rev. Lett.*, 103:117001, Sep 2009.

[95] Roger H. Koch, David P. DiVincenzo, and John Clarke. Model for $1/f$ flux noise in squids and qubits. *Phys. Rev. Lett.*, 98:267003, Jun 2007.

[96] SangKook Choi, Dung-Hai Lee, Steven G. Louie, and John Clarke. Localization of metal-induced gap states at the metal-insulator interface: Origin of flux noise in squids and superconducting qubits. *Phys. Rev. Lett.*, 103(19):197001, Nov 2009.

[97] F. Yoshihara, Y. Nakamura, and J. S. Tsai. Correlated flux noise and decoherence in two inductively coupled flux qubits. *Phys. Rev. B*, 81(13):132502, Apr 2010.

[98] Roger H. Koch, John Clarke, W. M. Goubau, J. M. Martinis, C. M. Pegrum, and D. J. van Harlingen. Flicker (1/f) noise in tunnel junction dc squids. *J. Low. Temp. Phys.*, 51:207–224, 1983.

[99] Radoslaw C. Bialczak, R. McDermott, M. Ansmann, M. Hofheinz, N. Katz, Erik Lucero, Matthew Neeley, A. D. O'Connell, H. Wang, A. N. Cleland, and John M. Martinis. 1/f flux noise in josephson phase qubits. *Phys. Rev. Lett.*, 99:187006, Nov 2007.

[100] Lara Faoro and Lev B. Ioffe. Microscopic origin of low-frequency flux noise in josephson circuits. *Phys. Rev. Lett.*, 100:227005, Jun 2008.

[101] T. Lanting, A. J. Berkley, B. Bumble, P. Bunyk, A. Fung, J. Johansson, A. Kaul, A. Kleinsasser, E. Ladizinsky, F. Maibaum, R. Harris, M. W. Johnson, E. Tolkacheva, and M. H. S. Amin. Geometrical dependence of the low-frequency noise in superconducting flux qubits. *Phys. Rev. B*, 79:060509, Feb 2009.

[102] F.C. Wellstood, C. Urbina, and John Clarke. Role of geometry on the color of flux noise in dc squids. *Applied Superconductivity, IEEE Transactions on*, 21(3):856–859, 2011.

[103] F. C. Wellstood, C. Urbina, and John Clarke. Flicker (1/f) noise in the critical current of josephson junctions at 0.09–4.2 k. *Appl. Phys. Lett.*, 85(22):5296–5298, 2004.

[104] M. Mück, M. Korn, C. G. A. Mugford, J. B. Kycia, and J. Clarke. Measurements of 1/f noise in Josephson junctions at zero voltage: Implications for decoherence in superconducting quantum bits. *Applied Physics Letters*, 86(1):012510, January 2005.

[105] J. Eroms, L. C. van Schaarenburg, E. F. C. Driessen, J. H. Plantenberg, K. Huizinga, R. N. Schouten, A. H. Verbruggen, C. J. P. M. Harmans, and J. E. Mooij. Low-frequency noise in Josephson junctions for superconducting qubits. *Appl. Phys. Lett.*, 89:122516, 2006.

[106] Daniel Sank, R. Barends, Radoslaw C. Bialczak, Yu Chen, J. Kelly, M. Lenander, E. Lucero, Matteo Mariantoni, A. Megrant, M. Neeley, P. J. J. O'Malley, A. Vainsencher, H. Wang, J. Wenner, T. C. White, T. Yamamoto, Yi Yin, A. N. Cleland, and John M. Martinis. Flux noise probed with real time qubit tomography in a josephson phase qubit. *Phys. Rev. Lett.*, 109:067001, Aug 2012.

[107] D. H. Slichter, R. Vijay, S. J. Weber, S. Boutin, M. Boissonneault, J. M. Gambetta, A. Blais, and I. Siddiqi. Measurement-induced qubit state mixing in circuit qed from up-converted dephasing noise. *Phys. Rev. Lett.*, 109:153601, Oct 2012.

[108] W. Schottky. ber spontane stromschwankungen in verschiedenen elektrizittsleit-ern. *Annalen der Physik*, 362(23):541–567, 1918.

[109] Hanhee Paik, D. I. Schuster, Lev S. Bishop, G. Kirchmair, G. Catelani, A. P. Sears, B. R. Johnson, M. J. Reagor, L. Frunzio, L. I. Glazman, S. M. Girvin, M. H. Devoret, and R. J. Schoelkopf. Observation of high coherence in josephson junction qubits measured in a three-dimensional circuit qed architecture. *Phys. Rev. Lett.*, 107:240501, Dec 2011.

[110] Kevin Bladh, David Gunnarsson, Abdelhanin Aassime, Marian Taslakov, Rob Schoelkopf, and Per Delsing. Noise performance of the radio-frequency single-electron transistor. *Phys. E*, 18(1-3):91–92, 2003.

[111] Neil M. Zimmerman and William H. Huber. Microscope of glassy relaxation in femtogram samples: Charge offset drift in the single electron transistor. *Phys. Rev. B*, 80:195304, Nov 2009.

[112] M. Gustafsson, A. Pourkabirian, G. Johansson, J. Clarke, and P. Delsing. Activation mechanisms for charge noise. 2012.

[113] C. M. Dawson and M. A. Nielsen. The solovay-kitaev algorithm. Preprint at http:/arxiv.org/abs/quant-ph/0505030, 2005.

[114] R. J. Schoelkopf, A. A. Clerk, S. M. Girvin, K. W. Lehnert, and M. H. Devoret. in *Quantum Noise in Mesoscopic Physics* Y. V. Nazarov, Ed., pages 175–203. Kluwer, Dordrecht, 2002.

[115] M. J. Biercuk, H. Uys, A. P. VanDevender, N. Shiga, W. M. Itano, and J. J. Bollinger. Optimized dynamical decoupling in a model quantum memory. *Nature*, 458:996, 2009.

[116] Yoav Sagi, Ido Almog, and Nir Davidson. Process tomography of dynamical decoupling in a dense cold atomic ensemble. *Phys. Rev. Lett.*, 105:053201, Jul 2010.

[117] D J Szwer, S C Webster, A M Steane, and D M Lucas. Keeping a single qubit alive by experimental dynamic decoupling. *Journal of Physics B: Atomic, Molecular and Optical Physics*, 44(2):025501, 2011.

[118] J. Du, X. Rong, N. Zhao, Y. Wang, J. Yang, and R. B. Liu. Preserving electron spin coherence in solids by optimal dynamical decoupling. *Nature*, 461:1265, 2009.

[119] G. de Lange, Z. H. Wang, D. Rist, V. V. Dobrovitski, and R. Hanson. Universal dynamical decoupling of a single solid-state spin from a spin bath. *Science*, 330(6000):60–63, 2010.

[120] C. A. Ryan, J. S. Hodges, and D. G. Cory. Robust decoupling techniques to extend quantum coherence in diamond. *Phys. Rev. Lett.*, 105:200402, Nov 2010.

[121] C. Barthel, J. Medford, C. M. Marcus, M. P. Hanson, and A. C. Gossard. Interlaced dynamical decoupling and coherent operation of a singlet-triplet qubit. *Phys. Rev. Lett.*, 105:266808, Dec 2010.

[122] Hendrik Bluhm, Sandra Foletti, Izhar Neder, Mark Rudner, Diana Mahalu, Vladimir Umansky, and Amir Yacoby. Dephasing time of gaas electron-spin qubits coupled to a nuclear bath exceeding $200\mu s$. *Nature Phys.*, 7:109–113, 2011.

[123] Michael J. Biercuk, Hermann Uys, Aaron P. VanDevender, Nobuyasu Shiga, Wayne M. Itano, and John J. Bollinger. Experimental uhrig dynamical decoupling using trapped ions. *Phys. Rev. A*, 79:062324, Jun 2009.

[124] M. Loretz, T. Rosskopf, and C. L. Degen. Radio-frequency magnetometry using a single electron spin. *Phys. Rev. Lett.*, 110:017602, Jan 2013.

[125] P. Bertet, I. Chiorescu, G. Burkard, K. Semba, C. J. P. M. Harmans, D. P. DiVincenzo, and J. E. Mooij. Dephasing of a superconducting qubit induced by photon noise. *Phys. Rev. Lett.*, 95:257002, Dec 2005.

[126] Y. M. Galperin, B. L. Altshuler, J. Bergli, and D. V. Shantsev. Nongaussian low-frequency noise as a source of qubit decoherence. *Phys. Rev. Lett.*, 96:097009, Mar 2006.

[127] E. Paladino, L. Faoro, G. Falci, and Rosario Fazio. Decoherence and $1/f$ noise in josephson qubits. *Phys. Rev. Lett.*, 88:228304, May 2002.

[128] Alexander Shnirman, Gerd Schön, Ivar Martin, and Yuriy Makhlin. Low- and high-frequency noise from coherent two-level systems. *Phys. Rev. Lett.*, 94:127002, Apr 2005.

[129] A. A. Clerk, M. H. Devoret, S. M. Girvin, Florian Marquardt, and R. J. Schoelkopf. Introduction to quantum noise, measurement, and amplification. *Rev. Mod. Phys.*, 82:1155–1208, Apr 2010.

[130] Ulrich Weiss. *Quantum Dissipative Systems*. World Scientific Publishing Company, 3rd edition, 2008.

[131] M. Grifoni, E. Paladino, and U. Weiss. Dissipation, decoherence and preparation effects in the spin-boson system. *The European Physical Journal B - Condensed Matter and Complex Systems*, 10(4):719–729, 1999.